A comparative study of atmospheric dynamics in the mesosphere and lower thermosphere (MLT) near Grahamstown (South Africa) and Adelaide (Australia)

A thesis submitted in fulfilment of the requirements for the degree of

DOCTOR OF PHILOSOPHY (SCIENCE)

of

RHODES UNIVERSITY

by

SANDILE BETHUEL MALINGA

May 2001

ABSTRACT

The observations made near Grahamstown (33.3°S, 26.5°E), South Africa and Adelaide (34.5°S, 138.5°E), Australia over the years 1987 to 1994 are used to study the dynamics of the mesosphere and lower thermosphere (MLT) region with a focus on ~90 km altitude. In particular this thesis deals with on the atmospheric mean flow and the solar diurnal and semidiurnal oscillations with a view to (i) deducing their patterns at the two sites, (ii) comparing the dynamic structures observed at the two sites with special emphases on longitudinal variations, and (iii) putting these observations in a global context by comparing with other ground-based observations, satellite observations and numerical simulations. The main findings are summarised below.

The mean flow and the tides at Grahamstown and Adelaide are characteristically variable at planetary time scales. Wavelet spectral and multiresolution analyses reveal that the dominant planetary oscillation is the quasi-16-day oscillation. However, no apparent correlation in the 16-day waves of the mean flow, the diurnal tide and the semidiurnal tide was found. The short-term fluctuations were also investigated using complex demodulation and bispectral techniques and it was found that some of the observed variations in tides could be due to non-linear wave-wave interactions.

The long-term trends of the mean flow and tides show patterns that are in broad agreement with theory, results from elsewhere (ground-based and satellite) and the results of the Global-Scale Wave Model and various models by Portnyagin and others. In general the mean flow, the amplitudes and phases of both tides were found to exhibit seasonal and interannual variations which are thought to be related to various factors including (i)

changes in the atmospheric mean environment, (ii) thermotidal forcing (iii) gravity wave effects, (iv) planetary scale influence, (v) long-term (e.g. quasi-biennial oscillation) modulation, and (vi) solar activity. There are significant longitudinal differences in the dynamic structure between Grahamstown and Adelaide. More especially, Grahamstown tends to have stronger mean flow and tidal activity than Adelaide. For tides, these differences are thought to be partly due to nonmigrating tidal modes but, in general, migrating modes were found to be dominant.

ACKNOWLEDGEMENTS

First, I would like to thank God Almighty for the privilege to be able to do this work and also for the strength and encouragement to complete it. Secondly, I would like to thank my wife Saynile from the bottom of my heart for the support, love, patience and encouragement during my research. Thank you for the sacrifices you made for me and for taking care of the little ones. *Ngiyabonga.* I would also like to thank my two children Sibusiso and Bongiwe, who were both born in the course of my PhD. Thank for your understanding and patience. I am back home now and daddy is "..*not* going to the Physics Department". I would also like to thank my parents who did whatever they could with the little that they have just to give me education. *Ngiyabonga.*

On the research side of things, this work would not have been possible without my supervisor Prof G. Poole who has been with me since my honours years. Thank you "Prof" for your guidance, support and for the numerous valuable things you have taught me. I would also like to thank Dr R. A. Vincent for the Adelaide data, without which this research would not have been possible. I would also like to thank Dr M. Hagan and acknowledge the CEDAR Database for the Global Scale Wave Model (GSWM-00) data. Many thanks also go to Prof Y. Portnyagin for giving me his model data. My gratitude also goes to Dr P. Nathanson and Dr J. Jonas especially on computer related matters. I would also like to thank Lee-Anne McKinnell for making it possible for me to save my work on a CD and the printing. I would also like to thank everyone at Physics more especially Althea Coupé and Serita Maree. I am also indebted to the Andrew Mellon Foundation for the financial support they give me and to John Gillam for his administrative assistance.

TABLE OF CONTENTS

LIST OF FIGURES

CHAPTER 2

CHAPTER 3

CHAPTER 4

CHAPTER 5

CHAPTER 6

CHAPTER 7

APPENDIX

LIST OF TABLES

ACRONYMS

A/D=Analogue-to-digital converter

AD = Adelaide

AO = Annual oscillation

CIRA-86= COSPAR International Reference Atmosphere: 1986

CMAM =Canadian Middle Atmosphere Model

COSPAR= Committee on Space Research

cpd = Cycles per day

CWT=Continuous wavelet transform

DC=Direct current

DCA = Deep convective activity

DSP = Doppler Spread Parameterization

DT = Diurnal tide

DTM = Diurnal Tide Model

DWT=Discrete wavelet transform

EPFD =Eliassen-Palm flux divergence

EW = Zonal

FCA=Full correlation analysis

GCM=General circulation model

GSWM = Global scale wave model

GT =Grahamstown

HF=High frequency

HRDI = High resolution Doppler imager

HWM-93= Horizontal wind model

IA = Interannual average

IB = Integrated (height) bin

IR = Infrared

ISR = Incoherent scatter radar

LF=Low frequency

MF=Medium frequency

MIA = Monthly interannual average

MLT=Mesosphere lower thermosphere

MSAO = Mesospheric semi-annual oscillation

MST= Mesosphere-stratosphere-troposphere

MWM = Mean wind model

NS = Meridional

NSM=Numerical spectral model

PRF=Pulse repetition frequency

QBO= Quasi-biennial oscillation

SA=spaced antenna (method)

SAO= Semi-annual oscillation

SAPR =Spaced-antenna partial-reflection

SB=Single (height) bin

ST = Semidiurnal tide

STFT = Short-time Fourier transform

STM = Semidiurnal tide model

u = Zonal

UARS = Upper atmosphere research satellite

UV = Ultraviolet

v = Meridional

WINDII = Wind imaging interferometer

CHAPTER 1 INTRODUCTION

1.1 THE THESIS

Many people, scientists and laypeople alike, have been concerned about various environmental issues like the ozone layer and global warming. These issues are related to the dynamics of the atmosphere and the oceans. In general, the atmosphere has a direct response to radiative effects and responds indirectly through feedback mechanisms that are largely dynamic in nature. For instance the asymmetric meridional (north-south) heating of the atmosphere results in mass transport that, in turn, results in the dynamic cooling/heating of the atmosphere. A related effect of this mass transport is the transportation of minor constituents as well as pollutants.

Another example involves gravity waves whose interaction with tides, may result in the modulation of acceleration, heating and turbulent diffusion [*Forbes et al.*, 1991]. The tidal modulation of gravity wave dissipation suggests significant latitudinal and local time changes in eddy diffusivity, which may affect the distribution of chemical species like O, O_3, OH and NO [*Forbes et al.*, 1991]. Possible scenarios may include the accumulation or depletion of certain chemical species and this would lead to a change in the local chemistry. A good example of this is the formation of the ozone hole at the poles during spring [*Harris*, 1993].

Even with the few examples outlined above, we can see coupling between the dynamic, thermal and chemical processes of the atmosphere, which may, at times, lead to serious environmental hazards. The examples given above are not, by any means, all-inclusive but just give us a feel of the numerous and often complicated and coupled processes of the atmosphere. Part of the complication stems from the fact that the atmosphere is an inhomogeneous and horizontally and vertically coupled system. In general, various atmospheric processes and motions of various scales assume significance at different horizontal (zonal/longitudinal and meridional/latitudinal) and vertical regions of the atmosphere. Added to this, there is also time dependence in these processes. It is for this reason that a thorough understanding of the atmosphere requires a four dimensional approach that considers the spatial and temporal structures. However, for practical reasons, it is difficult to conduct a comprehensive four-dimensional study of the atmosphere. Different studies usually focus on one or two of the various dimensions of atmospheric variation.

In this study, I am concerned with the comparison of the dynamics of the neutral atmosphere at

Grahamstown (33.3°S, 26.5°E, South Africa) and Adelaide (34.5°S, 138.5°E, Australia). These two sites are well positioned to allow for a study of the *horizontal* (and more specifically the *longitudinal*) structure of the atmosphere with minimal latitudinal effect. The importance of studying the influence of longitudinal factors on the dynamics of the atmosphere is to assist in model efforts, which have mostly concentrated on latitudinal dynamic structures. Of late, attempts are being made to incorporate longitudinal effects into models and it is hoped that this study will provide an experimental contribution to such theoretical simulations. At the same time, since the two sites are essentially at ~34°S, this study will also give an experimental perspective of the dynamics of the atmosphere around this *latitude*.

Vertically, instrument limitations restrict me to only consider the dynamics of the mesosphere and lower atmosphere (MLT) and more specifically a single height of ~90 km. Although the MLT contains less than 0.1% of the mass of the atmosphere [*Thomas*, 1996], its study is important for various reasons. *Thomas* [1996] lists just a few and these include the following: (i) changes in this region may give early warning signs of changes that may be delayed for years due the long atmosphere-ocean time lag; (ii) changes in the density of the upper atmosphere may affect the re-entry of space vehicles, and in the ionosphere it may affect space communications; (iii) the ability to correctly model the variability of the physical state of the upper atmosphere provides an excellent opportunity to test theory.

The time resolution of the Grahamstown and Adelaide data at my disposal allows for a detailed *temporal* analysis at an altitude of ~ 90 km. As a result there will be more focus on the short-term, seasonal and interannual trends of the MLT dynamics. In particular, I will study the temporal variations of the mean flow and of atmospheric thermal tides. These dynamic variables will be introduced in the next sections together with other related dynamic components of the atmosphere.

1.2 ATMOSPHERIC MOTION

1.2.1 The Mean Circulation

One of the major components of the dynamics of the MLT region is the mean flow, which is primarily governed by momentum deposition from various atmospheric waves like gravity waves, tides and planetary waves. At the same time, the mean wind also affects some of the

waves it interacts with in various ways. For instance, the vertical propagation of some these waves are dependent on the mean flow environment through which they propagate. Consequently, the mean flow affects, among other things, the deposition of momentum, atmospheric turbulence and the associated transportation of heat and chemical species.

The mean wind also plays a very important role in the thermodynamic structure of the atmosphere. The temperature structure above ~70 km is inconsistent with radiative equilibrium [*Murphy & Vincent*, 1998] and is dynamically sustained by the rising (falling) of air and the associated adiabatic cooling (heating) in the summer (winter) hemisphere. This requires that there should be some meridional transport of mass and hence heat and this is accomplished by the meridional mean flow

1.2.2 Atmospheric Waves

Apart from the mean flow, the dynamics of the MLT region is characterised by a significant and sometimes dominant contribution from various oscillatory components. In fact, the amplitudes of long period waves, tides as well as gravity waves in this region have comparable magnitudes to those of the prevailing flow [*Vincent*, 1984]. These waves have different sources of excitation, e.g. thermal, topographic, convective forcing, random forcing etc. Generally, the different waves have different characteristic vertical structures and some are prevented from propagating beyond certain atmospheric levels. It is however possible to have signatures of waves that are precluded from propagating beyond certain levels being recorded higher than theoretically expected. This usually occurs as a result of the modulation of the lower atmospheric environment by the precluded wave resulting in a similar modulation of some aspect of 'un-precluded' waves whose propagation and/or characteristics are dependent on the modulated atmospheric environment. In general, atmospheric waves have different time scales. In this thesis, I will consider four types of waves, namely, gravity waves, tides (in more detail), planetary waves and long-term (≥ 6 months) waves and all these waves will be introduced below.

1.2.2.1 Gravity Waves

Internal gravity waves are generated in the lower atmosphere and derive their name from the

fact that gravity is the source of the restoring force to pressure changes [*Thomas*, 1996]. These waves are excited via different means including topographic forcing [*McFarlane*, 1987;*Thomas*, 1996], convective forcing [*Fovell et al.*, 1992; *Thomas*, 1996; *Alexander*, 1996] and disturbed shear regions [*Thomas*, 1996]. To maintain a constant energy density, these waves have a tendency to propagate upwards with the wind and temperature amplitudes increasing exponentially [*Thomas*, 1996]. This amplification is due to the fact that the density of the atmosphere decreases with height. As explained by *Hines* [1972], upward propagating waves transport energy to regions where there are fewer gas molecules to carry the energy and, to accomplish this, the molecules must have large amplitudes of oscillation. *Hines* [1972] likens this to ocean waves that are approaching a sloping beach. Due to the fact that the energy is carried by increasingly shallow water, the waves increase in amplitude to compensate for this.

In the course of propagating upward, some of these waves reach their critical levels (see later in Chapter 4, Section 4.2.2) and are prevented from propagating further up. However, some waves propagate higher up and on reaching the mesosphere, become convectively unstable and break resulting in the overturning of the atmosphere that generates some eddy diffusion and some localized acceleration (also called wave stress or drag). This involves a transfer of momentum to the mean flow [*Thomas*, 1996]. Thomas points out that, the bulk of this momentum is carried by those waves whose periods lie between 15 minutes to several hours. A point worth noting is the fact that although the amount of momentum extracted from the lower atmosphere may be small by standards applicable in that region, it can be very large in the less dense upper atmospheric regions where it is deposited [*Hines*, 1972]. This is in line with *Meyer's* [1999] assertion that gravity waves transport energy efficiently and over large distances.

Calculations based on the assumption of a radiative equilibrium state (i.e. no net radiative heating) results in unrealistic temperature and dynamic structures of the mesopause region, for instance, the eastward winter wind of over 300 ms^{-1} compared to observed values of less than 70 ms^{-1} [*Hamilton*, 1996]. It is now well understood that internal gravity waves provide a substantial amount of the drag that is necessary to result in observed temperatures and speeds. This point will be revisited later on in Chapter 4. Gravity waves also interact with atmospheric tides — we will see a few examples in Section 1.2.2.2 and in Chapters 5 and 6.

1.2.2.2 Atmospheric Thermal Tides

Atmospheric solar tides are global-scale atmospheric waves that are harmonics of a solar day: the diurnal tide (DT, 24 h period) and semidiurnal tide (ST, 12 h period). These tides can be classified into two groups—migrating (Sun-synchronous) or non-migrating (Sun-asynchronous). The migrating tides propagate westward with the apparent motion of the Sun and have zonal wavenumbers that are equal to their frequency in cycles per day. The migrating diurnal and semidiurnal tides are generated by the periodic absorption of solar radiation by various atmospheric constituents. The primary forcing is due to the absorption of near infrared (IR), ultraviolet (UV) radiation, and other bands of solar radiation by various atmospheric constituents. The non-migrating modes, on the other hand, are generated by longitudinally non-uniform sources. Although generally small, the contribution of non-migrating tidal components can sometimes be comparable to that of their migrating counterparts. These non-migrating tidal components are partly responsible for longitudinal differences that have been observed between longitudinally separated sites.

Once generated, tides can either propagate upwards or be trapped around the region of excitation. As with gravity waves and for the same reasons outlined earlier, the amplitudes of those tides that propagate upwards increase with height. At different levels of the atmosphere, tides can interact with other atmospheric dynamic variables in various ways that are sometimes coupled. Just to mention a few of these processes we have the following: (i) tidal-mean flow interactions e.g. diurnal modulation of the mean flow and hence the background environment through which other waves propagate; (ii) gravity wave-tidal interactions which can either result in the amplification or damping of the tide; (iii) planetary wave-tidal interactions e.g. the non-linear interaction of the 2-day wave and the diurnal tide resulting in the semi-annual variation of the tidal amplitudes [*Norton and Thuburn*, 1999]. Tidal variables also vary at seasonal and interannual time scales as a result of long-term factors like the quasi-biennial oscillation, solar activity etc. In this thesis, I will investigate all these interactions and many more.

1.2.2.3 Planetary Waves

The next group of atmospheric waves of interest are Rossby-gravity normal modes, which

originate from the lower atmosphere. Based on the numerical simulation by *Salby* [1981 a, b], *Forbes et al.* [1995] pointed out that the atmospheric responses to broadband forcing results in oscillations whose periods are about 2, 5, 10 and 16 days. This is in line with *Ahlquist* [1982] who states that these normal modes, which are due to random forcing, are free waves and are determined by the resonant characteristics of the atmospheric mean state as opposed to forcing mechanisms.

In the 2-20 day period range, the quasi-2-day wave has been studied most extensively. This wave propagates westward and has a zonal wavenumber of ~3 [*Poole and Harris*, 1995]. The 2-day wave is a consistent summer phenomenon that lasts for a few weeks and tends to be stronger in the meridional component than in its zonal counterpart. Based on the features of this wave, *Salby* [1981c] suggested its identification with the wave number 3 Rossby-gravity normal mode of a windless and isothermal atmosphere. *Plumb* [1983], on the other hand, suggested that this wave could be due to the baroclinic instability of the easterly jet in the summer mesosphere. Another prominent wave in the 2-20 day period range is the 16-day wave, which I will consider in more detail in Chapters 4 and 5.

1.2.2.4 Long Period (≥ 6 months) Oscillations

The atmosphere has three common long period (≥ 6 months) oscillations, namely, the semi-annual oscillation (SAO), the annual oscillation (AO) and the quasi-biennial oscillation (QBO). *Shepherd* [2000] gives a review on the SAO and the QBO. Quoting reports from a number of sources, *Raghava and Ramkumar* [1997] mention that these three types of oscillations are responsible for ~90% of the variation in the zonal wind of the middle atmosphere in the low latitude regions.

While the existence of the annual oscillation in the tropics is difficult to explain, it is believed that at extratropical latitudes the signature of this oscillation in the zonal mean flow up to ~60 km is due to the annual variation in solar insolation and the deflection of the flow by the Coriolis force [*Raghava and Ramkumar*, 1997]. According to these authors, above 60 km the annual oscillation is due to the annual modulation of momentum fluxes that are transported and deposited in this region by gravity waves, tides and planetary waves. Early work on the mesopause SAO (MSAO) was reported by *Groves* [1972]. *Dunkerton* [1982] suggested that the

MSAO could be linked to the selective transmission of gravity waves and Kelvin waves through the stratospheric semi-annual oscillation. The semi-annual oscillation has also been observed in tidal amplitudes and will be considered in detail in Chapter 6.

1.3 THE STRUCTURE OF THE THESIS

In analysing the data from Grahamstown and Adelaide, I use a number of mathematical procedures, which are explained in Chapter 2, and are sometimes compared with other similar methods. The data that were analysed were obtained through a meteor radar at Grahamstown and a spaced antenna system near Adelaide. These two observing techniques are the subject matter of Chapter 3. This chapter also covers the implications of comparing results from different observing systems as well as the effects of height integration. Chapters 4 to 7 are devoted to the main results of the thesis. In Chapter 4, I present the short-term and long-term trends of the mean flow. Chapter 5 focuses on the short-term variations of both the diurnal tide and the semidiurnal tide with the corresponding long-term trends being covered in Chapters 6 and 7, respectively. Chapter 8 is the summary chapter and is followed by an appendix.

CHAPTER 2 DATA ANALYSIS TECHNIQUES

A number of data analysis methods have been used in the thesis. In this chapter we look at the theory behind these and briefly consider their practical application in this work with specific details of such application being made in the relevant sections. With the exception of the wavelet spectral software, which was obtained from *Torrence and Compo* [1995], I wrote the computer code in FORTRAN or MATLAB for the implementation of all the procedures that were actually used in the thesis. Although I wrote the actual program, the algorithm for bandpass filtering used in this thesis was from *Poole* [private communication].

2.1 COMMON STATISTICAL MEASURES

2.1.1 Averages

In this thesis, I have used both the arithmetic average and the weighted average. I have also used the vector average which will be discussed in detail in Section 2.3. We consider a time series $\{x_i \pm \Delta x_i: i = 1, 2, 3 \ldots, N\}$ of N observed data points x_i that have different errors Δx_i. In calculating the average value in such a case, it is necessary to use a *weighted average* that will bias this value in favour of the more accurately determined data points. The weighted average is given (e.g. *Topping* [1972]) by

$$\overline{x} = \frac{\sum_{i=1}^{N} w_i x_i}{\sum_{i=1}^{N} w_i}$$

Equation 2.1

where the weighting factor is

$$w_i = \frac{1}{(\Delta x_i)^2}$$

Equation 2.2

The standard deviation or the *standard error* of the weighted mean (Equation 2.1) is given [*Topping*, 1972] by

$$\Delta\bar{x} = \sqrt{\frac{\sum_{i=1}^{N} w_i (x_i - \bar{x})^2}{(N-1)\sum_{i=1}^{N} w_i}}$$

Equation 2.3

If, on the other hand, all the data points have equal weighting (i.e., obtained to the same accuracy), Equation 2.1 reduces to the *arithmetic average*

$$\bar{x} = \frac{1}{N}\sum_{i=1}^{N} x_i$$

Equation 2.4

The standard error of the above average reduces from Equation 2.3 and is given (e.g. *Topping* [1972]) as

$$\Delta\bar{x} = \sqrt{\frac{\sum_{i=1}^{N} (x_i - \bar{x})^2}{N(N-1)}}$$

Equation 2.5

2.1.2 Error Propagation

When dealing with data that have errors, one has to take into account the propagation of the error as computations are made. To do this, I let m_1, m_2, ..., m_N be the means of variables i=1,2,...,N and the corresponding standard errors be Δm_1, Δm_2, ...,Δm_N. Then the standard error of any function of m_1, m_2, ..., m_N i.e., $x=f(m_1, m_2, ..., m_N)$ is given [*Topping*, 1972] by

$$\Delta x = \sqrt{\left(\frac{\partial f}{\partial m_1}\right)^2 (\Delta m_1)^2 + \left(\frac{\partial f}{\partial m_2}\right)^2 (\Delta m_2)^2 + \ldots + \left(\frac{\partial f}{\partial m_N}\right)^2 (\Delta m_N)^2}$$

Equation 2.6

2.2 HARMONIC ANALYSIS

To deduce the amplitudes and phases of harmonic components (48 h, 24 h, 12 h), I harmonically analysed hourly horizontal wind velocities $\{x_t : t = 1, 2, ..., T\}$ of a 4-day data window (i.e. T= 96 hours). The hourly wind values are assumed to have negligible error and are assigned an equal weighting of 1 (see Chapter 4, Section 4.2.1 for details). Following the conventional theory of harmonic analysis, I deduced the cosine and sine harmonic components according to

$$a_n = \frac{2}{T}\sum_{t=1}^{T} x_t \cos\left(\frac{2\pi t}{T_n}\right)$$

Equation 2.7

and

$$b_n = \frac{2}{T}\sum_{t=1}^{T} x_t \sin\left(\frac{2\pi t}{T_n}\right)$$

Equation 2.8

respectively. Here n is the harmonic frequency in cycles per interval T and $T_n = T/n$. From Equation 2.7 and Equation 2.8 the amplitude A_n and phase ϕ_n (in hours) of the harmonic components are calculated from

$$A_n = \sqrt{a_n^2 + b_n^2}$$

Equation 2.9

and

$$\phi_n = \frac{T_n}{2\pi}\arctan\left(\frac{b_n}{a_n}\right)$$

Equation 2.10

respectively. Since I am assuming negligible error in the hourly wind velocities, the 4-day amplitudes and phases as calculated above have no error.

2.3 VECTOR AVERAGING

Sometimes it is necessary to average the amplitudes and phases obtained above. For instance, we might want to calculate the monthly or interannual average amplitudes or phases from the 4-day interval or monthly values. For this averaging I used the method of *vector averaging* [*Portnyagin*, private communication; *Braddick*, 1965]. This method has an advantage over algebraic averaging when there is large variance in the phase. In particular, vector-averaging gives 'tidal amplitude and phase that are consistently present throughout the studied month' [*Vial*, 1989]. That is, the extracted components represent the salient features of the atmosphere that are persistent and characteristic of long term behaviour of the interval being averaged.

Consider the amplitude A_i and phase ϕ_i where the index i= 1, 2, 3, ..., M is the index of the *4-day interval* or *month* and M the total number of amplitudes and phases to be averaged. It has to be stressed that the index i represents either the *4-day interval* values or *monthly* values. For simplicity, the n used in Section 2.2 to represent the n^{th} harmonic has been omitted such that in this section A_i and ϕ_i are, respectively, the time sequences of the amplitude and phase of a particular harmonic component whose period (in hours) is T. The standard errors for the above amplitudes and phases are correspondingly given by ΔA_i and $\Delta\phi_i$. The vector components are calculated according to

$$\alpha_i = A_i \cos\left(\frac{2\pi}{T}\phi_i\right) = A_i \cos(\omega\phi_i)$$

Equation 2.11

and

$$\beta_i = A_i \sin\left(\frac{2\pi}{T}\phi_i\right) = A_i \sin(\omega\phi_i)$$

Equation 2.12

where $\omega = 2\pi/T$ and the other terms are as already defined. The standard errors of the individual α_i and β_i are based on Equation 2.6 and are respectively given by Equation 2.13 and Equation 2.14 below

$$\Delta\alpha_i = \sqrt{[\cos(\omega\phi_i)]^2(\Delta A_i)^2 + [-\omega A_i \sin(\omega\phi_i)]^2(\Delta\phi_i)^2}$$

Equation 2.13

and

$$\Delta\beta_i = \sqrt{[\sin(\omega\phi_i)]^2(\Delta A_i)^2 + [\omega A_i \cos(\omega\phi_i)]^2(\Delta\phi_i)^2}$$

Equation 2.14

As mentioned in Section 2.2, the 4-day amplitudes and phases are assumed to have zero error such that, in this case, the standard errors of the individual α_i and β_i (i.e. $\Delta\alpha_i$ and $\Delta\beta_i$ as given by Equation 2.13 and Equation 2.14) are equal to zero because $\Delta A_i = 0$ and $\Delta\phi_i = 0$. However, in the case where A_i and phase ϕ_i represent monthly averages (which are based on 4-day interval amplitudes and phases), we have $\Delta A_i \neq 0$ and $\Delta\phi_i \neq 0$ so that $\Delta\alpha_i \neq 0$ and $\Delta\beta_i \neq 0$.

To calculate *monthly* averages, I started by calculating the *monthly* averages α and β using all the α_i and β_i values corresponding to the individual 4-day intervals within the month. Since in this case $\Delta\alpha_i = 0$ and $\Delta\beta_i = 0$, I used Equation 2.4 and Equation 2.5 to get α and β and the corresponding standard errors $\Delta\alpha$ and $\Delta\beta$. For the *interannual* averages (which are based on monthly averages, hence $\Delta\alpha_i \neq 0$ and $\Delta\beta_i \neq 0$), I used weighted average techniques (Equation 2.1 and Equation 2.2) to get the *interannual* averages α and β and the corresponding standard errors $\Delta\alpha$ and $\Delta\beta$.

From the *monthly/interannual* averages α and β and the corresponding standard errors $\Delta\alpha$ and $\Delta\beta$, I computed the *monthly/interannual* average amplitude and phase from

$$A = \sqrt{\alpha^2 + \beta^2}$$

Equation 2.15

and

$$\phi = \arctan(\delta)$$

Equation 2.16

respectively, where $\delta = \beta/\alpha$. The standard error of the average amplitude is based on Equation 2.6 and is given by

$$\Delta A = \sqrt{\left(\frac{\alpha}{A}\right)^2 (\Delta\alpha)^2 + \left(\frac{\beta}{A}\right)^2 (\Delta\beta)^2}$$

Equation 2.17

For the phase we start by finding the standard error of δ which is given by

$$\Delta\delta = \sqrt{\left(-\frac{\beta}{\alpha^2}\right)^2 (\Delta\alpha)^2 + \left(\frac{1}{\alpha}\right)^2 (\Delta\beta)^2}$$

Equation 2.18

Having found this, the standard error (in hours) of the average phase is given by

$$\Delta\phi = \left(\frac{1}{\omega}\right)\frac{\Delta\delta}{1+\delta^2}$$

Equation 2.19

The EW-NS phase difference is given by

$$\phi_d = \phi_{EW} - \phi_{NS}$$

Equation 2.20

so that the corresponding standard error is

$$\Delta\phi_d = \sqrt{(\Delta\phi_{EW})^2 + (\Delta\phi_{NS})^2}$$

Equation 2.21

2.4 COMPLEX DEMODULATION

In Section 2.2 I discussed the harmonic analysis procedure and then in Section 2.3 I discussed the procedure used to average the amplitudes and phases obtained in Section 2.2. In this section, I focus on a method that is effectively a 'local' form of harmonic analysis. Unless stated otherwise, the theory in this section is based on *Priestley* [1981]. To develop the theory behind

this method, I consider a non-stationary process consisting of a *'signal'* (first term of Equation 2.22) and *'noise'* (second term of the same equation). We can write

$$x(t) = \sum_{j=1}^{m} A_j(t) \exp(i\omega_j t) + z(t)$$

Equation 2.22

where the complex amplitude $A_j(t)$ drifts over time indicating the variation of the amplitude and phase of the j^{th} harmonic component with time. The detection of a particular component and the estimation of its changing amplitude and phase can be done by using the *complex demodulation* method [*Priestley*, 1981; *Bloomfield*, 1976]. This 'local' harmonic analysis produces an 'evolutionary' amplitude and phase determined by the values of the series in the neighbourhood of t. In this analysis, the component of interest, which has amplitude A_p, and frequency ω_p, is shifted to a frequency near zero by multiplying $x(t)$ by exp $(-i\omega_d t)$ where $\omega_d \approx \omega_p$ is the *demodulation frequency*. The demodulated signal is

$$x_d(t) = e^{-i\omega_d t} x(t) = A_p(t) e^{i(\omega_p - \omega_d)} + \sum_{j \neq p}^{m} A_j(t) e^{i(\omega_j - \omega_d)} + e^{-i\omega_d t} z(t)$$

Equation 2.23

By passing x_d through an appropriately designed low-pass filter, all the 'noise' and 'signal' components can be removed leaving the component of interest which has now been shifted to $(\omega_p - \omega_d) \sim 0$. It is important to note that even though $z(t)$ has a continuous spectrum, we can assume that it has no component at ω_p because such a component would be indistinguishable from $A(t)\exp(-i\omega_p t)$. The filtering process can be represented as follows

$$x_{df}(t) = \sum_{u=-\infty}^{\infty} g_u x_d(t-u) = \sum_{u=-\infty}^{\infty} g_u x(t-u) e^{-i\omega_d (t-u)}$$

Equation 2.24

where $\{g_u\}$ is a real and symmetric filter i.e., $g_u = g_{-u}$. As already mentioned above, the second and last terms of Equation 2.23 have negligible contribution to x_{df} and, therefore, we can safely

consider a one-term signal with ω_p and the form

$$x_p(t) = A_p(t)\cos(\omega_p t + \phi_p) = \frac{1}{2}A_p(t)\left[e^{i(\omega_p t+\phi_p)} + e^{-i(\omega_p t+\phi_p)}\right]$$

Equation 2.25

where $A_p(t)$ changes slowly such that it can be considered to be constant in the effective range of $\{g_u\}$. By substituting Equation 2.25 into Equation 2.24 and rearranging we get

$$x_{df}(t) = \frac{1}{2}A_p(t)\left[H(\omega_d - \omega_p)e^{-i[(\omega_d-\omega_p)t-\phi_p]} + H(\omega_d + \omega_p)e^{-i[(\omega_d+\omega_p)t+\phi_p]}\right]$$

Equation 2.26

where the transfer function is real and symmetric and is given by

$$H(\omega) = \sum_{u=-\infty}^{\infty} g_u e^{-i\omega u}$$

Equation 2.27

If the filter is designed such that $H(\omega) \sim 0$ for $|\omega| > 2\omega_d$ and noting that $\omega_d \sim \omega_p$, the second term of Equation 2.26 becomes negligible and we may write

$$\alpha_t \sim \frac{1}{2}A_p(t)H(\omega_d - \omega_p)\cos[(\omega_d - \omega_p)t - \phi_p]$$

Equation 2.28

and

$$\beta_t \sim \frac{1}{2}A_p(t)H(\omega_d - \omega_p)\sin[(\omega_d - \omega_p)t - \phi_p]$$

Equation 2.29

From Equation 2.28 and Equation 2.29, we can get the instantaneous amplitude from

$$A_p(t) \sim \frac{2\sqrt{\alpha_t^2 + \beta_t^2}}{H(\omega_d - \omega_p)}$$

Equation 2.30

and the instantaneous "phase" from

$$\psi(t) = \arctan\left(\frac{\beta_t}{\alpha_t}\right) \sim (\omega_d - \omega_p)t - \phi_p$$

Equation 2.31

From Equation 2.31 it follows that if $x(t)$ contains a harmonic component with frequency ω_p, this component can be detected from a plot of $\psi(t)$ versus t. Such a graph is expected to be approximately linear and have a slope and y-intercept of $(\omega_d - \omega_p)$ and $-\phi_p$, respectively. From this graph we can, therefore, deduce the frequency (ω_p) and hence period of interest T_p. In this work complex demodulation will be used for studying the time variation of the amplitudes and period of the different harmonic components (e.g. Chapter 5, Section 5.4).

2.5 CORRELATION ANALYSIS

Wind parameters have variations of different time scales as a result of different forcing mechanisms, modulating mechanisms and similar effects. One of the ways that can be used to identify these mechanisms is by using correlation analysis. For instance, good correlation between two processes might imply that these processes are either interdependent or have a common forcing mechanism. It is also of interest to study the coherence (in time) of the different atmospheric parameters. This coherence can help in assessing the different degrees of sensitivity of these parameters to changing atmospheric conditions and forcing. Such studies require the use of either the auto-correlation or cross-correlation which can be found in time series analysis textbooks (e.g. *Diggle* [1990]). However, the problem with the traditional correlation methods is that they are designed for equally spaced observations. As we will see in later chapters, most real life situations, have forced data gaps due to instrument failure, poor data etc. To overcome this problem, I used the *semi-variogram* (γ_{xx}), which is capable of computing the auto-correlation and cross-correlation functions for irregularly spaced data. Note that here I adopted the terminology of *Journel and Huijbregts* [1978] as opposed to the term of *variogram* as used by *Diggle* [1990].

2.5.1 The Semi-variogram Method

We consider two data points $x(t)$ and $x(t+k)$ where t is the time and k is the time lag between the two points. Following *Journel and Huijbregts* [1978], the variability between these two values is characterised by the variogram, which is the expectation of the random process $[X(t)-X(t+k)]^2$, that is

$$2\gamma_{xx}(t,k) = E[X(t) - X(t+k)]^2 = Var[X(t) - X(t+k)]$$

Equation 2.32

where $E\{\}$ is the expectation operator. The function γ_{xx} is referred to as the "semi-variogram" [*Journel and Huijbregts*, 1978]. The variogram, as expressed above, is a function of two variables (t and k), and therefore requires several realisations $[x_1(t), x_1(t+k)]$, $[x_2(t), x_2(t+k)]$, ..., $[x_n(t), x_n(t+k)]$ in order calculate it [*Journel and Huijbregts*, 1978]. However, we usually have one realisation $[x(t), x(t+k)]$, which is measured at various times. This problem is solved by introducing the intrinsic hypothesis (see *Journel and Huijbregts* [1978] for details). The essence of this hypothesis is that the variogram only depends on the lag k and not the time t [*Journel and Huijbregts*, 1978]. *Journel and Huijbregts* [1978] point out that this allows us to estimate the variogram as the mean of the squared differences of data pairs $[x(t_i), x(t_i+k)]$ separated by k i.e.

$$2\gamma_{xx}(k) = \frac{2}{N(k)}\sum_{i=1}^{N(k)}\gamma_x(t_i,k) = \frac{1}{N(k)}\sum_{i=1}^{N(k)}[x(t_i) - x(t_i+k)]^2$$

Equation 2.33

where $N(k)$ is the number of observed pairs that are separated by lag k. By using second order stationarity, *Journel and Huijbregts* [1978] also expressed the semi-variogram as

$$\gamma_{xx}(t,k) = \frac{1}{2}E[X(t+k) - X(t)]^2 = C(0) - C(k)$$

Equation 2.34

where C is the covariance (see *Journel and Huijbregts* [1978] for details). From Equation 2.34 the auto-correlation can be expressed as

$$\rho_{xx}(k) = \frac{C(k)}{C(0)} = 1 - \frac{\gamma_{xx}(k)}{C(0)}$$

Equation 2.35

When grouping m semi-variograms we use a weighted average expressed as [*Journel and Huijbregts*, 1978]

$$\bar{\gamma}_{xx}(k) = \frac{\sum_{i=1}^{M} N_i(k)\gamma_{x_x x_i}(k)}{\sum_{i=1}^{M} N_i(k)}$$

Equation 2.36

Before we conclude this section, we will consider the a few properties of the semi-variogram which will enable us to interpret the semi-variograms shown later in the thesis (e.g. Chapter 4, Section 4.2.1). In Figure 2.1 I have shown a schematic diagram of the usual shape of the semi-variogram. In accordance with Equation 2.33 and Equation 2.35, $\gamma_{xx}(0) = 0$ and this is due to the fact that the auto-correlation at $k = 0$ is 1. As k increases the correlation between two points $x(t)$ and $x(t+k)$ decreases such that γ_{xx} tends to increase linearly. Further increase in k results in complete independence between samples that are k apart such that at some $k > a$, the auto-correlation approaches zero and hence $\gamma_{xx}(k)$ fluctuates about a constant value C called the *sill* [*Diggle*, 1990; *Clark*, 1979]. The sill is equal to the sample variance [*Clark*, 1979]. The linear region is referred to as the *range* of influence and is denoted by a [*Clark*, 1979; *Journel and Huijbregts*, 1978]. This range of influence reflects the coherence of the studied parameter over time.

As mentioned earlier, wind parameters tend to vary at different time scales due to various

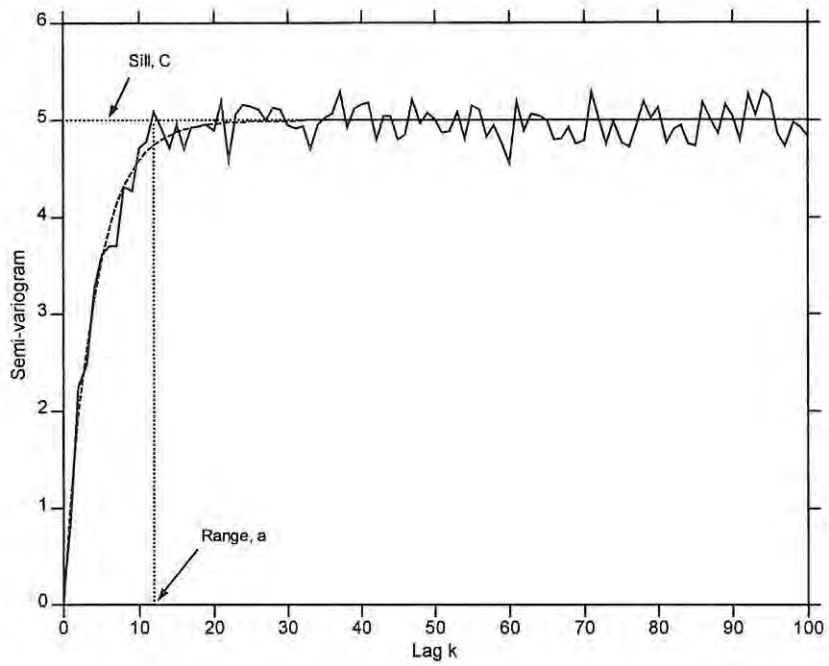

Figure 2.1 A schematic diagram of the semi-variogram.

factors. These different-time-scale factors form nested structures [*Journel and Huijbregts*, 1978] each with a characteristic semi-variogram $\gamma_{x_i x_i}(k)$ such that the 'total' γ_{xx} (k) is a superposition

$$\gamma_{xx}(k) = \gamma_{x_1 x_1}(k) + \gamma_{x_2 x_2}(k) + \ldots + \gamma_{x_m x_m}(k)$$

Equation 2.37

These different structures result in the form of the semi-variogram departing from the usual form illustrated in Figure 2.1. In this thesis I am not going to look in detail at these different types of semi-variograms; the reader is referred to *Journal and Huijbregts* [1978] for details.

2.6 SPECTRAL METHODS

2.6.1 Auto-spectrum

We have already touched on harmonic analysis (Section 2.2) in which the *exact* periods of

specific spectral components are assumed to be known *a priori* and we set out to find the amplitude and phase of those components. However, we will see later (e.g. Chapter 5, Section 5.4) that the periods of some spectral components are time variant and therefore it is sometimes desirable to deduce the atmospheric wave activity without making any prior assumption regarding the dominant spectral components. For this purpose I have used both the auto- and the cross-spectral techniques. The auto-spectra was obtained by Fourier methods according to (see e.g. *Otnes & Enochson* [1978])

$$P_{xx}(f) = \frac{1}{N}\overline{X(f) * X(f)}$$

Equation 2.38

where $X(f)$ is Fourier transform of the time series $x(t)$ of length N and is given by (e.g. *Mallat* [1989])

$$F(\omega) = \int_{-\infty}^{\infty} x(t)e^{-i\omega t}dt$$

Equation 2.39

with $\omega = 2\pi f$ and f being the frequency. $X^*(f)$ is the complex conjugate of $X(f)$.

The integration (Equation 2.39) is over all the time and, therefore, Fourier transform methods are best suited for stationary time series where the frequency content of the signal does not change with time. This limitation is due to the fact that it is impossible to deduce, with accuracy, the frequency and its exact time of occurrence i.e. a signal cannot be represented as a point on a time-frequency plane [*Valens*, 1999; *Polikar*, 1996]. This is due to the fact that frequency cannot be measured instantaneously and, as pointed out by *Kaiser* [1994], any claim that a signal has a frequency ω_0 means that the signal has been observed for at least one period i.e. for an interval $\Delta t \geq 1/\omega_0$.

The shortcoming of the Fourier transform methods poses a problem because most geophysical processes are non-stationary and are typically characterised by trends, drifts, and transient changes leading to changes in both amplitude and frequency with time. For instance in the

present work, the diurnal tide might only be dominant during, say, the first half of the month with the semidiurnal tide assuming dominance during the second half of the month. The Fourier spectrum of such a time series will have peaks at diurnal and semidiurnal frequencies. However, this would also be the case for a situation where the dominance of the diurnal and the semidiurnal tides is reversed. In the current work I am not only concerned with the spectral content of the data but also the time evolution of the relevant spectral activity.

One way around the above Fourier transform limitation is to cut the signal into smaller parts that are analysed separately. Over the years a number of methods have been developed to achieve this. One such method is the short-time Fourier transform (STFT) that was introduced by Dennis Gabor (1946) [*Misiti et al.*, 1996]. In the STFT the signal is windowed and the Fourier transform is then applied on the short portion of the signal that is assumed to be stationary. Mathematically this process can be represented by (e.g. *Mallat* [1989])

$$SF(\omega, k) = \int_{-\infty}^{\infty} x(t)g(t-k)e^{-i\omega t}dt$$

Equation 2.40

where g is the windowing function.

The precision of the time-frequency representation depends on the width of windowing function (technically called the support of the window). In the traditional Fourier transform method (Equation 2.39) there is good resolution in the frequency domain (and no resolution in time) because the window used in this case last the whole duration of the signal. The introduction of a shorter window in the STFT gives some time resolution but this is at the expense of frequency resolution. The narrower the window, the better the time resolution and the poorer the frequency resolution and vice versa.

In a nutshell, the trade-off between *time resolution* and *frequency resolution* implies that any good time-frequency representation of a signal can be achieved by using a narrower (wider) window when looking at high (low) frequency components. Therefore, for any method to have a good time-frequency representation of a signal it must have a window function whose width is dependent on the frequency being analysed at the particular instant. This is the problem with

the STFT since it has a fixed window function. Although I use the STFT in this thesis, I have resorted to wavelets (see Section 2.7) in situations where both the spectral content and its time evolution, and especially the latter, are of importance. This is because wavelets have a variable 'windowing' process and hence have superior *time resolution* and *frequency resolution* capabilities. Before, we get to wavelets, however, lets look at the Fourier cross-spectrum.

2.6.2 Cross-spectrum

Sometimes it is necessary to determine the dominant spectral components in two time series and this is achieved by using cross-spectral techniques. Consider two stationary processes $\{x(t)\}$ and $\{y(t)\}$. In a similar fashion to Section 2.6.1, we can use Fourier methods to write the cross-spectrum as (see e.g. *Otnes & Enochson* [1978])

$$P_{xy}(f) = \frac{1}{N}\overline{X(f) * Y(f)}$$

Equation 2.41

which is a complex function. Following *Priestley* [1981] on whom the rest of the information in this section is based, Equation 2.41 can be expressed as

$$P_{xy}(f) = c_{xy}(\omega) - iq_{xy}(\omega) = a_{xy}(\omega)\exp[i\phi_{xy}(\omega)]$$

Equation 2.42

where $c_{xy}(\omega)$ and $q_{xy}(\omega)$ are the *co-spectrum* and *quadrature* spectrum representing the covariance between the coefficients of the "in-phase" and the "quadrature" components of $x(t)$ and $y(t)$, respectively. $a_{xy}(\omega)$ is the cross-amplitude spectrum and represents the average of the product of the amplitudes of components in $x(t)$ and $y(t)$ that have frequency ω. The phase spectrum $\phi_{xy}(\omega)$ represents the "average value of the phase-shift" $\{\phi_x(\omega) - \phi_y(\omega)\}$ between the components of $x(t)$ and $y(t)$ with frequency ω. To quantify the degree of correlation between the two signals we use the *squared coherency*, which is mathematically given by [e.g. *Chatfield*, 1989]

$$C_{xy}(\omega) = \frac{a_{xy}^2(\omega)}{P_{xx}(\omega)P_{yy}(\omega)}$$

Equation 2.43

This coherency is a measure of the square of the linear correlation between $x(t)$ and $y(t)$ at ω. The closer $C_{xy}(\omega)$ is to zero (one) the less (higher) the correlation of the bivariate process at ω. These properties make it possible for one to test if there are any oscillatory components that are linearly related between any two wind components, or between the winds at Grahamstown and Adelaide, for instance. Such relations can be an indication of the existence or absence of any interdependence or common mode of excitation. We can also deduce the average phase shift between the components observed at Grahamstown and Adelaide, which will help in assessing the possible role played by non-migrating solar tidal modes in longitudinal tidal variations. The average phase difference between the zonal and the meridional components can also be found through this method. The application of this technique will become clear in Chapter 6, Section 6.2 and in Section 6.4.1.

2.7 WAVELET ANALYSIS

2.7.1 Wavelets

As discussed in Section 2.6.1, wavelets have a superior frequency and time resolution capability than the STFT. A wavelet is a waveform that is effectively limited in duration and its average value is zero [*Misiti et al.*, 1996]. The term *wavelet* is used to describe a set of functions $\psi_{ab}(t)$ that are deduced from the translation and dilation/scaling of a specific wavelet $\psi(t)$ called the *mother wavelet* or *basic wavelet*. Wavelets have two important properties, namely, *admisibility* and *regularity conditions*. *Valens* [1999] points out that square integrable functions $\psi(t)$ that satisfy the admissibility condition

$$\int \frac{|\Psi(\omega)|^2}{|\omega|} d\omega < +\infty$$

Equation 2.44

can be used as a tool to first analyse and thereafter reconstruct, without loss, the original signal,

which will be discussed to some length in Section 2.7.4. In Equation 2.44, $\Psi(\omega)$ is the Fourier transform of $\psi(t)$. As noted by *Valens* [1999], the admissibility condition implies that

$$|\Psi(\omega)|^2|_{\omega=0} = 0$$

Equation 2.45

which in turn implies that the average value of the wavelet as a function of time is zero ($\int \psi(t)dt = 0$) and hence it must be oscillatory, that is, it must be a wave. The regularity conditions on the other hand, state that the wavelet function must be smooth and have concentration in both time and frequency [*Valens*, 1999]. Regularity is complex and can be explained by using vanishing moments (see *Valens* [1999] for details)

The mother wavelet can take different forms (see examples in *Misiti et al.* [1996]), which have to meet the admissibility constraints [*Starck et al.*, 1998] and is mathematically related to the set of corresponding wavelets by

$$_{ab}(t) = \frac{1}{\sqrt{a}}\psi\left(\frac{t-b}{a}\right)$$

Equation 2.46

where b and a are the position and scale factor of ψ respectively. In this thesis I use the morlet wavelet and the Daubechies wavelet (see *Misiti et al.* [1996])

2.7.2 Continuous Wavelet Transform (CWT)

The continuous wavelet transform (CWT) is the sum over time of a signal $x(t)$ multiplied by the scaled and shifted wavelets and is mathematically given by [*Misiti et al.*, 1996]

$$C(a,b) = \int_R x(t)\psi_{a,b}(t) = \int_R x(t)\frac{1}{\sqrt{a}}\psi\left(\frac{t-b}{a}\right)dt$$

Equation 2.47

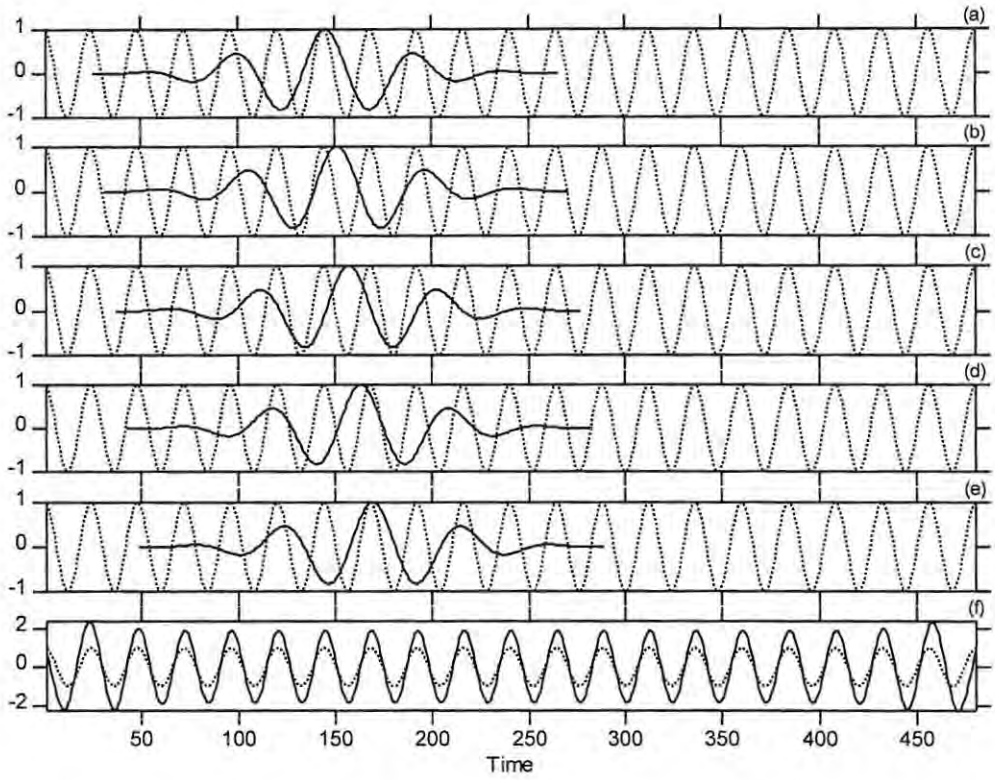

Figure 2.2 The translation of a morlet wavelet (solid line) over the cosine signal (dotted line) is shown in (a) to (e) for time steps that are a quarter of a cycle long. Figure (f) shows the continuous wavelet transform (solid line) and the signal (dotted line).

and yields the *wavelet coefficients* C which depend on scale a and position b. C gives the degree of correlation between the wavelet and a portion of the signal around b. The more closely the (scaled) wavelet resemble the particular portion of the signal, the higher the value of C [*Misiti et al.*, 1996]. The process of calculating the CWT is illustrated in Figure 2.2 in which the wavelet is translated by quarter of a cycle for illustration purposed whereas in the actual computation the time steps are smaller.

Misiti et al. [1996] summarises the actual implementation as follows: (i) Starting with the smallest scale and starting at the beginning of the signal, we compare the wavelet and the signal and calculate the corresponding C. (ii) Then advance the wavelet in time and repeat step (i). (iii) Steps (i) and (ii) are repeated until the whole signal is covered. (iv) Having covered the whole signal for a given scale a, the scale is changed and steps (i) to (iii) are

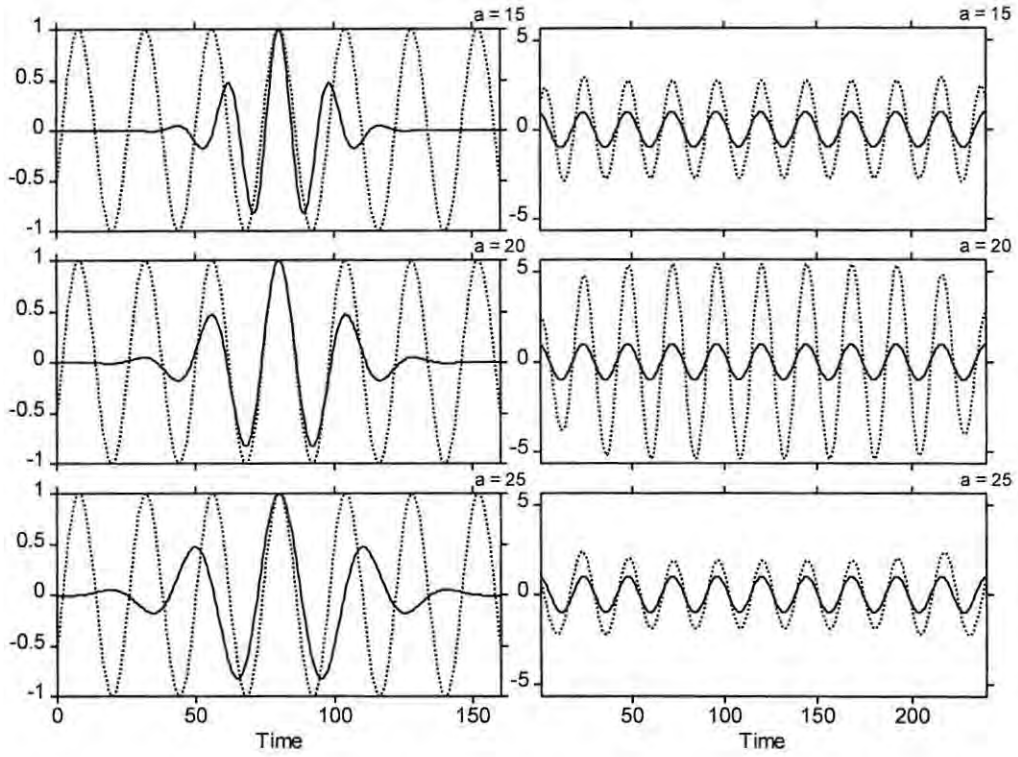

Figure 2.3 The figures on the left show scaled (real) morlet wavelets (solid lines) for different scales a indicated in the top right corner of each panel. The dotted line shows a sinusoidal signal with a Fourier period of 24 time units. The panels on the right show the same sinusoidal signal (solid line) and the CWT (dotted line) for the corresponding scale a.

carried out again. Steps (i) to (iv) are repeated until all desired scales have been covered.

As expected, there is greater similarity between the wavelet and the signal in the positions on Figure 2.2(a) and (e). Position (c) gives maximum negative correlation, while (b) and (d) give zero correlation. As a result, the calculated CWT is a sinusoidal function that is in phase with the sinusoidal signal as shown on Figure 2.2(f). In this figure we also see that the CWT has larger peaks towards the edges and this is due to edge effects. The 2-D CWT resulting from the repeated implementation of steps (i) to (iv) above has magnitudes that depend on whether a particular segment of the signal has a spectral component that corresponds to the current scale or not. That is, if a signal at some position has a spectral component that corresponds to the current scale the resulting wavelet coefficient will be large. For instance in Figure 2.3, we have a sinusoidal signal with a period of $T = 24$ time units being analysed by a (real) morlet wavelet.

For this particular morlet wavelet the scale that corresponds to a Fourier period of $T = 24$ is $a_T = 20$ and hence the large CWT in the middle row of Figure 2.3.

So far we have been talking about scale in wavelet analysis but we are more accustomed to the frequency or period. The scale and the frequency are, in fact, inversely related to each other and the constant of proportionality is different for each wavelet. This proportionality constant can be deduced by finding the wavelet power spectrum of a cosine signal of known frequency and finding the scale of the largest power (see *Torrence home page* at http://paos.colorado.edu/research/wavelets/faq.html#scale). The ratio between this scale and the frequency of the cosine gives the proportionality constant.

Having deduced the CWT, we can evaluate the wavelet power spectrum according to [*Torrence & Compo*, 1998]

$$P(a,b) = |C(a,b)|^2$$

Equation 2.48

and the corresponding phase is given by [*Torrence & Compo*, 1998]

$$\phi(a,b) = \arctan[\mathrm{Im}(C(a,b)/\mathrm{Re}(C(a,b)]$$

Equation 2.49

The wavelet software that was used for spectral analysis was provided by C. Torrence and G. Compo and is available at URL: http://paos.colorado.edu/research/wavelets/ [*Torrence and Compo*, 1998]

2.7.3 Time-Frequency Localization

I have already pointed out that what makes a wavelet an effective analysis tool is not just its ability to deduce the spectrum of a signal but also its good time-frequency resolution. In this section I consider the latter feature in detail, under what is referred to as time-frequency

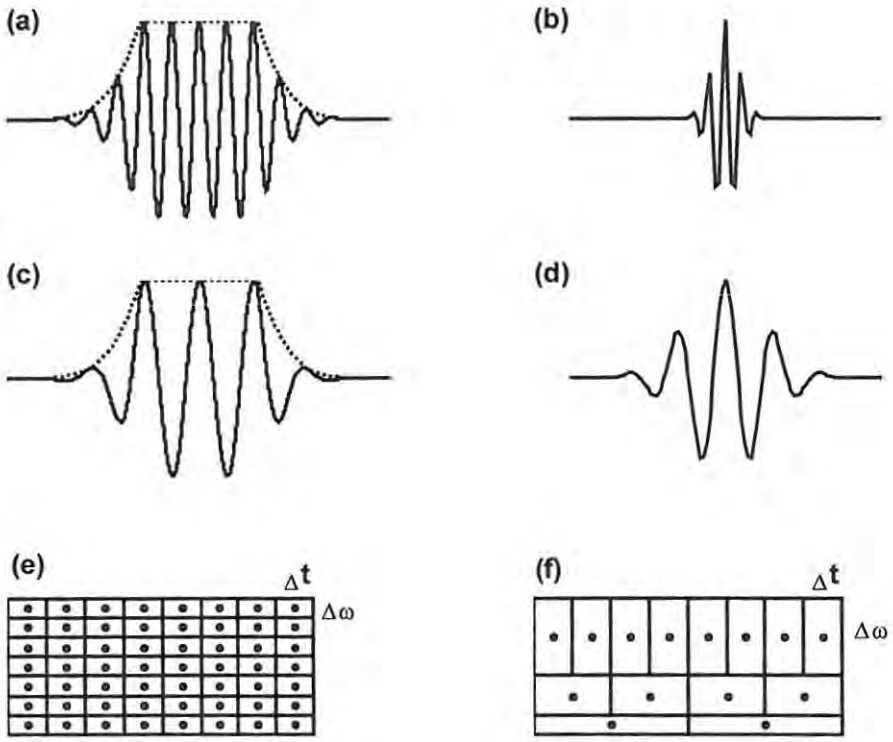

Figure 2.4 Comparison of the STFT and wavelet window functions. (a) and (c) show the windowed Fourier transform functions $g_{\omega,b}(t)=\mathrm{Re}\{e^{-i\omega t}g(t-b)\}$ (solid line) and the window $g(t)$ (dotted line) for signals with different frequencies. (b) and (d) show the (real) morlet wavelets $\psi_{a,b}(t)$ for different scales. (e) and (f) illustrate the resolution cells of the STFT and wavelets, respectively. The vertical dimension of each cell is $\Delta\omega$ and the horizontal dimension is Δt (Based on *Polikar* [1996], *Daubechies* [1992], *Mallat* [1989] and *Misiti et al.* [1996]).

localization. A comparison of Equation 2.40 and Equation 2.47 shows that wavelet analysis, unlike the STFT analysis, uses a variable 'window' function. I use window in inverted commas because wavelet analysis does not use a window in the strict sense, but instead, the wavelet itself performs both the correlating and windowing process. Schematically, the different widths of the window functions implemented in the STFT and wavelet analysis are illustrated in Figure 2.4. For both the STFT and the CWT, the signal is only compared within the region of support of $g_{\omega,b}(t)$ (see Equation 2.40) and $\psi_{a,b}(t)$ respectively such that the signal values outside this region make no contribution to the resulting coefficients. Consequently, we have a local analysis that yields a localised time-frequency picture of the signal.

The difference between the two methods becomes clear when we consider the fact that the windowed Fourier transform functions (Figure 2.4(a), (c)) have a constant width (which is determined by the fixed width of $g(t)$) (see Equation 2.40) and are just filled by sinusoidal functions of varying frequencies. In contrast, the effective width of the wavelets (Figure2.4(b), (d)) depends on the scale (frequency) (see also Equation 2.47): small scale (i.e. high frequency) wavelets are narrower (Figure 2.4(b)) and large scale (low frequency) wavelets are broader (Figure 2.4(d)). This difference can also be understood by looking at the resolution cells of the STFT and wavelets that are shown in Figure 2.4(e) and (f), respectively. The vertical dimension of each cell is $\Delta\omega$ and the horizontal dimension is Δt and the area ($\Delta t\Delta\omega$) of all resolution cells is constant. The dot within each cell represents the time-frequency localization centre corresponding to the respective $g_{\omega,b}(t)$ or $\psi_{a,b}(t)$. For wavelets, the resolution cells vary with scale a such that for small a there is finer temporal resolution (Δt) and coarser frequency resolution ($\Delta\omega$) and the opposite is true for large a. From the distribution of time-frequency localization cells, it is also clear that the high frequency (small scale) components are better resolved in time and therefore one can 'zoom-in' on the short-lived high frequency components like transients [*Daubechies*, 1992]. At the same time, the wide low frequency (large scale) cells, ensure that the long period cycles are captured within the wide window and hence the corresponding frequency better analysed.

2.7.4 Multiresolution Analysis (MRA)

So far the computation of the wavelet transform, has been made by the direct integration over all the necessary scales and positions. Around 1986, a new method of performing the discrete wavelet analysis known as *multiresolution analysis* (MRA) was developed. *Kaiser* [1994] summarises this method as follows. Starting with a signal $x(t)$ with discrete samples x and regular sample interval $\Delta t = \tau > 0$. The signal x is then split into a "approximation/blurred" version A^1 at a coarser scale $\Delta t = 2\tau$ and "detail" D^1 at a finer scale $\Delta t = \tau$. This process is repeated on A^1 giving more blurred versions A^2, A^3, ... and more details D^2, D^3, ... that have been removed from A^j at every scale $\Delta t = 2^j\tau$ where j is the level. The details D^j can be written as a superposition of wavelets $\psi_{a,b}$ that are associated with a very special mother wavelet that is

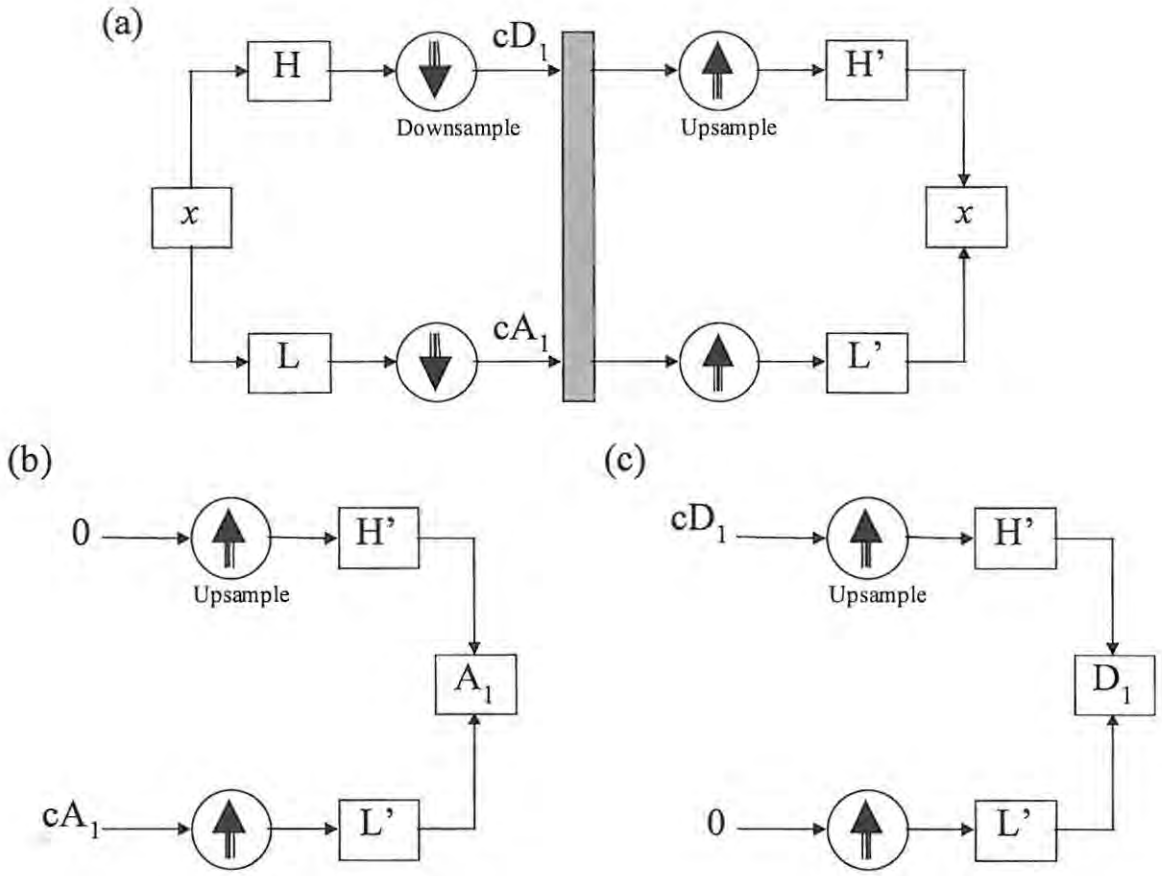

Figure 2.5 Multiresolution analysis. (a) Single level decomposition and reconstruction of a signal x. (b) Reconstruction of approximations and (c) reconstruction of details. H stands for high-pass filter and L for low-pass filter and the corresponding conjugate filters are represented by primes. (Modified from *Misiti et al.* [1996])

formed recursively by use of "filter coefficients" which are in turn associated with the blurring operation. Following the blurring process, the signal can be constructed according to $x(n) = A^J + \sum D^j$. This whole process is described in more detail below.

The implementation of the above process is schematically shown on Figure 2.5(a). Unless stated otherwise, the rest of this section is based on the book by *Misiti et al.* [1996]. The signal x is convolved with the low-pass filter (L) and the high-pass filter (H) resulting in 'approximations' discrete wavelet transform (DWT) coefficients (cA_1) and 'details' DWT coefficients (cD_1) respectively. Since this step results in twice as much data as the original signal, the two sets of coefficients are *downsampled* by suppressing every second coefficient. This results in aliasing, which can be subsequently accounted for. Whereas wavelet

decomposition involves filtering and downsampling, wavelet reconstruction involves *upsampling* and filtering. By carefully designing the decomposition and reconstruction filters in such a way that they are closely related but not identical and hence forming what is referred to as *quadrature mirror filters*, the aliasing that was introduced earlier can be cancelled out. An important point to note is that these filters also determine the shape of the analysing wavelet. As opposed to starting by drawing the analysing wavelet, it is customary to first design the appropriate quadrature mirror filters and use these to create the wavelet (see *Misiti et al.* [1996] for details).

The coefficients are upsampled by inserting zeros between coefficients. These lengthened versions of cA_1 and cD_1 are then passed through the reconstruction low-pass and high-pass filters respectively and the output is then combined to yield the signal x. Instead of reconstructing the signal directly, we can start by reconstructing the approximation A_1 and the detail D_1 as shown in Figure 2.5(b) and (c). In this case, the upsampled version of cA_1 is again passed through the reconstruction low-pass filter and on the high-pass filter zeros are fed in. The filter outputs are combined to give the approximation A_1 as shown in Figure 2.5(b). A similar process is followed in the reconstruction of the detail D_1 (Figure 2.5(c)). The approximations and details reconstructed in this manner are true constituents of the original signal x and hence can be combined to form this signal i.e. $x = A_1 + D_1$.

The above technique can be extended to multilevel decomposition and reconstruction as schematically shown in **Figure 2.6**. An arrow between any two boxes in this figure represents a complete decomposition-reconstruction process or unit. That is, at each level j of the multilevel analysis, the approximations A_j and details D_j are formed using the scheme outlined above. While the details are set aside, the approximations are further analysed to yield A_{j+1} and details D_{j+1} and so on. This process gives a number of alternative ways of reassembling the original signal i.e.

$$x = A_1 + D_1 = A_2 + D_2 + D_1 = A_3 + D_3 + D_2 + D_1 = A_J + \sum_{j \le J} D_j$$

Equation 2.50

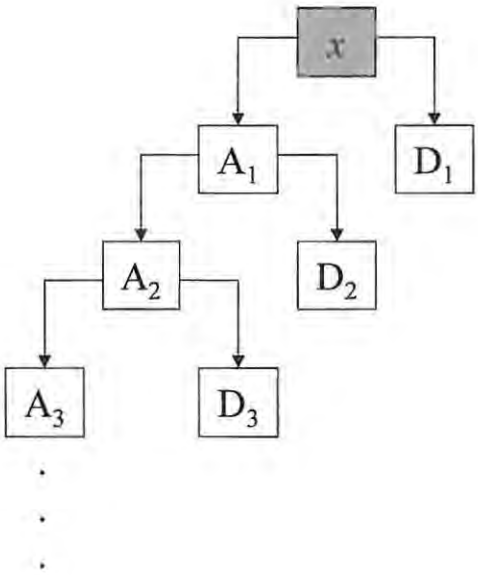

Figure 2.6 Multilevel decomposition and reconstruction. The arrows joining the boxes represent a complete decomposition-reconstruction process. (Modified from *Misiti et al.* [1996])

where the details associated with the indices $j \leq J$ are confined in the scale range $a = 2^{j} \leq 2^{J}$ and the 'details' associated with the indices $j > J$ are actually the approximation at level J and can be represented as

$$A_J = \sum_{j>J} D_j$$

Equation 2.51

The original signal can also be given by the sum of all details i.e.

$$x = \sum_j D_j$$

Equation 2.52

Following *Misiti et al.* [1996], we define resolution as $1/a$ such that resolution increases with decreasing scale. Hence the finer details are assessed at small scales and as the scale increases the signal becomes successively coarser with decreasing resolution.

While it might not seem obvious, there are a number of advantages that are associated with the process decomposing and reconstructing a signal. First and foremost is the capability of multiresolution analysis to hierarchically reveal the embedded signal information at successively changing scales or resolutions. As pointed out by *Mallat* [1989], the information revealed by looking at an image at different resolutions characterizes different physical structures that are embedded in the signal. Coarser resolution reveals the "context" and finer resolution the "modalities" of the image [*Mallat*, 1989]. This way of looking at things is not only restricted to 2-D signals (e.g. an image in *Mallat's* case) but also applies to 1-D cases as well. Other applications of multilevel decomposition and reconstruction derive from the fact that the resulting coefficients can be used in a number of ways including signal de-noising and compression, detection of discontinuities and breakdown points in signals, studying long and short term trends, identification of pure frequencies and signal suppression [*Misiti et al.*, 1996].

2.8 BISPECTRUM

The traditional power spectral methods (Section 2.6) have a shortcoming when analysing a signal that may be a product of a non-linear processes — a situation that can arise, for instance, if a wave is propagating through a medium with a non-linear response [*Hinich and Clay*, 1968]. For instance taking the example used by *Kamalabadi et al.* [1997] of a quadratic process of the form

$$z(t) = x(t) + \varepsilon x^2(t), \quad \varepsilon \neq 0$$

Equation 2.53

where $x(t) = A_1\cos(\omega_1 t+\phi_1) + A_2\cos(\omega_2 t+\phi_2)$. In this case, the output $z(t)$ will contain the original cosinusoidal terms with (ω_1, ϕ_1), (ω_2, ϕ_2) and additional terms with $(2\omega_1, 2\phi_1)$, $(2\omega_2, 2\phi_2)$, $(\omega_1+\omega_2, \phi_1+\phi_2)$ and $(\omega_1-\omega_2, \phi_1-\phi_2)$ [*Kamalabadi et al.*, 1997]. Such behaviour is referred to as *quadratic phase coupling* [*Kamalabadi et al.*, 1997; *Nikias and Raghuveer*, 1987]. The problem arises when one just observes $z(t)$ without prior knowledge that it is a product of

quadratic coupling or some other non-linear process. This problem is made clearer by an example used by *Nikias and Raghuveer* [1987], who considered two processes of the form

$$p(t) = \cos(\omega_1 t + \phi_1) + \cos(\omega_2 t + \phi_2) + \cos(\omega_3 t + \phi_3)$$
$$q(t) = \cos(\omega_1 t + \phi_1) + \cos(\omega_2 t + \phi_2) + \cos(\omega_3 t + (\phi_1 + \phi_2))$$

Equation 2.54

where ω_1 and ω_2 are harmonically related according to $\omega_3 = \omega_1+\omega_2$. The phases ϕ_1, ϕ_2 and ϕ_3 are independent, random and uniformly distributed variables in the range $[0, 2\pi]$. Since ϕ_3 is independent of the other phases, it follows that in the case of $p(t)$, ω_3 is an independent harmonic whereas for $q(t)$, the harmonic ω_3 is a product of the phase coupling between ω_1 and ω_2. Traditional spectral methods (Section 2.6) fail to detect this coupling because they suppress phase information [*Kamalabadi et al.*, 1997; *Nikias and Raghuveer*, 1987]. In fact, the power spectrums of p(t) and q(t) are identical and have impulses at ω_1 ,ω_2 and ω_3 [*Nikias and Raghuveer*, 1987].

The solution to the above problem is the use of the higher-order moments of a sequence. In particular, we have to use a method based on the third-order moment (μ_3), called the *bispectral* method. *Nikias and Raghuveer* [1987] showed that the contribution to the third-order moment (hence the bispectrum) solely comes from the phase coupled components. Also, *Widdel et al.* [1994] explained that for a random process the Gaussian distribution is completely described by the first-order (i.e. mean, μ_1) and the second-order (i.e., covariance, μ_2), while the higher-order moments are identically zero. Therefore a deviation from a Gaussian distribution will result in μ_3 (and hence the bispectrum) being different from zero [*Rüster*, 1994; *Hinich and Clay*, 1968]. This is true for all non-linear processes generated by multiplicative interactions of different frequency components of the process [*Rüster*, 1994]. As a result, bispectral techniques have been used extensively in work that deals with the study of non-linear wave-wave interactions [e.g. *Rüster*, 1994; *Kamalabadi et al.*, 1997]. (However, as a word of caution, *Rüster* [1994] and *Widdel et al.* [1994] point out that some linear processes have a non-Gaussian distribution.) From the information above, it follows that the bispectrum of $p(t)$ will be identically zero (indicating absence of phase coupling) while that of $q(t)$ will not be.

Unless stated otherwise, the information below regarding the computation of the bispectrum is

based on *Nikias and Raghuveer* [1987]. We consider a time series $\{x_i: i=1, 2, \ldots, N\}$. While *Nikias and Raghuveer* [1987] split the series into K windows with M samples each (i.e. $N = KM$), I adopted a slightly different approach that of choosing a window of length M which was advanced by $\sim M/4$ until the whole series was covered. All samples x_i for a given data window are mean corrected using the mean of the corresponding window. Then for each window w the 3rd order columant is computed using the expression

$$r_w(m,n) = \frac{1}{M}\sum_{t=a}^{b} x(t)x(t+m)x(t+n)$$

Equation 2.55

where a and b are chosen such that $1 \le (t+m) \le M$ and $1 \le (t+n) \le M$. These columants are then averaged to give the average columant

$$R(m,n) = \frac{1}{K}\sum_{w=1}^{K} r_w(m,n)$$

Equation 2.56

By using the normalization factor given by *Priestley* [1981] together with the definition of the bispectrum as given by *Nikias and Raghuveer* [1987] we can express the bispectrum as

$$\hat{B}(\omega_1,\omega_2) = \left(\frac{1}{2\pi}\right)^2 \sum_{m=-L}^{L}\sum_{n=-L}^{L} R(m,n)\exp[-j(\omega_1 m + \omega_2 n)]$$

Equation 2.57

where $L<M-1$. In this thesis I have used the magnitude squared bispectrum [*Clark & Bergin*, 1997] i.e.

$$B(\omega_1,\omega_2) = \left|B(\omega_1,\omega_2)\right|^2$$

Equation 2.58

CHAPTER 3 OBSERVATIONAL TECHNIQUES

3.1 INTRODUCTION

As already mentioned in Chapter 1, the atmosphere is a complex and inhomogeneous fluid whose physics and chemistry changes from one height region to another. As a result of this and the fact that every observational method relies on some specific condition or feature of the atmosphere, it is difficult to design a technique that is capable of monitoring the whole height range of the atmosphere. Therefore, the optimum operation of a given technique will be limited to the height range with the appropriate characteristics. Generally, the techniques used to probe the atmosphere can broadly be classified into (i) *in situ* techniques, (ii) passive remote sensing and (iii) active remote sensing [*Harris,* 1993]. The first two techniques will not be discussed in detail and the reader is referred to *Harris* [1993] from whom most of the information in this section is obtained.

Briefly, the *in situ* observational methods involve placing a probe in the atmosphere. Such a probe can be attached to a balloon, kite, aircraft and spacecraft (including satellites). Possible probes include electrostatic sensors, ion and neutral mass spectrometers, retarding potential analysers, ion drift metres, omega navigation and telemetry equipment [*Harris,* 1993]. It is important to mention at this point that the Upper Atmosphere Research Satellite (UARS) [*Reber et al.* 1993] that was launched on 12 September 1991 has played a significant role in advancing the study of the atmosphere. On board this satellite are two instruments—the High Resolution Doppler Imager (HRDI) and the Wind Imaging Interferometer (WINDII), which are capable of measuring wind parameters. Details about the HRDI and the WINDII instruments are not going to be discussed in this thesis and can be found in *Hays et al.* [1993] and *Shepherd et al.* [1993], respectively.

Passive remote sensing, on the other hand, entails the measurement of some phenomenon whose variation is dependent on the atmosphere. From this variation some atmospheric property can be inferred. A good example for such application is the conclusion made by Gauss that the atmosphere has an ionised layer based on observed temporal variation of the magnetic field on the ground. The third category of observational techniques is active remote sensing. In this class of observational techniques, a specific feature of the atmosphere is actively stimulated and its response is used to deduce some characteristic of the atmosphere. The methods used in this category generally fall into two types—optical and radio equipment. The observation

systems at Grahamstown and Adelaide fall under the radio techniques. Under this class there are various systems, which include mesosphere-stratosphere-troposphere (MST) radars, Incoherent Scatter Radar (ISR), Low Frequency (LF) systems, meteor radars, and spaced antenna systems. The systems used at Grahamstown and Adelaide fall in the last two types (in that order) and these will be discussed in more detail in Section 3.2 and Section 3.3, respectively.

3.2 METEOR RADAR

3.2.1 Introduction

Meteor radars have been used extensively in the study of the MLT region for over 4 decades. The echoing principle is based on the meteoroids that continually bombard the upper atmosphere. When these meteoroids encounter the increasing density of the atmosphere they incandesce and ablate. If the meteoroids are sufficiently large, the above process is accompanied by the production of visible light and a column of ionisation [*Roper*, 1984; *Valentic et al.*, 1996]. The high velocities (11-72 km/s geocentric with an average of 42 km/s) of the meteoroids ensure efficient ionisation [*Roper*, 1984]. Practically, a meteor radar transmits a signal, which is later reflected by the ionised trail. If the meteor trail moves as a result of the motion of the wind in which it is embedded, the returned signal is Doppler shifted and it is from this shift that wind velocities can be determined. These procedures will become clearer when we discuss the Grahamstown meteor radar in the next section.

3.2.2 The Grahamstown Meteor Radar

3.2.2.1 General

The Grahamstown meteor radar started operating in April 1986 with a continuous run starting in October of the same year. The description made here is mainly based on *Poole* [1988, 1990]. The Grahamstown radar is a monostatic, phase-coherent radar designed to have an all-sky coverage. It is situated at 33.3°S, 26.5°E with an observing region with a radius of ~200 km and an assumed height range of ~80-110 km which is the height range of high meteor count.

3.2.2.2 Hardware

The Grahamstown radar is based on the BR Chirpsounder (Model 9034) and the whole arrangement consists of a transmitter, receivers, antennas and other electronic and computer hardware. A schematic diagram of some of the hardware described below is shown on Figure 3.1.

(a) *Transmitter and Receiver*

The transmitter operates at a fixed frequency of f_0=27.99 MHz and has a mean transmitter power of ~30 W. It was designed to deliver a nominal power of 100 W to a matched load. The transmission frequency f_i is offset by -40 Hz with respect to receiver tuned frequency f_0. This offset helps in the determination of the sense of the drift i.e. away or towards the radar. Two frequency synthesizers determine the tuned frequency together with the transmitted frequency. The receiver instrumentation consists of two matched low-noise receivers with programmable IF bandwidths of 0-40 Hz, 0-500 Hz and 0-2500 Hz.

Being monostatic, the radar requires transmit-receive switching which is controlled by a 500 Hz rectangular waveform. The transmit-receive switching is not contiguous i.e. there is a dead-time between transmit and receive periods. The switching process introduces transient effects that are partially smoothed by a "gain-weighting" circuitry. The system has two receivers that are switched at 250 Hz between two of four antennas (see Part (b) below) as shown on the timing diagram in Figure 3.1. The switching of each receiver input is synchronized with the switching between the receiver output and two low-pass filters. Due to the crystal filters in the IF stages some delay is introduced in the receivers. To achieve the synchronization discussed above, this delay is compensated by a similar delay in the receiver output/low-pass filter switching. The separation of the signals from the two channels (antennas) using the same receiver is made possible by using the 2.5 kHz bandwidth. Any remaining cross-talk effect is taken into consideration in the subsequent processing.

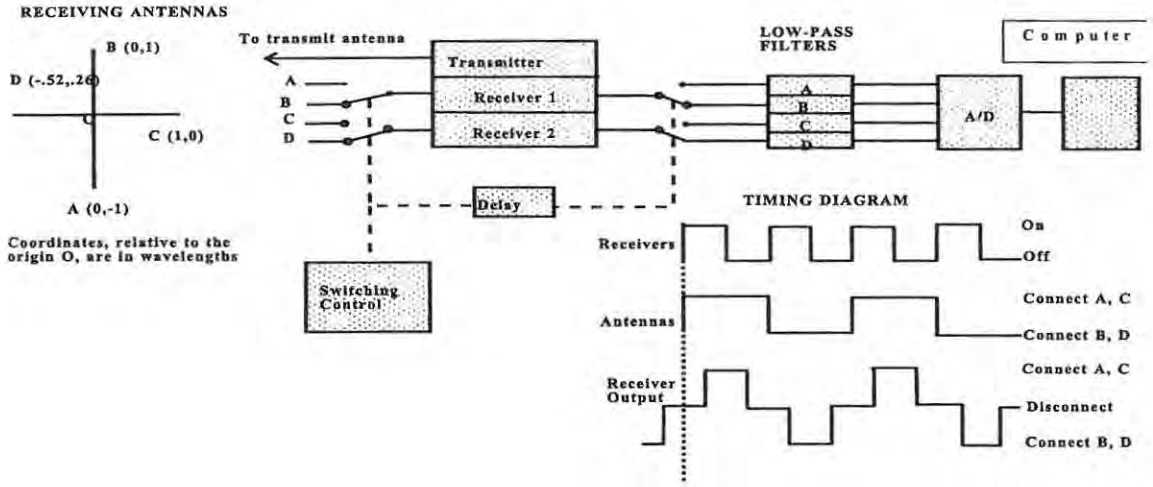

Figure 3.1 The schematic diagram of the Grahamstown meteor radar (modified from *Poole* [1988]).

(b) *Antenna Array*

The antenna array consists of five antennas—one transmitting and four receiving. These antennas are simple half-wave dipoles and are mounted about one-third of a wavelength above a flat ground surface. The spatial arrangement of the antennas is as shown in Figure 3.1 with their axes along the north-south meridian resulting in two oppositely directed broad lobes along the zonal (east-west) direction and elevated at ~45°. As a result of this antenna orientation, the system is characterised by anisotropy with zonal components being more accurately determined than their meridional counterparts. To make the surface conducting, the ground under the antennas is covered with a 1 m^2 coarse galvanized wire grid [*Roux*, 1988]. The single transmitting antenna is about 200 m from the four receiving antenna array. Apart from mere reception, the receiving array is used to determine the direction of arrival of an echo by comparing the phase of the reflected signal at each of the four receiving antennas. For this function, antennas A, B and C are used to determine a set of possible directions while D is used

for resolving the ambiguity.

(c) *Electronics and Computer Hardware*

The system has four low-pass filters that are connected in turn to the two receivers. Other hardware components include an A/D converter and a computer. The functions of all these components will be made clear in the next section.

3.2.2.3 Data acquisition and signal processing

The transmitter sends an incident signal at a frequency of f_i ($=f_0$-0.000040) MHz and square-wave modulated at 500 Hz. On hitting an ionised meteor trail, the signal is reflected to the receiving antennas. This signal passes through the receivers to the low-pass filters. These filters have a cut-off of ~100 Hz such that the 500 Hz switching frequency, mentioned above, together with its higher harmonics are filtered out from the receiver output leaving a pure audio tone. Connected to the filters is an A/D converter, which continuously samples each channel at 256 Hz. In the original system, the digitised samples from possible meteors that satisfy a set amplitude threshold were transferred to a computer disc for later processing. In this processing, the echo signals were Fourier transformed to determine the frequency and phase of the signal for each channel. For a possible echo to be considered genuine the spectral line characteristics of the four receiving channels have to be consistent to within a set limit. Following a system upgrade in 1990, this preliminary processing takes place on site in real time.

Having deduced this information, the next task is to determine the wind velocity and for this we use the frequency computed above. With the tuning of the receivers to f_0, a receiver input signal with a frequency equal to f_0 produces a DC output, otherwise an audio output at the appropriate frequency difference is produced. If the meteor trail is stationary such that there is no Doppler shifting, the frequencies of the incident signal f_i and that of the reflected signal f_r are equal. In this case, the receiver output is a signal with frequency equivalent to the difference of the transmitted and received frequencies, which is 40 Hz. Under normal circumstances, the trail is moving with the wind such that there is a Doppler shift which causes the receiver output to deviate from 40 Hz by the frequency difference $f_d = f_r - f_i$. This frequency difference is

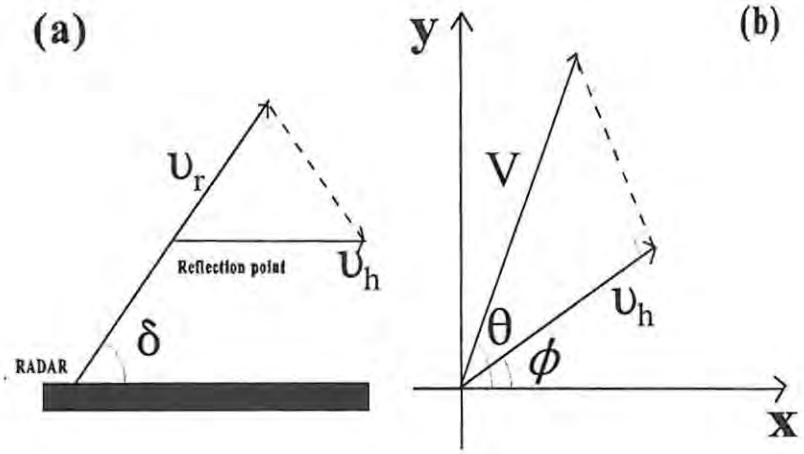

Figure 3.2 (a) The line-of-sight velocity v_r. (b) The horizontal wind component of the drift velocity and the horizontal wind **V** as seen from above.

proportional to the line-of-sight drift velocity, given by

$$v_r = \frac{c(f_r - f_t)}{2 f_t}$$

Equation 3.1

where c is the phase velocity of the incident signal and is assumed to be equivalent to the velocity of light for our purpose. Assuming that the vertical wind is zero, we have a horizontal component given by

$$v_h = v_r \cos \delta^{-1}$$

Equation 3.2

where δ is the elevation (Figure 3.2), which is measured by the system.

Using Figure 3.2(b), we can write

$$v_h = V\cos(\theta - \phi)$$

Equation 3.3

where **V** represents the mean horizontal velocity. From the same figure we can also write

$$v_{hx} = V\cos(\theta - \phi)\cos\phi = V(\cos\theta\cos^2\phi + \sin\theta\sin\phi\cos\phi)$$

Equation 3.4

and similarly

$$v_{hy} = V\cos(\theta - \phi)\sin\phi = V(\cos\theta\cos\phi\sin\phi + \sin\theta\sin^2\phi)$$

Equation 3.5

The velocity vector **V** is calculated from the averages of v_{hx} and v_{hy} over 1-hour time bins. The averages are weighted to compensate for the system anisotropy mentioned in Section 3.2.2.2, Part (b). The averages of $\cos^2\varphi$, $\sin^2\varphi$ and $\cos\varphi\ \sin\varphi$ are equal to half, half and zero, respectively such that

$$\overline{v}_{hx} = \frac{1}{2}V\cos\theta = \frac{v_x}{2}$$

Equation 3.6

and

$$\overline{v}_{hy} = \frac{1}{2}V\sin\theta = \frac{v_y}{2}$$

Equation 3.7

In our case the x and y axis represent the zonal (east-west, EW) and meridional (north-south, NS) direction, respectively such that Equation 3.6 and Equation 3.7 give the corresponding zonal and meridional velocity components.

3.3 THE SPACED ANTENNA SYSTEM

3.3.1 Introduction

The dynamics of the MLT region has been studied for many years using the spaced antenna technique. As mentioned by *Hocking and Thayaparan* [1997] this method was originally employed total reflection but has subsequently been modified to use partial reflection. *Fraser* [1984] points out that although the medium frequency (MF, 0.3-3 Mhz, [*Harris*, 1993]) and high frequency (HF, 3-30 Mhz, [*Harris*, 1993]) radars have a generic name of "partial reflection", the mechanism involved is more complex than that. According to this author, the echo mechanism ranges from reflections due to sharply bounded irregularities in the refractive index to scattering due to quasi-isotropic irregularities with scales that are of the order of half the wavelength of the radar. Echoes can be observed from minimum heights of 50-60 km (depending on the sensitivity of the system) to heights of total reflection in the E or F regions [*Fraser,* 1984].

The predominant variation of the refractive index is vertical but there are also significant horizontal variations [*Fraser*, 1984]. It is the resultant horizontal variation that modulates the incident wavefront such that the 'reflected or scattered wave is equivalent to an angular spectrum of plane waves' [*Fraser*, 1984]. As pointed out by *Fraser* [1984], the angular spectrum components interfere forming a Fresnel diffraction pattern on the ground. This diffraction pattern moves as a result of the movement of the reflection regions. However, the diffraction pattern moves with twice the velocity of the medium in which the irregularities are embedded—an effect known as the "point-source" effect [*Fraser,* 1984]. When the diffraction pattern moves past a stationary antenna an e.m.f. is induced and its amplitude varies (radiowave fading) [*Fraser,* 1984]. *Fraser* [1984] further explains that a comparison of the fading as recorded by at least three spaced antennas gives an estimate of the horizontal pattern velocity from which the horizontal velocity of the reflecting irregularities is inferred. The data analysis is usually done by using correlation techniques (see Section 3.3.2.3).

3.3.2 The Adelaide Spaced Antenna Radar

3.3.2.1 General

The Adelaide MF radar uses partial reflection backscattered radio waves that are sampled by three spaced antennas. The wind obtained using this method is, therefore, known as Spaced-Antenna Partial-Reflection (SAPR) wind or simply spaced-antenna (SA) wind. The radar is situated at Buckland Park (34.5°S, 138.5°E), which is ~40 km north of Adelaide and operates at a frequency of 1.98 MHz [*Harris*, 1993]. Even though the actual site is ~40 km from Adelaide, in this thesis I will refer to Adelaide as the actual observational site and *not* Buckland. The description in Section 3.3.2.2 and Section 3.3.2.3 is based on *Harris* [1993] who gives a detailed description of the radar and the method of data analysis.

3.3.2.2 Hardware

(a) *Transmit-Receive Instrumentation*

The transmitting array of the MF radar consists of four half-wave dipoles that are suspended at a height of 30 m (which is about ¼ of a wavelength) in a square formation with sides of ~75 m. There are two transmission modes—the linear right-hand (Ordinary or O-mode) and the left-hand (Extra-ordinary or E-mode) circular polarization modes. While the O-mode is usually transmitted during the day, the E-mode is transmitted at night.

The receiving array of the system consists of 89 crossed dipoles resulting in 178 independent elements (half of which are in a near north-south orientation and the other half in the near east-west orientation). This array arrangement occupies ~1 km^2 with the crossed dipoles being 11 m above ground. The signals from the 178 elements are carried independently to the central control room through a coaxial cable that is an integral number of half-wavelengths in length. In order to improve the signal-to-noise ratio for wind measurements, four elements are grouped together to form a single antenna. This also improves the reliability of the signal because it is not necessary for all four elements to have an adequate return.

3.3.2.3 Data acquisition and processing

Before 1991 data were captured by magnetic tape either as digitised "complex" receiver outputs (an in-phase component and a quadrature component) or wind that has been processed by the Full Correlation Analysis (FCA; see *Harris* [1993] for details) using a online Nova IV Eclipse. Following the installation of new receivers and associated higher pulse repetition frequency (PRF) and shorter duty cycles, the raw signal returns were analysed in real time through the FCA.

3.4 METEOR-SAPR COMPARISON

As already mentioned in Chapter 1, this thesis is mainly concerned with observations made at Grahamstown and Adelaide. This study has a number of important factors which include the following: (i) it involves sites that are essentially at the same latitude (~34°); (ii) the observations are simultaneous; (iii) the extraction of various dynamic components (e.g. mean wind, amplitudes and phases of harmonic components etc) uses the same numerical methods. Apart from the fact this will enable us to study the dynamics of the MLT region at Grahamstown and Adelaide, the above factors respectively allow (most importantly) for the study of longitudinal differences with (i) minimum latitudinal influence, (ii) no time difference, and (iii) no numerical analysis effects. However, the Grahamstown-Adelaide comparison is complicated by two major factors. First, Grahamstown and Adelaide use different observing techniques, namely, a meteor radar and an MF space antenna method, respectively. As already outlined in Section 3.2.1, a meteor technique relies on reflections from meteor trails for the deduction of winds. For spaced antenna methods, the received signal is due to reflection as well as scatter from weakly ionised irregularities in the mesospheric D region and by neutral air and humidity fluctuations in the tropospheric and stratospheric regions [*Hocking and Thayaparan*, 1997]. This being the case, there is a possibility that the type of motion being measured by the two techniques is not exactly the same. Also, the physics governing the meteor trails and the ionisation irregularities in the mesosphere are not the same and there are bound to be differences depending on the uncorrelated diurnal, seasonal variation of the relevant parameters. The second complication is due to the fact that unlike the Adelaide system, the meteor radar at Grahamstown does not have height resolution and this raises the question as to whether I am comparing atmospheric components from the same height or not. To make the

Grahamstown-Adelaide comparison as meaningful as possible, these two major complications have to be addressed.

3.4.1 Comparison of the Meteor-Spaced Antenna techniques

There seem to be some consensus on the ability of meteor radars to give accurate wind results in the MLT region whereas doubts have been expressed on the type of motion being measured by the spaced antenna technique. Suggested types include motion of turbulence embedded in the wind, wave motions, or ionisation drifts due to electromagnetic effects (see *Hocking and Thayaparan* [1997] and references therein).

A number of comparative studies have been conducted that address some of these issues. From their multi-instrument study, *Hines et al.* [1993], concluded that the MF/HF partial reflection method gives good results of winds up to ~80 km but fail above this height. These authors concluded that at higher heights this method gives motion that is related to gravity-wave propagation at the level of scattering. These authors went on to challenge the view that partial-reflection techniques measure true wind. The doubts raised by *Hines et al.* [1993] have, however, been contradicted in various degrees by various authors based on meteor-spaced antenna comparative studies. While these studies do not show perfect comparison between the meteor system and the spaced antenna system, they seem to suggest that observed differences are not an indication of fundamental differences in what is being measured by the two methods.

Cervera and Reid [1995] compared results obtained by an VHF (54.1 MHz) meteor radar and an MF (1.98 MHz) spaced antenna radar in the height range of 80-98 km at Adelaide. The two radars are separated by about 600 m and the data used by these authors was collected simultaneously over 10 days. *Cervera and Reid* [1995] found that the two methods compared favourably in the zonal wind below 90 km. More specifically, these authors found that the semidiurnal tide phases and the mean winds deduced by the two methods were in good agreement, leading them to conclude that the two techniques were measuring the same phenomenon. However, above 90 km, the spaced antenna method underestimates the meteor wind results.

Another comparison of co-located VHF meteor and MF spaced antenna systems was conducted

at London, Canada by *Hocking and Thayaparan* [1997]. This study focussed on the 85-94 km height range and is based on observations made over 2 years. The results of the comparison as presented by *Hocking and Thayaparan* [1997] can be summarised as follows. Monthly values of the mean wind, diurnal and semidiurnal tidal amplitudes and phases, which involve 120 values, show that only 23 (19%) showed poor comparison. Further, these authors mention that none of the remaining 97 values 'could be rejected as different at the 95% confidence level' and the observed differences can be solely attributed to statistical effects. Of the 97 results, 38 were found to be excellent and 59 were good. *Hocking and Thayaparan* [1997] found that disparities between the two techniques were more pronounced during the equinoxes. From their results these authors concluded that the MF space antenna method is a reliable means of studying synoptic neutral wind motion of periods of ≥12 h at 85-94 km altitudes. Further support for the good comparison between the meteor and the spaced antenna methods, came from *Valentic et al.* [1997]. These authors found that the two methods show good agreement in the mean flow, the amplitudes and phases of the diurnal tide, the semidiurnal tide, and the 2-day wave.

Although the results presented by *Cervera and Reid* [1995], *Hocking and Thayaparan* [1997] and *Valentic et al.* [1997] show that differences between the meteor radar method and the spaced antenna method do occur, it would seem that these do not suggest that the two methods are measuring two different atmospheric phenomena. It is on these premises that I will regard results from both methods as a true representation of the motion of the *neutral atmosphere* in the MLT region. This leaves us with the height issue, which will be discussed in the next section.

3.4.2 Height integration

3.4.2.1 Implementation

As already mentioned, the Grahamstown radar does not have height resolution. Different methods can be employed in an attempt to overcome this problem. *Malinga et al.* [1998] used correction factors deduced from long-term results from *Vincent et al.* [1998]. Another method involves comparing winds from a meteor system without height resolution with exact height data from a system with height resolution. The exact height is chosen to be close to the nominal centre height of the radar without height resolution. For instance, *Portnyagin et al.* [1993a, b]

compared Molodezhnaya meteor data for a nominal height of 95 km with spaced antenna data for exact heights of 94 km and 96 km made at Mawson. Considering nominal error bar of 2-5ms^{-1}, these authors found overall good agreement for mean zonal flow [*Portnyagin et al.*, 1993a]. However, their meridional flow had differences whose plausible explanation were mesoscale variations in gravity wave forcing. Based on the good agreement observed in the mean zonal wind, *Portnyagin et al.* [1993a] suggested that any observed differences are not due to fundamental differences in the technique (i.e. differences in interpretation of data based on meteor trail scattering or scattering from plasma inhomogeneities), or at the very least such differences are filtered out by monthly averaging. This suggestion is in line with the conclusion made at the end of the previous section.

Another alternative is to implement a method that is similar to that used by *Fraser et al.* [1995] which is based on the fact that the meteor height distribution has a near-Gaussian profile (e.g. Figure 3.3). These authors weighted the partial reflection data with a function that represent the meteor echo distribution. This gave them height sampling profile that is equivalent to that of meteor winds. *Portnyagin et al.* [1993a] report some unpublished work by Yu. Portnyagin who investigated the interpretation of Gaussian-weighted averages and found that the weighted averages consistently gave a reliable estimate of the wind at a nominal height of 95 km. Further work on the assessment of the effects of height averaging was done by *Lysenko et al.* [1994]. These authors used height-resolved meteor radar data observations made at Kazan to assess the effect of averaging over the whole meteor region. They compared the prevailing wind and the amplitude and phases of the diurnal tide and the semidiurnal tide for a single height of 95 km and for data averaged over the 80-110 km height region. They found good agreement, which led them to conclude that meteor observations without height resolution give results that are an adequate representation of wind parameters at mid-latitudes in the mesopause region. Therefore, a similar conclusion can be made regarding the Grahamstown observations except that the centre height is lower due to the sensitivity of the system as we will see below.

In this thesis, I implemented a Gaussian weighting procedure due to the fact that the meteor profile at Grahamstown is near-Gaussian (Figure 3.3) with a centre height z_0 = ~90 km and an equivalent width of a ~20 km. This height distribution is based on preliminary results obtained at Grahamstown by *Poole* [1999, private communication]. In an attempt to incorporate height

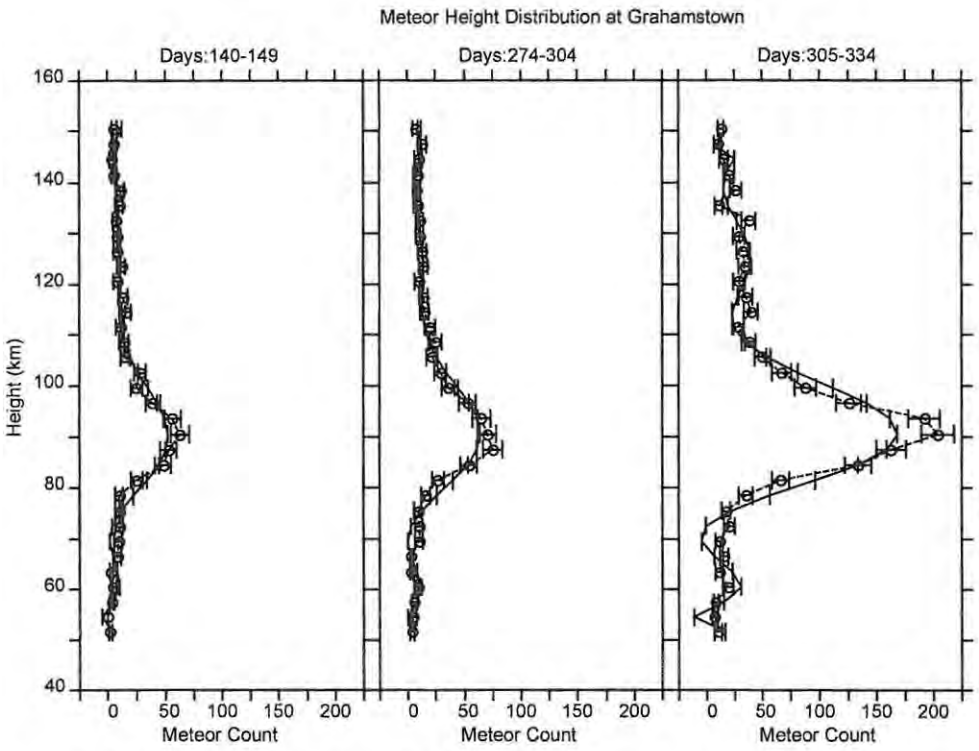

Figure 3.3 Preliminary results of the height distribution of observed meteors at Grahamstown obtained by the joint use of the meteor radar and another ionospheric chirpsounder in 1999.

resolution in the Grahamstown observing system, Poole used the meteor radar in conjunction with an older chirpsounder. Although this distribution is based on limited observations (due to equipment unreliability) and should be treated cautiously, it is consistent with the results obtained by *Weiss* [1959]. This author presented results for some 6400 sporadic meteors whose brightness is in the range of 3-6 magnitude and were observed using a system operated at 27 MHz. Of particular significance is the fact that these system characteristics are close to those of the Grahamstown radar, which has a limiting magnitude of +5. *Weiss'* [1959] summary table (his Table 1) reveals that the mean heights of the meteor distributions for various years and months are in the range of 88.9-91.2 km with maximum rms deviation of 7.47 km.

From the profiles illustrated in Figure 3.3, it follows that the wind results at Grahamstown which are inherently a *near-Gaussian-weighted-average* of the wind in the ~80-110 km altitude range, will be biased towards the ~90 km centre height. Therefore, we can reasonably assume that the wind observed at Grahamstown is, with some measure of confidence, a good presentation of the wind at ~90 km altitude. This is in line with the conclusion made by *Lysenko et al.* [1994] as explained above. To facilitate comparison with the height integrated

observations at Grahamstown, I formed Gaussian-weighted means of the hourly Adelaide wind velocities according to

$$x = \frac{\sum_{z=78}^{102} w_z x_z}{\sum_{z=78}^{102} w_z}$$

Equation 3.8

where x_z is the hourly horizontal wind average speed (zonal or meridional) at some height z and

$$w_z = \exp\left[\frac{-\pi(z - z_0)^2}{a^2}\right]$$

Equation 3.9

where the estimates of a and z_0 are given above. Adelaide height bins range from 78 to 98 km and, therefore, to achieve symmetry about 90 km I have used the wind values for 98 km to calculate the weighted wind speeds for 100 km and 102 km.

3.4.2.2 The effects of height integration

We require that the Gaussian weighted and averaged wind profiles at Adelaide give a good enough representation of the wind at ~90 km, which is assumed to be the case at Grahamstown. To assess if this is indeed true at Adelaide, I compared wind at this site for a *single* 2 km bin (SB) at ~90 km and a 24 km Gaussian weighted *integrated* bin (IB) centred at ~90 km. I will compare the IB and SB values of various atmospheric variables, namely, the monthly averages of the mean flow, tidal amplitudes and phases. At this point, I will not go into the details of how these monthly average values were computed. This will be discussed at more appropriate sections (Chapter 4, Section 4.3.1.1 for the mean flow; Chapter 6, Section 6.3.1.1 for tides).

Starting with the mean flow, we observe that the zonal mean flow (Figure 3.4) generally shows better agreement between IB and SB values from autumn through to mid-spring with the other times indicating that height integration tends give underestimated mean flow values (see

especially the interannual average, IA). The corresponding distributions of velocity differences (Figure 3.6) show that the majority of the differences are negative, indicating that height integration tends to reduce the mean flow. The largest average (-5.1 ± 0.4 ms^{-1}) is in summer with the other seasons having averages of less than 3 ms^{-1} and the long-term average is ~2 ms^{-1}. The meridional mean flow is less sensitive to height integration during all seasons as shown by the good agreement illustrated in Figure 3.5. Average differences (Figure 3.7) are < 1 ms^{-1} and positive differences show a marginal majority.

Figure 3.8 and Figure 3.9 show the zonal and meridional vector monthly amplitudes of the diurnal tide at Adelaide. Unlike mean flow values, diurnal tidal amplitudes show larger effects of height integration which is most likely related to the short vertical wavelengths (~ 30 km) of this tide. In general SB values are larger than IB values with long-term average differences of ~-4 ms^{-1}(Figure 3.10 and Figure 3.11). The zonal and meridional amplitude differences, as depicted by Figure 3.10 and Figure 3.11, show similar seasonal patterns characterised by larger (averages ~-3 to ~-5 ms^{-1}) in summer and the equinoxes with smaller (averages ~2 ms^{-1}) differences in winter. The comparison of the zonal and meridional phases is shown on Figure 3.12 and Figure 3.13, respectively. The phases of IB and SB show a higher degree of similarity than corresponding amplitudes. This can also be seen from the distribution of the associated differences (Figure 3.14 and Figure 3.15), which show the dominance (≥55 %) of 1 h differences with all long-term and seasonal averages being < 1 h.

Semidiurnal amplitudes (Figure 3.16 and Figure 3.17), unlike their diurnal counterparts, are less affected by height integration more especially in the case of the meridional component. The zonal amplitude discrepancies tend to be large (averages ~2 ms^{-1}) during the equinoxes and winter compared to summer (average < 1 ms^{-1}) (see Figure 3.18). The meridional amplitude difference averages (Figure 3.19) are < 2 ms^{-1} with the 1ms^{-1} bin being the most dominant (50 %). The zonal phases (Figure 3.20) of IB and SB compare very well with corresponding difference distributions (Figure 3.22) being predominantly (63 %) centred at 0 h with averages of < 0.5 h. The meridional phases of IB and SB (Figure 3.21), like their zonal counterparts, compare very well with the largest discrepancies recorded during the equinoctial transitions that join two solstitial phase states that are associated with the phase bi-modality (see later

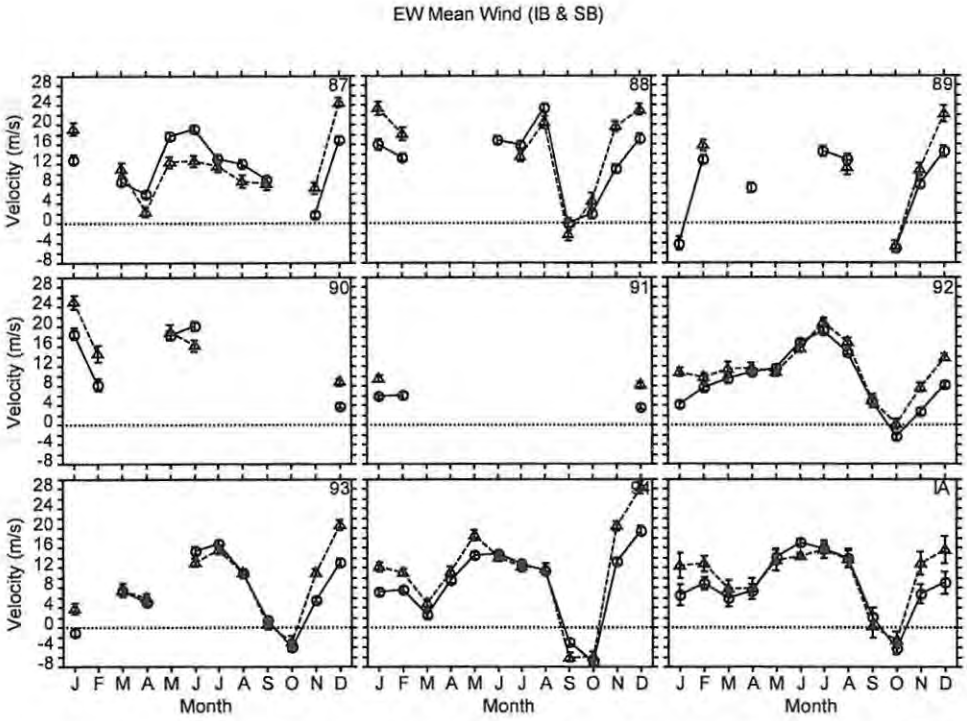

Figure 3.4 The zonal mean flow at Adelaide for the integrated (height) bin (IB) (circles) and the single bin (SB) (triangles) for the years 1987-1994 and the IA. The error bars represent one standard error of the mean (1 α).

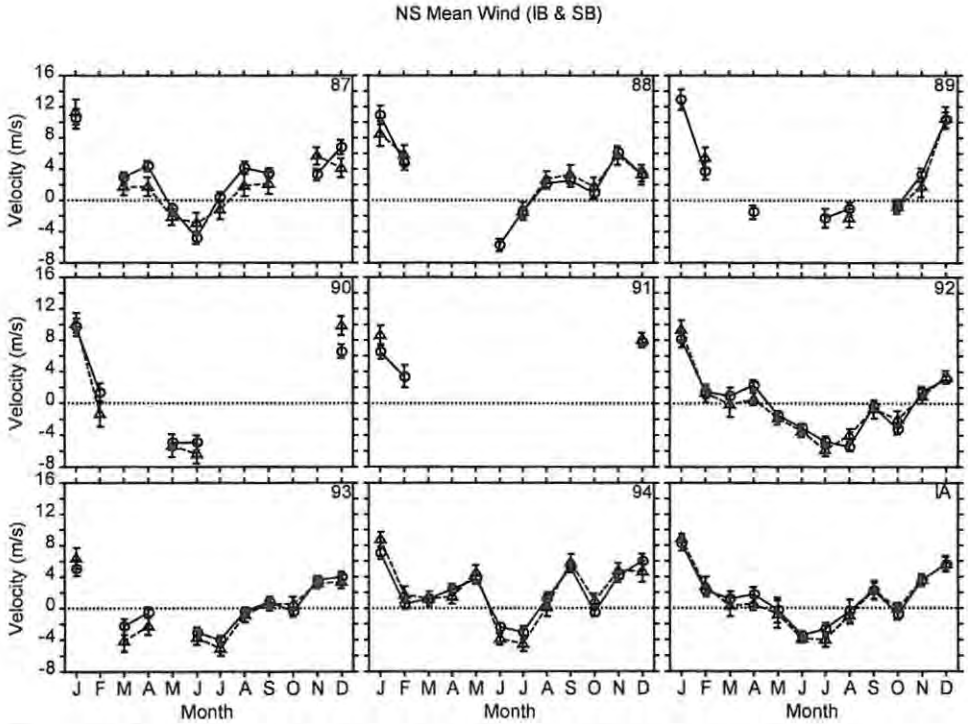

Figure 3.5 Same as **Figure 3.4** but for the meridional mean flow.

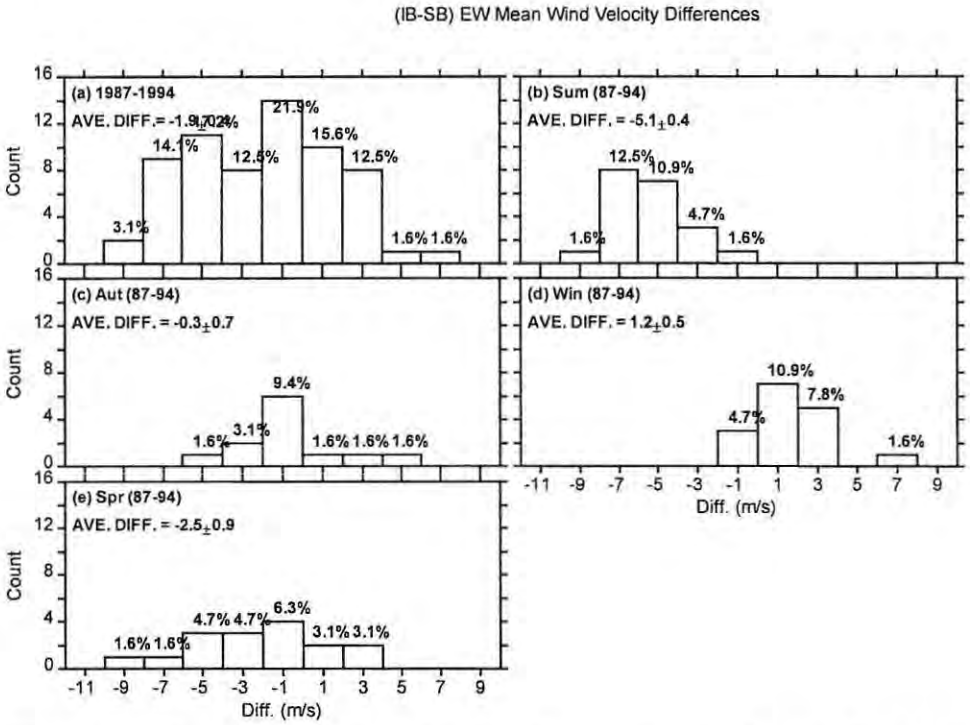

Figure 3.6 The distribution of the (IB-SB) zonal mean flow differences at Adelaide for the years 1987-1994. The weighted average differences are also given and the percentage count of each bar.

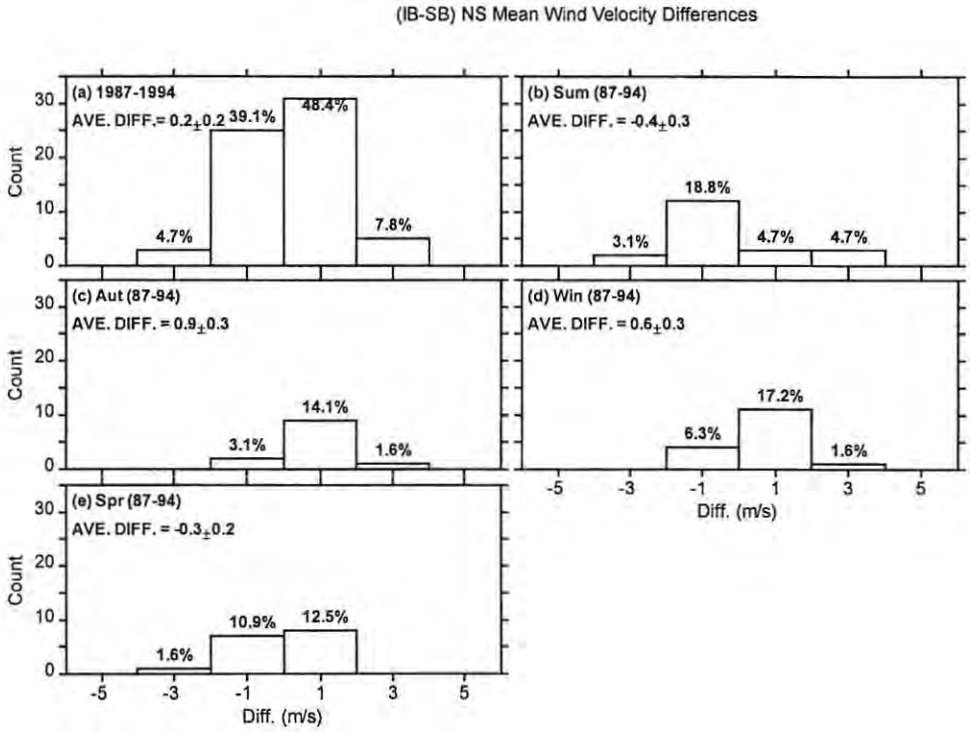

Figure 3.7 Same as **Figure 3.6** but for the meridional mean flow.

Chapter 7, Section 7.3.1). The difference distributions (Figure 3.23) of the meridional phases are also dominated (55 %) by the 0 h bin with averages being < 0.5 h once again. These results reveal that both the amplitude and phases of the semidiurnal tide are less sensitive to height integration effects. This is consistent with the fact that this tide, unlike the diurnal tide, has a larger vertical wavelength.

To summarise we observe that the mean flow and the semidiurnal tidal amplitudes are comparatively insensitive to the effects of height integration and have (IB-SB) differences with 8-year averages with absolute values of ~0-2 ms^{-1}. In general height integration tends to reduce the wind parameters with the exception of the meridional mean flow where there as may positive differences as there are negative ones. The diurnal tide, due to its short vertical wavelength, is more sensitive to height integration and its amplitude has (IB-SB) differences with 8-year averages of ~-4 ms^{-1}. The phases of both tides are less affected by height integration and the corresponding (IB-SB) differences have 8-year averages of < 1 h with the diurnal tide having larger [0.7±0.1 h (EW) and 0.8±0.1 h (NS)] averages than the semidiurnal tide [0.2±0.1 h (EW) and 0.1±0.1 h (NS)]. In general, height integration tends to delay the phases resulting in a bias towards positive (IB-SB) differences.

Based on the above results, we can conclude that the Gaussian weighted and averaged wind values, are a reasonable representation of the Adelaide wind at 90 km. From this I can claim, with a reasonable level of confidence, that I am comparing atmospheric variables at altitude levels of ~90 km at Grahamstown and Adelaide. With the conclusion reached in Section 3.4.1 about the ability of the spaced antenna method to measure neutral wind, the above statement can be extended to mean that I can reasonably assume that I am comparing the dynamics of the *neutral* atmosphere at ~90 km between Grahamstown and Adelaide.

It is on these premises that most of the differences observed between Grahamstown and Adelaide will be attributed, in the first instance, to differences in the dynamic structures between the two sites. This does not, by any means, imply that height related effects should be ignored, but it only means that we can, to some extent, assume that their contribution is small at least in so far as monthly atmospheric parameters are concerned. It may well be that with

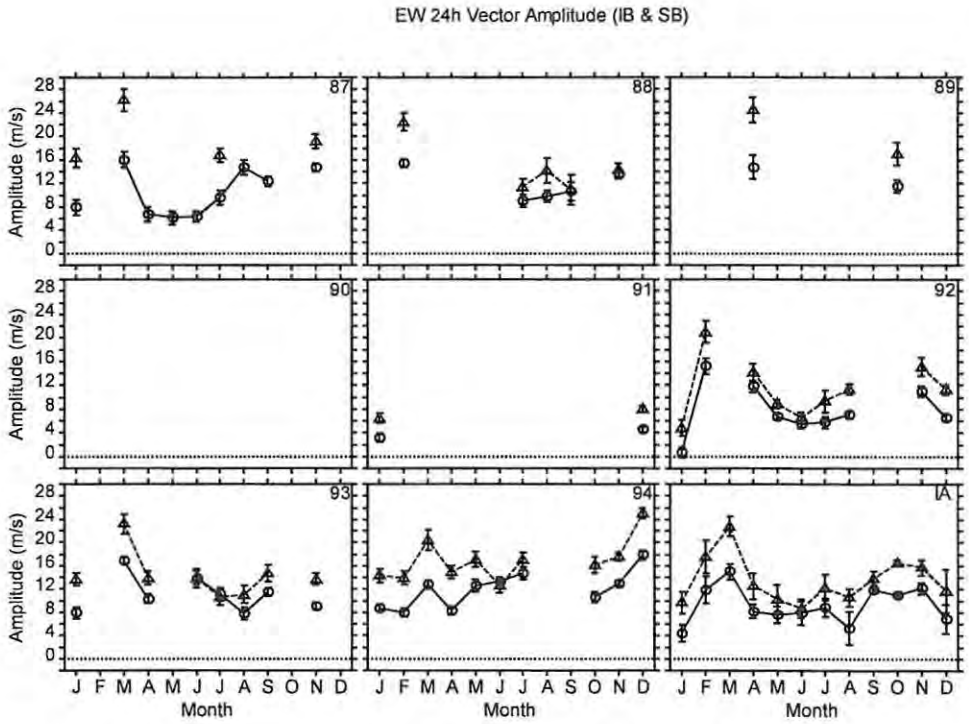

Figure 3.8 The zonal amplitudes of the diurnal tide Adelaide for the integrated (height) bin (IB) (circles) and the single bin (SB) (triangles) for the years 1987-1994 and the IA. The error bars represent one standard error of the mean (1 α).

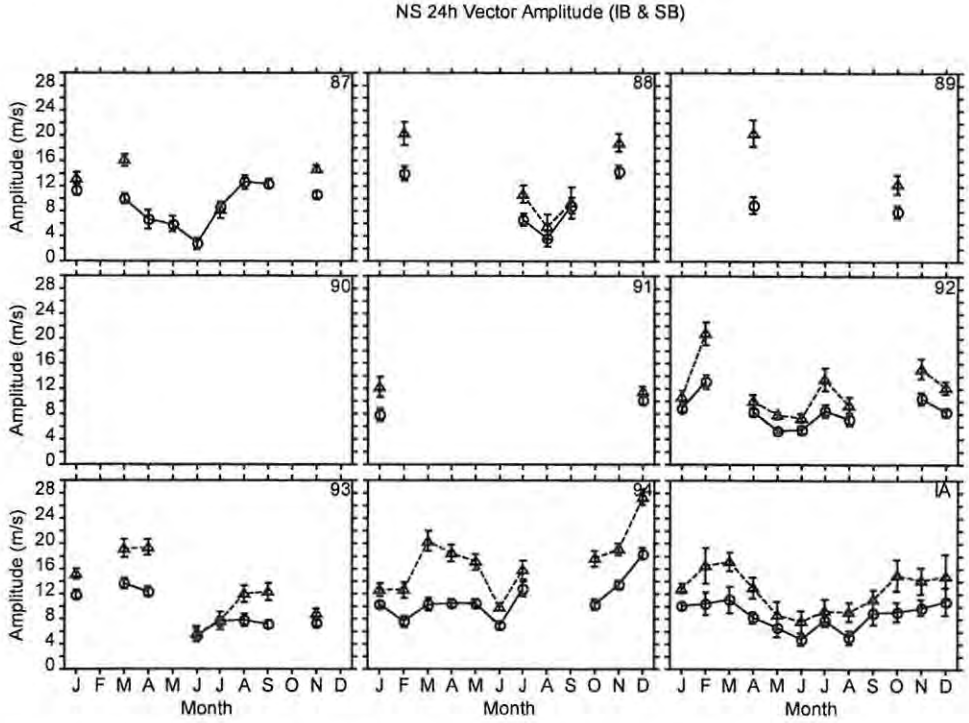

Figure 3.9 Same as **Figure 3.8** but for meridional amplitudes.

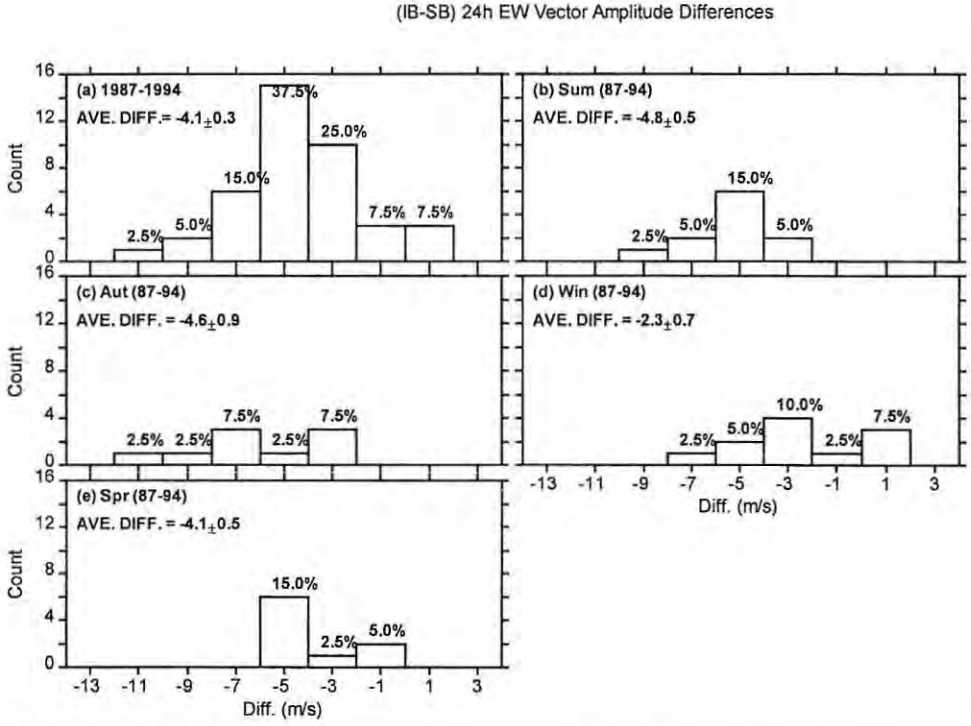

Figure 3.10 The distribution of the (IB-SB) zonal amplitudes differences for the diurnal tide at Adelaide for the years 1987-1994. The weighted average differences are also given and the percentage count of each bar.

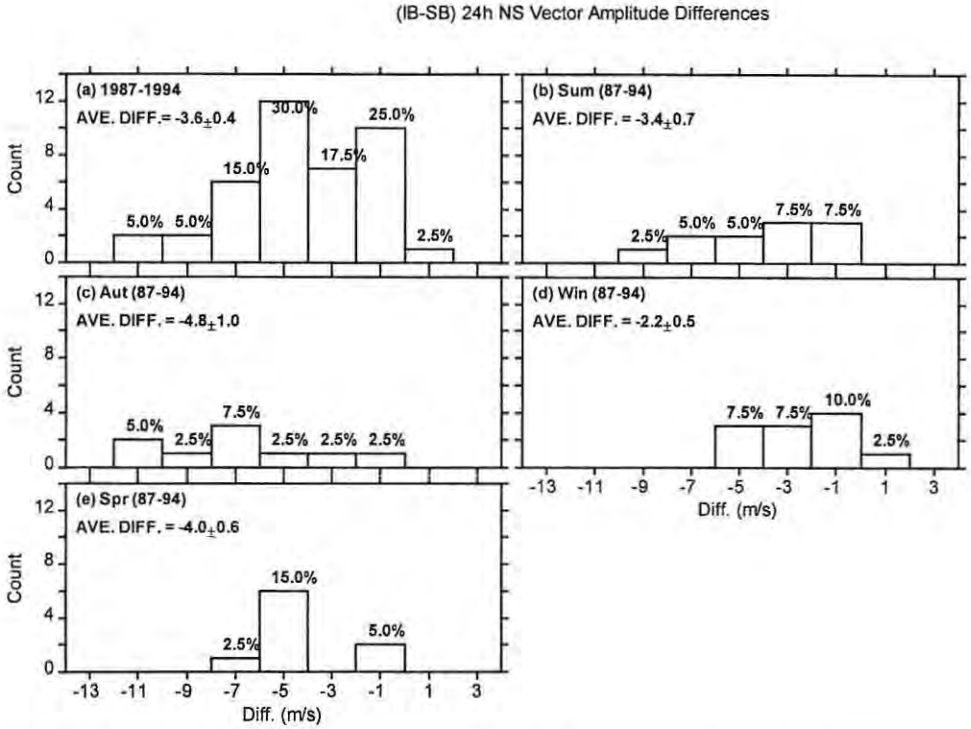

Figure 3.11 Same as **Figure 3.10** but for the meridional amplitudes.

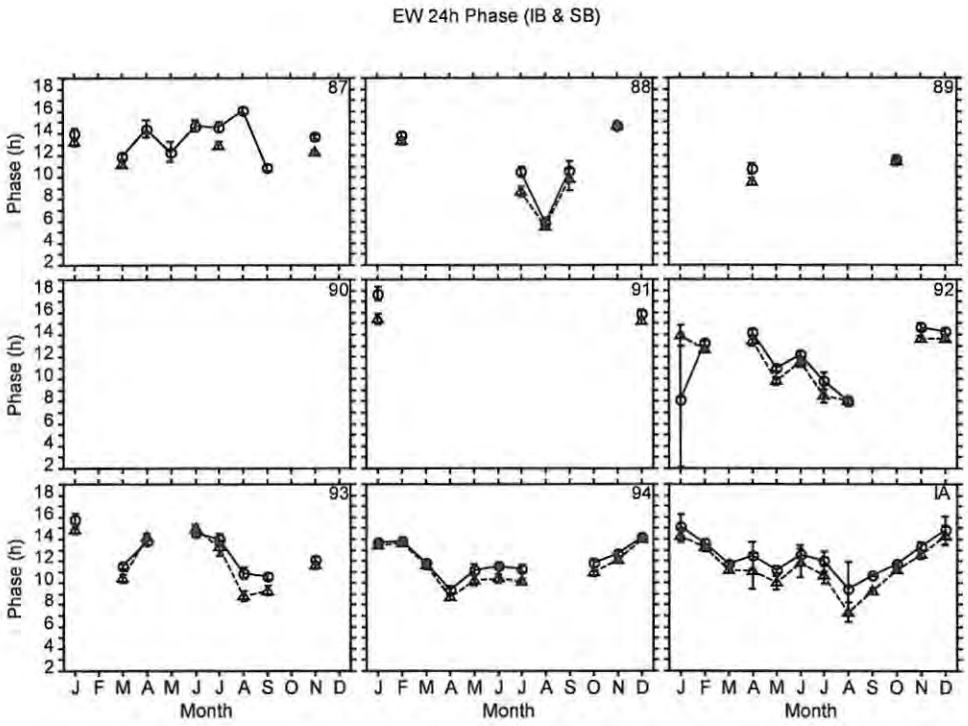

Figure 3.12 The zonal phases of the diurnal tide at Adelaide for the integrated (height) bin (IB) (circles) and the single bin (SB) (triangles) for the years 1987-1994 and the IA. The error bars represent one standard error of the mean (1 α).

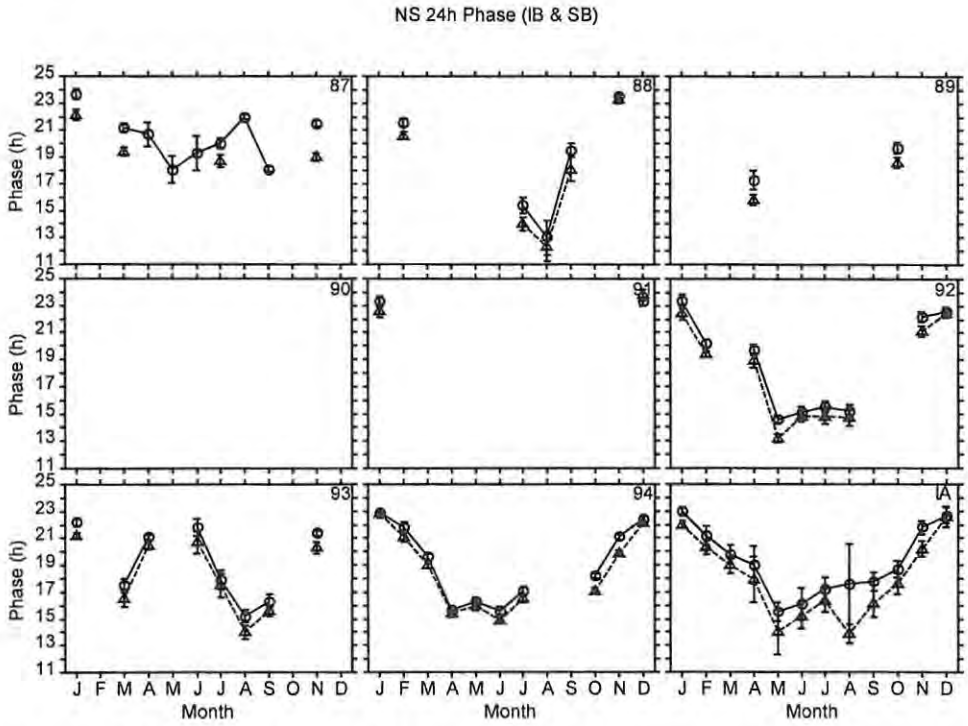

Figure 3.13 Same as **Figure 3.12** but for meridional phases.

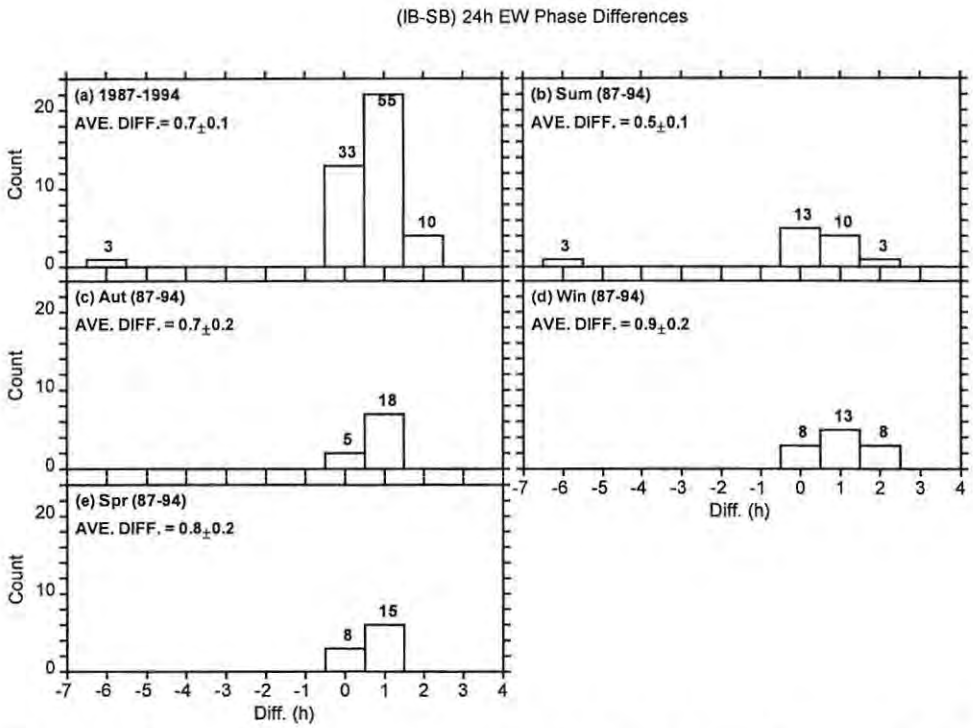

Figure 3.14 The distribution of the (IB-SB) zonal phase differences for the diurnal tide at Adelaide for the years 1987-1994. The weighted average differences are also given and the percentage count of each bar.

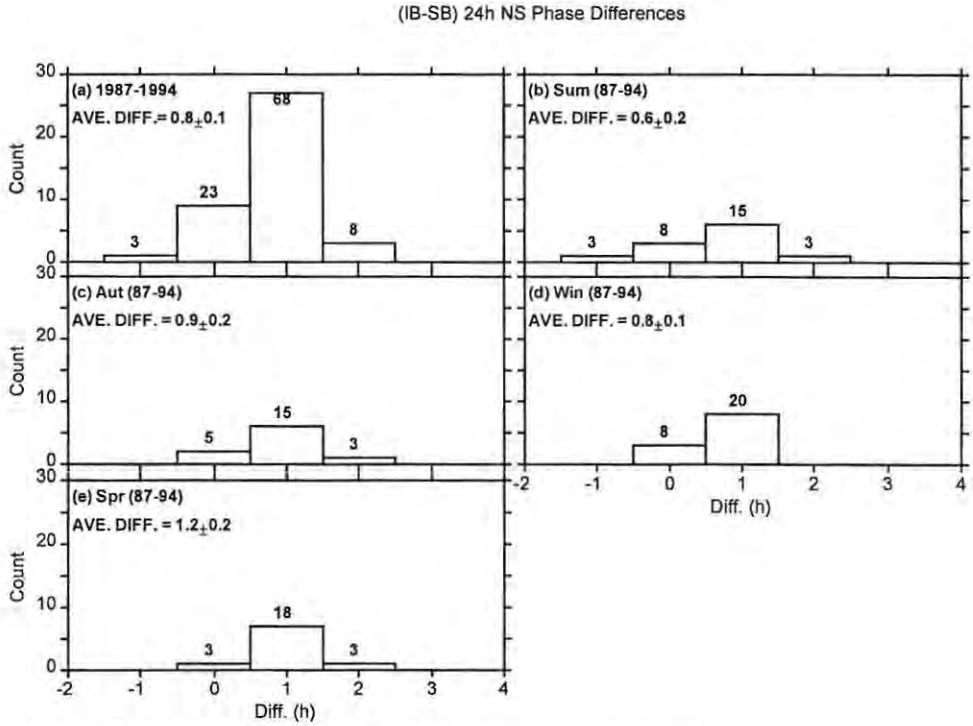

Figure 3.15 Same as **Figure 3.14** but for meridional phases.

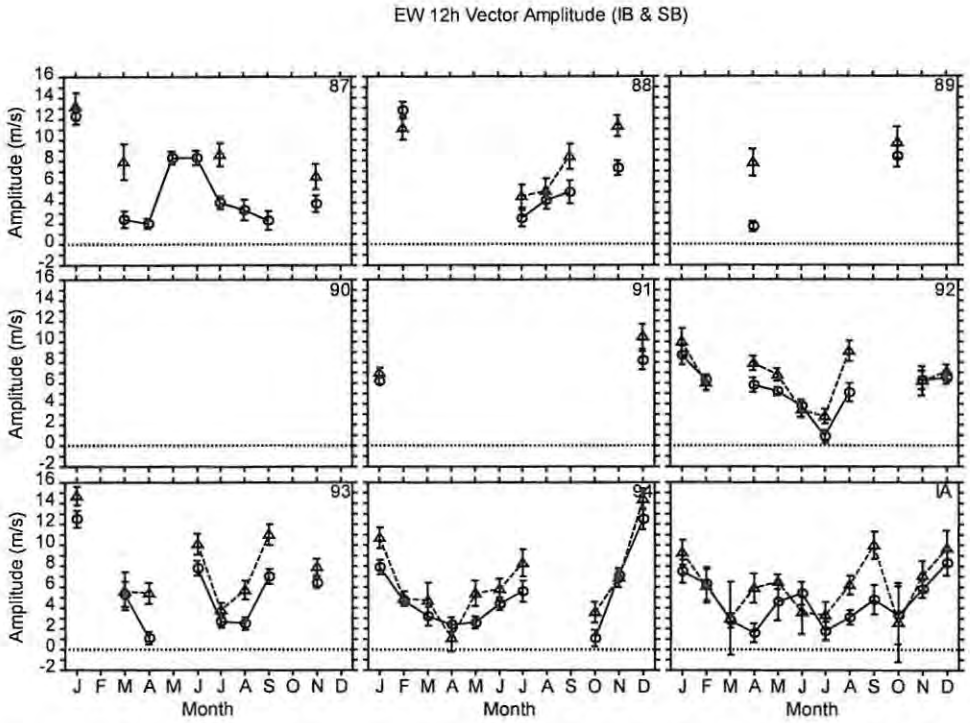

Figure 3.16 The zonal amplitudes of the semidiurnal tide at Adelaide for the integrated (height) bin (IB) (circles) and the single bin (SB) (triangles) for the years 1987-1994 and the IA. The error bars represent one standard error of the mean (1 α).

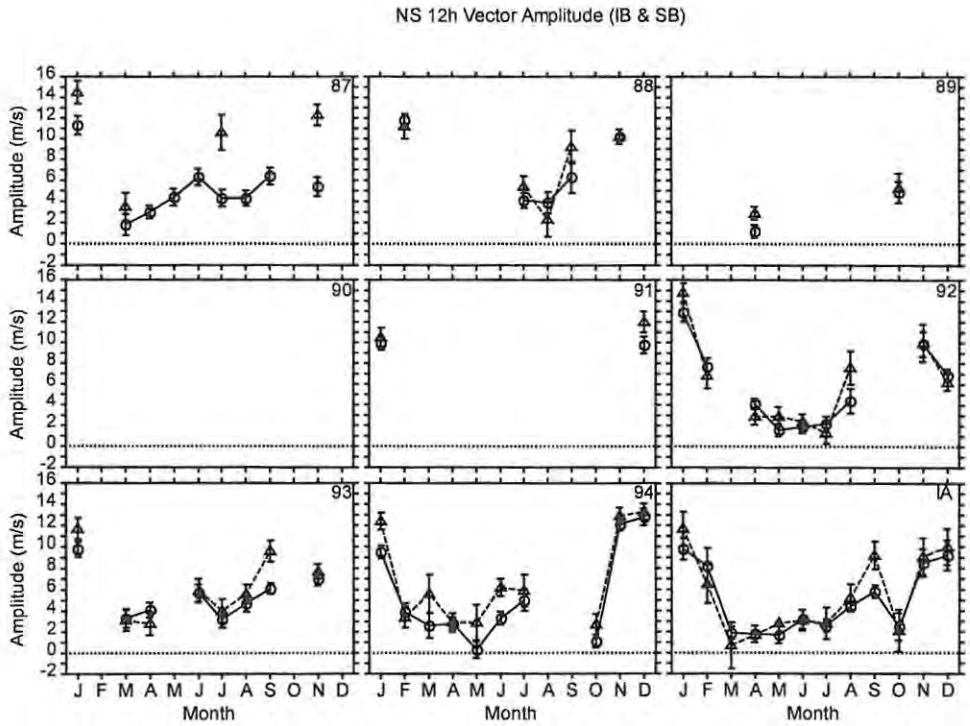

Figure 3.17 Same as **Figure 3.16** but for meridional amplitudes.

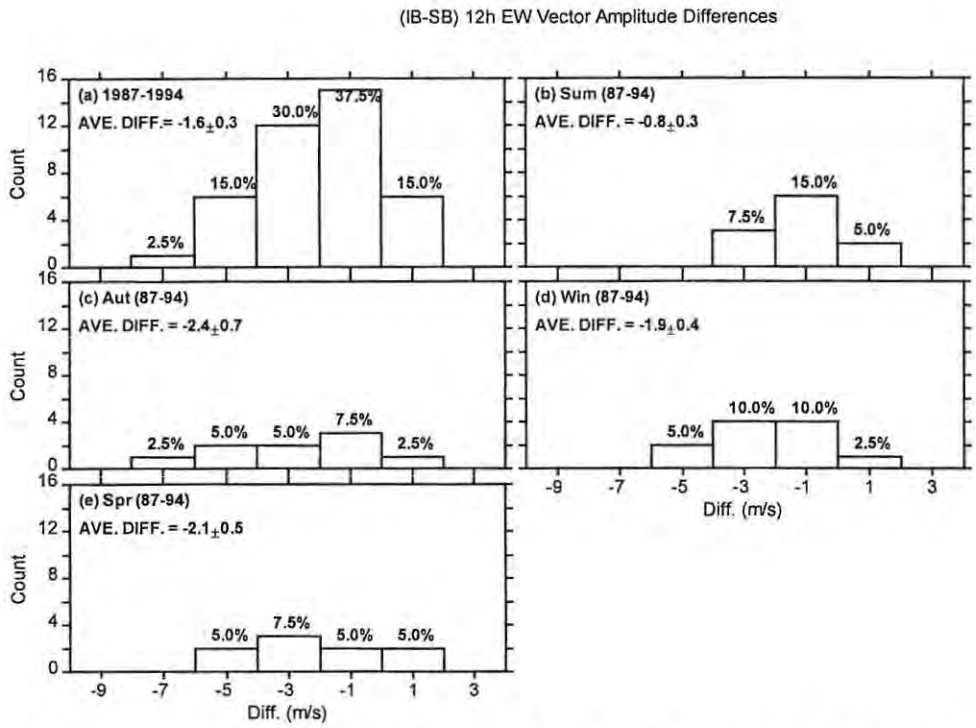

Figure 3.18 The distribution of the (IB-SB) zonal amplitude differences for the semidiurnal tide at Adelaide for the years 1987-1994. The weighted average differences are also given and the percentage count of each bar.

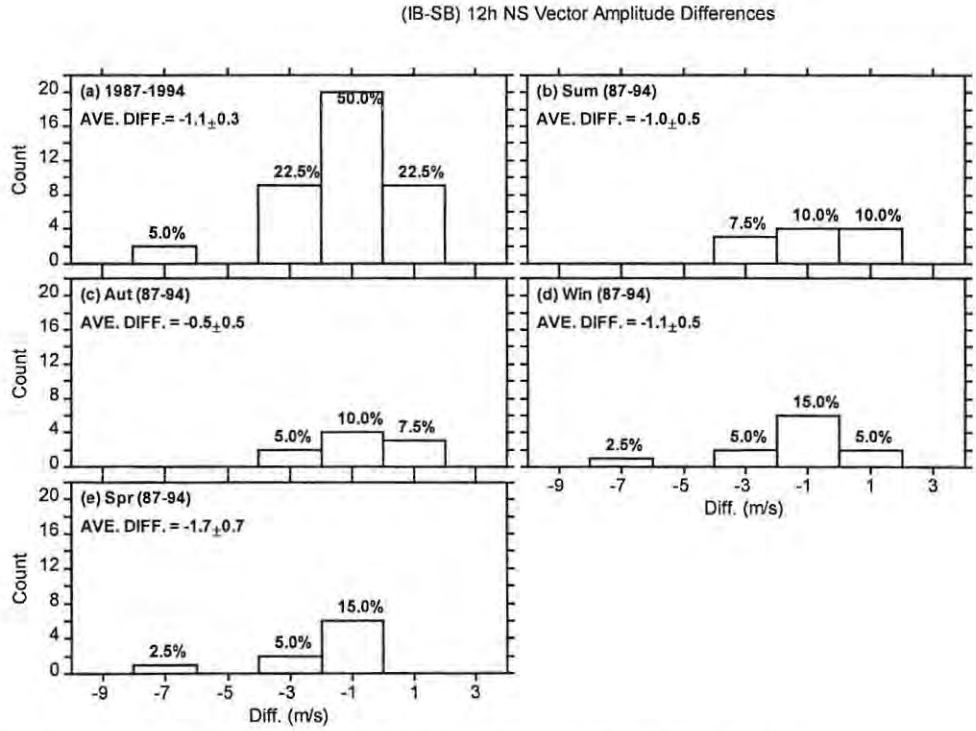

Figure 3.19 Same as **Figure 3.18** but for meridional amplitudes

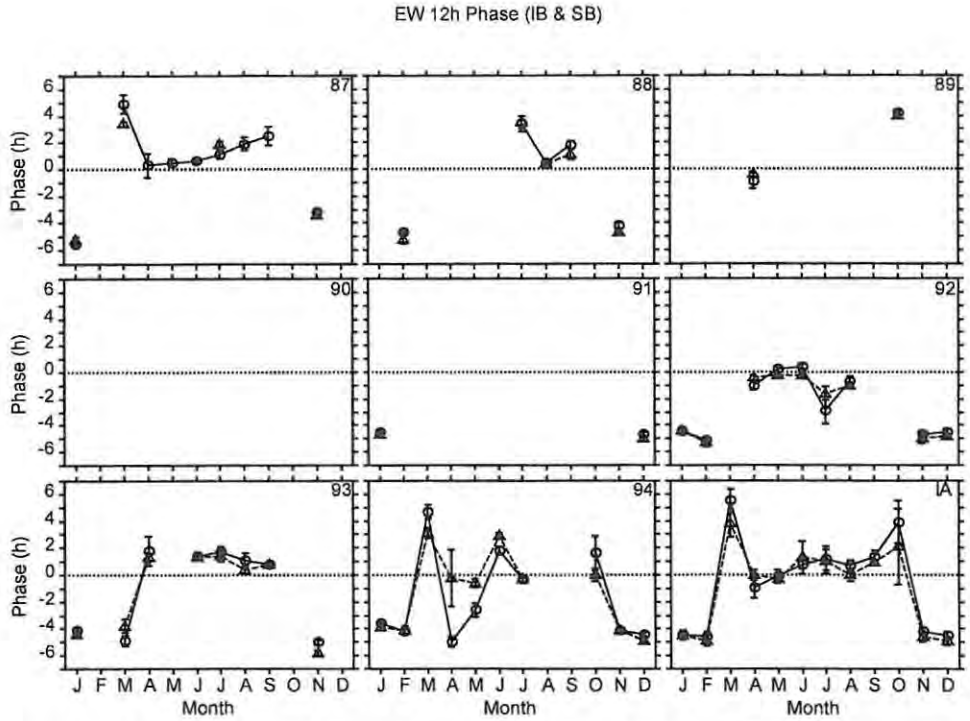

Figure 3.20 The zonal phases of the semidiurnal tide at Adelaide for the integrated (height) bin (IB) (circles) and the single bin (SB) (triangles) for the years 1987-1994 and the IA. The error bars represent one standard error of the mean (1 α).

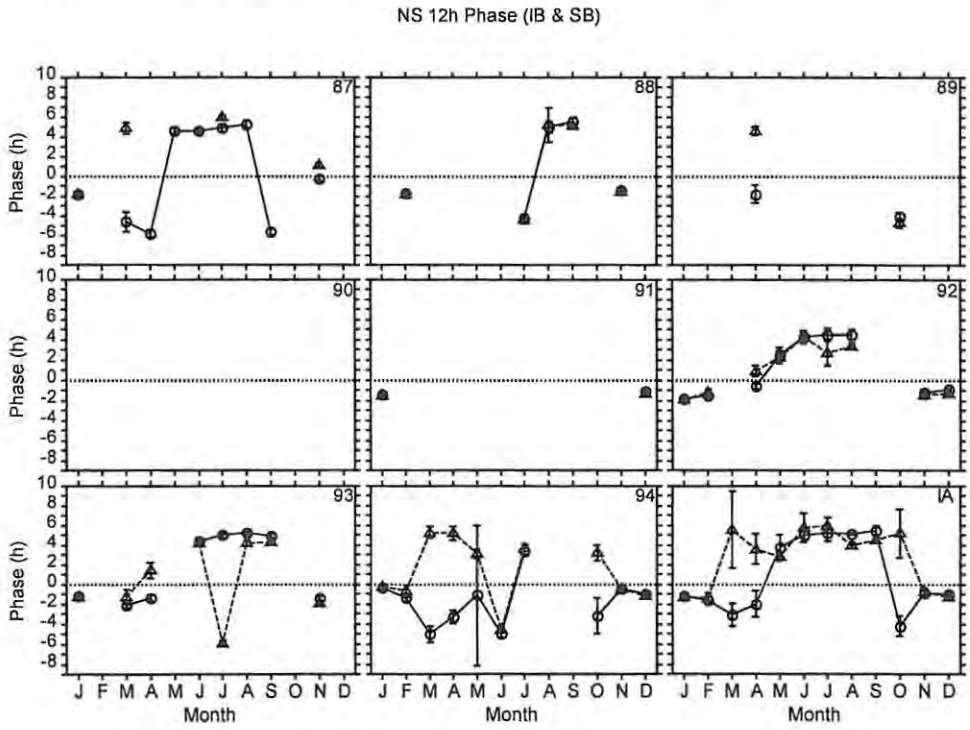

Figure 3.21 Same as **Figure 3.20** but for meridional phases.

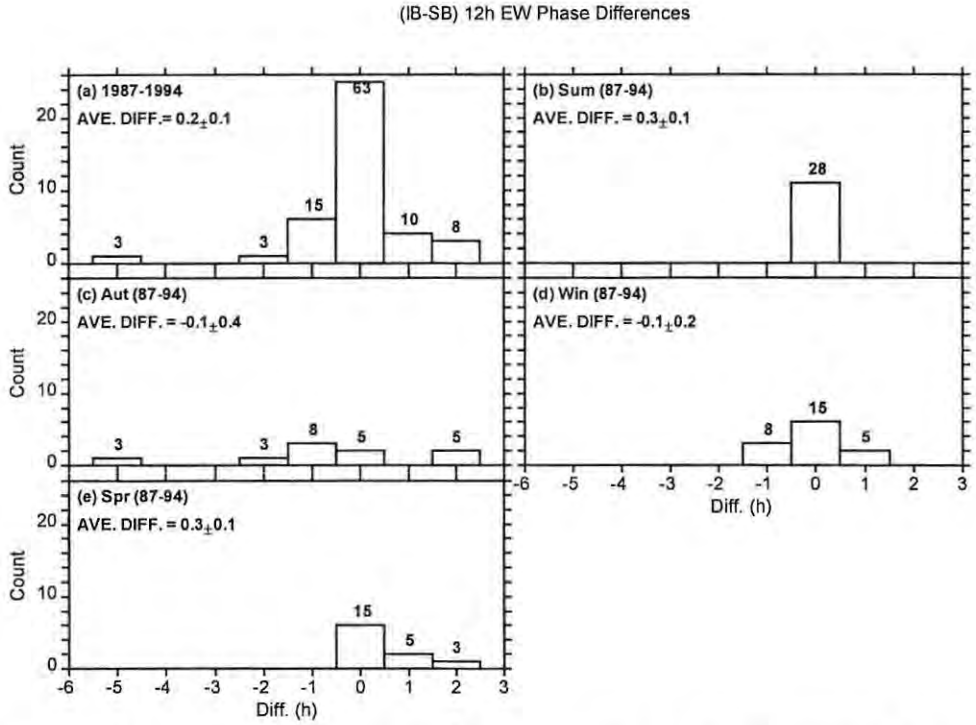

Figure 3.22 The distribution of the (IB-SB) zonal phase differences for the semidiurnal tide at Adelaide for the years 1987-1994. The weighted average differences are also given and the percentage count of each bar.

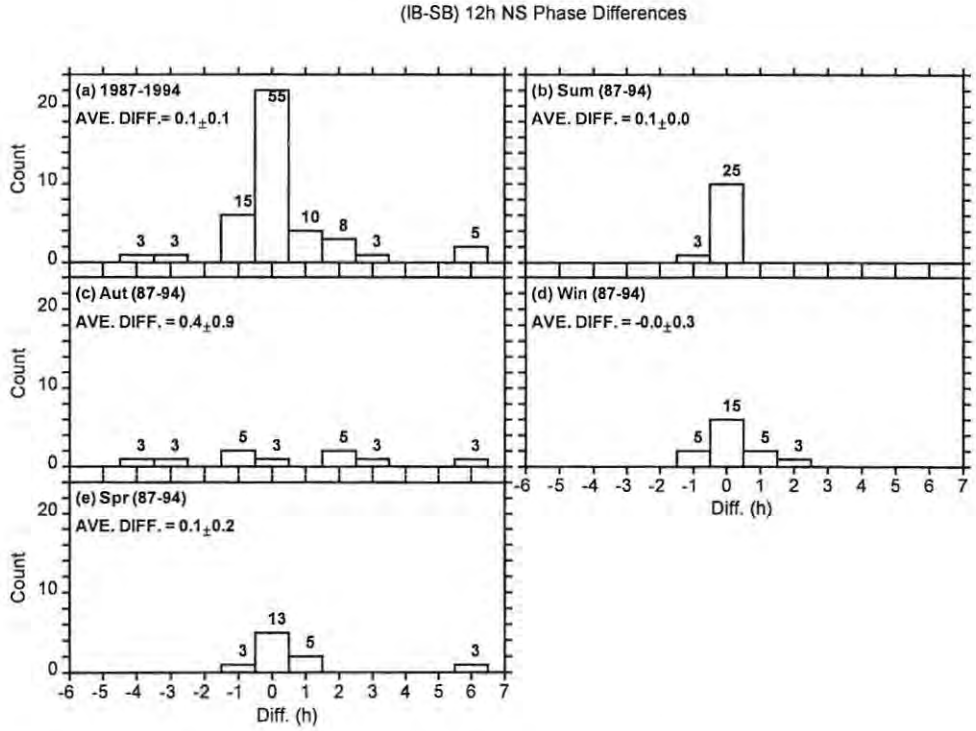

Figure 3.23 Same as **Figure 3.22** but for meridional phases.

regard to short-term variations (e.g. Chapter 4 and Chapter 5), height effects have a significant influence on the observed differences between Grahamstown and Adelaide. However, such a possibility will not be considered here and can possibly be investigated in the future.

CHAPTER 4 THE MEAN FLOW

4.1 INTRODUCTION

One of the major components of the dynamics of the MLT region is the mean flow and different aspects of this circulation have been studied by various authors (e.g. *Portnyagin et al.* [1993a]; *Nakamura et al.* [1996]; *Charles and Jones* [1999]; *Namboothiri et al.* [1999]; *Fritts et al.* [1999]. It has been established that this circulation is primarily governed by momentum deposition from various atmospheric waves like gravity waves, tides and planetary waves. This impartation of momentum to the mean wind plays an important role in the atmospheric momentum balance. At the same time, the mean wind also affects some of the waves it interacts with in various ways. For instance, the mean flow sometimes acts as a filter that absorbs waves that are directed in a particular direction at different altitudes depending on their phase speeds. This selective blocking result in the alteration of the dominant direction of propagation of the waves and this has profound implications on, among other things, the deposited momentum, atmospheric turbulence and the associated transportation of heat and chemical species.

The mean wind also plays a very important role in the thermodynamic structure of the atmosphere. Within most of the stratosphere and mesosphere, higher and lower temperatures are recorded in the summer and winter polar regions, respectively [*Holton*, 1982]. However, above ~70 km the temperature field is reversed such that higher and lower temperatures occur in the winter and summer polar regions, respectively [*Holton*, 1982 and reference there in]. This temperature structure is inconsistent with radiative equilibrium [*Murphy & Vincent*, 1998] and is dynamically sustained by the rising (falling) of air and the associated adiabatic cooling (heating) in the summer (winter) hemisphere. To maintain mass continuity, the meridional mean flow carries mass to and from the poles and, in this way, the mean flow plays a role in the transportation of heat in the MLT region. Like other air motions, the mean flow also makes some contribution to the transportation of minor species [*Thomas*, 1996].

In the following sections I will investigate the behaviour of the mean flow at Grahamstown and Adelaide and see if it is consistent with theory and observations elsewhere. First I will concentrate on the short-term variations (Section 4.2) of the mean flow and then later (Section 4.3) focus on the long-term variations of this circulation.

4.2 SHORT-TERM VARIATIONS OF THE MEAN WIND

4.2.1 Short-term variations and Correlations

The results reported in this thesis regarding the mean flow and tides are based on hourly averages of horizontal wind components. I considered all these hourly data points to have an equal weighting of 1 and, in addition, I assumed that the error in these was negligible compared to the 'error' due to the variations of the components being extracted. In fact, *Roper* [1984] explains that while any reasonably designed meteor radar is expected to have short term instrumental errors, these are significantly less than the "error" due to random components in the mean and tidal quantities. According to *Roper* [1984], the accuracy of individual line-of-sight velocities is of the order of 2-3 ms^{-1} for the mean flow and tides. At Grahamstown it is estimated that the line-of-sight velocity component can be in error by at most 4 ms^{-1} [*Malinga and Poole,* 1997] and the hourly averages of the zonal and meridional wind components are expected to have greater precision depending on the hourly meteor counts which are on average ~20 meteors/hour.

In my study I have deduced the mean wind by averaging 4-day (96-hour) time sequences of hourly averaged horizontal (zonal and meridional) wind velocities. This 4-day data window was advanced by 1 day and the average of the data window was attributed to the second day of the interval. The reason I choose 4-day data windows was to (i) filter out the high frequency (periods $\leq$ 4-day) planetary waves like the quasi-two-day wave, and (ii) to statistically improve the resulting mean winds and the deduced harmonic components (Chapters 5 to 7). To be regarded as an *acceptable data window* (see also in Chapter 5, Section 5.2), each of the 4-day intervals had to have at least 2/3 of the possible data points within the interval (i.e. 64 hourly wind values) and each day within the interval had to also have at least 2/3 of the possible data within a day (i.e. 16 hourly wind values). In the case of the mean wind, as opposed to that of oscillatory components (Section 5.2), the missing data points were simply ignored and no interpolation was carried out. This is not expected to have a significant effect on the deduced mean wind especially with the fairly stringent criteria I have applied to accept a 4-day data window.

In Figure 4.1 and Figure 4.2, I have plotted the mean wind for the years 1987 to 1994 and the

corresponding interannual average (IA) at Grahamstown and Adelaide, respectively. Positive and negative values of the velocity represent the eastward and westward wind flow for the zonal mean circulation, respectively. In like manner, positive and negative velocities represent northward and southward flows of the meridional mean circulation, respectively. For the error bars, I have used one standard error of the mean. From these figures we see that at both sites the mean flow is variable from day to day. Before going into a detailed analysis of these, a few features are worth noting and will be further emphasized when I deal with the long-term trends (Section 4.3). For both Grahamstown and Adelaide the zonal mean wind tends to have higher *speed* than its meridional counterpart. By 'speed' here and elsewhere I am referring to the absolute value of the zonal and meridional components. The zonal (meridional) mean flow is strongly and frequently eastward (northward/equatorward) at both sites.

Apart from the underlying seasonal patterns, which will be dealt with in (Section 4.3), we observe that both the zonal and the meridional components at the two sites, as shown in Figure 4.1 to Figure 4.4, are characteristically variable. This variability exhibits differing time scales and is due to local changes as well as planetary scale fluctuations. For instance, the zonal wind at Grahamstown in 1987 between May and September, exhibits a periodic behaviour with periods of ~20 days which is superimposed on a slowly varying seasonal component. Such planetary scale modulation has been observed by other authors like *Charles and Jones* [1999] and will be dealt with in detail in Section 4.2.2. In general these short-term variations are not necessarily correlated between Grahamstown and Adelaide (see Figure 4.3 and Figure 4.4). This is to be expected because the spatial scale of daily variations of wind components is ~2000 km [*Lysenko et al.*, 1994] which is much smaller than the ~10 000 km separation between the two sites.

To quantitatively assess the level of persistence of these day-to-day variations, I have used variogram techniques, which, as mentioned in Chapter 2, Section 2.5, can handle data gaps. Figure 4.5 and Figure 4.6 show the semi-variogram and the auto-correlation for Grahamstown respectively and corresponding figures for Adelaide are shown in Figure 4.7 and Figure 4.8. For both Grahamstown and Adelaide the range of influence on the variograms is at least 4-days partly because I have used 4-day data windows. Since these windows are advanced by 1 day each time, samples separated by lags that are less or equal 4 days are not independent and

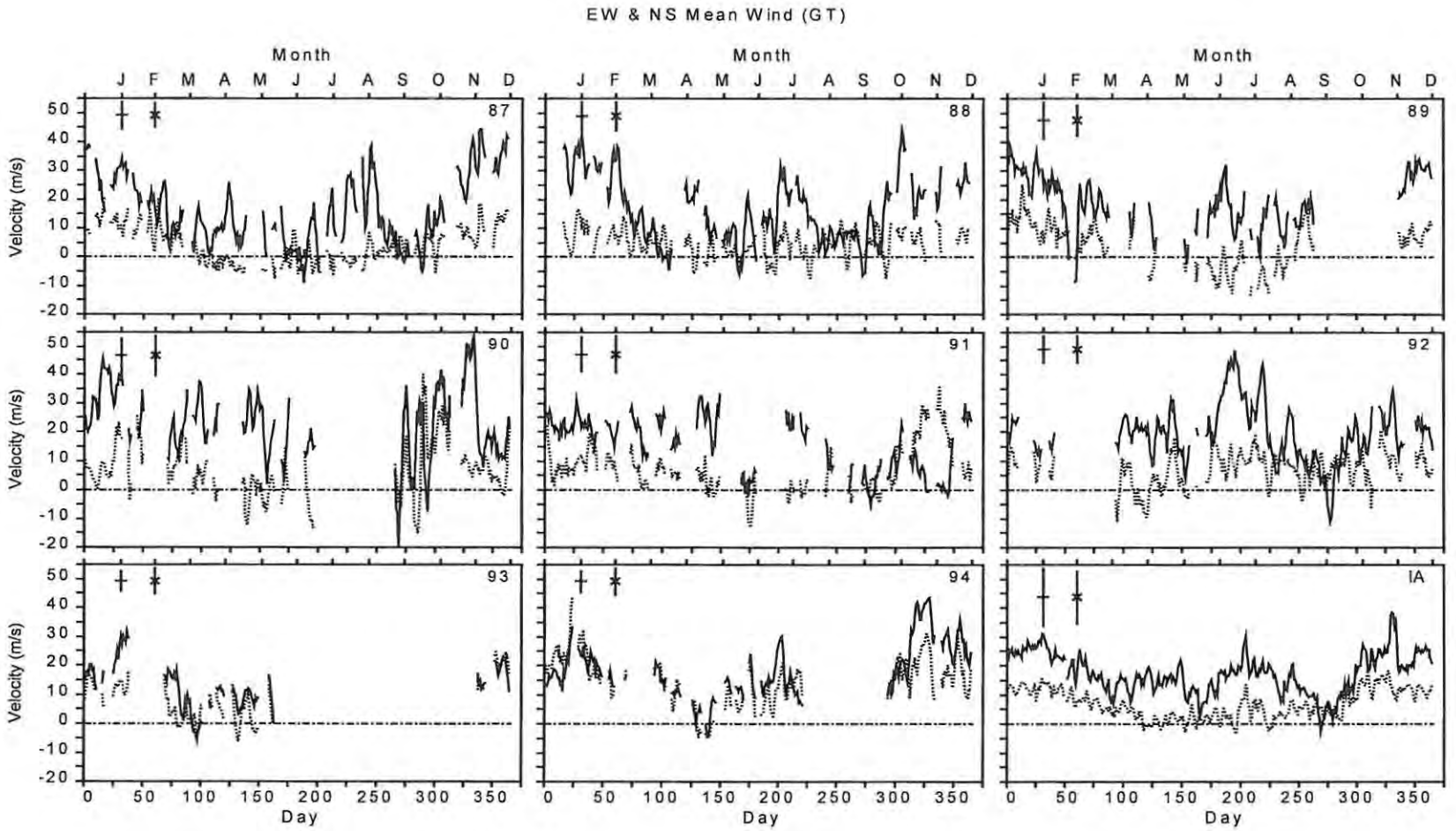

Figure 4.1 The zonal (solid line) and the meridional (dotted line) mean wind for the years 1987-1994 and for the corresponding 8-year interannual average (IA) for Grahamstown. The maximum error (one standard deviation of the mean, i.e., 1 α) for each series is shown at the top left hand corner with symbol '-' and 'x' representing the zonal and the meridional series, respectively. More details about the figure are given in the text.

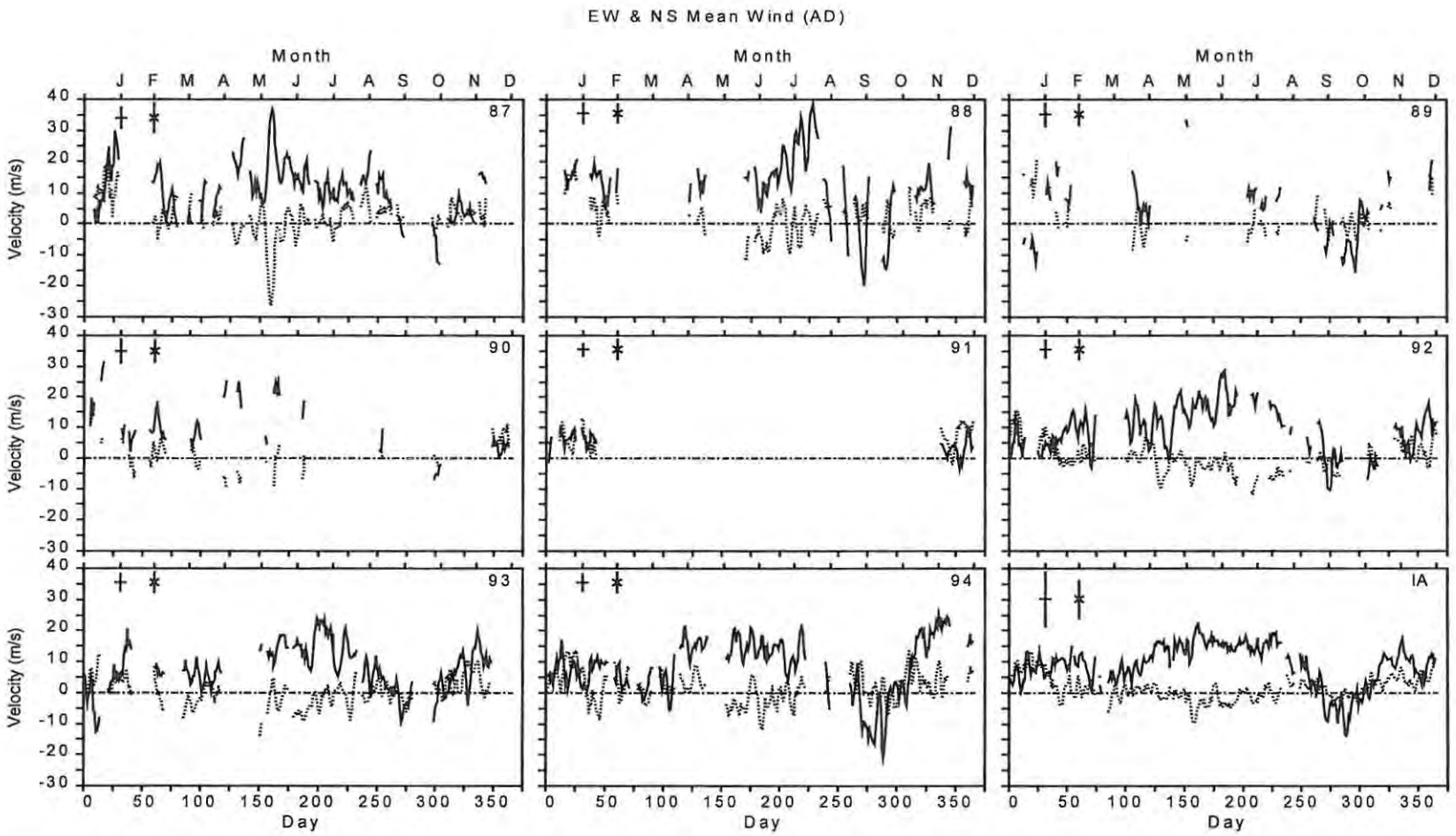

Figure 4.2 Same as **Figure 4.1** but for Adelaide.

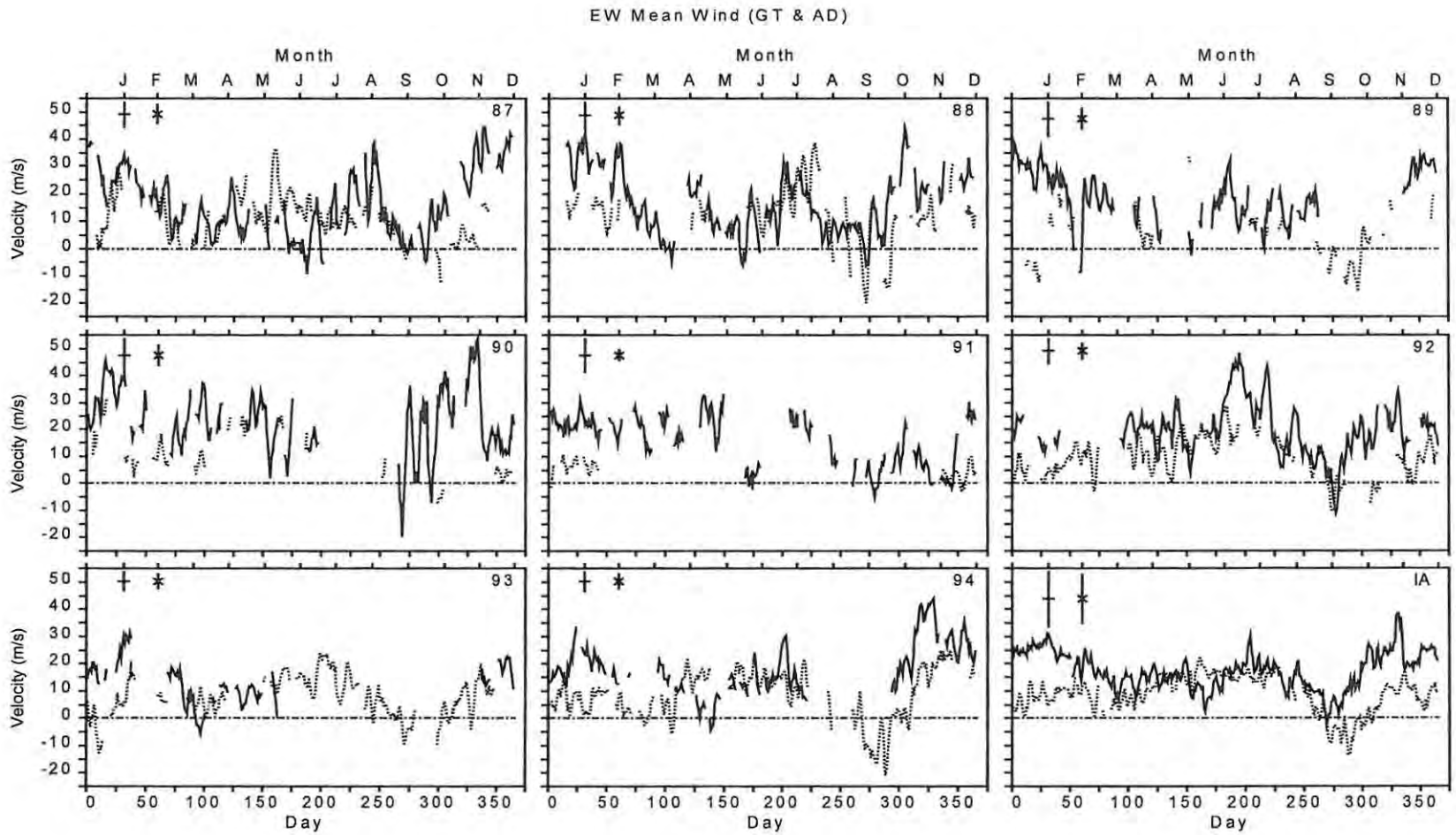

Figure 4.3 The zonal mean wind at Grahamstown (solid line) and Adelaide (dotted line) for the years 1987-1994 and for the IA. The maximum error (one standard deviation of the mean, i.e., 1 α) for each series is shown at the top left hand corner with symbol '-' and 'x' representing the Grahamstown and the Adelaide series, respectively. More details about the figure are given in the text.

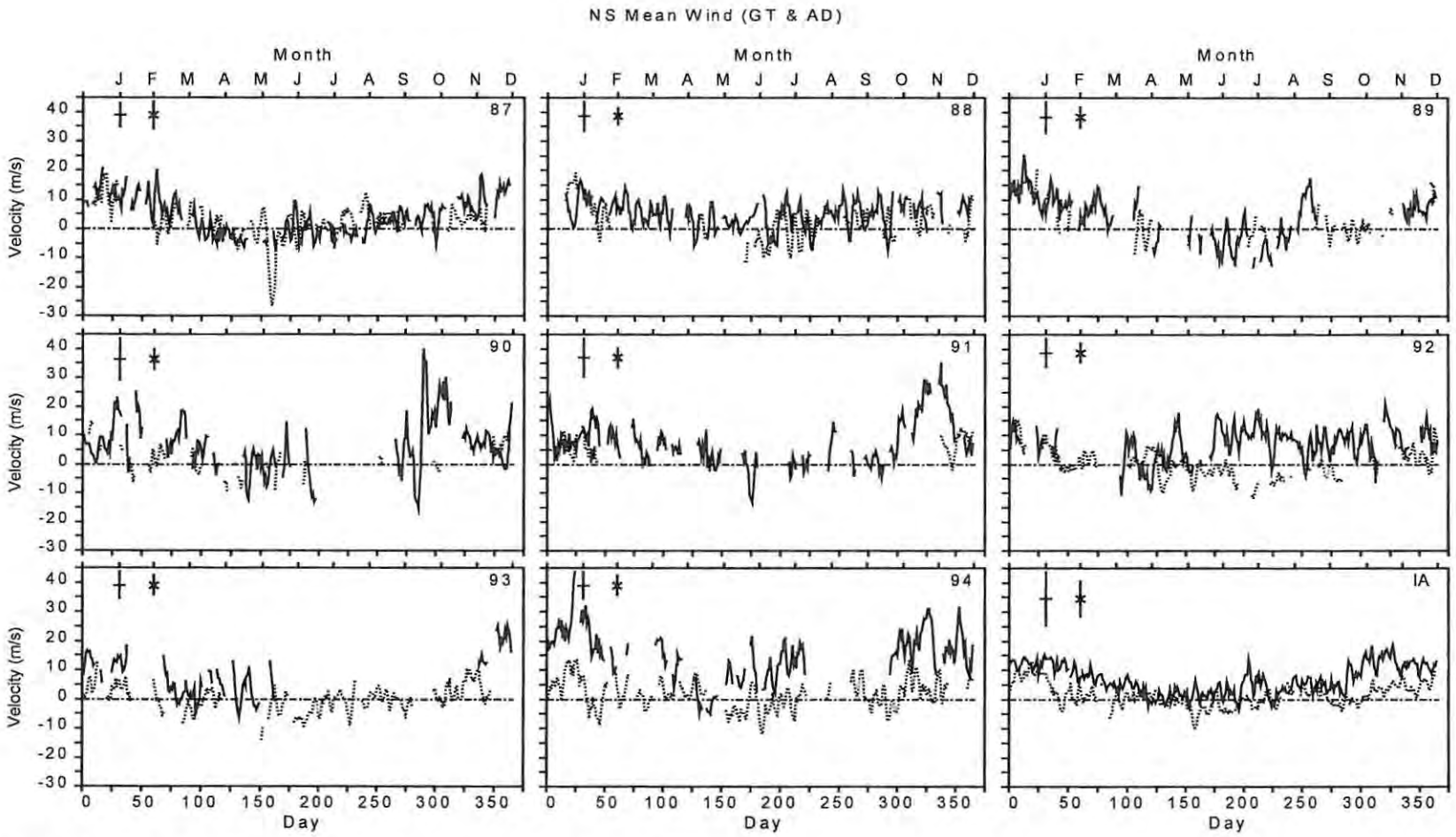

Figure 4.4 Same as **Figure 4.3** but for the meridional mean flow.

hence the influence on the variograms and correlations. The short duration of coherency are a consequence of the complex nature of the sources of the variations which may include, among other things, gravity waves and transient planetary waves [*Vincent*, 1990]. By wave transience, I am referring to the time variation of local wave activity [*Smith*, 1985]. However, it is interesting to note that there are years when there is sustained reasonable (>0.5) correlation beyond the 4-day lag at both sites as shown by Figure 4.6 and Figure 4.8. In some cases this high degree of continuity extends to lags of ~20 days and this is more frequent at Grahamstown than at Adelaide. Interannually, the variograms and the corresponding correlation functions of the two sites differ from one year to another indicating an interannual variation in the source of the short-term fluctuations. This is to be expected bearing in mind the complexity of the sources of the variations.

At both Grahamstown and Adelaide, the variograms and correlation functions of the zonal component generally differ from those of the meridional component. This suggests that the sources of the variability in the two components are different, or that these two components respond differently to the same sources of the variations. Some of the noticeable differences in the semi-variograms of the zonal and the meridional components include (i) the absence of parabolic rise and hence polynomial trends [*Clark*, 1979] in the meridional component, (ii) the sill and hence the variance of the meridional component is mostly smaller than that of the zonal component. The second difference is a direct result of the large fluctuations observed in the zonal component compared to the meridional component (Figure 4.1 and Figure 4.2). Having said that, it is however worth noting that there are years when the variograms and correlation functions of the zonal component are, to some extent, similar to the those of the meridional component. This indicates that at times the two horizontal wind components have similar responses to atmospheric changes. Some variograms exhibit oscillatory fluctuations indicating planetary modulation.

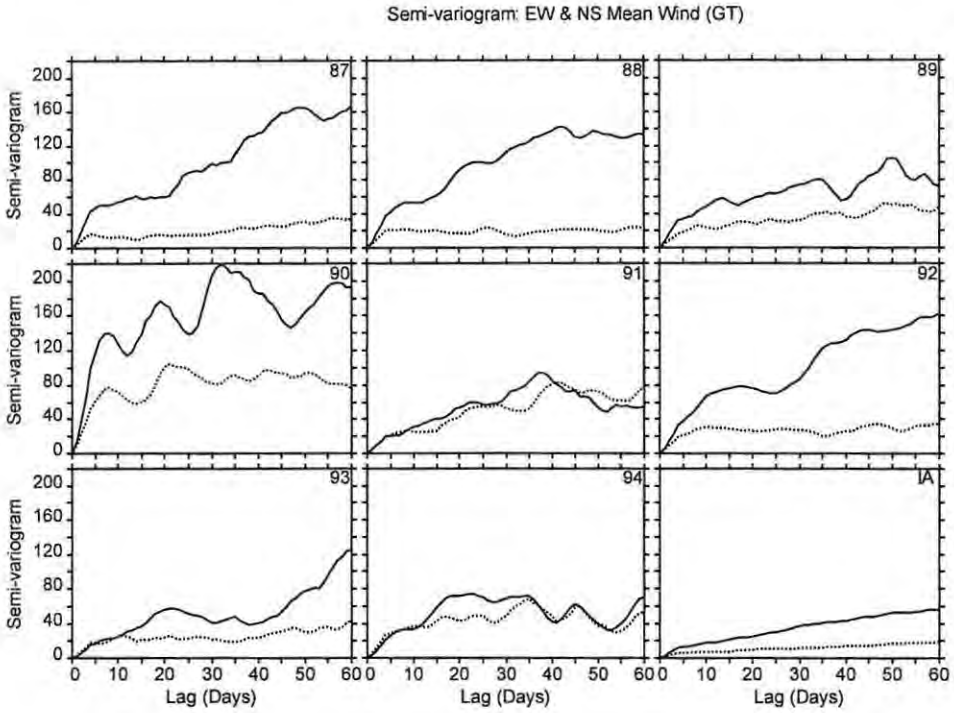

Figure 4.5 The semi-variogram of the zonal (solid line) and meridional (dotted line) for the years 1987-1994 and for the corresponding 8-year interannual average (IA) for Grahamstown. The year is indicated on the top right corner of each panel and the IA is similarly marked.

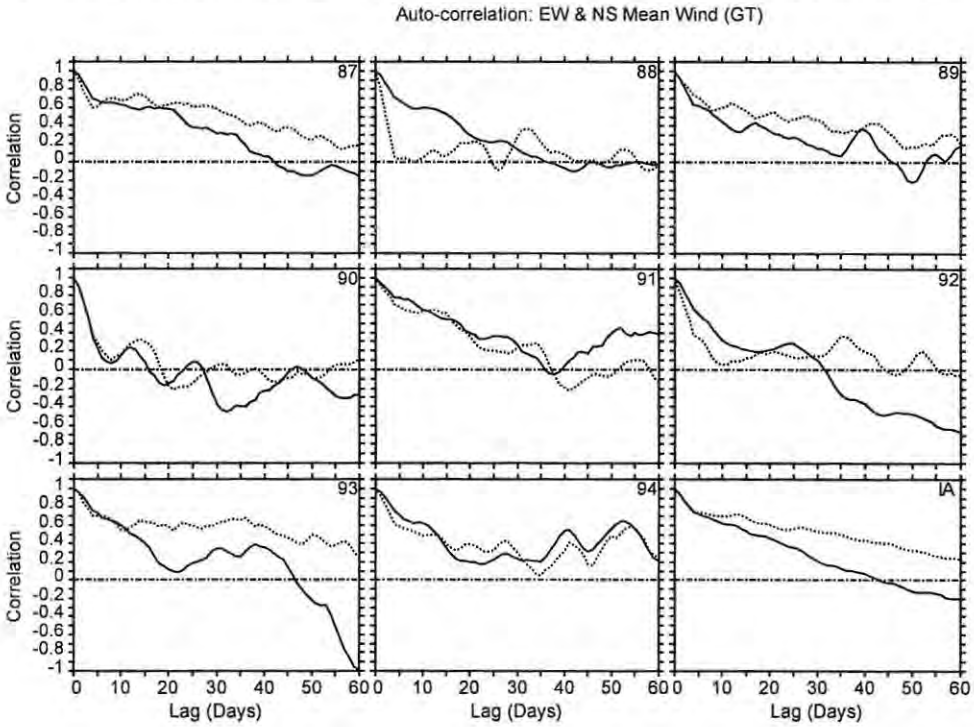

Figure 4.6 The auto-correlation of the zonal (solid line) and meridional (dotted line) for the years 1987-1994 and for the corresponding 8-year interannual average (IA) for Grahamstown. The year is indicated on the top right corner of each panel and the IA is similarly marked.

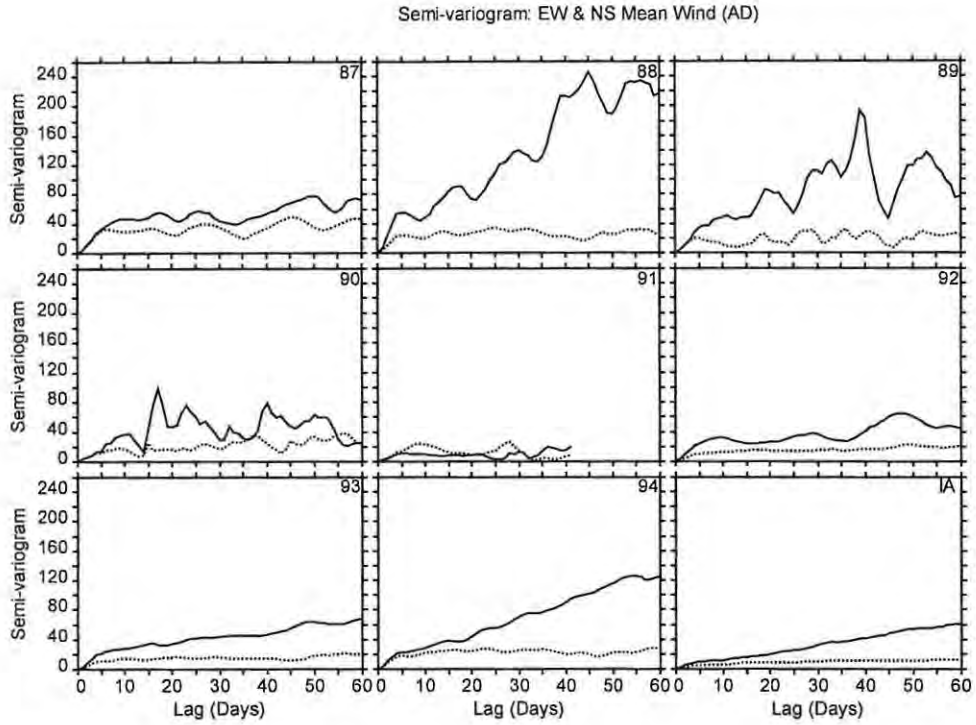

Figure 4.7 The semi-variogram of the zonal (solid line) and meridional (dotted line) for the years 1987-1994 and for the corresponding 8-year interannual average (IA) for Adelaide. The year is indicated on the top right corner of each panel and the IA is similarly marked.

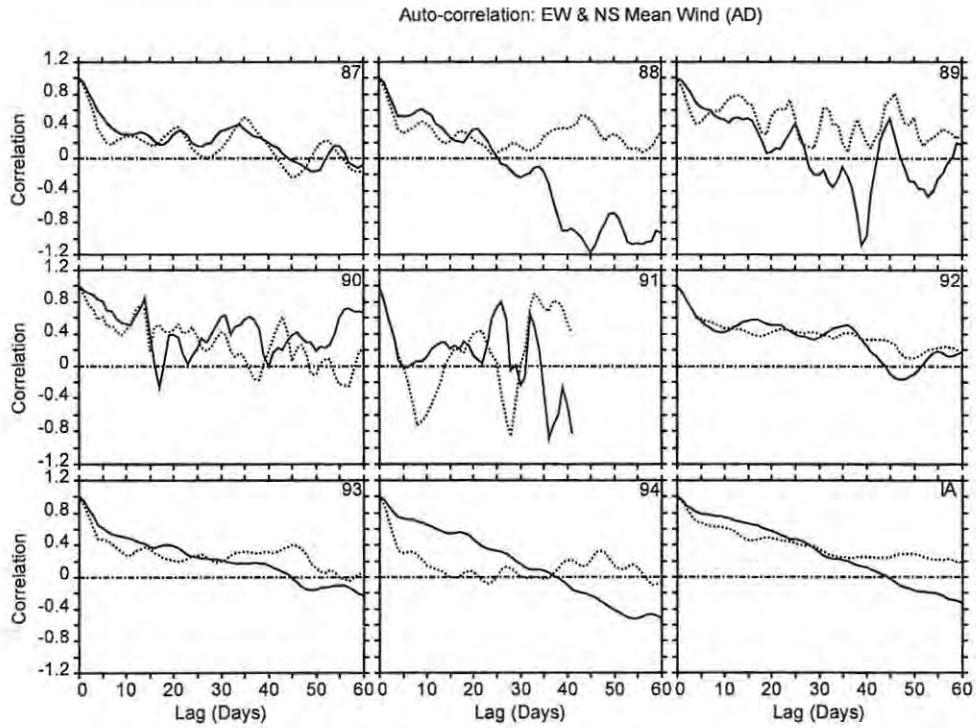

Figure 4.8 The auto-correlation of the zonal (solid line) and meridional (dotted line) for the years 1987-1994 and for the corresponding 8-year interannual average (IA) for Adelaide. The year is indicated on the top right corner of each panel and the IA is similarly marked.

4.2.2 Spectral and Multiresolution Analysis (MRA)

In Section 4.2.1 I focussed on the variations in the behaviour of the mean flow and the correlations in these variations. In the process of doing this, I did not attempt to accurately characterise these fluctuations in terms of their periodicities. Consequently, I could not tell with certainty if these variations were a result of regular effects (e.g. the modulation of the mean wind field by periodic waves), or they were merely random fluctuations. In this section, I am going to use wavelet spectral and multiresolution techniques to determine the regularity or otherwise of the short-term variations of the mean flow.

The advantage of using the wavelet approach is twofold. First, as already mentioned in Chapter 2, Section 2.7, this method offers a better time-frequency resolution and is better suited to handle non-stationary time series. This is particularly important because the planetary waves that modulate the mean flow are not necessarily long-lived but are sometimes characterised by transient bursts of activity [*Smith*, 1985; *Vincent*, 1990]. Therefore, it is important to get a better localisation in time and frequency of the various periodic components and hence the use of wavelet spectral methods. Secondly, the observations made in Section 4.2.1 indicate that the variation in the mean flow is a superposition of fluctuations with different characteristic time scales ranging from days to months or even years. The wavelet multiresolution capabilities enable us to look at these fluctuations in detail by successively removing the lower scale (i.e. high frequency) fluctuations while successively leaving a coarser signal. That is, it allows us to hierarchically reveal mean flow information at successively changing scales or resolutions. In this way I am able to characterise different physical structures that are embedded in the mean circulation.

In this thesis I have used the Daubechies (*dbN*) family of wavelets for the multiresolution analysis (MRA) where N is the order of the wavelet. In particular, I have used the 5^{th} order Daubechies wavelet, *db5*. While the properties of Daubechies wavelets are suitable for the decomposition and reconstruction processes of the MRA, this wavelet family has a drawback in that it does not have a well-defined relationship between its scales and the Fourier frequencies. This poses a problem in this analysis because I am interested in Fourier periods or frequencies, which have a clearly understood physical interpretation and are commonly used. To solve this

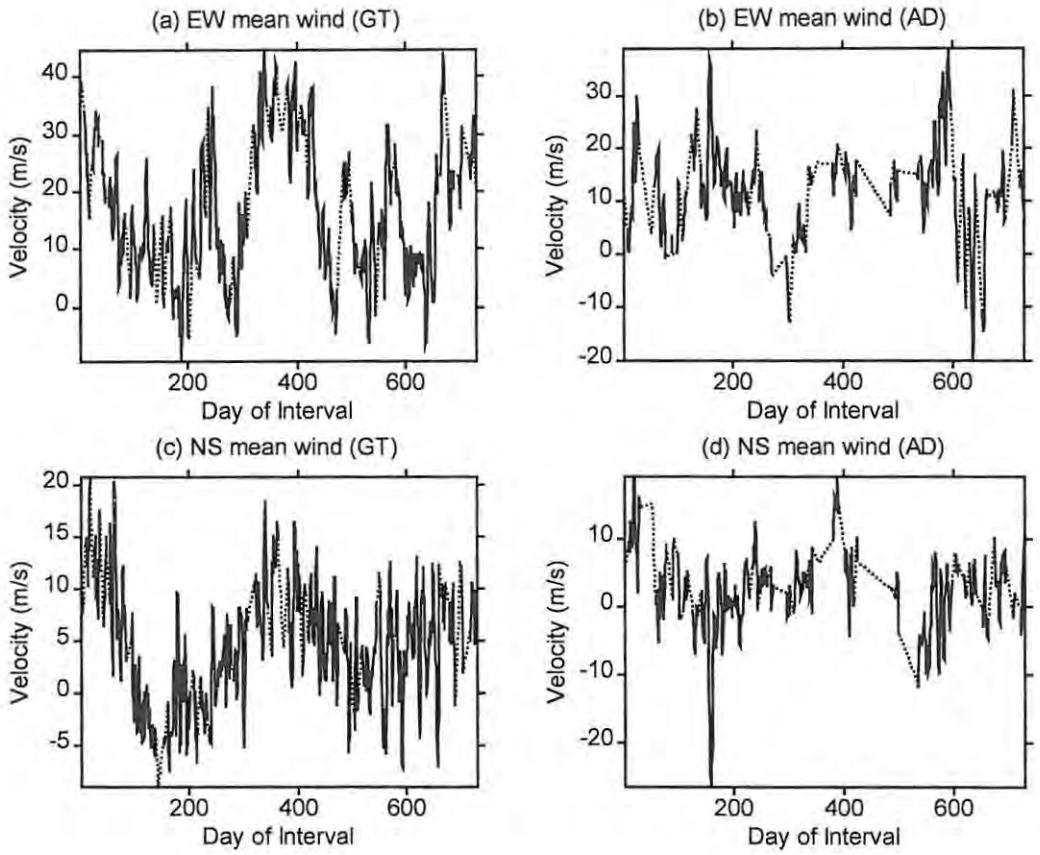

Figure 4.9 The mean wind data at Grahamstown and Adelaide for 1987-1988 with day 1 on the x-axis representing 1 January 1987. Dotted lines indicate linearly interpolated data.

problem, I have also used wavelet software from *Torrence and Compo* [1995]. More specifically, I have used a Morlet wavelet from their software. Although this wavelet is incapable of decomposing and reconstructing a signal, is has a well-defined relationship between its scales and the Fourier periods and is therefore suitable for the spectral analysis of the details. The scale:Fourier-period ratio for the Morlet wavelet with parameter 6 as was used here is about 1:1.03 (see *Torrence and Compo* [1995, file **wave_bases.m**] and *Torrence and Compo* [1998]).

For this analysis I have chosen the duration starting January 1987 to December 1988 because it is the longest 2-year interval with superior data availability as shown by Figure 4.1 and Figure 4.2. Based on this, I do not expect the linear interpolation that was performed to fill the missing data in this section to have a significant negative impact on the analysis. See Figure 4.9 for the

result of the interpolation.

Figure 4.10 and Figure 4.11 show the mean-corrected horizontal mean wind components at Grahamstown and Adelaide, respectively. The corresponding wavelet spectra for periods of up to about 20 days are also shown. In these figures and other similar ones that follow, the top scale along the *x*-axis is used for the year with each year number representing the beginning of the year. The yellow solid line represents the cone-of-influence [*Torrence & Compo*, 1998]. For any given time, all the periods above the yellow line are expected to suffer from edge effects [*Torrence & Compo*, 1995, **wavelet.m**]. The red dashed lines represent 95 % confidence levels [*Torrence & Compo*, 1995, **wave_signif.m**]. Both Grahamstown and Adelaide show significant planetary activity although in the latter there is clear evidence of the influence of data gaps on the pattern. In general, the spectra show a number of planetary scale oscillations with the quasi-16-day (periods of ~12-20 days) oscillation being the most frequent and dominant for both the zonal and the meridional flows and at both sites. There is also a significant contribution of spectral components with periods of about 8-10 days.

To get an even more detailed picture of the wave activity in the mean flow, I extracted the embedded structures in the circulation and analysed these separately using MRA (Figure 4.12 and Figure 4.13). The top row of the panels in these figures represents the zonal (u, black line) and the meridional (v, red line) velocities of mean flow that has been mean-corrected after data gaps had been linearly interpolated. In rows 2 to 5 and starting from the left, the 1st column (of panels) show the low frequency '*approximations*' (A_m) that reveal the "context" of the signal information for levels m starting from 1 to 4. The finer resolution '*details*' (D_m) or "modalities" are shown in the 2nd column. The ranges of the scale s for the *approximations* and *details* are also shown. The spectra of the "details" obtained by using *Torrence and Compo's* software are shown in the 3rd and 4th columns. In some cases and, in particular, those that have short periods, care should be taken as the red dashed line can be mistaken for the spectral power colour code of red. One way of telling them apart is by using the fact that yellow and green regions always surround a genuine power colour code of red.

The MRA panels clearly reveal the different physical structures that are imbedded in the

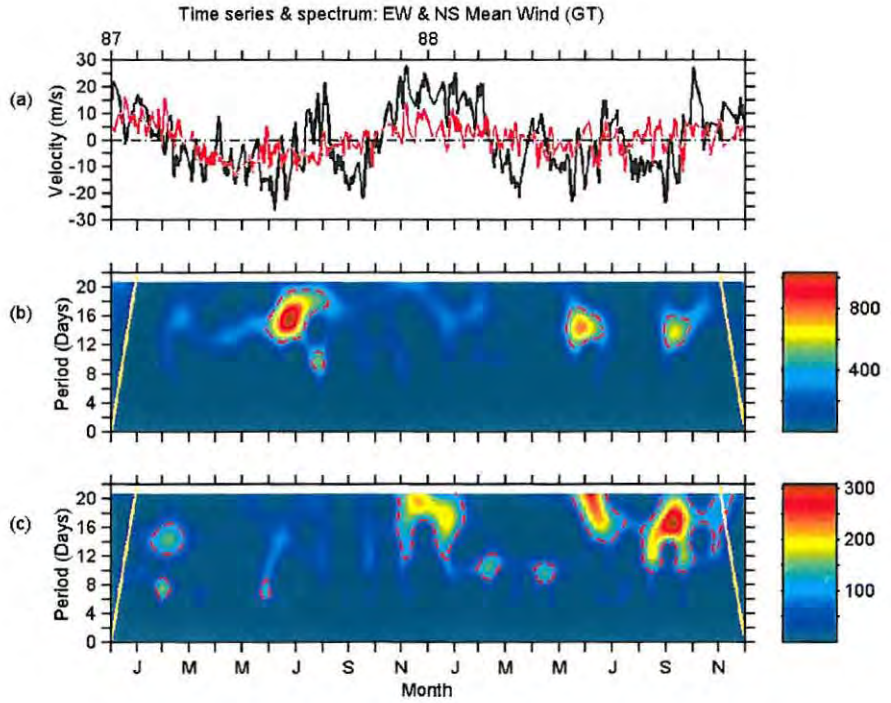

Figure 4.10 The velocity and spectrum of the mean flow at Grahamstown. (a) The zonal (black line) and the meridional (red line) mean flow velocity. (b) The wavelet spectrum of the zonal velocity. (c) The wavelet spectrum of the meridional velocity. See main text for further details.

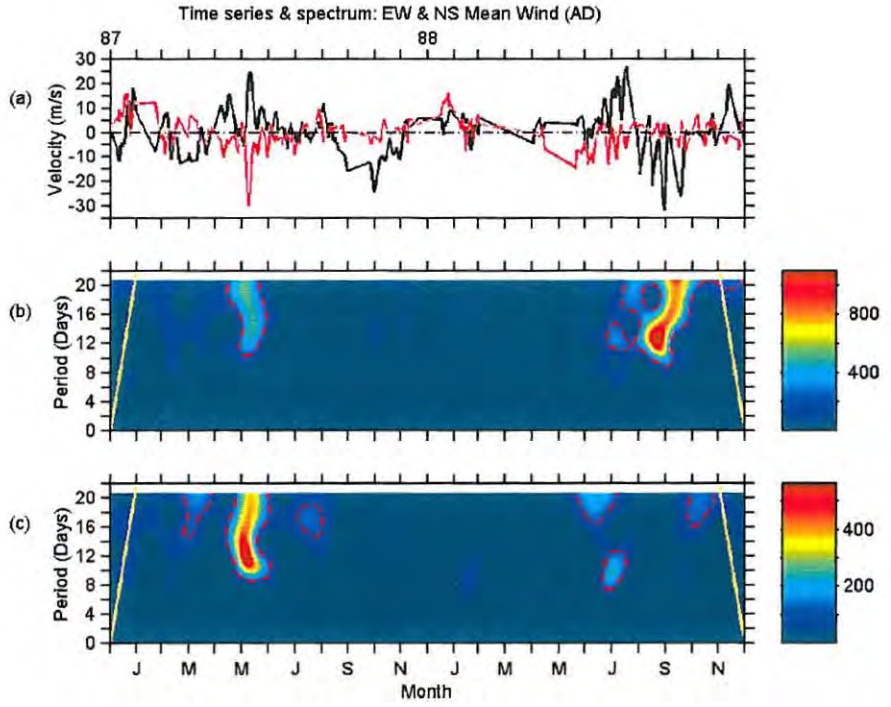

Figure 4.11 Same as **Figure 4.10** but for Adelaide.

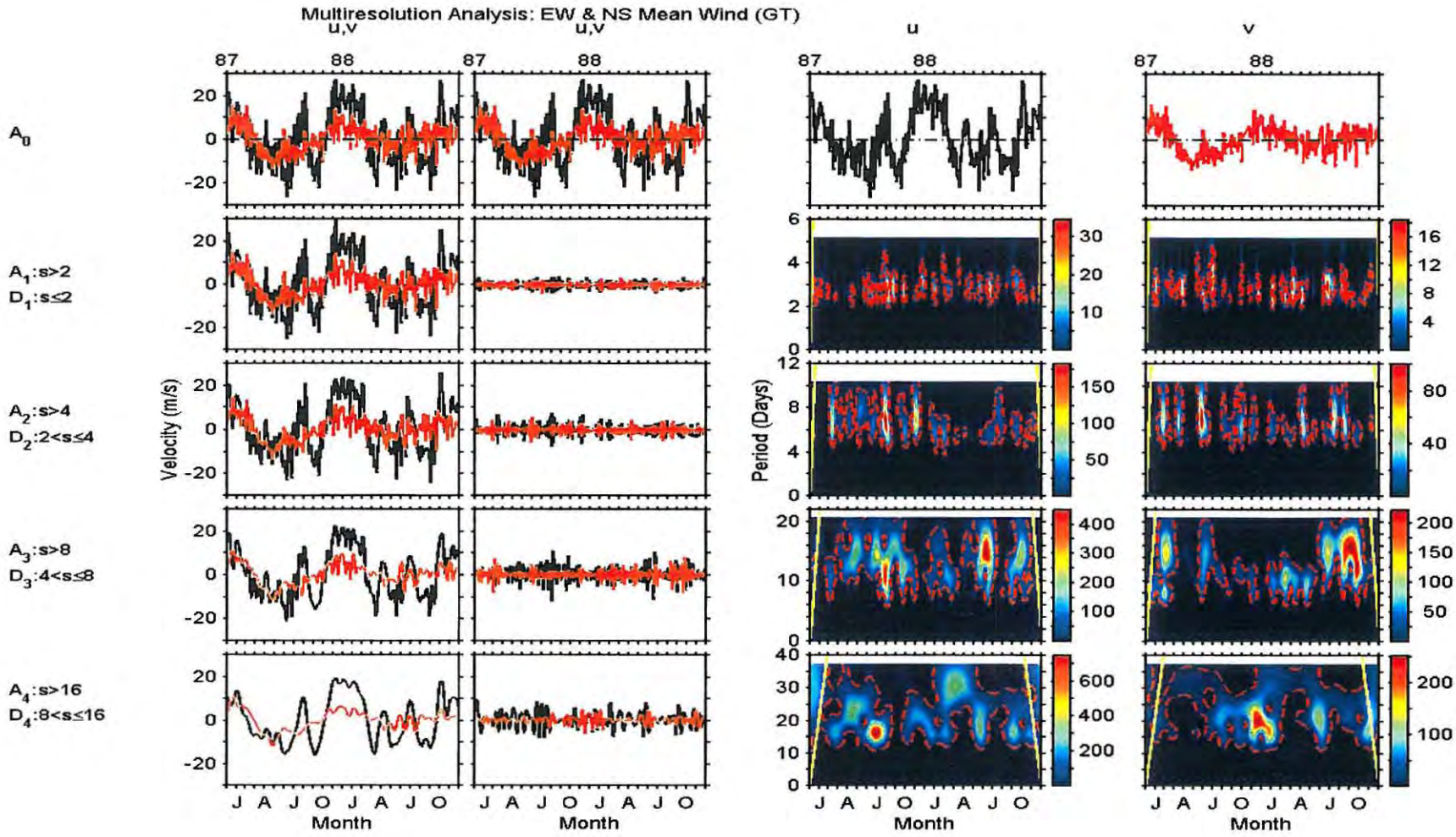

Figure 4.12 For the mean flow at Grahamstown: The original signal A_0 (top row). For rows 2-5 and starting from the left, I have (1st column) the *approximations* (A_m where m is the level), (2nd column) the *details* (D_m), (3rd column) the spectrum of the zonal details and (4th column) the spectrum of the meridional details. The black and red time series lines represent the zonal (u) and meridional (v) mean flow respectively. The scale (s) ranges are shown and the units of the colour bars are arbitrary.

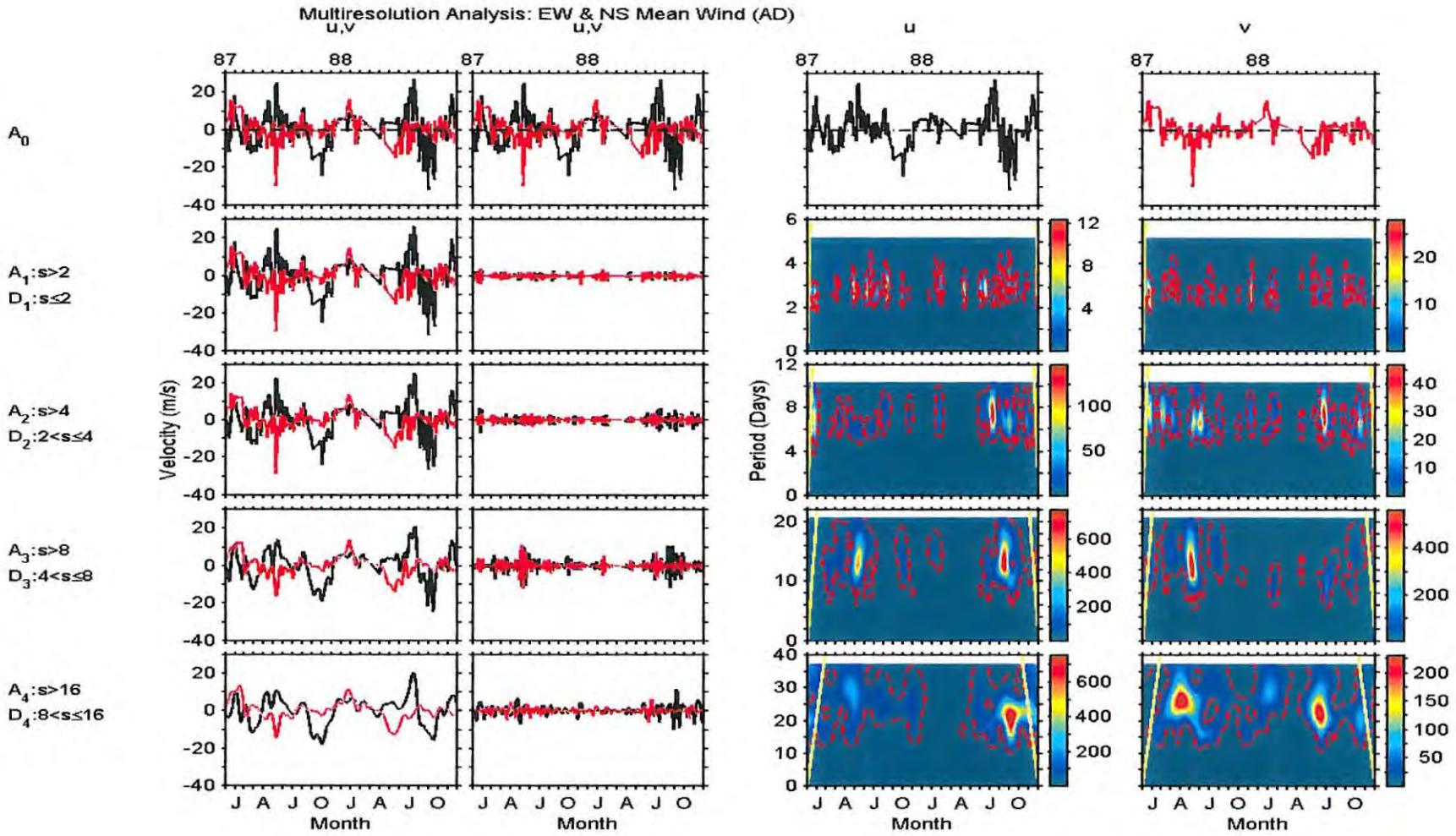

Figure 4.13 Same as **Figure 4.12** but for Adelaide.

variable mean flow. Specifically, the long-term seasonal trend emerges in the *approximations* as the *details* are being successively extracted. The short period components tend to have transient activity and they generally do not make a significant contribution to the total variation as shown by the details of levels 1 and 2. However, there are times (especially for D_2 at both sites) when there is a relatively high injection of energy even at these low levels. The strong spectral components for D_2 have periods of about 5-6 days. As the resolution level decreases, the significance of the details increases as shown by the time series of D_3 and D_4 and the corresponding spectra. These levels show significant planetary scale activity at periods of ~10 days and ~16 days. The 16-day oscillation is by far the most dominant at both Grahamstown and Adelaide and will be the subject of the next section.

The poor showing of the 2-day wave, which is a well known and dominant summer phenomenon, and the 5-day wave (another familiar planetary wave [*Espy et al.*, 1997]), in my results is partly due to the use of a 4-day data window which would have a filtering effect on these waves. In general, my results are consistent with radar observations that show oscillations with planetary periods (2-20 days) in the 80-100 km altitude range [*Forbes et al.*, 1995; *Vincent,* 1990; *Kazimirovsky et al.*, 1988; *Tsuda et al.*, 1988; *Manson et al.*, 1981]. Oscillations with these periods have also been observed in mesospheric temperatures [*Espy & Witt*, 1996; *Espy et al.*, 1997]. In line with observations made by *Eckermann et al.* [1997] at the equatorial MLT region, my results (see D_4) also show longer period (> 20 days) oscillations but these are not going to be dealt with in detail here.

As pointed out by *Forbes et al.* [1995], the periodicities of about 2-, 5-, 10-, and 16-days that are observed in the MLT region are similar to those in the troposphere and the stratosphere. These transient waves have been shown by longitudinal studies to be westward propagating [*Vincent*, 1990]. Although the sources of these waves are not known with certainty, it is widely assumed that they are due to Rossby-gravity normal modes originating from the lower atmosphere [*Vincent*, 1990; *Williams and Avery*, 1992; *Forbes et al.*, 1995]. These waves, as mentioned in Chapter 1, Section 1.2.2.3, are free waves that are due to random forcingand are determined by the resonant characteristics of the atmospheric mean state as opposed to forcing mechanisms [*Ahlquist*, 1982].

Vincent [1990] gives some characteristic features of some of these oscillations and points out that, in general, these normal modes are vertically evanescent and only locally propagate in vertical regions with westward winds and equatorward temperature gradients. This is made even clearer by *Williams and Avery* [1992] who explain that the wave can only propagate vertically if it satisfies a mean wind filter relation given by $\bar{u}$-$c > 0$ where $\bar{u}$ is the mean zonal wind and c is the horizontal phase speed of the wave. This implies that a wave will be blocked from propagating vertically when it reaches its *critical level* which is the level at which its phase speed is equal to the horizontal wind speed. This filtering effect will become clear in the next few sections.

4.2.3 The 16-day Oscillation

Results from the previous section reveal that the 16-day oscillation is the most dominant planetary scale wave in the ~2-40-day period range. Published work (e.g. *Williams and Avery* [1992]) shows that the period of this wave is variable and the peak power is not necessarily at 16 days and this is also confirmed by my results. *Williams and Avery* [1992] found that the centroid period of the quasi-16-day wave varies from 12 to 17 days and 12 to 19 days in the troposphere/lower stratosphere and the mesosphere, respectively. However, for brevity I will henceforth omit the prefix 'quasi'.

Since the lower atmospheric mean flow is westward (eastward) in summer (winter) [*Kazimirovsky et al.*, 1988], we would expect that the long-period (> 10 days) waves (being westward propagating) will, in accordance with the above mean wind filter relation, be able to propagate into the upper levels of the atmosphere in winter but be trapped in the lower atmosphere in summer. My results (Figure 4.10 to Figure 4.13) show that although the wave is frequent and strongest in winter and the equinoxes, there are instances when it is at least above the 95 % confidence level in summer. While this might seem to contradict expectations, the mesospheric summer 16-day wave has been detected in hydroxyl temperatures [*Espy et al.*, 1997], winds [*Williams and Avery*, 1992], and has also been simulated [*Forbes et al.*, 1995]. *Williams and Avery* [1992] found significant 16- and 5-day wind oscillations right through the year at almost all heights in the 0-100 km height range at Pokar Flat (65°N, 147°W). In fact their results show the peak (~6 ms^{-1}) of the 16-day wave to be in summer at about 85 km. However, from their results, one would have expected this wave to be precluded from

propagating above ~60km based on its phase speed of -15.8 ms^{-1} and the presence of westward (negative) flows with comparable speeds during the summer months at this height [*Williams and Avery*, 1992].

A number of authors [*Williams and Avery*, 1992; *Forbes et al.*, 1995; *Espy et al.*, 1997] have advanced two mechanisms that could possibly explain the occurrence of the 16-day wave in the summer mesosphere above the strong and westward filtering flow in the stratosphere. The first is a cross-equatorial ducting of the wave into the summer mesosphere. This process, which was also simulated by *Forbes et al.* [1995], involves the generation of the 16-day wave in the lower levels of the winter hemisphere. This wave then propagates vertically through the winter eastward flow. *Espy et al.* [1997] mention that during its propagation, the wave energy is shifted to regions whose wind is weakly eastward relative to the wave. This results in the diffraction of the wave from its source region in the winter hemisphere into the equatorial waveguide/duct created by the penetration of the mesospheric eastward flow across the equator. [*Forbes et al.*, 1995; *Espy et al.*, 1997].

In their simulations, *Forbes et al.* [1995] found that the meridional flow in the MLT region did not show a strong 16-day response except in the polar regions and did not show any evidence of cross-equatorial penetration. On the other hand, their zonal 16-day response was characterised by strong amplitudes (5-30 ms^{-1}) in the winter MLT region and showed an intrusion into the summer hemisphere up to ~30 ° latitude. Looking at Figure 4.12, we see that, contrary to the results of *Forbes et al.*, the meridional component at Grahamstown has a significant 16-day wave in summer. While we cannot draw a strong conclusion based on this single event, it raises the possibility of another source of the summer mesospheric 16-day wave other than cross-equatorial ducting. This brings us to the second possible source of the 16-day wave in the summer hemisphere.

Williams and Avery [1992] point out that the total zonal wind field consists of the mean and the 16-day component, which is the dominant long-period tropospheric wave. The implication of this is that the critical level of a particular wave will be subjected to a 16-day periodicity. Therefore, gravity waves will propagate vertically or be trapped at a 16-day period depending on their phase speed [*Williams and Avery*, 1992]. This periodic transmissivity results in a similarly modulated breaking or viscous dissipation of gravity waves and hence a modulated

momentum flux divergence which could act as a source of a "secondary" 16-day wave in the MLT which eventually spreads to both hemispheres [*Forbes et al.*, 1995]. At the same time it should be noted that *Forbes et al.* [1995] demonstrated that gravity wave stress can significantly reduce the 16-day response in the winter MLT region and eliminate interhemispheric ducting. There is therefore a possibility of a complicated interaction between the ducting and the gravity wave mechanism.

A general observation made at Grahamstown and Adelaide is that the 16-day wave does not always show correlation between the zonal component and the meridional component. This lack of correlation suggests that, by and large, the relevant sources of the observed variations are different or that each component responds differently to the same source. This is consistent with the fact even if there are no mean wind variations, the zonal and meridional velocities of Rossby waves have different horizontal characteristics [*Salby & Roper*, 1980]. Another possible explanation for the lack of correlation with regard to the 16-day wave could be the interhemispheric ducting of this wave, which, as found by *Forbes et al.* [1995], has a strong zonal response and no meridional response. The periodic transmissivity mechanism could also enhance a particular component and not the other depending on the directions of the transmitted gravity waves. This mechanism can also explain the lack of correlation in the behaviour at Grahamstown (Figure 4.12) compared to Adelaide (Figure 4.13) bearing in mind that the distribution of gravity waves, especially the orographically generated ones, is geographically dependent.

A comparison of the 16-day wave for the years 1987 to 1990 at Grahamstown is shown in Figure 4.14 and Figure 4.15 for the zonal and meridional mean flows, respectively. Only Grahamstown was considered for this analysis because of its superior data availability compared to Adelaide. From these figures we observe that there are interannual variations in the behaviour of the 16-day wave. *Espy et al.* [1997] also observed interannual variations in the summer temperature16-day wave and suggested that these could be linked to the equatorial quasi-biennial oscillation (QBO). As mentioned earlier, a ducting channel is created by the penetration of the mesospheric eastward flow across the equator and the subsequent shifting of the zero transition line that separates the westward and the eastward jets [*Forbes et al*, 1995]. It

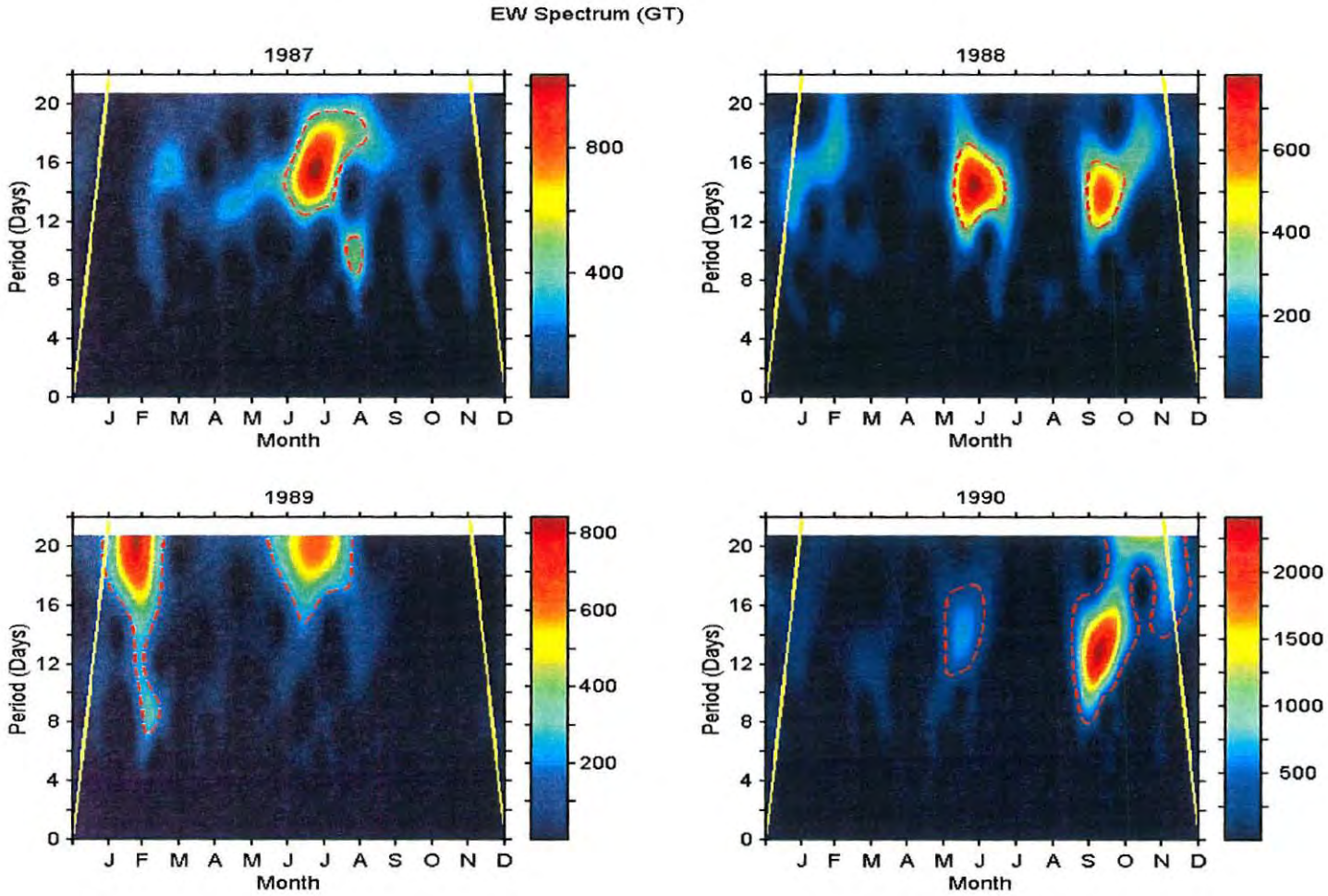

Figure 4.14 The zonal spectrum of the mean flow at Grahamstown. The colour bars are in arbitrary units and the yellow line and the red dashed lines are used as before.

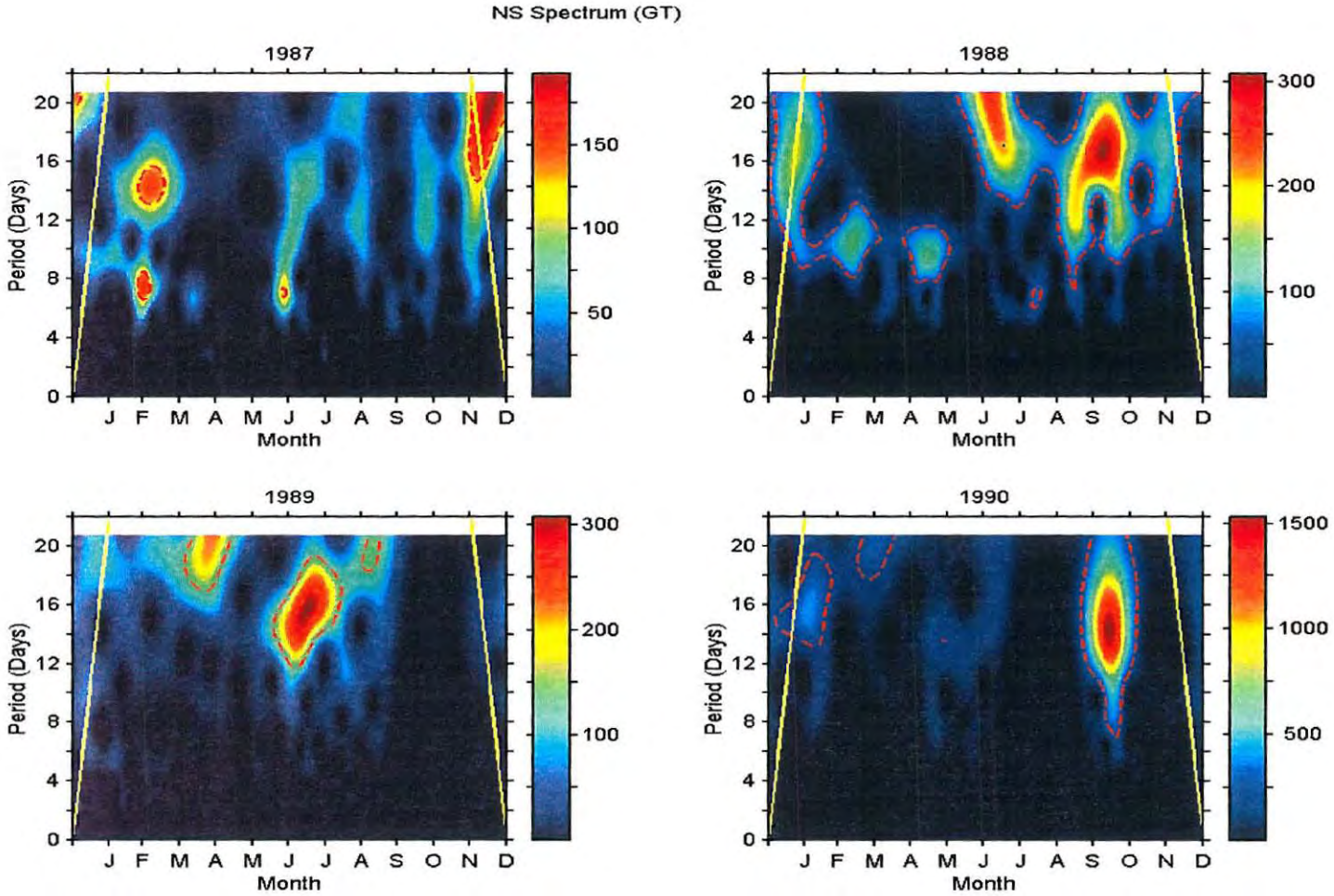

Figure 4.15 Same as **Figure 4.14** but for meridional mean flow.

is this fact that prompted *Espy et al.* [1997] to argue that the 20-30 ms^{-1} westward and the 10-20 ms^{-1} eastward flows (see *Espy et al.* [1997] for reference) that are associated with the QBO could significantly alter this ducting channel in the $\pm 15°$ equatorial band of the QBO. The zero line would effectively be shifted towards the summer hemisphere during the eastward phase of the QBO and this modification would extend up to ~35 km, the maximum height of the QBO. Therefore, the equatorial oscillations can alternately widen or narrow the ducting channel and can also modulate the normal mode structure and hence allow the 16-day oscillation to penetrate into the high-latitude summer mesosphere [*Espy et al.*, 1997]. The four years studied by these authors seem to confirm this.

With the exception of October 1988/90, my results do not show any sign of a 2-year regularity in the meridional 16-day wave. With regard to the zonal 16-day wave, there is a hint of a possible 2-year regularity at least qualitatively especially when comparing the 1987/89 pair to the 1988/90 pair. For the 1988/90 pair the 16-day wave peaks are in May/June and September/October and the spectral peaks have periods of ~14 days. On the other hand, the 1987/89 pair has a peak in June/July and the period of the peak is somewhat larger than 14 days. According to *Namboothiri et al.* [1999], the equatorial QBO at the 40-50 hPa level had a westward phase in 1987 and 1989 while the eastward phase occurred in 1988 and 1990. From the argument presented by *Espy et al.* [1997], the conditions would be more favourable for the 16-day wave in 1988 and 1990 but looking at my results only 1990 seems to be consistent with expectations for both the zonal and the meridional components.

4.3 LONG-TERM VARIATIONS

Thus far we have considered short-term variations in the behaviour of the mean flow at Grahamstown and Adelaide. We have seen that these variations are a superposition of fluctuations with different time scales ranging from several days to months, seasons and years. In this section I will concentrate on the long-term trends of the mean flow. More specifically I will consider the seasonal trends (Section 4.3.1) and the interannual trends (Section 4.3.2). In the first sub-section, I look at the monthly means within a given year and in this way delineate the seasonal changes that characterize each year. In the second sub-section I look at the year-to-year fluctuations for a given month. In all this I follow, as much as it is possible, a structured format of first comparing the zonal and the meridional components at Grahamstown (GT) and

then at Adelaide (AD). I thereafter compare the zonal component at Grahamstown and Adelaide followed by a comparison of the meridional component at the two sites. In general this is the format I will follow even in Chapter 6 and 7, which deal with the long-term trends of the tides.

4.3.1 Seasonal Trends

4.3.1.1 Local Seasonal Trends

Figure 4.16 and Figure 4.17 show the mean flow variation at Grahamstown and Adelaide, respectively. Monthly means were deduced from averages of available hourly wind velocities within the month. A monthly average was considered to be acceptable if at least 50 % of the possible hourly wind values for that month were recorded. The error bars represent one standard error of the mean (i.e. 1 α). It should be pointed out that at times the standard error of the mean is so small that it is masked by the symbols used to represent the data points. The statistics that are relevant to Figure 4.16 and Figure 4.17 are summarised in Table 4.1. At both Grahamstown and Adelaide, the zonal mean flow is generally stronger than the meridional mean flow but there are times when the two are comparable e.g. in 1994 at Grahamstown. In general, the zonal mean flow shows greater seasonal variability (with changes of up to ~35 ms^{-1}) compared to the meridional mean flow. At Grahamstown, the zonal flow is always eastward whereas at Adelaide it sometimes turns westward. On the other hand, the meridional flow at both sites is mostly northward/equatorward (positive) but also shows some southward/poleward (negative) and more so at Adelaide. Generally, the negative (westward/southward) flows are weaker than the positive circulation.

The seasonal trend of the zonal mean circulation at Grahamstown tends to have a primary maximum (which can be as high as ~40 ms^{-1}) in November or summer and a secondary maximum in winter. Although the zonal mean flow at Adelaide also peaks around the solstices, the primary peak is in winter with the secondary one occurring in summer. *Fleming et al.* [1996] presented results of the zonal mean zonal wind at 30°S and 95 km from HRDI, WINDII, and the COSPAR International Reference Atmosphere (CIRA) model CIRA-86 and the Horizontal Wind Model (HWM-93) (see *Fleming et al.* [1996] and references therein for

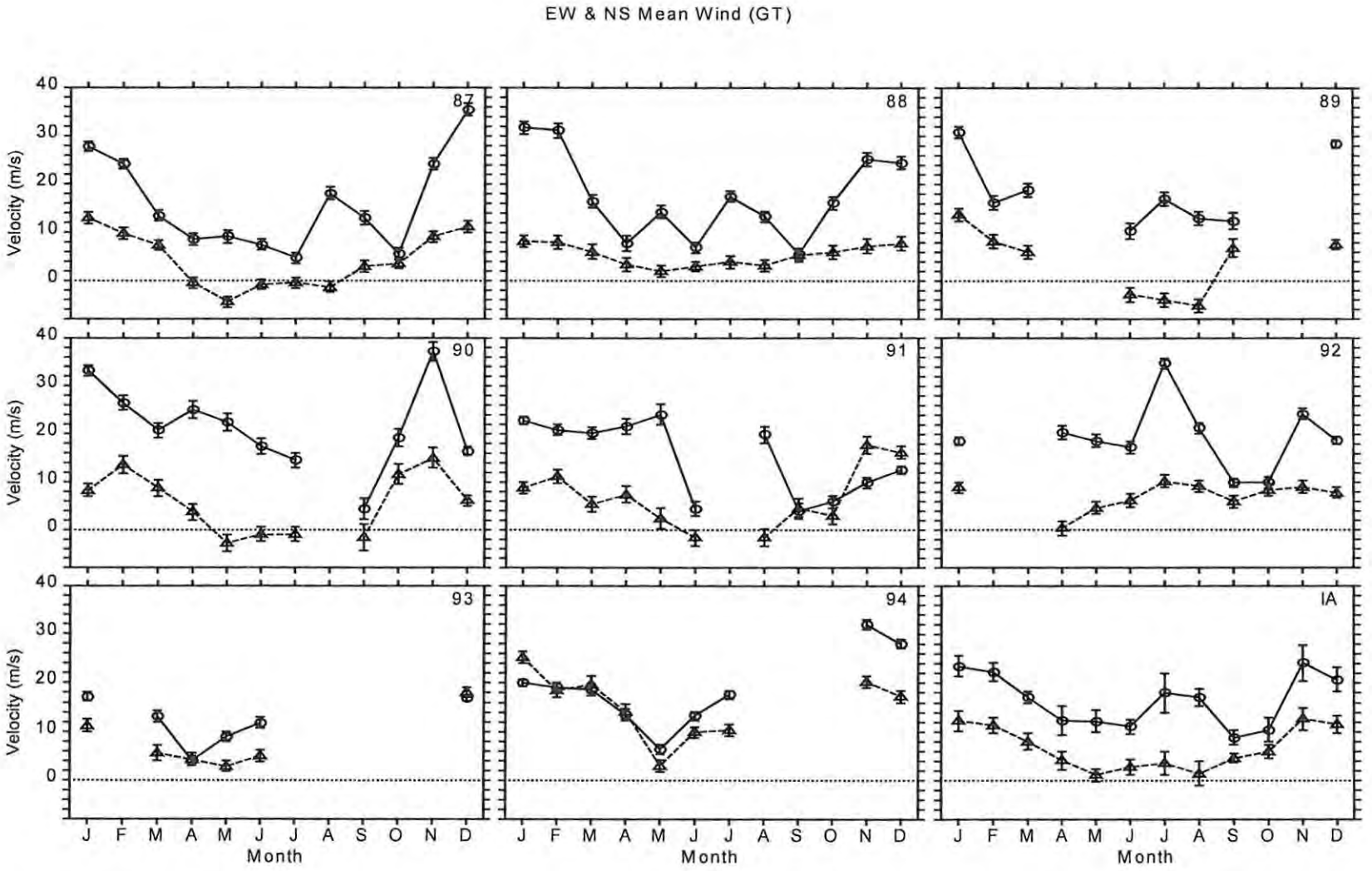

Figure 4.16 The zonal (circles) and the meridional (triangle) mean wind at Grahamstown for the years 1987-1994 and the IA. The error bars represent one standard error of the mean (1 α).

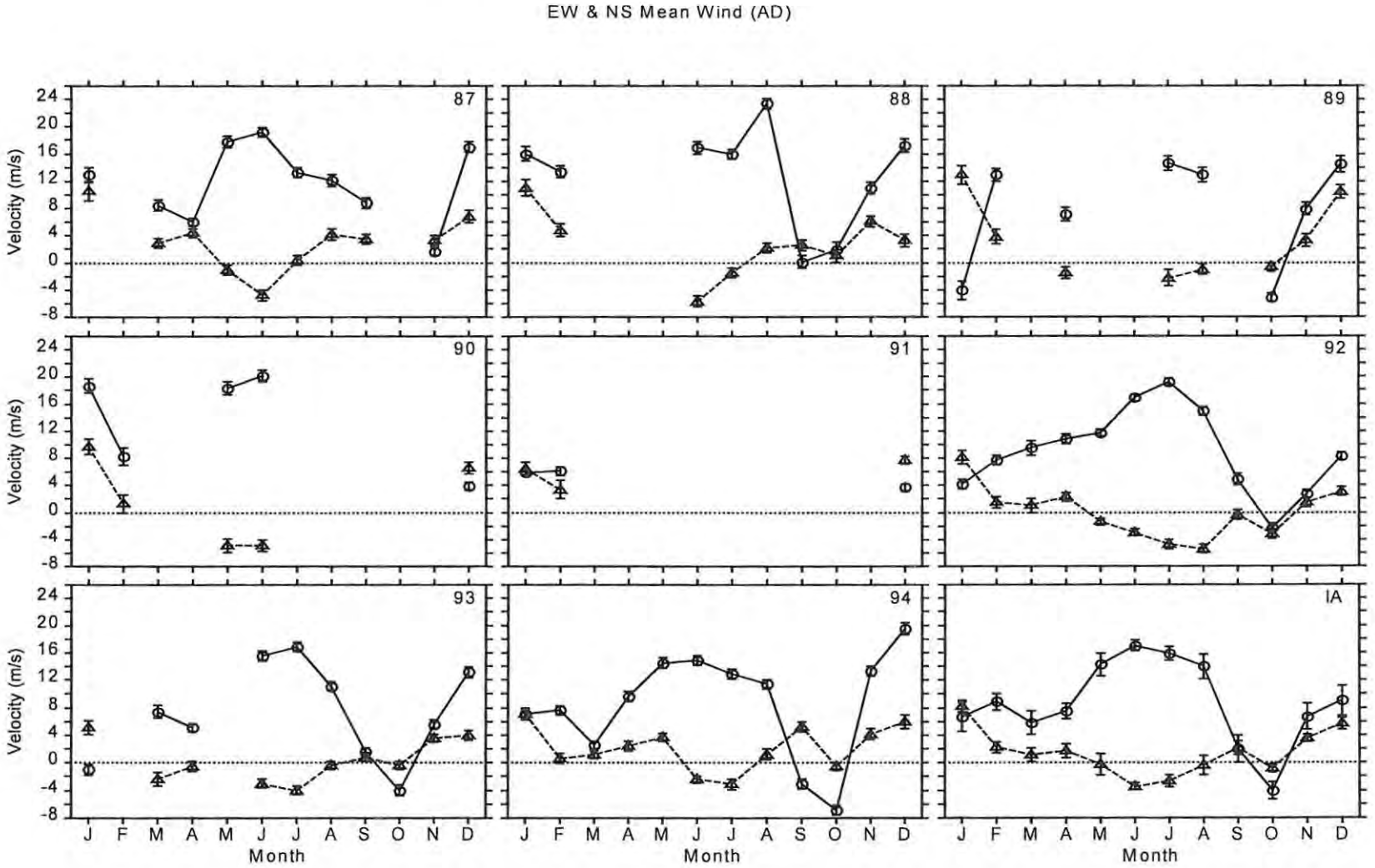

Figure 4.17 Same **Figure 4.16** but for Adelaide.

COMPONENT	VARIABLE	GRAHAMSTOWN	ADELAIDE
ZONAL	Speed (ms^{-1})	17.7±0.9	9.9±0.7
	Eastward Speed (ms^{-1})	17.7±0.9	10.4±0.7
	Occurrence Rate [Eastward Speed] (%)	100	89.9
	Westward Speed (ms^{-1})	-	3.9±0.8
	Occurrence Rate [Westward Speed] (%)	0	10.1
MERIDIONAL	Speed (ms^{-1})	7.6±0.6	3.2±0.3
	Northward Speed (ms^{-1})	8.7.±0.6	3.8±0.4
	Occurrence Rate [Northward Speed] (%)	82.3	63.8
	Southward Speed (ms^{-1})	1.9±0.4	2.4±0.3
	Occurrence Rate [Southward Speed] (%)	17.7	36.2

Table 4.1 The statistics of the monthly mean flow variables at Grahamstown and Adelaide for the 8-year (1986-1994) period. The speeds are 8-year averages and the percentages refer to all the data during the same period.

details). In line with the Grahamstown observations, the general trend in HRDI, WINDII, CIRA-86 and HWM-93 results exhibits an eastward primary peak (~20-45 ms^{-1}) in summer and a secondary peak autumn/winter.

Fleming et al. [1996] pointed out that the eastward summer jet is a consequence of the thermal wind balance resulting from the cold polar region and the associated steep meridional temperature gradient that underlies the 70-90 km altitude band of the summer middle and high latitudes. These authors found that the winter flow, apart from being weaker, was more variable. For the same height and latitude (i.e. 30°S and 95 km), *Fleming et al.* [1996] harmonically analysed the HRDI, WINDII, CIRA-86 and HWM-93 zonal mean zonal wind and found that it consisted of an annual mean of ~5-25 ms^{-1}, an annual harmonic amplitude of ~8-25 ms^{-1} and a semi-annual harmonic amplitude of ~7 ms^{-1}.

The seasonal pattern of the meridional flow at Grahamstown and Adelaide is characterised by strong northward flow from November to January/February and a weak northward or southward flow from about March to October. The HRDI and WINDII results for 30°S and

95 km show a similar pattern with strong ($\geq$10 ms^{-1}) northward flow from spring to the end of summer or to autumn and a weak northward or southward flow from autumn to through to the end of winter or to spring [*Fleming et al.*, 1996]. In 1994 the Grahamstown meridional flow is abnormally strong reaching about 25 ms^{-1} in January and, in fact, exceeding the zonal flow during this month. For this year, the meridional mean flow is about 10 ms^{-1} or more with the exception of May when both the zonal and the meridional flows at Grahamstown are at their weakest (< 10 ms^{-1}). Although results from HRDI and WINDII are variable, they generally show positive (negative) flows during the winter period of the northern (southern) hemisphere [*Fleming et al.*, 1996]. *Fleming et al.* [1996] report that the annual harmonic amplitude of the meridional mean flow for the UARS observations are 5-15 ms^{-1} with a peak northward flow in December-January in the 45°S-45°N latitude band. This flow represents a flow from the summer to the winter hemisphere and is consistent with the ageostrophic meridional flow induced by the deposition of gravity wave momentum [*Fleming et al.*, 1996]. The UARS results also suggest the presence of a weaker (~5 ms^{-1}) semi-annual component in the meridional flow at low latitudes increasing to 10-12 ms^{-1} at mid-latitudes [*Fleming et al.*, 1996].

In Figure 4.18 I have compared the long-term average (IA) of the mean flow at Grahamstown and Adelaide to the "Mean Wind Model" (MWM) by *Portnyagin & Solovjova* [2000] for a height of 90 km and 32.5°S latitude. Since the wind parameters for Grahamstown and Adelaide are height integrated, I have also plotted figures for averaged model mean flows. A Gaussian weighting procedure similar to that described in Chapter 3, Section 3.4.2.1, was used to average the model amplitudes for heights 70-110 km. The weighting of this form was chosen to give a height distribution similar to that of meteors at Grahamstown (Chapter 3, Figure 3.3). Before going any further, it has to be mentioned, however, that data from both Grahamstown and Adelaide were used in the MWM, DTM (see Chapter 6, Section 6.3.1.1) and STM (see Chapter 7, Section 7.2.1.1), therefore, the results from this model are not completely independent of the respective observations made at the two sites. Looking at Figure 4.18 we observe that height averaging does not have a big impact on the model results. The zonal mean flow of the model is similar to Grahamstown for the first four months of the year and tends to follow the pattern at Adelaide for the rest of the year. Qualitatively the observed meridional mean flow is similar to the model flow but the model southward flow reach stronger peaks (~-8 ms^{-1}) and tends to start

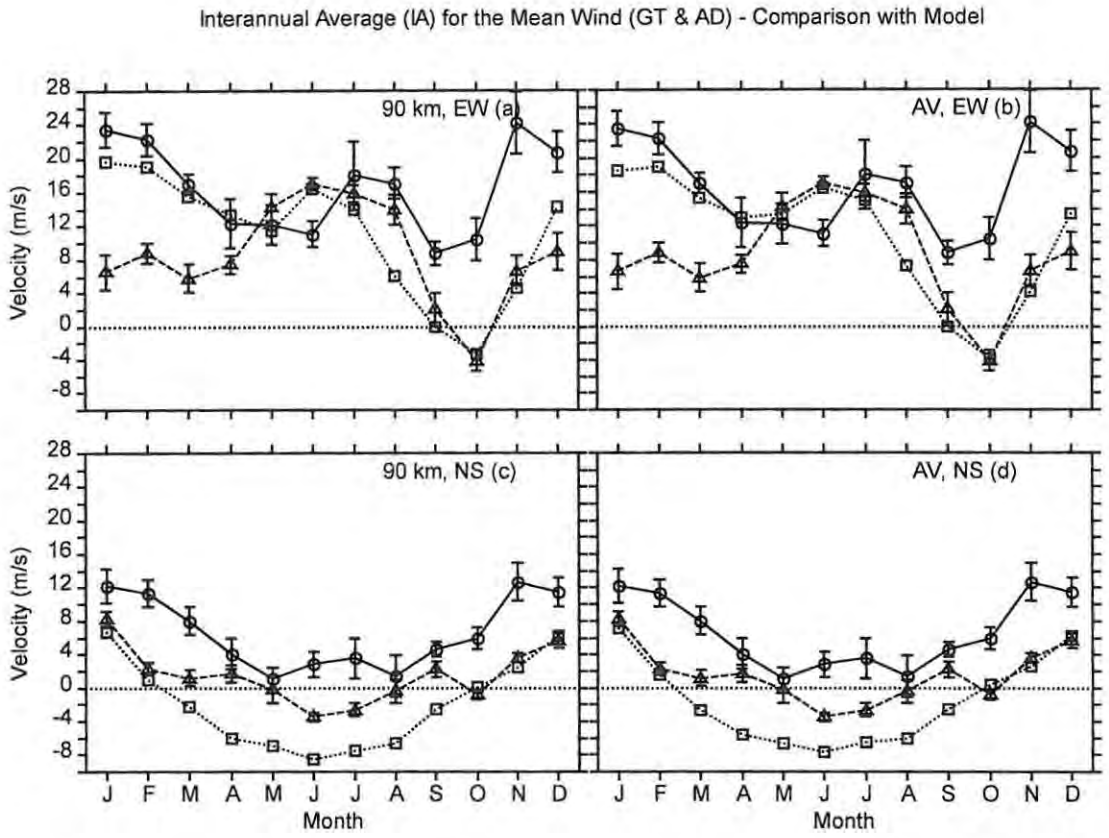

Figure 4.18 Comparison of the mean wind IAs at Grahamstown and Adelaide with the MWM. (a) Zonal mean wind with different symbols representing Grahamstown IA (circles), Adelaide IA (triangles), and MWM (squares) for model heights of ~90 km. (b) Same as (a) but for Guassian weighted model mean winds. (c) and (d) are similar to (a) and (b) respectively but for meridional mean winds.

earlier in the year.

The seasonal behaviour of the zonal and the meridional mean flow observed at Grahamstown and Adelaide are in broad agreement with satellite results and MWM and can best be explained by considering the interaction of the mean flow and gravity waves [*Hocking*, 1996; *Thomas*, 1996]. As mentioned in Chapter 1, Section 1.2.2.1, calculations based on the assumption of a radiative equilibrium state results in unrealistic temperature and dynamic structures of the mesopause region. Gravity waves are widely believed to be responsible for providing the substantial amount of the drag that is necessary to result in observed temperatures and speeds.

In general these waves have differing phase velocities and are directed in all orientations [*Hocking*, 1996]. The phase speeds of these gravity waves are thought to be dependent on the wind speed at the excitation region of the wave and typical ranges for tropospherically generated waves are ± 50 ms^{-1} [*Murphy & Vincent*, 1998]. Considering an eastward background mean wind vertical profile, *Hocking* [1996] explains that as the waves propagate up, the eastward ones will reach height levels (below ~70 km) at which they will be filtered by the mean wind as explained in Section 4.2.2. Consequently, the gravity wave spectrum at ~70 km will be dominated by westward propagating waves [*Hocking*, 1996]. At some level (above 70 km), the westward wave amplitudes, depending on their initial values, become exceedingly large that they break down as a result of convective overturning or shear instability and in the process pass on some westward momentum to the mean flow [*Hocking*, 1996; *Thomas*, 1996]. This westward wave drag subsequently slows down and, if large enough, reverses the eastward mean flow at about 80 km [*Hocking*, 1996; *Hamilton*, 1996; *Thomas*, 1996].

The above drag force also influences the meridional flow. To understand this, we consider a radiative equilibrium state in which the enhanced solar heating of the equatorial region results in a meridional pressure force. This force tries to accelerate some meridional flow but the Coriolis forces turns this flow into a zonal flow called geostrophic flow [*Hocking*, 1996; *Thomas*, 1996]. This zonal flow induces a meridional Coriolis force of its own which opposes the meridional acceleration thus preventing meridional flow [*Hocking*, 1996]. However, the presence of gravity wave drag disturbs this radiative equilibrium that only involves the pressure force and Coriolis force. Consequently, there should be a balance between three forces, namely, the meridional pressure force, the Coriolis force and wave drag [*Thomas*, 1996]. In particular, wave drag alters the zonal mean flow and, consequently, destabilizes the equilibrium between the meridional Coriolis and pressure forces resulting in some meridional flow [Hocking, 1996]. In this case equilibrium is attained when [*Hocking*, 1996]

$$\frac{d}{dz}\langle u'w'\rangle = fv_0 \tag{4.1}$$

where $\langle u'w'\rangle$ is the vertical flux of zonal momentum, v_0 represents the meridional mean flow, f the Coriolis parameter ($= 2\Omega\sin\varphi$ with Ω the Earth's rotation rate and φ the latitude).

The meridional flow resulting from the balance of the various forces is responsible for mass transportation across latitude circles. To maintain mass continuity, compensation for this meridional transportation comes in the form of upward (downward) flow in summer (winter) [*Thomas*, 1996]. The rising air expands and cools adiabatically and it is this dynamical cooling that causes low summer temperatures especially in the high latitude mesopause region at a time when insolation is at its highest [*Thomas*, 1996; *Murphy & Vincent*, 1998]. On the other hand, the wintertime poleward flow results in sinking and the associated adiabatic warming [*Thomas*, 1996]. According to *Thomas* [1996], wave drag tends to slow down the summertime wind flow and by so doing reduces the Coriolis force and so turns the wind equatorward. Conversely, in winter the meridional flow is poleward [*Thomas*, 1996]. This is consistent with the strong northward flows observed from late spring to late summer and the weak northward/southward flow from around autumn to mid spring that is shown by the IA panels of Grahamstown and Adelaide (Figure 4.21). This is also somewhat similar to the annual cycle that is characterised by northward (southward) flows in summer (winter) observed in the climatological mean of the years 1967-1986 at Molodezhnaya (68°S, 45°E) [*Portnyagin et al.*, 1993a].

To conclude this section, I will combine the zonal (u_0) and meridional (v_0) components of the mean flow into what I will refer to as the *horizontal* mean flow velocity (V_0) that is defined by some magnitude and direction, which are given by

$$V_0 = \sqrt{u_0^2 + v_0^2}$$

Equation 4.1

and

$$\phi_0 = \arctan\left(\frac{v_0}{u_0}\right)$$

Equation 4.2

respectively.

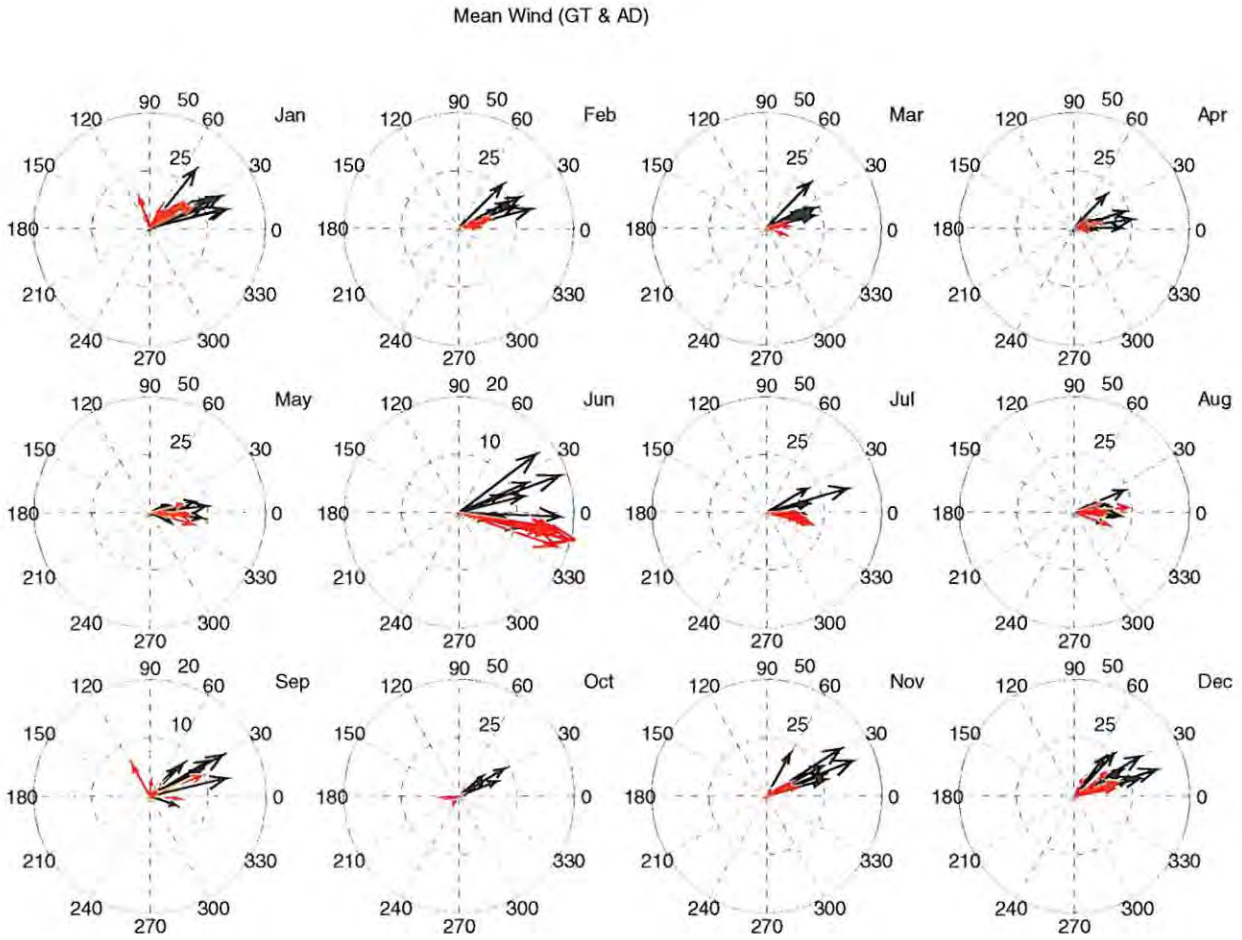

Figure 4.19 The horizontal mean flow velocity for Grahamstown (black arrows) and Adelaide (red arrows) for different months. The numbers that are positioned next to the radial lines on the outer circle give the angles in degrees. The east, north, west and south directions coincide with angles 0°, 90°, 180° and 270°, respectively. The radii of the inner and the outer circles, in ms^{-1}, are also indicated.

The horizontal mean flow velocity (Figure 4.19) has complicated seasonal trends but tends to have larger magnitudes at Grahamstown than at Adelaide. In general, the magnitudes at Adelaide are confined to the 25 ms^{-1} circle. Note that the June and September panels on Figure 4.19 have similar scales that are, however, different from those of the other months and so care should be taken in comparing the months. The directions are seasonally dependent as would be expected from the seasonal variation of the respective zonal and meridional mean flows. The velocity vectors are predominantly in the first and forth quadrants with a few exceptional cases, which are exclusively at Adelaide, when the flows are in the second and third quadrants. Starting from January the mean flow is predominantly towards the north-east in line with the summer northward and eastward jets at the two sites (Figure 4.16 and Figure 4.17). As months progress, the flow turns towards a predominantly eastward flow around May consistent with the zonal eastward winter jet which coincides with weak northward or southward flow (Figure 4.16 and Figure 4.17). From thenceforth they revert back to the January/summer situation.

4.3.1.2 Longitudinal Seasonal Trends

A one-to-one comparison of the zonal mean flow at Grahamstown and Adelaide is shown in Figure 4.20 and a similar comparison for the meridional component is illustrated in Figure 4.21. The zonal and the meridional speeds at Grahamstown are about twice those at Adelaide. For the zonal flow, the differences between Grahamstown and Adelaide are more pronounced during the summer solstice and the equinoxes as shown by the IA in Figure 4.20. On the other hand, the winter flows are more comparable at the two sites except in 1992 when the zonal flow at Grahamstown has a solstitial primary peak in winter contrary to the typical summer maximum. Figure 4.22 shows the distributions of the differences (GT-AD) of the zonal velocities between Grahamstown and Adelaide. It is important to note that the differences referred to here are velocity (vector) differences as opposed to speed (scalar) differences. An example will make the distinction between these two differences clear. Consider a difference of a smaller eastward (positive) flow at Grahamstown and a relatively larger westward (negative) flow at Adelaide. The velocity difference would give a positive difference whereas the speed difference would be negative. Therefore, a positive difference merely means relatively more eastward (northward) flow at Grahamstown than at Adelaide for the zonal (meridional) mean flow. Consistent with a "*stronger*" zonal mean flow at Grahamstown, negative differences

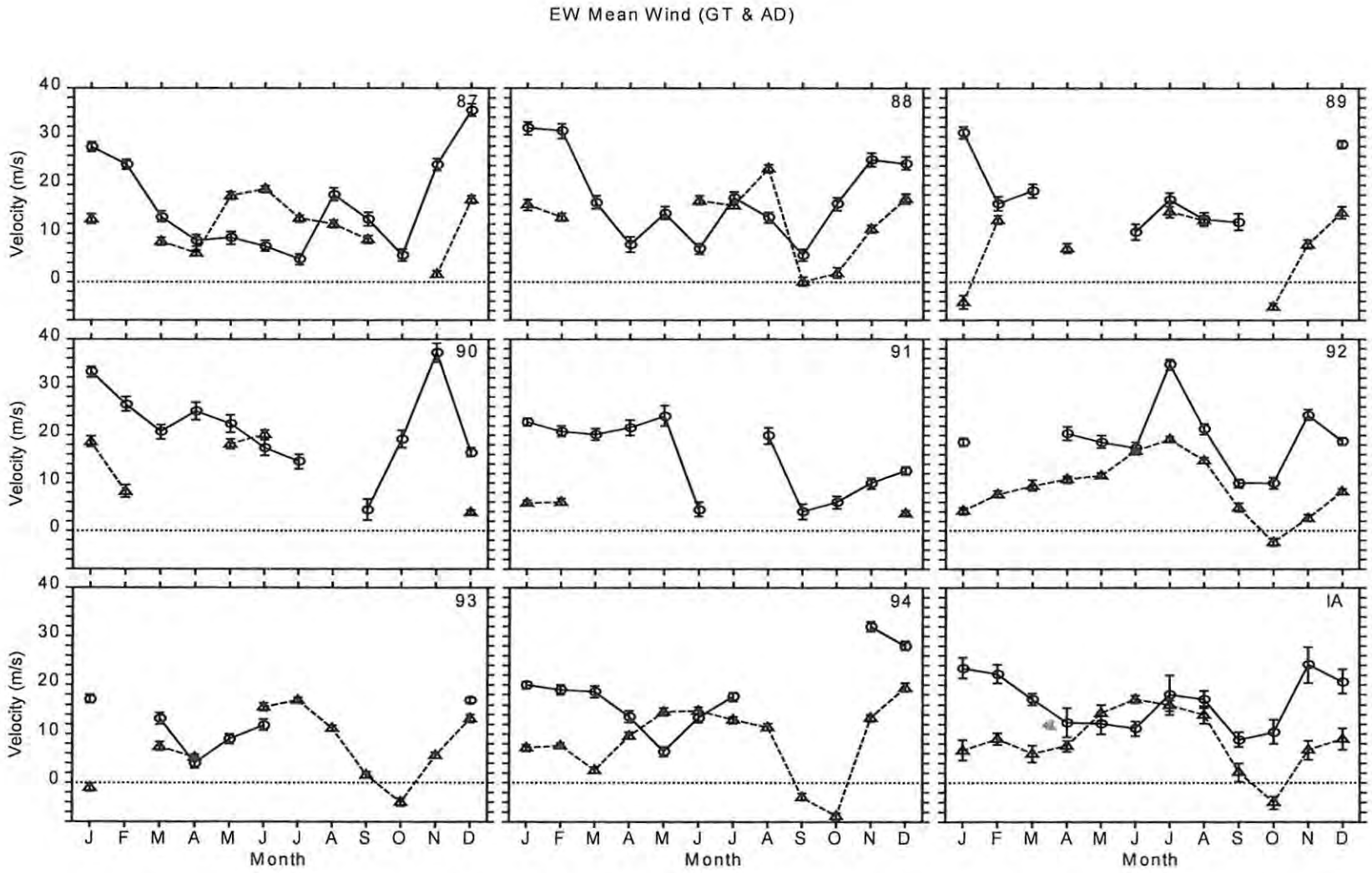

Figure 4.20 The zonal mean wind at Grahamstown (circles) and Adelaide (triangle) for the years 1987-1994 and the IA. The error bars represent one standard error of the mean (1 α).

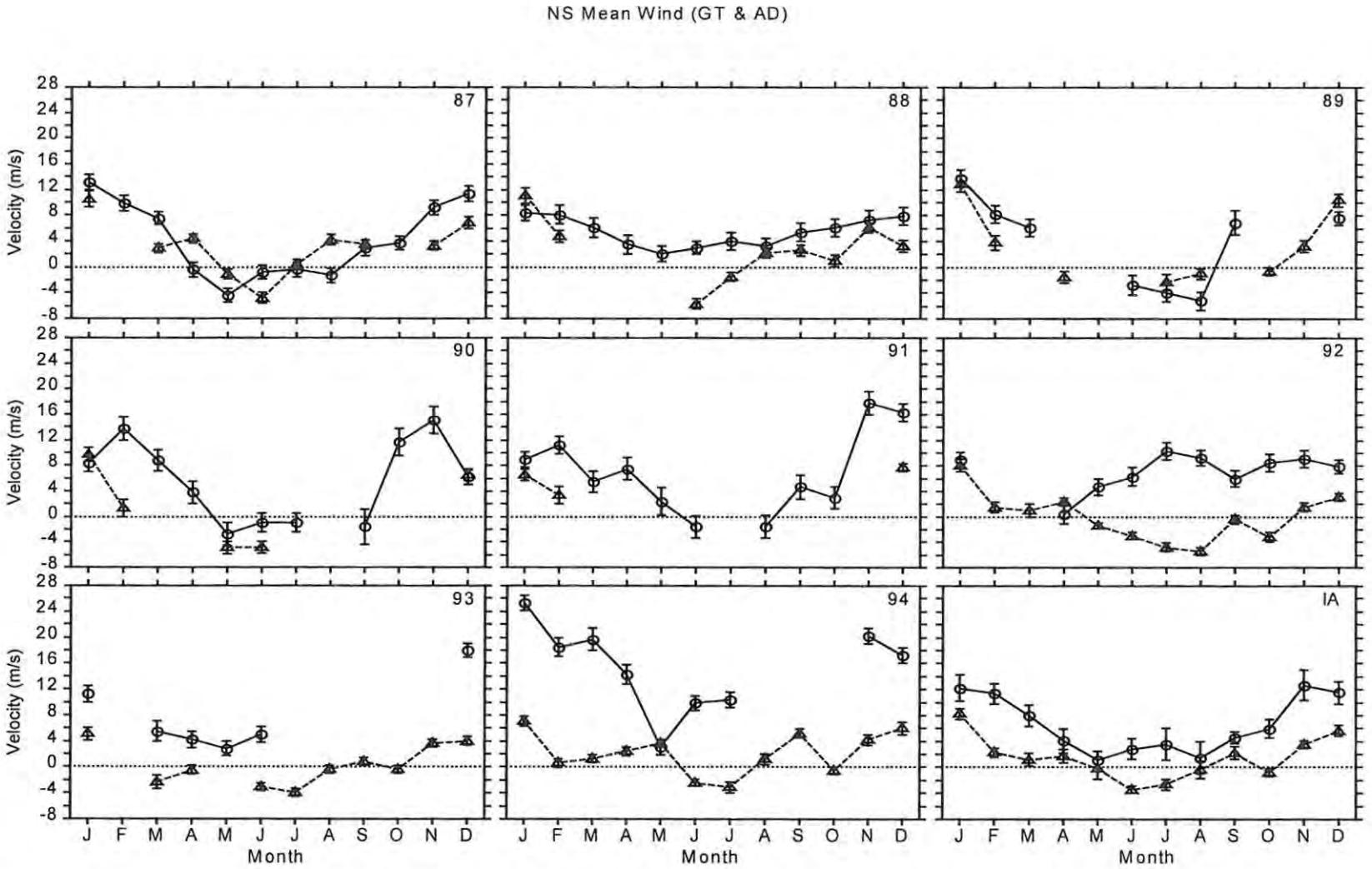

Figure 4.21 Same as Figure 4.20 but for the meridional flow.

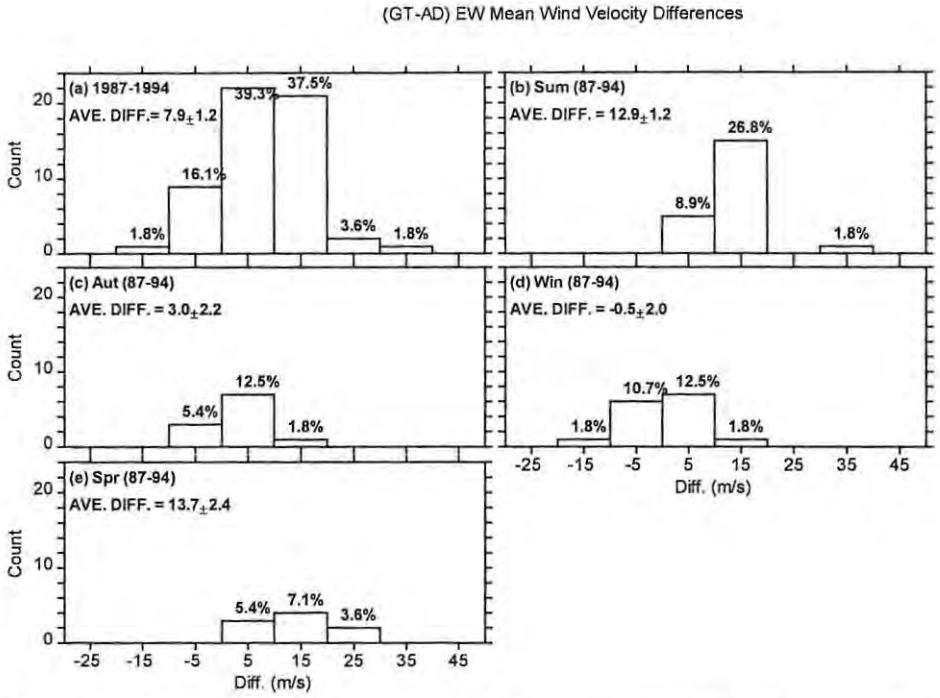

Figure 4.22 The distribution of the differences (GT-AD) of the zonal mean flow velocities at Grahamstown and Adelaide. Count represent the number within each bin and the number on the *x*-axis represents the centre velocity of each bin. The percentages on top give the bin count as a percentage of the total. The average difference is also indicated.

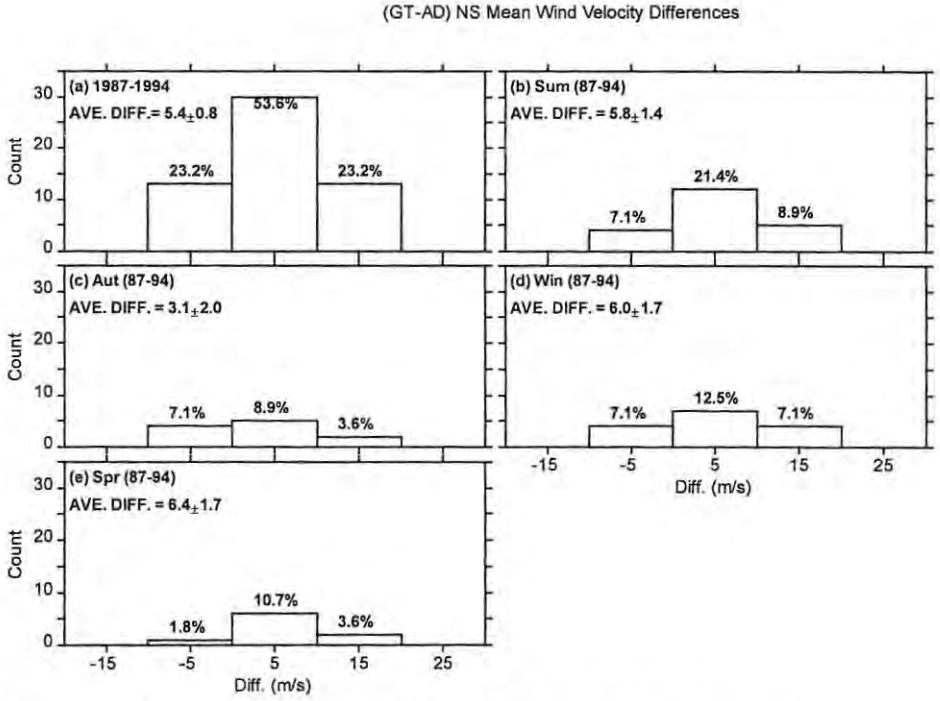

Figure 4.23 Same as **Figure 4.22** but for the meridional mean flow.

contribute less than 20 % of the differences. The term "*strong*" here means relatively more eastward or northward for the zonal or meridional mean flow, respectively. A large proportion (~77 %) of the positive differences are in the range 0-20 ms^{-1}. The 8-year average difference is 7.9 ± 1.2 ms^{-1} with the largest discrepancies occurring in summer (average = 12.9 ± 1.2 ms^{-1}) and spring (average = 13.7 ± 2.4 ms^{-1}).

For the meridional flow (Figure 4.21), there is better agreement between Grahamstown and Adelaide with some years (e.g. 1987-1989) showing a very high degree of similarity. These higher levels of similarity are also reflected in IAs in Figure 4.21. The distribution of differences between the two sites for the meridional flow is shown in Figure 4.23. The meridional flow at Grahamstown, like its zonal counterpart, is stronger even though in this case there is a slightly larger percentage (~23 %) of stronger Adelaide flow. About 54 % of the differences in the meridional mean flow are in the 0-10 ms^{-1} bracket with the –10-0 ms^{-1} and 10-20 ms^{-1} brackets having ~23 % each. The 8-year average difference is 5.4 ± 0.8 ms^{-1} with the autumn having an average of ~3 ms^{-1} while the other seasons have averages of ~6 ms^{-1}.

Since Grahamstown and Adelaide are in latitudinal proximity it is not clear why the former has stronger winds but a number of factors could be responsible for this. Comparing the mean wind at Obninsk (54°N, 38°E) and Saskatoon (52°N, 107°W) at about 95 km, *Forbes et al.* [1995] found a 10 ms^{-1} difference between the two sites and they suggested that it could be due to a stationary planetary wave. In particular, they thought that it could be a thermospheric signature of the zonal wavelength 1 planetary wave that has been detected in the stratosphere (see *Smith* [1985]). Similar suggestions of a possible link between stationary planetary waves and longitudinal differences in the mean flow were also made by *Kazimirovsky et al.* [1988] based on observations made at sites on the 52°N latitude but with different longitudes.

To see how planetary waves can influence the longitudinal structure of the mean flow we have to consider a few points presented by *Smith* [1985] who explains that a stationary or steady travelling wave with constant amplitude and structure (i.e., one that is not transient), will not interact with the mean flow except through dissipative processes. However, if there is simultaneous presence of a stationary and a travelling wave with the same zonal wavenumber, such that the two interfere resulting in transient variation in the wave amplitude, the resulting alternating constructive and destructive interference can substantially alter the spatial and

temporal fluctuation of eddy heat as well as momentum fluxes, which will cyclically excite the mean flow [*Smith*, 1985]. As pointed out by *Smith*, this can happen even if the travelling wave is not characterised by any vertical or meridional tilt, and hence has no eddy heat or momentum flux associated with it.

Some of these stationary planetary waves are Rossby waves. According to *Hamilton* [1996] the large-scale deviations of atmospheric circulation from 'zonal symmetry' that is observed in the extratropical middle atmospheric region indicate the presence of Rossby waves which originate from the troposphere. Quoting work by other authors as an example, Hamilton maintains that most of the features observed in the middle atmospheric large scale circulation can be explained in the context of the superposition of small amplitude Rossby waves on a 'zonally-symmetric' mean state. Of particular significance are the stationary waves that are generated as a result of the flow over topography and other similar zonal contrasts at the lower boundary layer [*Hamilton*, 1996].

Particularly significant are the stationary waves that are dominant in the winter tropospheric and stratospheric flow and are due to zonal contrasts like non-uniform topography, and the anisotropic distribution of diabatic heating [*Alpert et al.*, 1983; *Hamilton*, 1996]. According to linear theory only those stationary Rossby planetary waves with very large zonal scales (i.e. zonal waves 1 and 2) can propagate upwards into the strong winter eastward strastospheric mean flow and are otherwise precluded from propagating in the summer westward mean flow of the stratosphere [*Alpert et al.*, 1983; *Hamilton*, 1996 and references therein]. While the presence of these waves at the MLT region might explain the discrepancy between Grahamstown and Adelaide, the observed discrepancies for the zonal mean flow are larger in summer than in winter (Figure 4.20), which contradicts expectations. From the seasonal transmissivity described above, one would expect to have a longitudinally invariant zonal mean flow in summer and a longitudinally varying one in winter due to the superimposed stationary waves. With the available data, I cannot present a definitive explanation for this but cross-equatorial ducting, which was discussed earlier, could partly be responsible.

Another possible source of the discrepancy between Grahamstown and Adelaide could be a difference in the interface level between the oppositely directed stratospheric and mesospheric jets. This transition height can sometimes be different even for geographically close sites. For

instance Monpazier [(44.5°N, 1°E), {1979-1980}], Garchy [(47°N, 3°E), {1970-1976}] and Durham [(43°N, 71°W), {1978/1979}] have summer transition heights of ~ 86 km, 82 km and ~78 km respectively (see *Manson et al.* [1987] and references therein). However, a point of caution is that, in this case, these differences could also be influenced by interannual changes because the years involved (see contents of curly brackets) are different. *Portnyagin et al.* [1993a] suggested that mean flow differences between Molodezhnaya (68°S) and Mawson (67°S) which are 1000km apart could be connected to the relative displacements of the of the mean flow cells over spatial scales of the order of 1000 km. The higher occurrence rates of the westward flows and the southward flows at Adelaide compared to Grahamstown (see Table 4.1, page 94), seem to suggest that the interface level at the two sites could be at different altitudes.

4.3.2 Interannual Variations

On Figure 4.24 and Figure 4.25 I have shown the interannual variation of the zonal and the meridional mean wind with the first figure being for Grahamstown and the second for Adelaide. A comparison of the zonal mean flow at Grahamstown and Adelaide is shown in Figure 4.26 with Figure 4.27 showing a similar comparison but for the meridional mean flow. The horizontal lines (solid and dashed) represent the monthly interannual average (MIA), which is the average for the 8 years for a given month.

In general the zonal and the meridional mean flows at both sites follow different interannual trends (Figure 4.24 and Figure 4.25). This shows that although the gravity wave drag influences both the zonal and the meridional mean flows in some way, there are other factors that come into play. Considering the fact that the zonal mean flow shows a higher degree of interannual variability than the meridional flow, it seems logical to conclude that the zonal (rather than the meridional) mean flow is more sensitive to the majority of these other factors. While no concrete identification of these other factors can be made, one likelihood is the difference in the horizontal characteristic of the zonal and the meridional velocities of Rossby waves [*Salby & Roper*, 1980], which would most probably also have different responses to interannual changes. Another striking feature is that different months have different interannual trends. That is, if say certain years have high velocities in January there is no guarantee that other months would

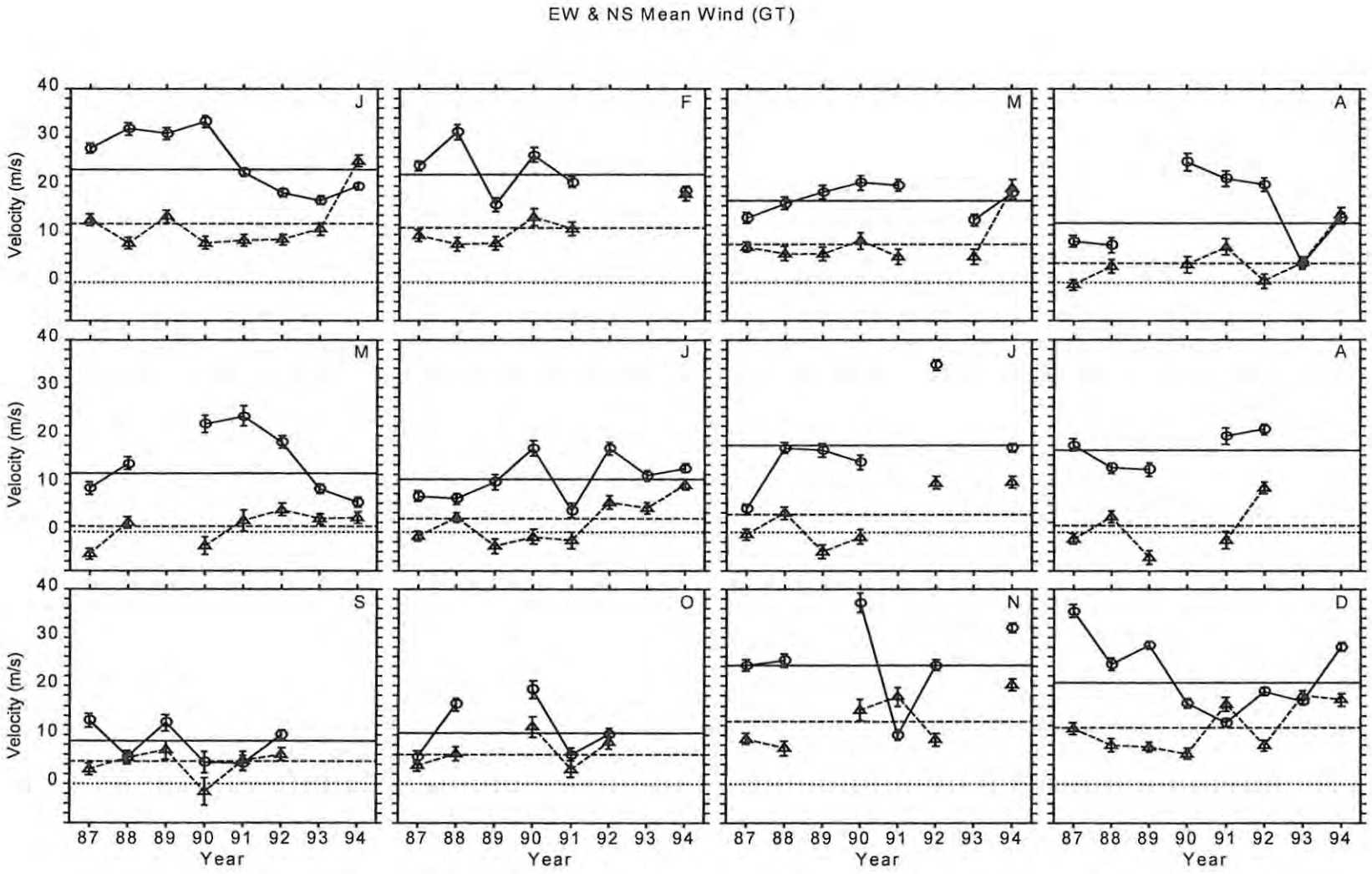

Figure 4.24 The zonal (circles) and the meridional (triangle) mean wind at Grahamstown for the years 1987-1994. The error bars represent one standard error of the mean (1 α). Each panel represents the month given at the top right hand corner starting with January. The horizontal solid line and the horizontal dashed line represent the zonal and the meridional monthly interannual average (MIA) of the given month respectively.

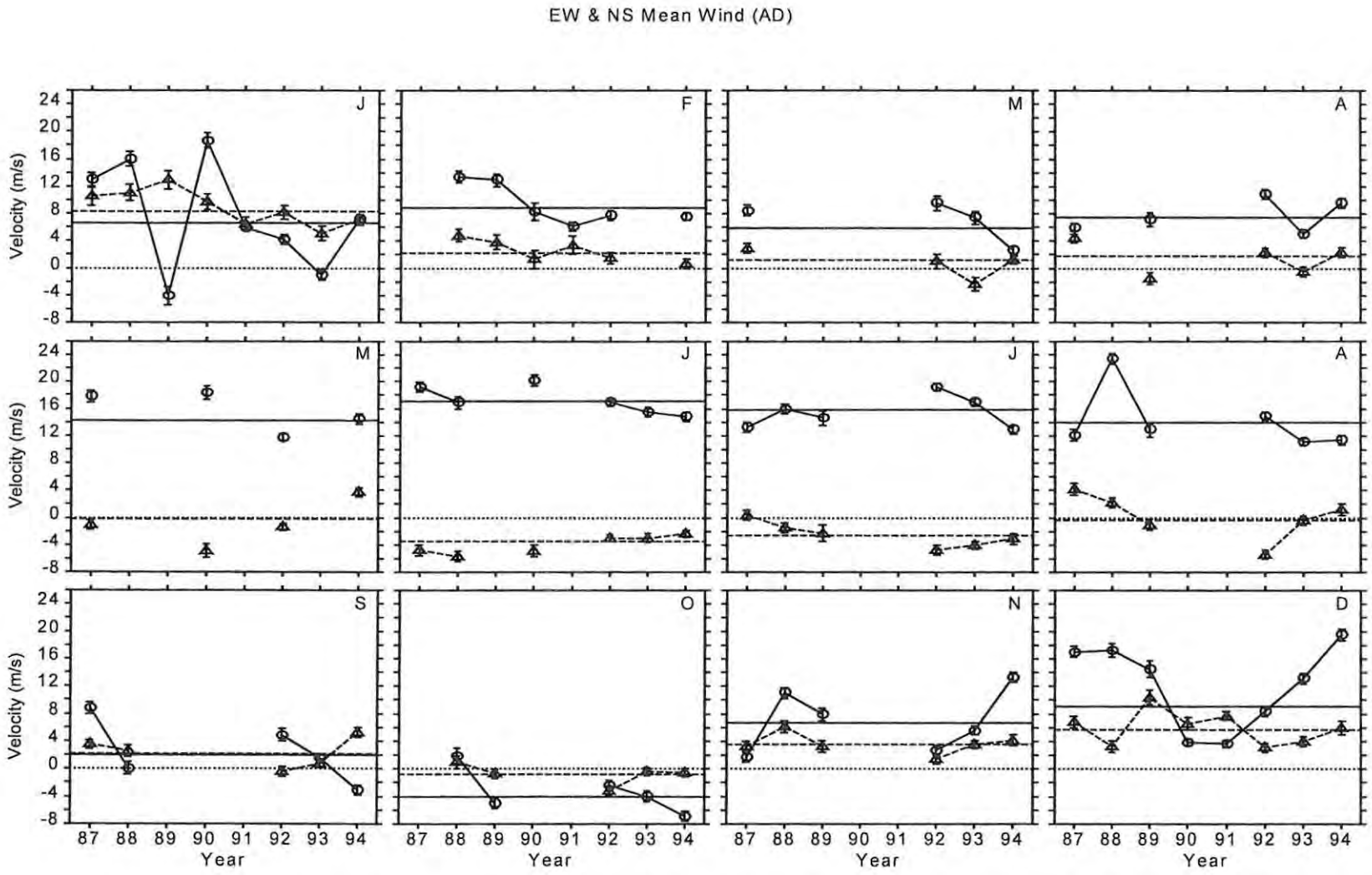

Figure 4.25 Same as **Figure 4.24** but for Adelaide.

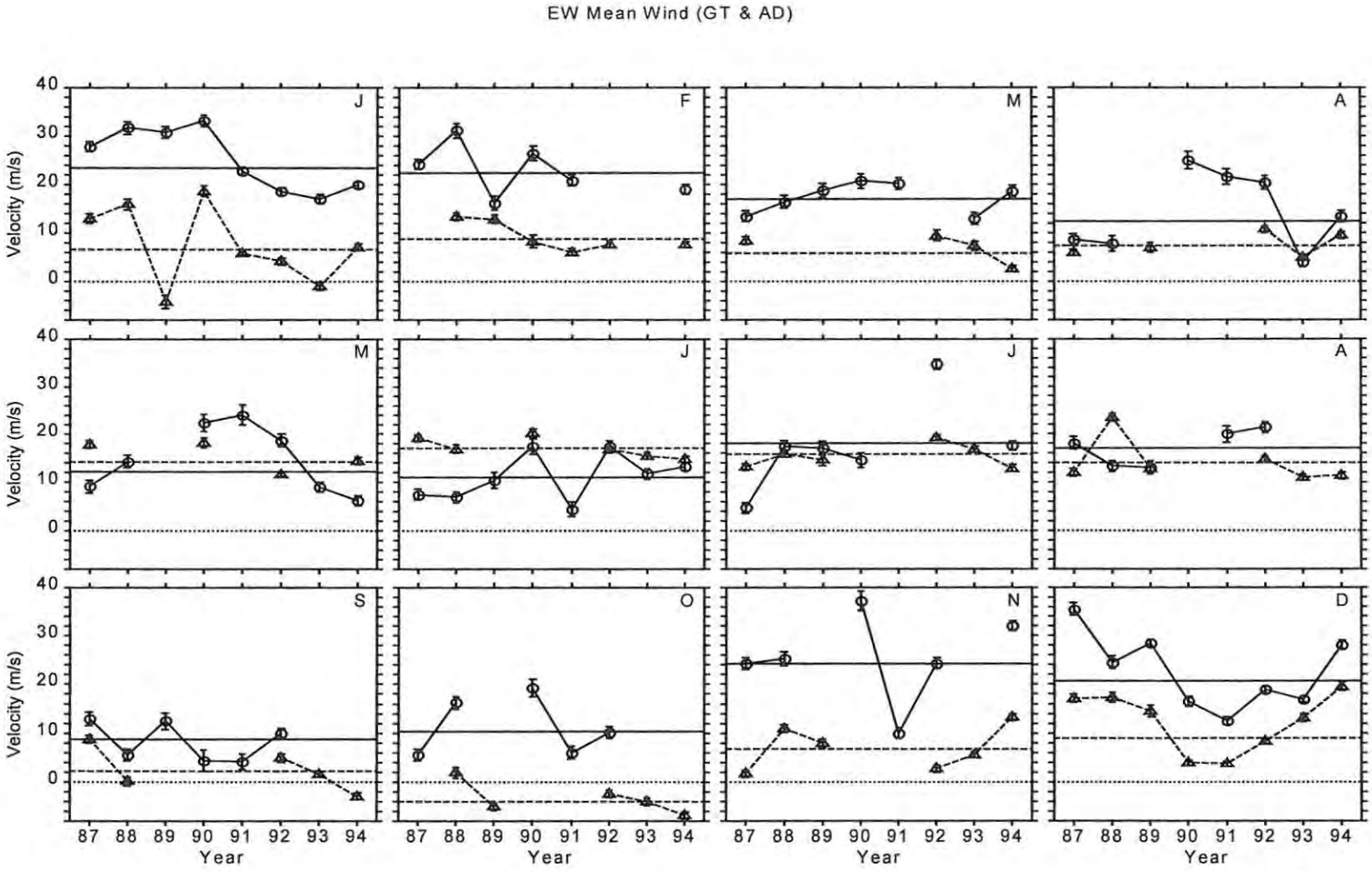

Figure 4.26 The zonal mean wind at Grahamstown (circles) and Adelaide (triangles) for the years 1987-1994. The error bars represent one standard error of the mean (1 α). Each panel represents the month given at the top right hand corner starting with January. The horizontal solid line and the horizontal dashed line represent the Grahamstown and the Adelaide monthly interannual average (MIA) of the given month respectively.

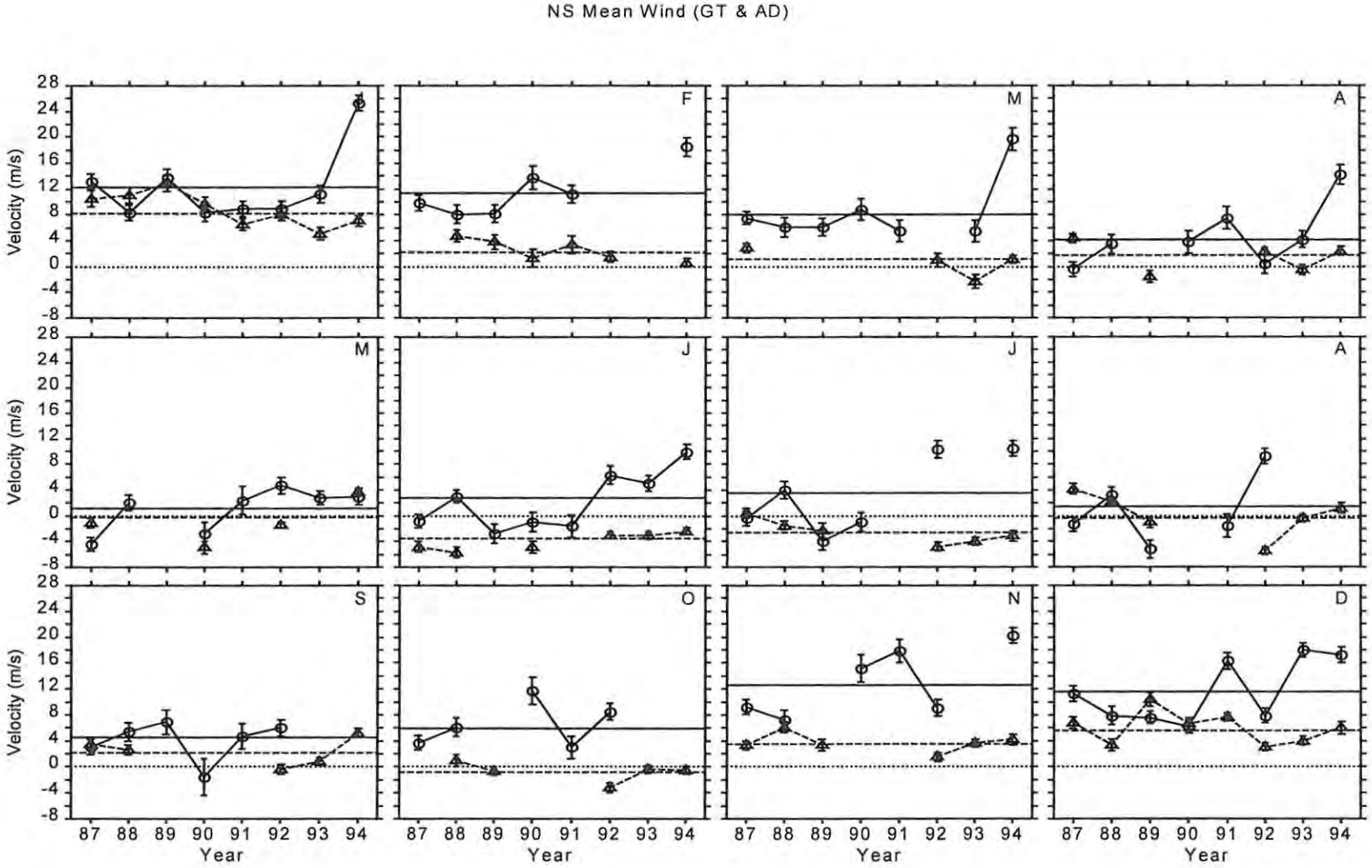

Figure 4.27 Same as **Figure 4.26** but for the meridional mean flow.

have large velocities during those years as well. This means that the interannual variation can also have a monthly/seasonal dependence.

A number of specific features are worth mentioning here and the most interesting of these are the strong similarities in the interannual variation at Grahamstown and Adelaide during the summer months for the zonal mean flow (Figure 4.26). The general trend during these months at both sites shows that the first three/four years (1986-1990) have zonal mean flows that tend to be larger than the MIA. December 1993/1994 also show a similar tendency whereas the other years tend to have values that are below the MIA for the summer months. This suggests that the observed behaviour might be due to global or latitudinal factors. Judging by the lack of correlation between Grahamstown and Adelaide during other times it is most likely that the dominant sources of the interannual variations during these times are more local or longitudinal in nature. Another noticeable feature is that the zonal mean flow at Grahamstown over the years tends to be larger than the Adelaide flow from October to March/April and are comparable for the other months (see Figure 4.26). This enhanced flow has been mentioned earlier but the important thing here is its consistency from year to year. This suggests that there is an interannually consistent physical feature that is longitudinally dependent and tends to intensify (suppress) the eastward flow at Grahamstown (Adelaide) during this time.

In comparison to the zonal mean flow, the meridional mean flow shows more stability from year to year especially at Adelaide. A feature that stands out is the abnormally large meridional mean wind at Grahamstown in 1994, which has already been pointed out. By and large, the meridional mean flow at Grahamstown and Adelaide do not show a systematic interannual behaviour and the flow is generally comparable at the two sites. Based on a long data series (1968-1986) at Molodezhnaya (68°S, 45°E), *Portnyagin et al.* [1993a] investigated the interannual and secular variations at this site. Although these authors could not come to firm conclusions they suggested that some of the observed changes were possibly linked to anthropogenic effects and ozone excitation. They also found a possible link to changes in *in situ* solar, particle, or Joule forcing. The investigation of a connection between solar activity and the mesospheric flow naturally requires long data and has not been convincingly addressed. While some research work supports the existence of such a connection (e.g. *Sprenger and*

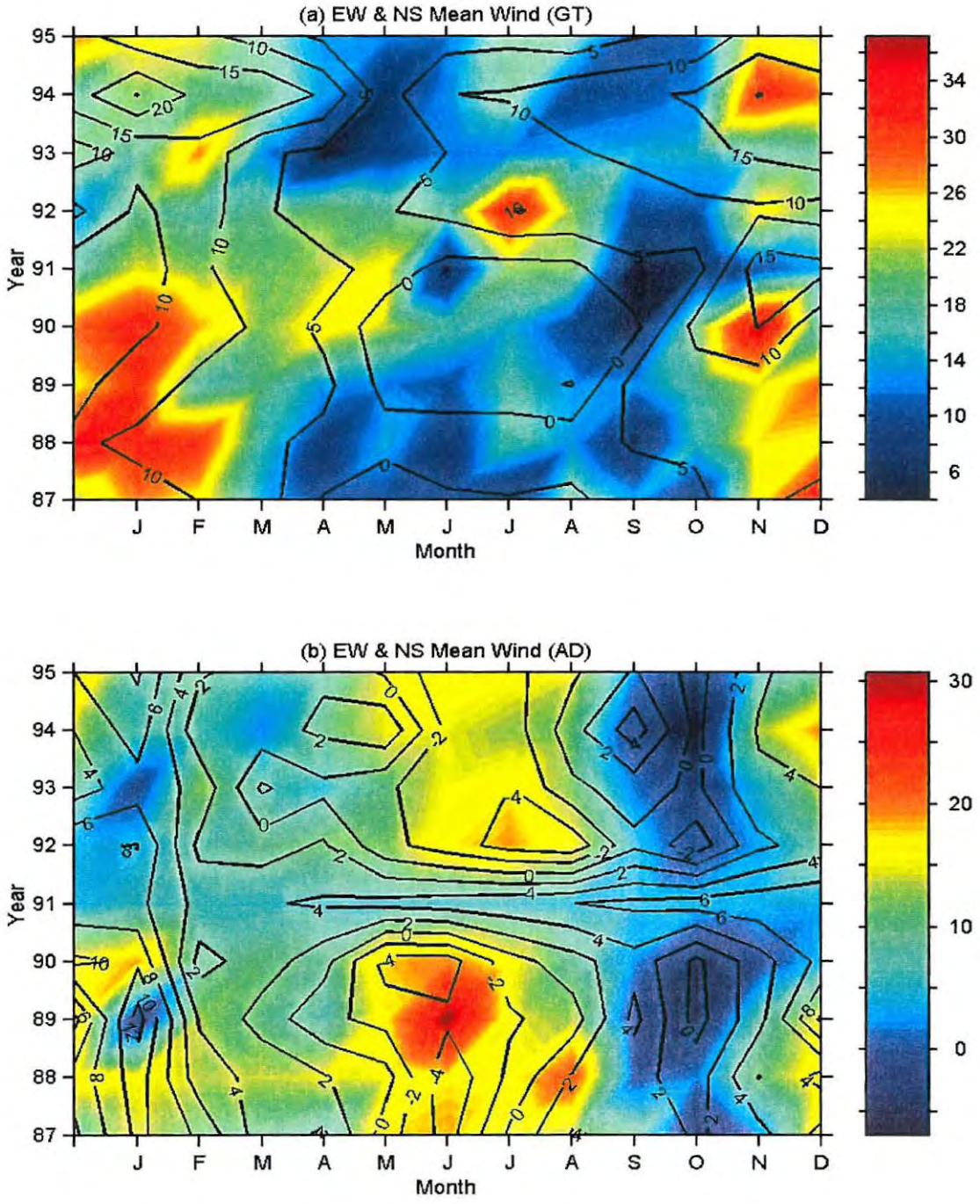

Figure 4.28(a) The zonal (colour-plot) and the meridional (contour-plot) mean flow at Grahamstown and (b) The same as (a) but for Adelaide. The units of the colour bars and the contours are ms^{-1}.

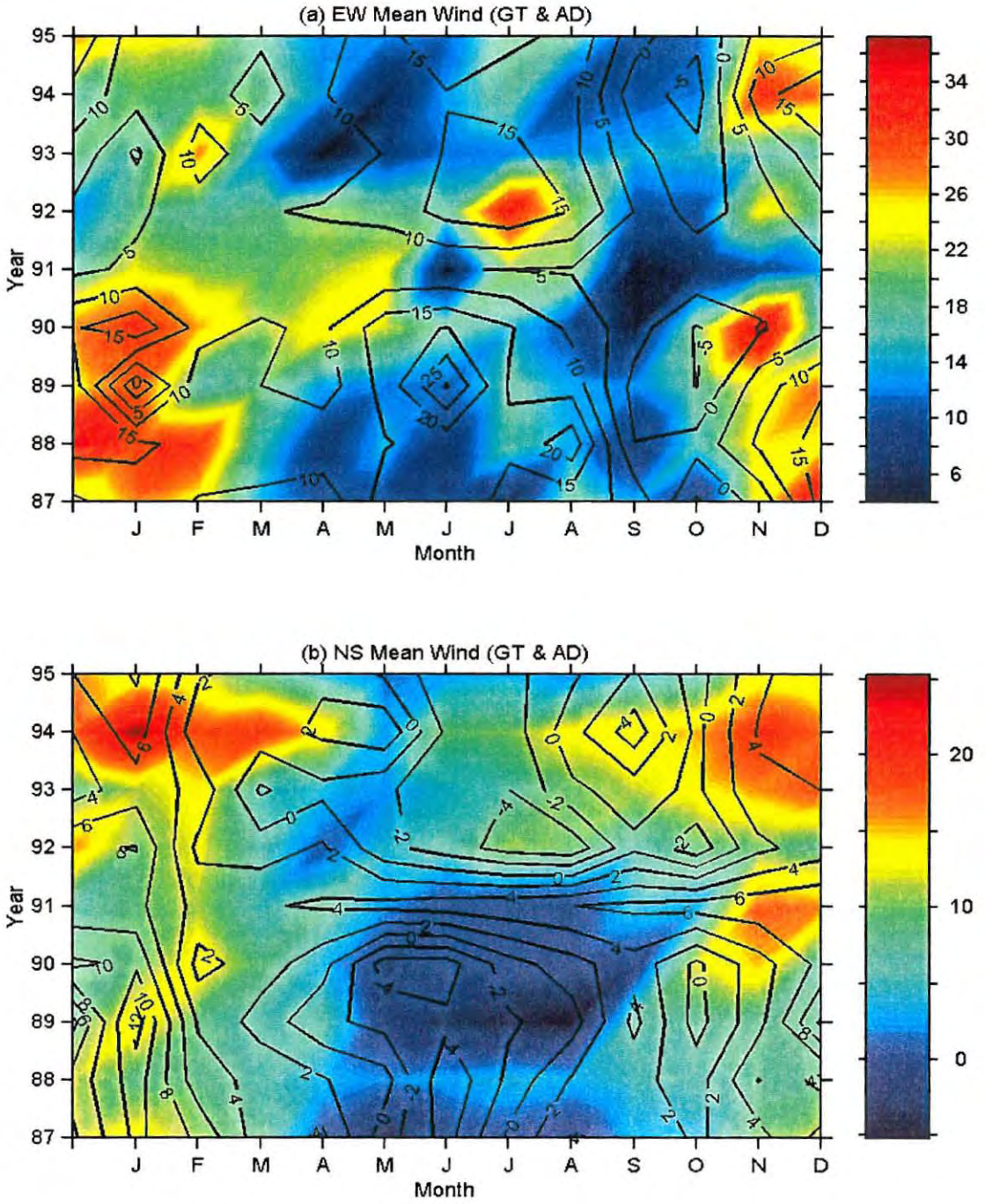

Figure 4.29(a) The zonal mean flow at Grahamstown (colour-plot) and Adelaide (contour-plot). (b) The same as (a) but for the meridional mean flow. The units of the colour bar and the contours are in ms^{-1}.

Schminder [1969]; *Namboothiri et al.* [1993]), there is also evidence to the contrary (e.g. *Eckermann et al.* [1997]; *Namboothiri et al.* [1999]).

To conclude this section and for completeness, I present 3-D plots (Figure 4.28 and Figure 4.29) that capture both the seasonal trends discussed in Section 4.3.1 and the interannual trends discussed in this section. These figures highlight most of the features discussed under Section 4.3.

CHAPTER 5 SHORT-TERM TIDAL VARIATIONS

5.1 INTRODUCTION

The diurnal and the semidiurnal tides are some of the strong features of the dynamics of the MLT region. In Chapters 6 and 7, I will consider these tides in more detail e.g. their forcing mechanisms and long-term trends with special emphasis on the comparison of Grahamstown and Adelaide. However, for now I just want to study their short-term variations. In general, the diurnal and the semidiurnal tide show great variability on day-to-day time scales (e.g. *Charles & Jones* [1999]). *Vial et al.* [1991] mentioned that the phrase "variable tide" is somehow contradictory because a "tide" is supposed to be a steady state atmospheric response with a period that is an exact harmonic of a solar day. These authors point out that the day-to-day variability of the tide of some meteorological variable, if it is indeed tidally related, implies that its period is not exactly determined.

In general, these day-to-day variations may have a large local component, that is, spatially uncorrelated while time averaged results show a substantially improved spatial correlation [*Walterscheid*, 1981]. The source of the short-term variations of tides is not fully understood and this is further complicated by the fact that the there could be several mechanisms involved which could act together or independently [*Teitelbaum & Vial*, 1991]. A number of mechanisms have been put forward in an attempt to explain this short-term variation but the extent of the contribution of each of these is not known [*Vial et al.*, 1991]. In the next section (Section 5.2), I will briefly consider these short-term variations as observed at Grahamstown and Adelaide. This will be followed by spectral analysis of these variations (Section 5.3), which would lead to a more detailed investigation of possible causes of observed fluctuations in Section 5.4.

5.2 SHORT-TERM VARIATIONS AND CORRELATIONS OF TIDES

As is Chapter 4, I have used 4-day data windows, which were advanced by 1 day each time. I have also used the same rejection criteria outlined in Section 4.2.1 such that the *acceptable data window* used in this chapter has the same definition as that in Section 4.2.1. To extract the amplitudes (Figure 5.1 to Figure 5.8) and the phases (not shown) of the tides, I used the harmonic analysis method described in Chapter 2, Section 2.2 with all the data points assigned

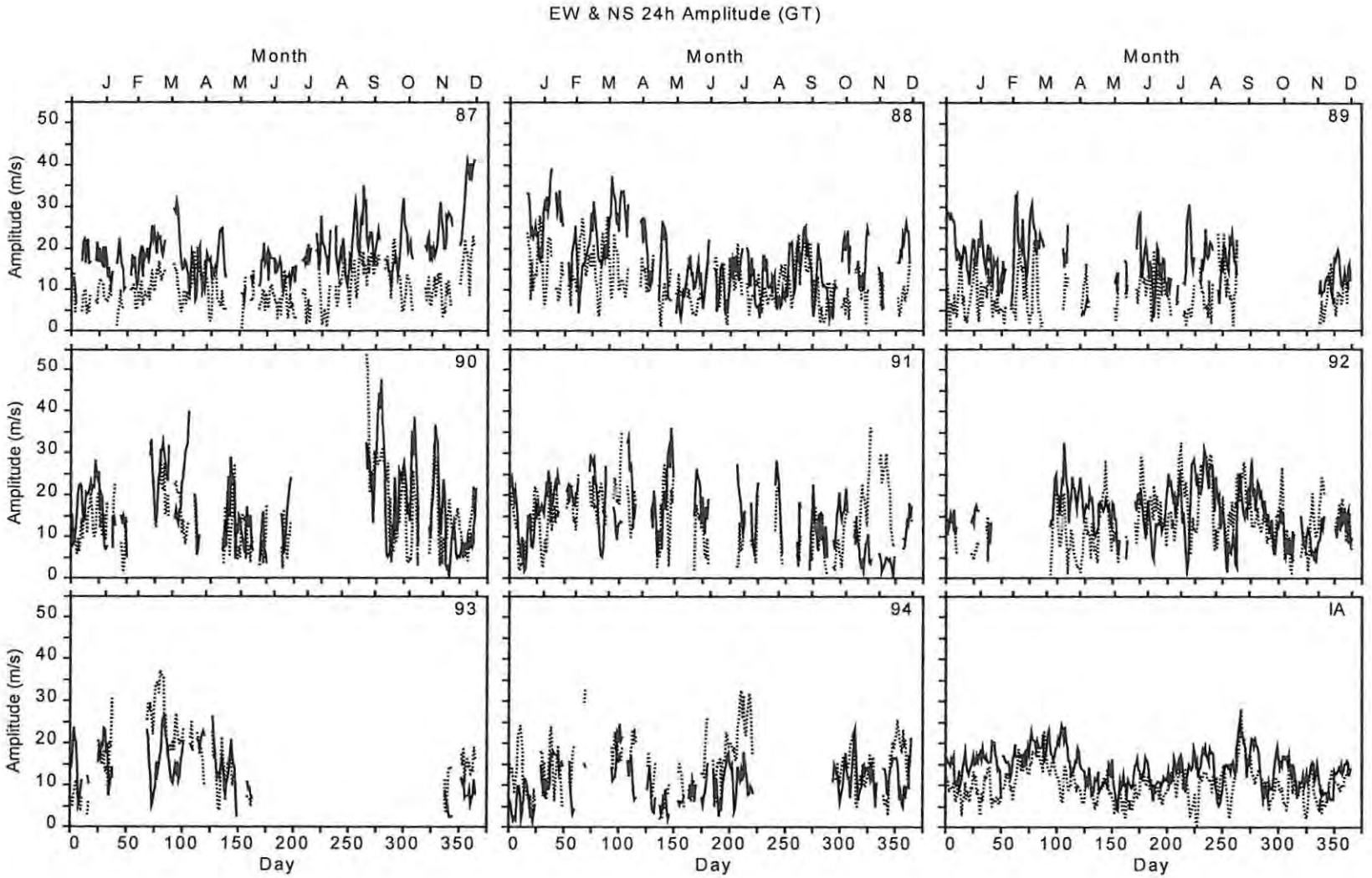

Figure 5.1 The zonal (solid line) and the meridional (dotted line) amplitudes of the diurnal tide for the years 1987-1994 and for the corresponding 8-year interannual average (IA) for Grahamstown. The year is indicated on the top right corner of each panel and the IA is similarly marked.

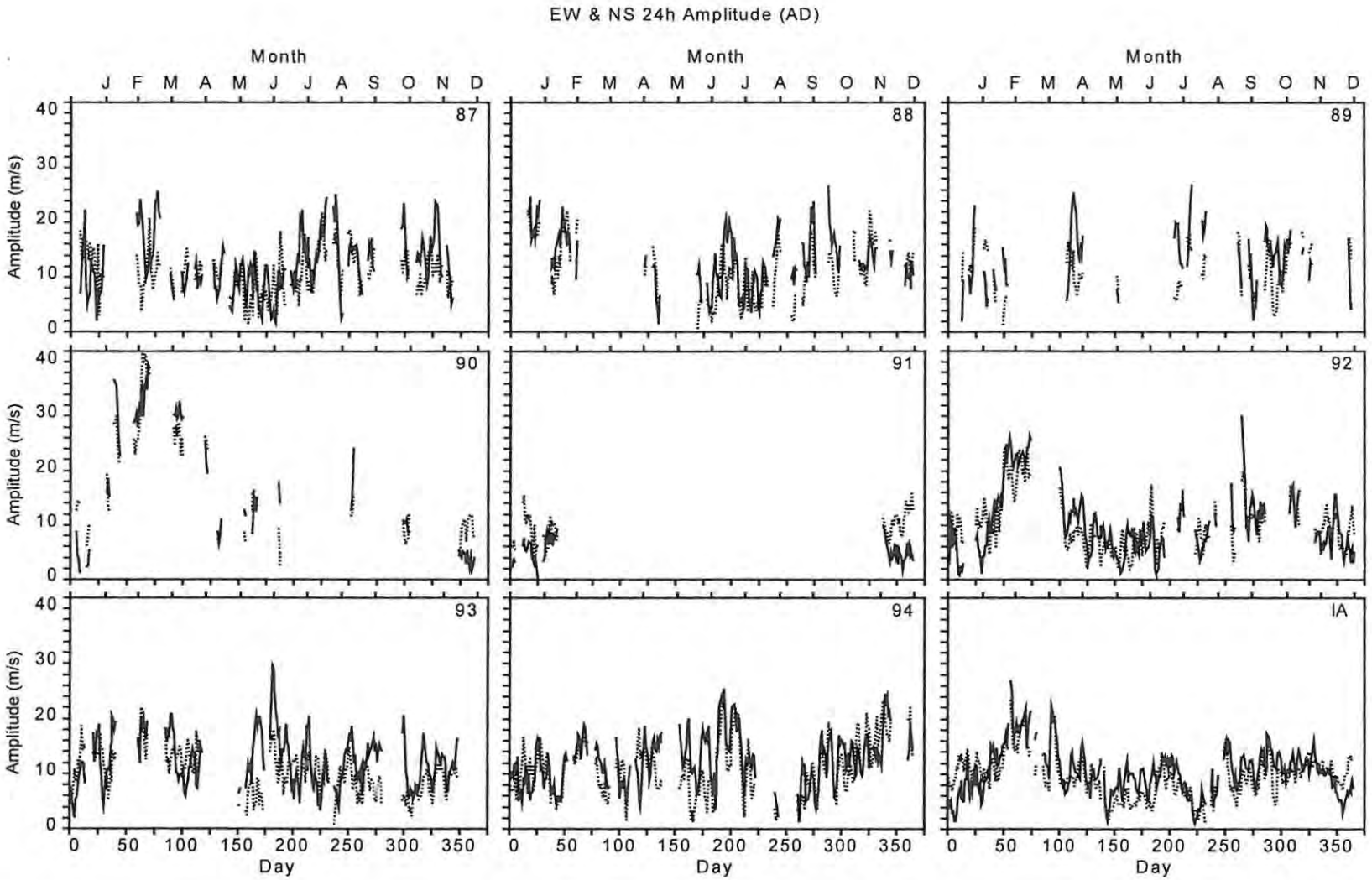

Figure 5.2 Same as **Figure 5.1** but for Adelaide.

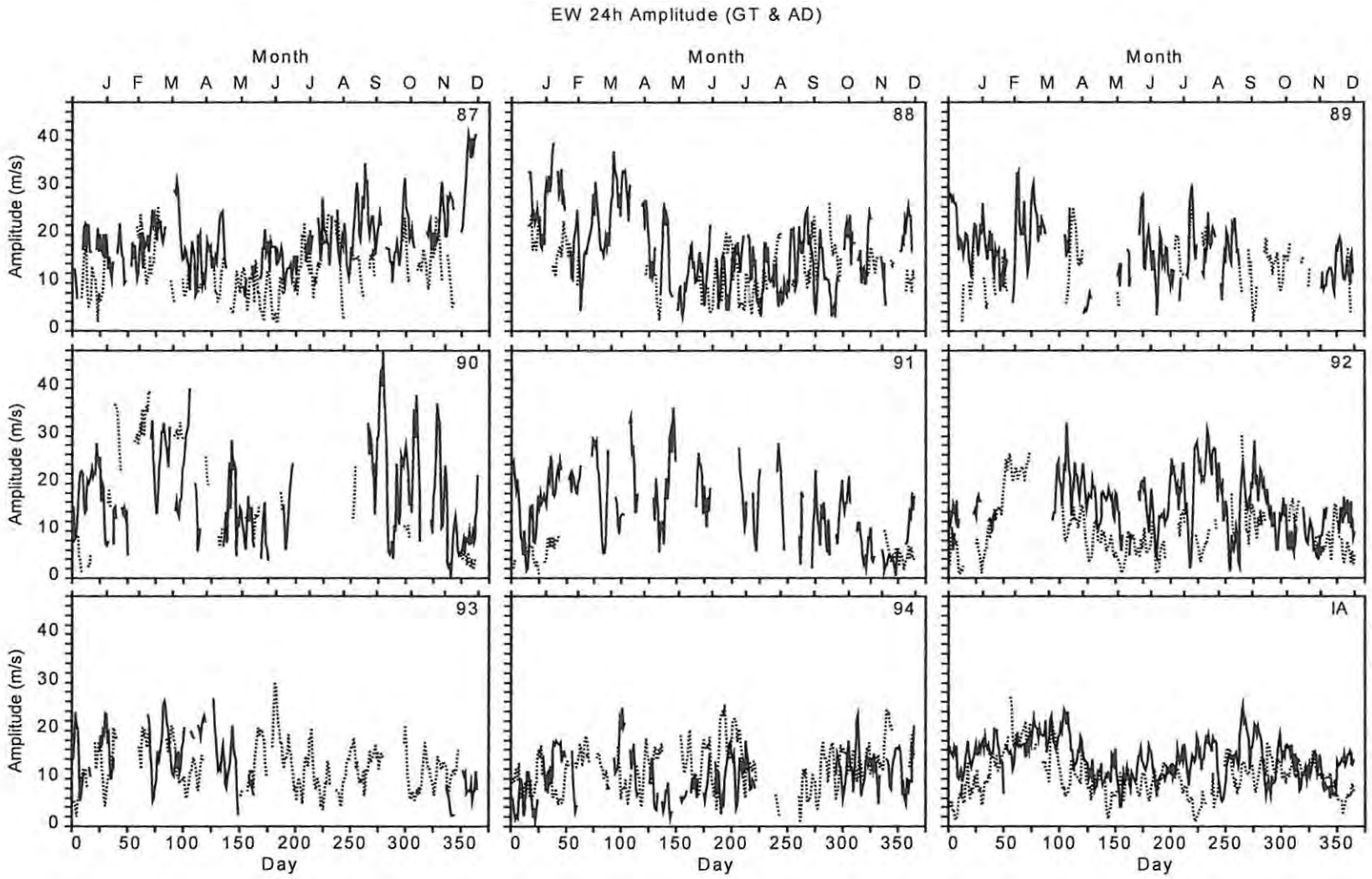

Figure 5.3 The zonal amplitudes of the diurnal tide at Grahamstown (solid line) and Adelaide (dotted line) for the years 1987-1994 and for the IA. The year is indicated on the top right corner of each panel and the IA is similarly marked.

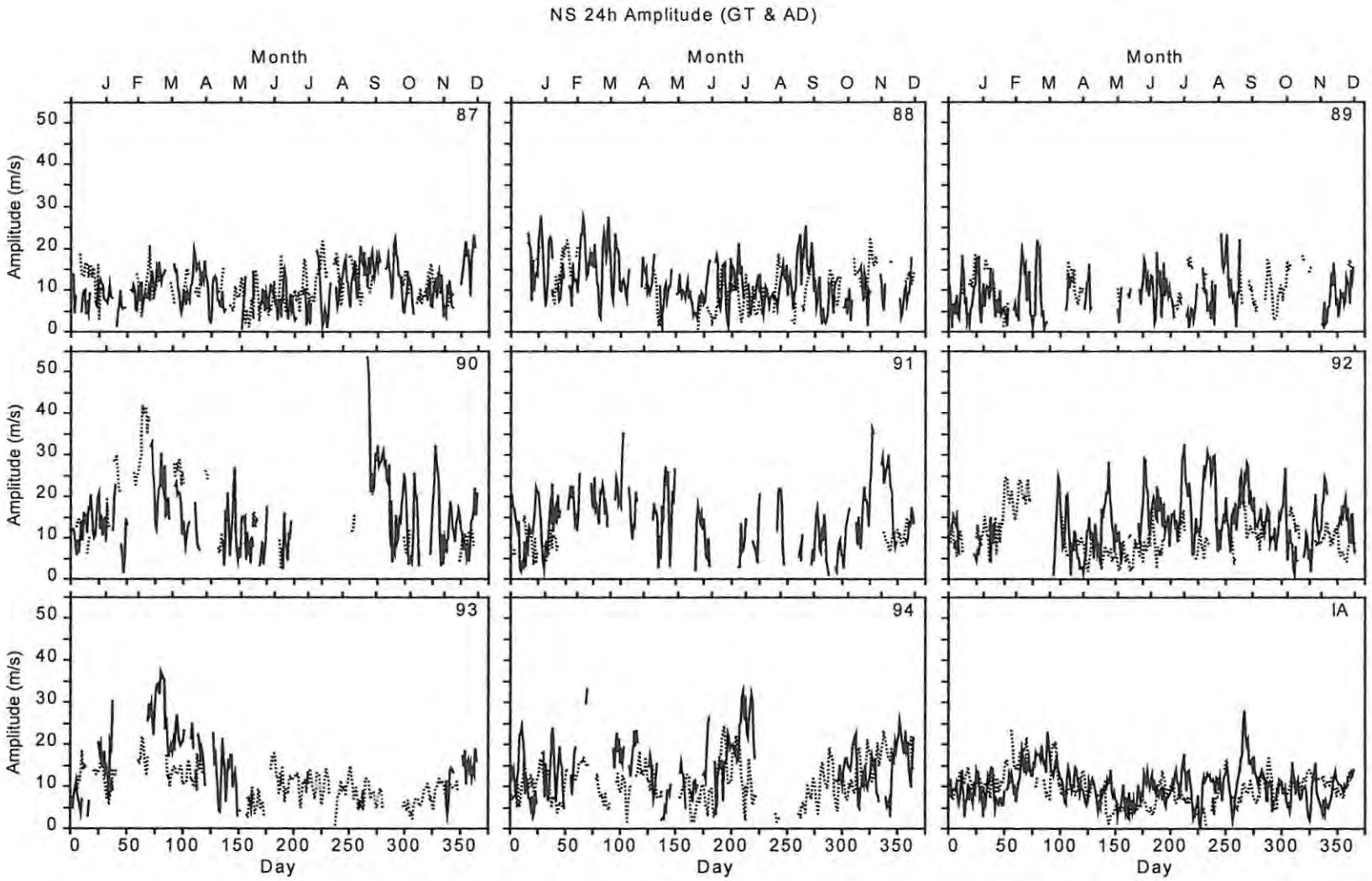

Figure 5.4 Same as **Figure 5.3** but for meridional amplitudes.

an equal weighting of one. The phase of a tide is the local solar time (LST) of the first maximum eastward (northward) for the zonal (meridional) component of the tide. For a 4-day interval there is some ambiguity in the phase as defined above and to maintain consistency, I have measured the phase with respect to the first odd-numbered day of the interval. As opposed to ignoring the data gaps of an *acceptable data window* as I did for the mean flow (Section 4.2.1), for the extraction of tidal components I have filled data gaps by some harmonic analysis procedure [*Pancheva*, private communication, 2000]. What I did essentially in this harmonic filling procedure was to first extract the amplitudes and phases of the 12-, 24- and the 48-h oscillatory components of the *acceptable data window* (with gaps) using a harmonic analysis. I then used these amplitudes and phases to estimate and fill the missing data points. After this I used harmonic analysis once again to extract the improved amplitudes and phases of the oscillatory components.

Starting with the diurnal tides, I focus on the variations of the zonal and meridional amplitudes at Grahamstown (Figure 5.1) and Adelaide (Figure 5.2). All IAs in this chapter have been computed by vector averaging (see Chapter 2, Section 2.3). These figures show long-term trends that are not clearly discernable and will be discussed in detail in Chapter 6. Superimposed on these long-term trends are short-term fluctuations of varying time scales. A direct comparison of the zonal amplitudes of Grahamstown and Adelaide is shown on Figure 5.3 and a similar comparison for the meridional comparison is illustrated on Figure 5.4. There is no obvious correlation in the short-term variations at Grahamstown to those at Adelaide.

I have also conducted a similar analysis for the semidiurnal tide and the figures that correspond to those of the diurnal tide are illustrated on Figure 5.5 to Figure 5.8. The short-tern variations which, in some instances, are indicative of planetary modulation that were observed in the diurnal tide can also be seen in both components of the semidiurnal tide at both sites. I also performed an analysis similar to that described in Chapter 4, Section 4.2.1 that used the semi-variogram, and the auto-correlation to study the persistence of the variations in the fluctuations of diurnal and semidiurnal tidal amplitudes. As this analysis does not yield any critical information other than something along the lines of the general comments made in the similar analysis in Chapter 4, the relevant figures have been omitted.

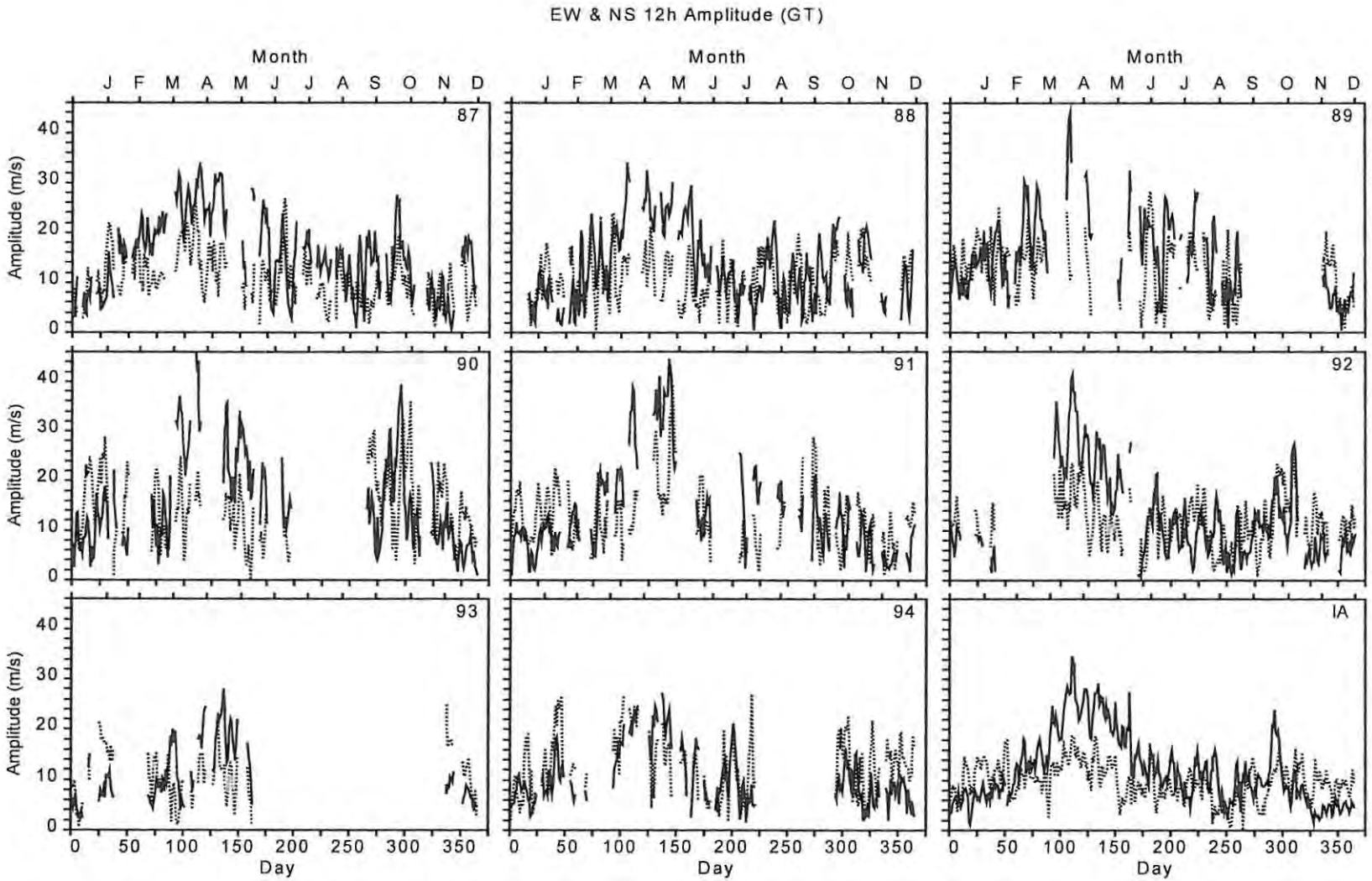

Figure 5.5 The zonal (solid line) and the meridional (dotted line) amplitudes of the semidiurnal tide for the years 1987-1994 and for the corresponding 8-year interannual average (IA) for Grahamstown. The year is indicated on the top right corner of each panel and the IA is similarly marked.

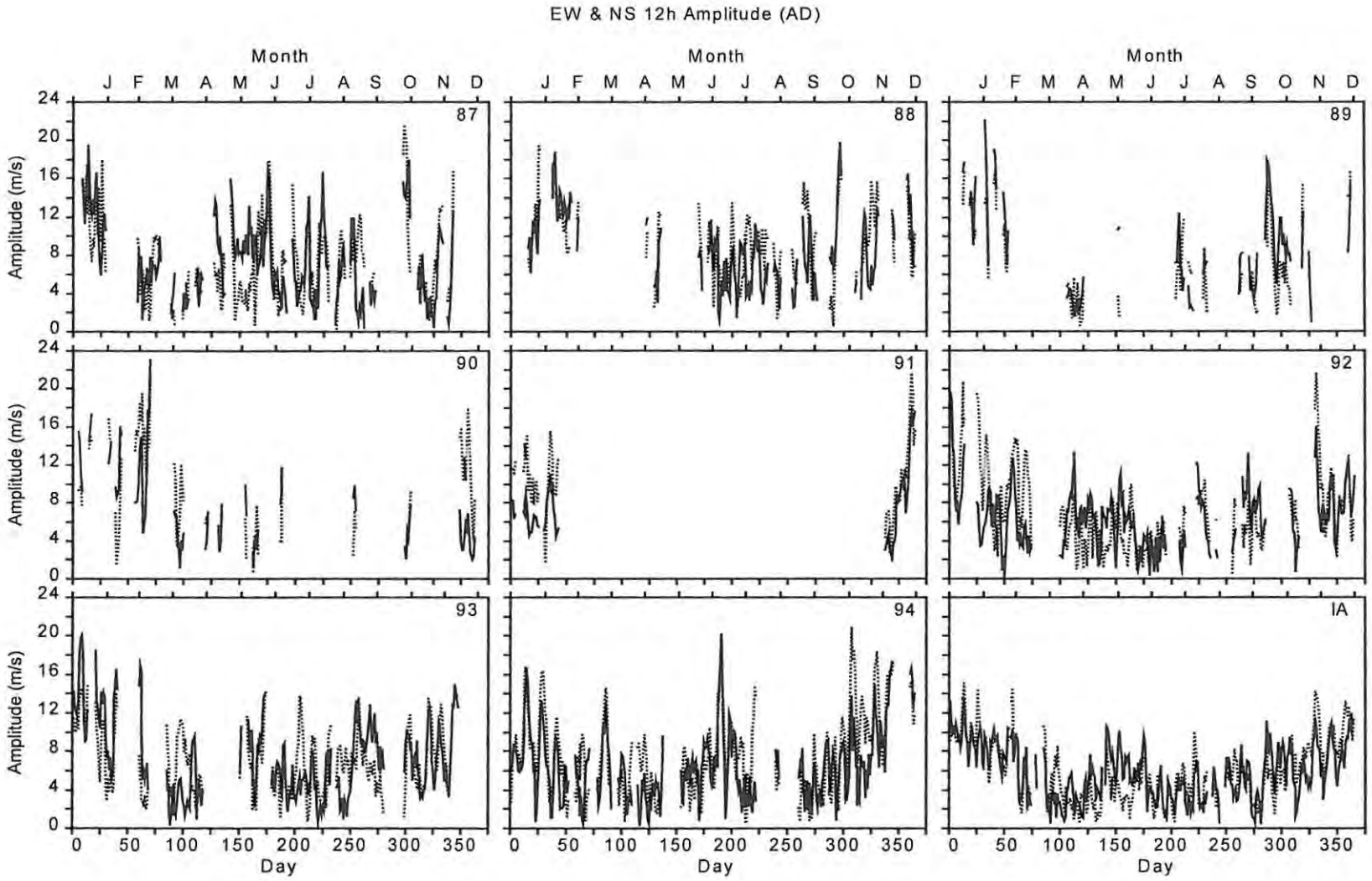

Figure 5.6 Same as **Figure 5.5** but for Adelaide.

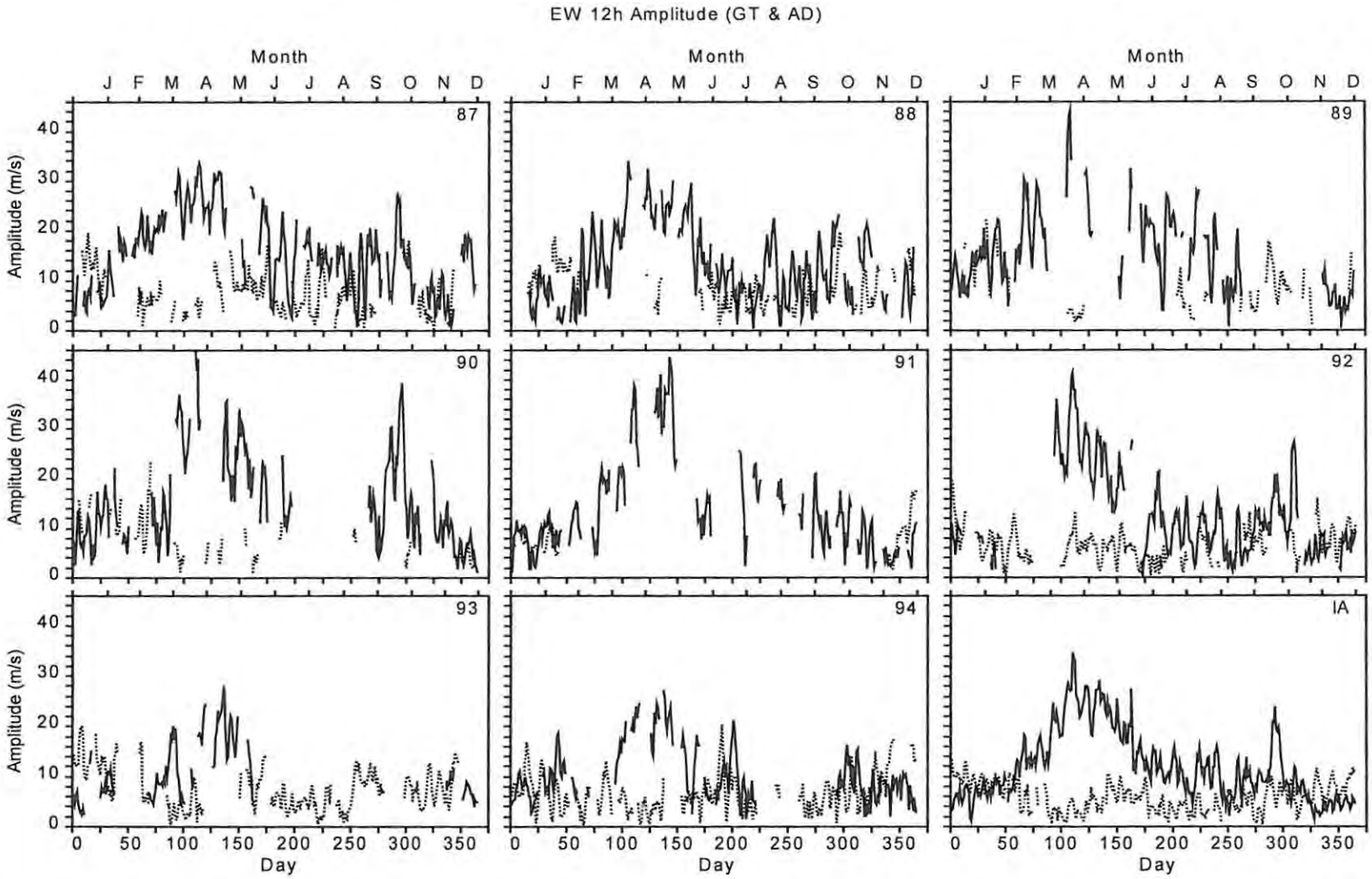

Figure 5.7 The zonal amplitudes of the semidiurnal tide at Grahamstown (solid line) and Adelaide (dotted line) for the years 1987-1994 and for the IA. The year is indicated on the top right corner of each panel and the IA is similarly marked.

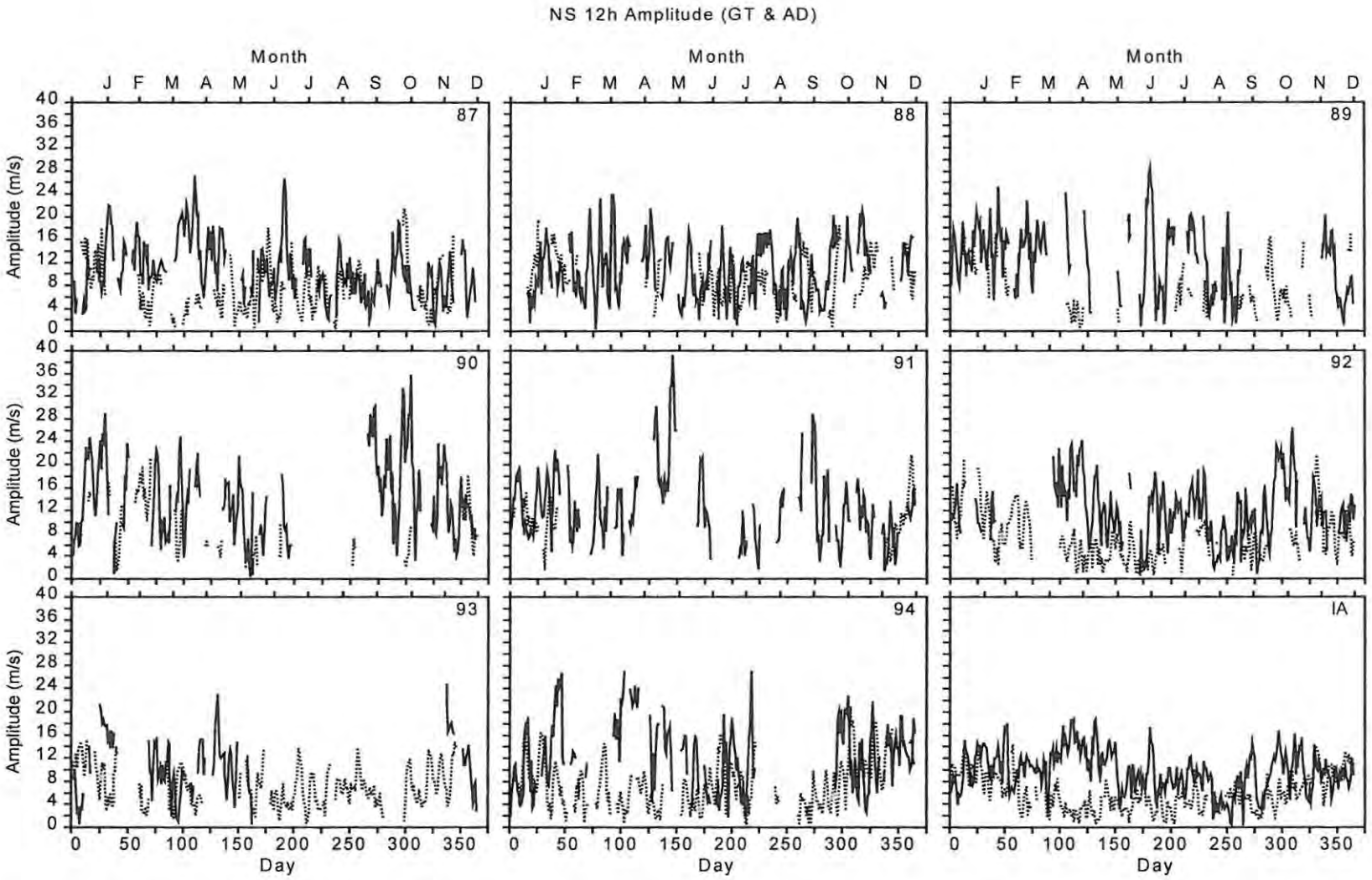

Figure 5.8 Same as **Figure 5.7** but for the meridional amplitudes.

In general, the results presented above indicate that both the amplitudes of the diurnal and the semidiurnal tides are characterised by short-term changes. A number of mechanisms have been suggested as possible causes of these short-term variations but, as mentioned in the introduction, the extent of the contribution of each of these is not known. The first mechanism involves the variation of tidal forcing due to the variations in water vapour, cloud cover [*Vial et al*, 1991] and ozone [*Bernard*, 1981]. The change in background propagations conditions is another possible cause. *Bernard* [1981] pointed out that classical theory indicates that tidal amplitudes and phases (in particular) are very sensitive propagation conditions. Rapid variation in the wind and temperature may result in partial tidal reflections. This is closely related to the assertion by *Poulter* [1980] that temperature discontinuities and negative temperature gradients cause a partial or total reflection of tidal modes. These reflected modes can, in turn, result in a change of the tidal structure through mode superposition, which, as indicated by *Forbes* [1990] and *Vial & Teitelbaum* [1984], can considerably change the tidal structure on a day-to-day basis even if the phase shifts between the modes are small (1-2 h). The third possible mechanism is the injection of energy near tidal frequencies due to local or synoptic scale fluctuations [*Vial et al.*, 1991]. The fourth mechanism, is the non-linear interaction of planetary waves and tides (e.g. *Teitelbaum & Vial* [1991]; *Clark & Bergin* [1997]; *Kamalabadi et al.* [1997]; *Beard et al.* [1999] and *Pancheva* [2000]) and will be discussed in more detail in Section 5.5.

The last possible mechanism involves gravity wave-tidal interactions, which have been investigated by various authors (e.g. *Walterscheid* [1981], *Fritts & Vincent* [1987], *Forbes et al.* [1991], *Wang & Fritts* [1991], *Lu & Fritts* [1993]). Upward propagating gravity waves encounter a total wind field that consists of the mean flow (see Chapter 4) and tidal wind and is therefore temporal. *Fritts & Vincent* [1987] developed a model to investigate the effects of the different environments on the propagation and saturation of high-frequency (period < 1 h) gravity waves. Their model predicts that in an environment where $\bar{u}$-c increases with height the gravity wave amplitude and the momentum flux should also increase. At the region where the above growth stops, a large momentum flux divergence and the acceleration of the mean flow are expected. These authors, found that this tidally linked mean flow acceleration generates a nontidal (i.e. not thermotidally excited) 'tide' with a phase advance of ~6 h compared to the thermal tide. As a result of this 'tide' the apparent tide is advanced in phase and its amplitude is altered compared to the thermal tide [*Fritts & Vincent*, 1987].

While there is agreement on the phase advance, different views have been expressed regarding amplitude alterations. Contrary to the amplitude reduction suggested by *Fritts & Vincent* [1987], analytic model results by *Lu & Fritts* [1993] predict an enhancement of apparent tidal amplitudes although these results were sensitive to other factors which were not investigated in detail. By conducting different calculations *Lu & Fritts* [1993] concluded that the gravity wave forcing of tides may be very variable and is dependent on the tidal environment and the characteristics of the gravity wave spectrum being modulated. These authors also concluded that whether gravity wave forcing results in amplitude decreases (e.g. *Fritts & Vincent* [1987], *Forbes et al.* [1991]) or increases (e.g. *Wang & Fritts* [1991] and their study) depend on the details of the tidally modulated filtering of gravity waves. In fact *Walterscheid* [1981] mentions that the strength of such forcing depends on the intensities, phase velocities and the coherence of these waves and may exhibit substantial day-to-day variability. As a result of this, the induced nontidal component will be variable and not purely periodic. Therefore, attempts to fit sinusoids on consecutive days of data affected by these wave induced accelerations will result in the extracted tidal amplitudes and phases being similarly variable [*Walterscheid*, 1981].

5.3 SPECTRAL AND MULTI-RESOLUTION ANALYSIS OF TIDES

Figure 5.9 and Figure 5.10 show the short-term variation of the amplitude of the diurnal tide during the years 1987 and 1988 and the corresponding spectral components for Grahamstown and Adelaide, respectively. These figures show that for the 2-20 day period range, the strong spectral components have periods of ~10 days while the others have periods that can be associated with the 16-day wave (i.e. ~12-20 day period range). The meridional amplitudes at Adelaide are particularly dominated by the 16-day oscillation even though the corresponding spectral power is small making the accuracy of this observation doubtful. As was the case with the mean flow (Chapter 4, Section 4.2.3), the occurrence of the planetary activity is not necessarily correlated between the zonal and the meridional component at both sites.

Figure 5.11 and Figure 5.12 reveal a more detailed structure of the planetary scale variation of the diurnal tidal amplitudes. The spectra of the details at different levels show that there are spectral components with periods of ~2-3 days, ~7-8 days, ~10 day and ~16-20 days. Although

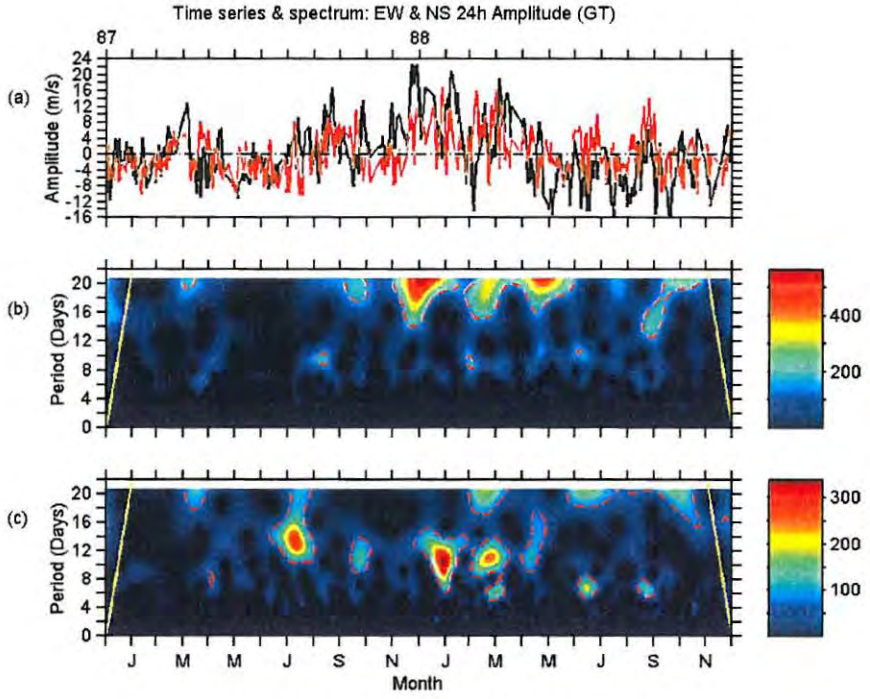

Figure 5.9 The amplitude of the diurnal tide at Grahamstown and its spectra. (a) The zonal (black line) and the meridional (red line) amplitude. (b) The wavelet spectrum of the zonal amplitudes. (c) The wavelet spectrum of the meridional amplitudes. Colour bars are in arbitrary units.

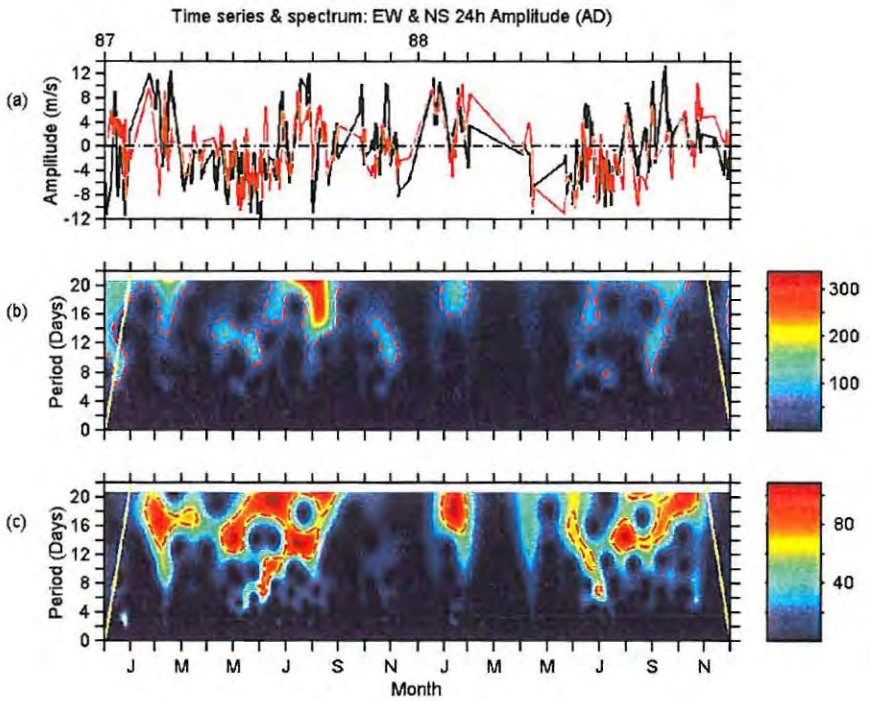

Figure 5.10 Same as **Figure 5.9** but for Adelaide.

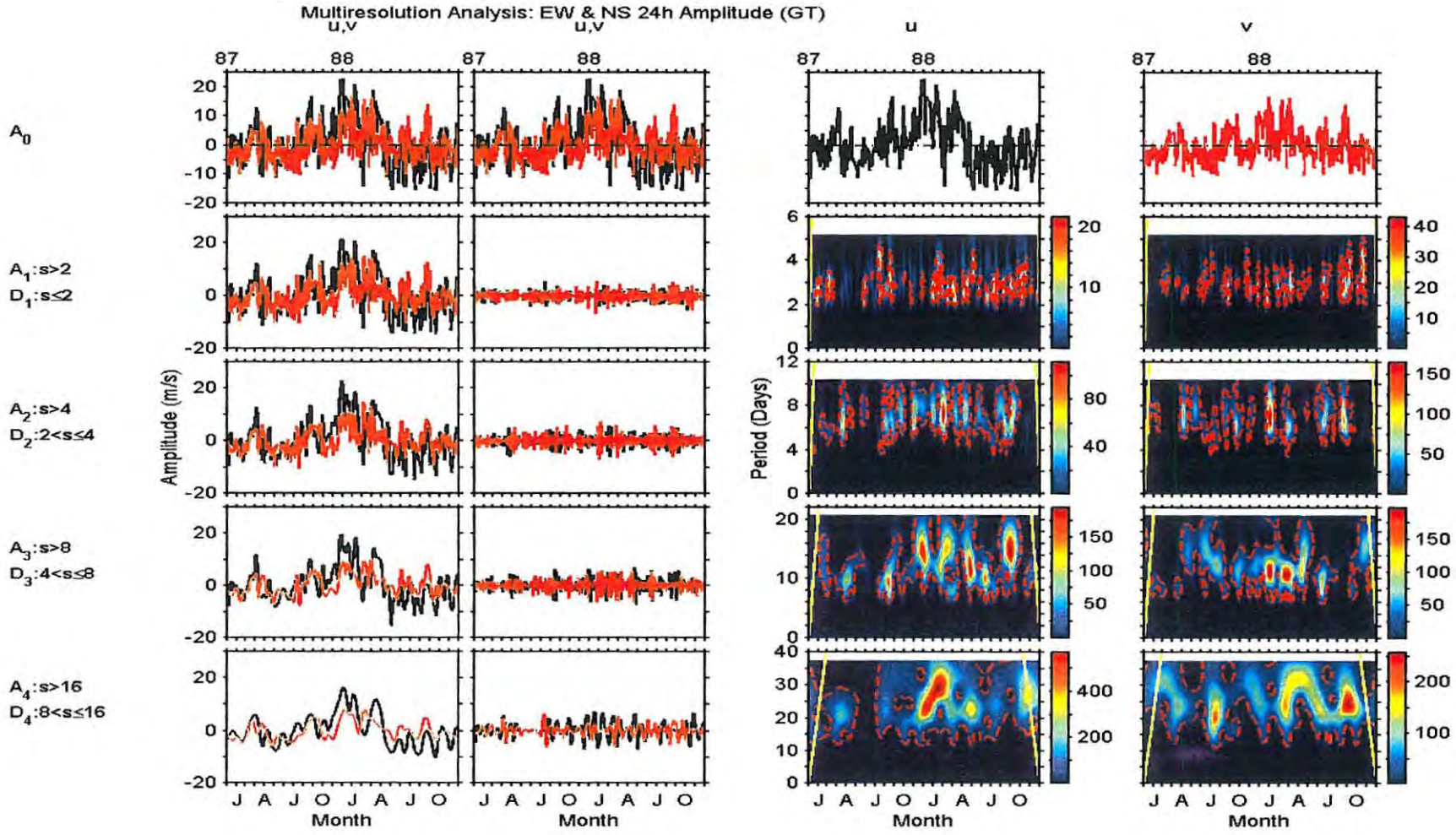

Figure 5.11 For the diurnal tide at Grahamstown: The original signal A_0 (top row). For rows 2-5 and starting from the left, I have (1st column) the *approximations* (A_m where m is the level), (2nd column) the *details* (D_m), (3rd column) the spectrum of the zonal details and (4th column) the spectrum of the meridional details. The black and red time series lines represent the zonal (u) and meridional (v) amplitudes respectively. The scale (s) ranges are shown and the units of the colour bars are arbitrary.

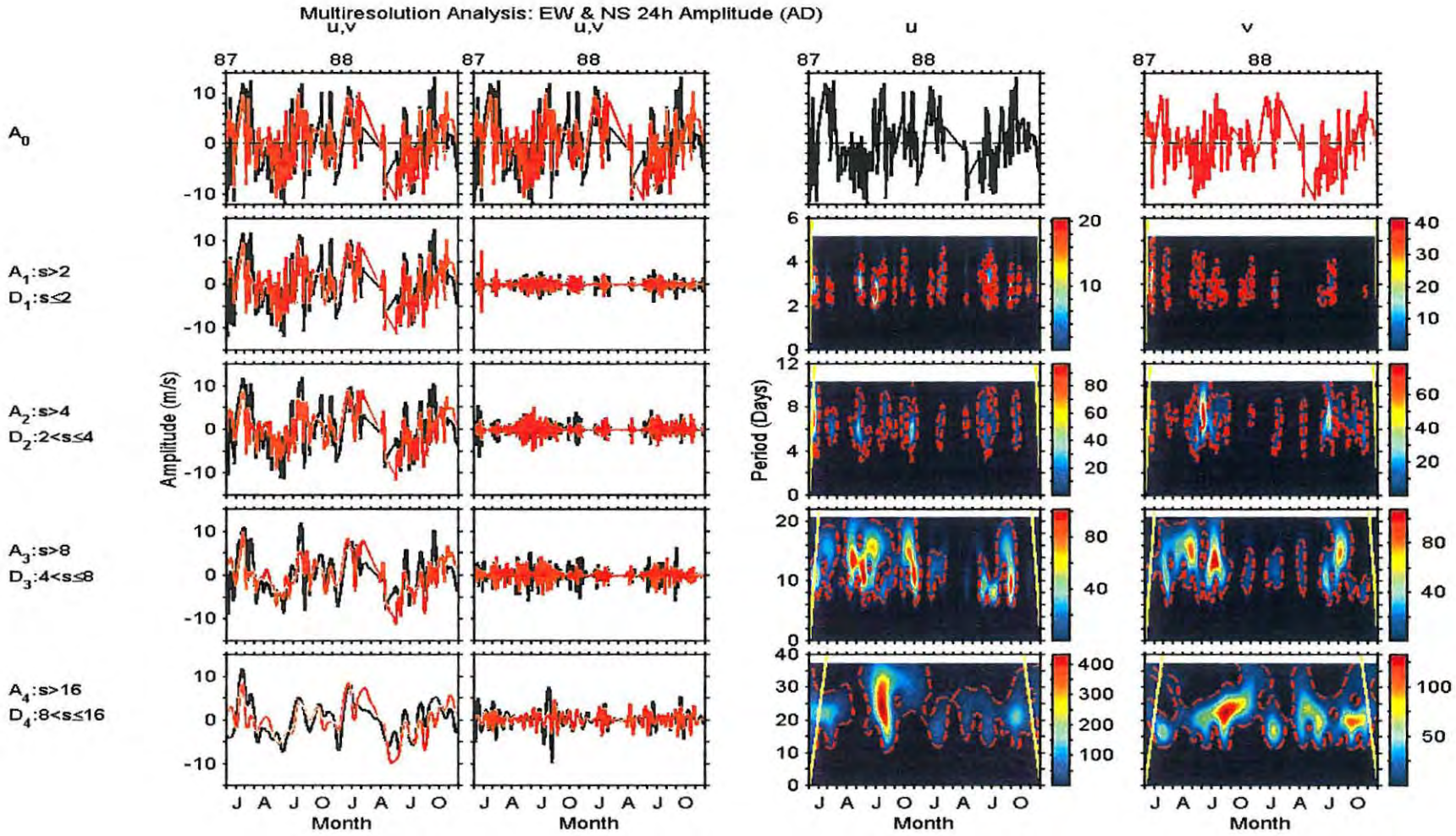

Figure 5.12 Same as **Figure 5.11** but for Adelaide.

the strongest components at both sites have periods >20 days, my focus is on those planetary scale components with periods of ~2-20 days and no further comment will be made in relation to the former components in this thesis. In the ~2-20-day period range the dominant components are those associated with 16-day wave and those with periods of ~10 days. In general, Grahamstown tends to have stronger planetary spectral components than Adelaide and there is no apparent correlation in the planetary activity between the two sites indicating that the horizontal extent of the planetary waves is shorter than the distance between the two sites. The spectra of the details also emphasize the fact alluded to earlier that the zonal planetary activity is not necessarily correlated to its meridional counterpart. As this is similar to the observation made in the case of the mean flow, one is led to believe that some of the reasons advanced in Chapter 4, Section 4.2.3 for the lack of such correlation could possibly apply here also.

Coming to the semidiurnal tide, I have plotted the short-term variations and the corresponding spectra in Figure 5.13 and Figure 5.14. The multiresolution analysis of the semidiurnal tide is shown in Figure 5.15 and Figure 5.16. From all the figures, one can see most of the features that were observed in relation to the diurnal tide. Considering both tides, we observe that in general there is a strong showing of the 16-day wave in the short-term variations of tidal amplitudes. We will recall that this periodicity was also found to dominate the planetary scale spectrum of the mean flow (Section 4.2.2 and 4.2.3). A question that comes to mind is whether the 16-day oscillation in the tidal amplitudes is related to that in the mean flow or not. Such a link seems possible if we consider gravity wave-mean flow interactions in conjunction with gravity wave-tidal interactions. As discussed in Section 4.2.3 there is a possibility of a 16-day selective transmissivity of gravity waves due to the 16-day modulation of the mean flow. Such a situation can result in similar periodicity in the gravity wave-tidal interactions described in Section 5.2. If this is the case, some correlation in the mean flow 16-day wave and the tidal 16-day wave might be possible. However, a comparison of similar figures for the tides and mean flow reported in this thesis (e.g. Figure 4.10/Figure 5.9/Figure 5.13, Figure 4.12/Figure 5.11/Figure 5.15) does not show obvious correlation between the mean flow and the tidal 16-day waves nor is there any apparent correlation in the 16-day wave of the diurnal tide to that of the semidiurnal tide. However, future and more detailed analysis of the possible link between the mean flow and tidal 16-day waves is needed before any firm conclusion about this matter can be made. For now, I will simply concentrate on the tidal amplitude short-term variations.

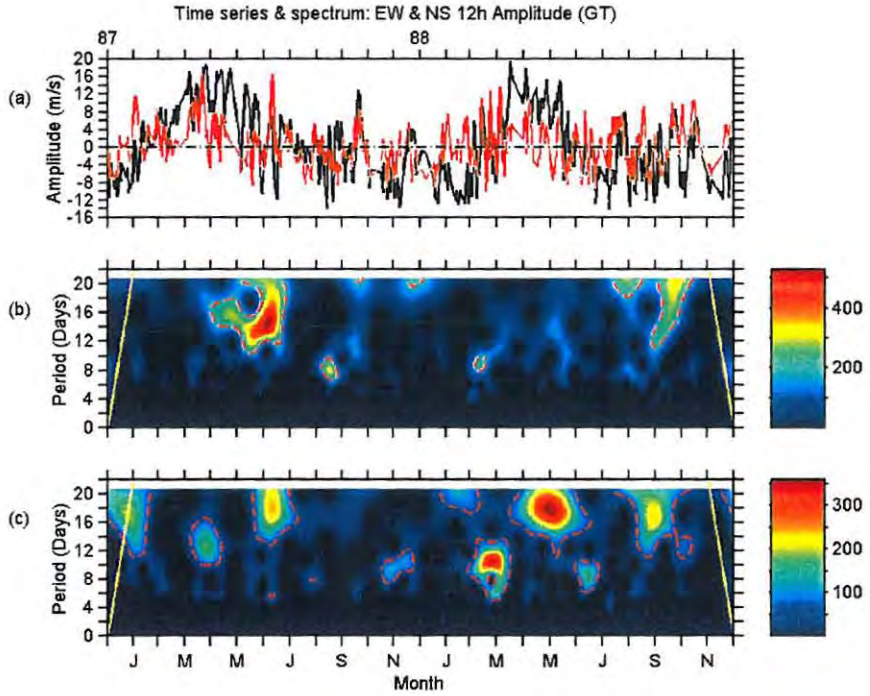

Figure 5.13 The amplitude of the semidiurnal tide at Grahamstown and its spectra. (a) The zonal (black line) and the meridional (red line) amplitude. (b) The wavelet spectrum of the zonal amplitudes. (c) The wavelet spectrum of the meridional amplitudes.

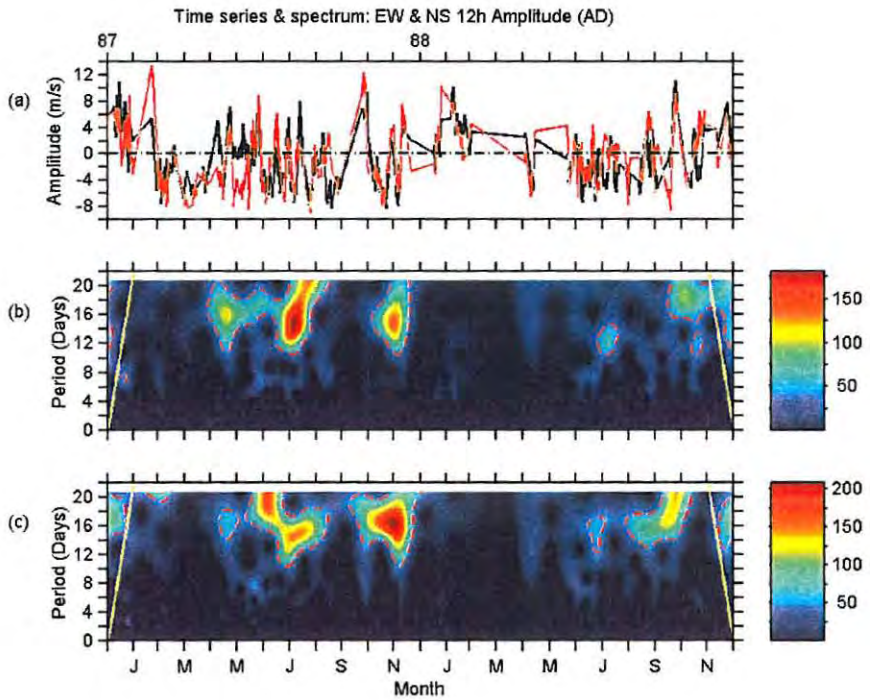

Figure 5.14 Same as **Figure 5.13** but for Adelaide.

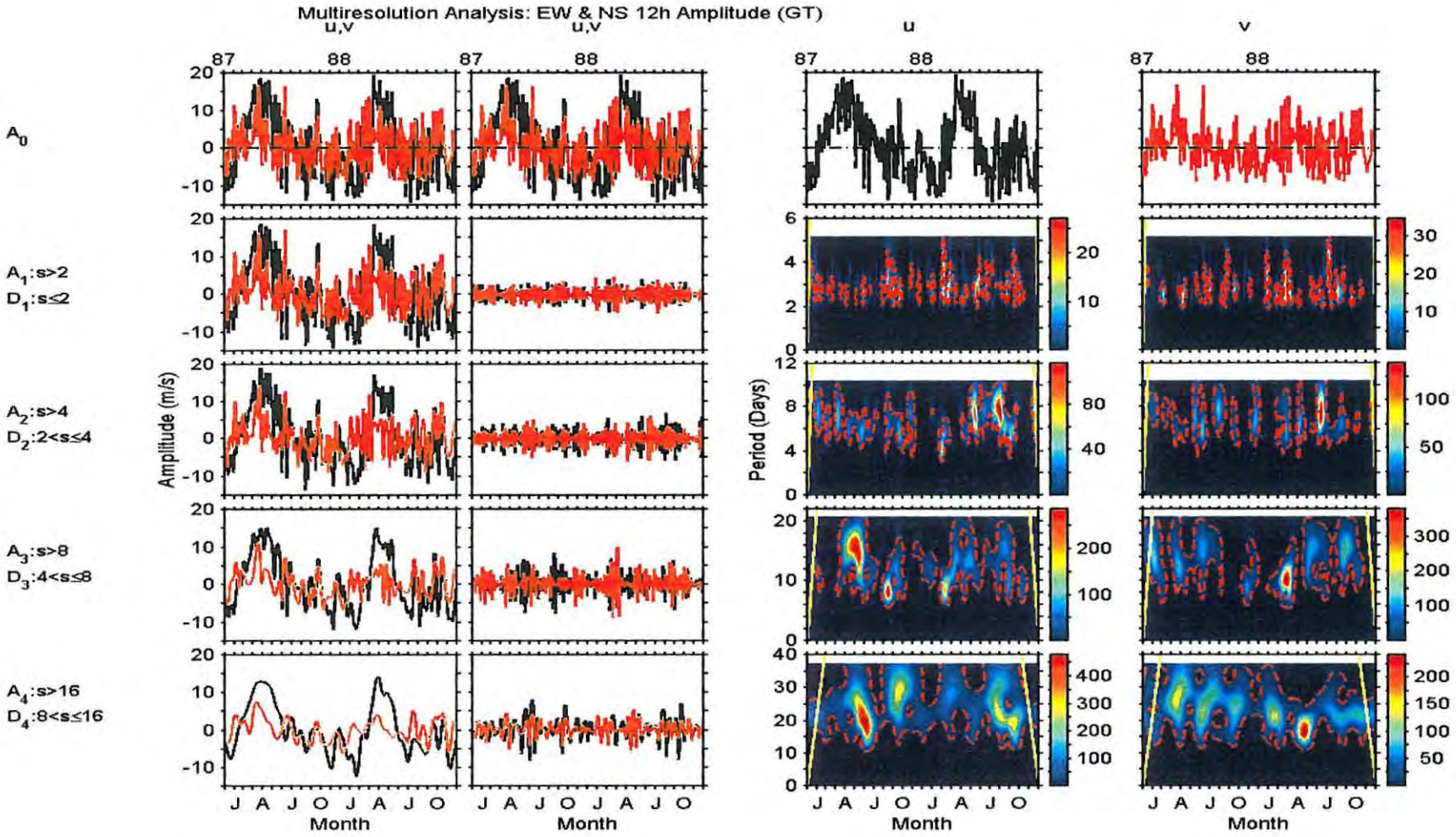

Figure 5.15 For the semidiurnal tide at Grahamstown: The original signal A_0 (top row). For rows 2-5 and starting from the left, I have (1st column) the *approximations* (A_m where m is the level), (2nd column) the *details* (D_m), (3rd column) the spectrum of the zonal details and (4th column) the spectrum of the meridional details. The black and red time series lines represent the zonal (u) and meridional (v) amplitudes respectively. The scale (s) ranges are shown and the units of the colour bars are arbitrary.

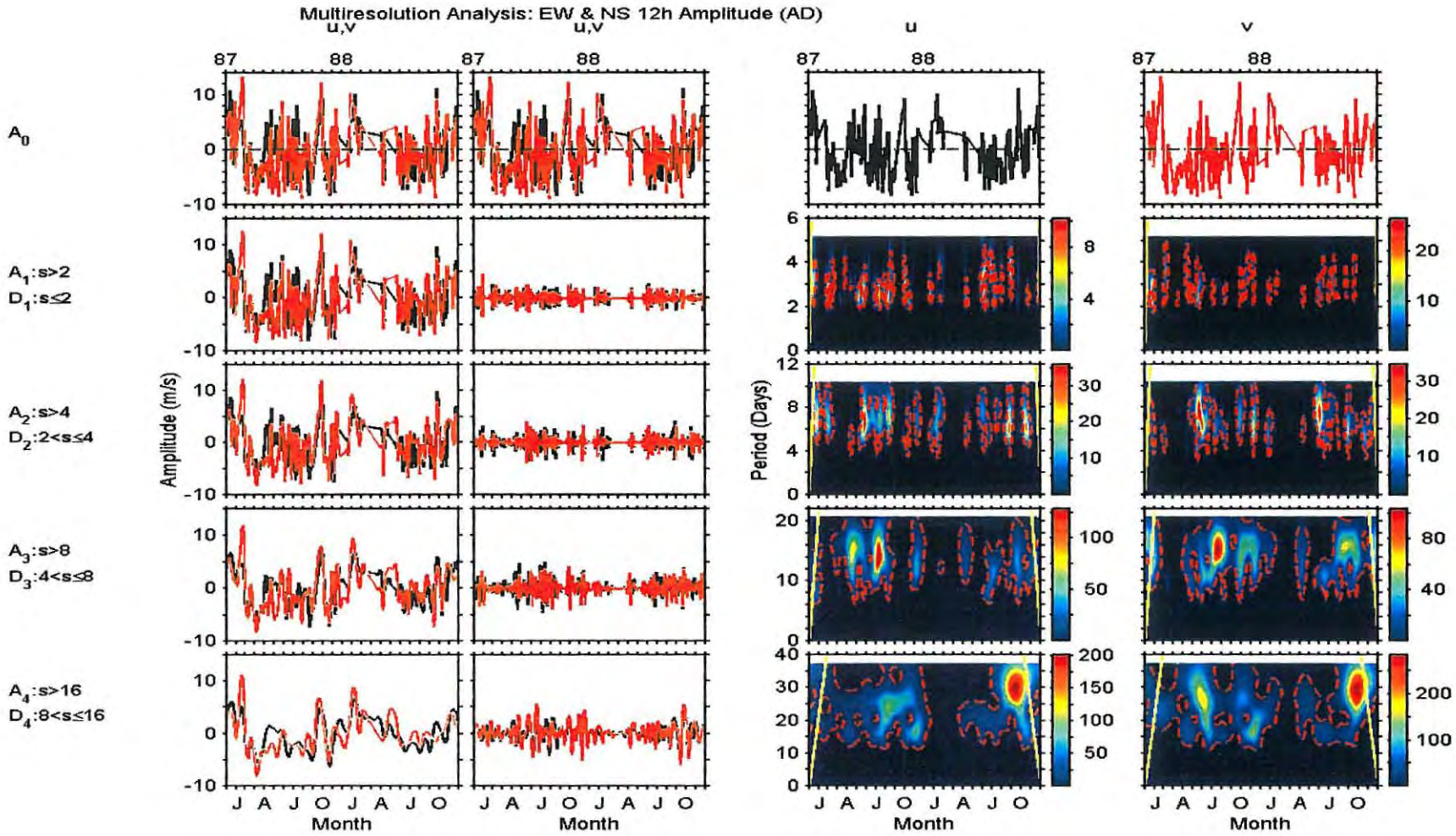

Figure 5.16 Same as **Figure 5.15** but for Adelaide.

5.4 INSTANTANEOUS AMPLITUDE AND PERIOD/PHASE VARIATIONS

In this section, I will conduct a more detailed analysis of the amplitudes using hourly amplitudes as opposed to the 4-day amplitudes used in the previous section. In addition, I have also calculated instantaneous tidal periods. I have specifically considered the meridional hourly values for three intervals from 1 June to 12 July 1987 (Case 1), 1 July to 11 August 1987 (Case 2) and 1 August to 11 September 1987 (Case 3). These 42-day long intervals were especially chosen because they help us understand certain atmospheric features especially when it comes to non-linear interactions (Section 5.5). Data gaps in this section and the one that follows have not been given any special treatment and are merely assumed to have velocities of 0 ms^{-1}. This is not expected to seriously affect the results because the data gaps for all the three cases are few and not very long.

For my investigation, I have used the complex demodulation method (Chapter 2, Section 2.4). This method is capable of giving the instantaneous amplitude (A_t) and "phase" (ψ_t) at every data point of the series being analysed. For Case 1, I have illustrated the instantaneous amplitude and phase in Figure 5.17(b) and (c), respectively. We will recall that the slope of the "phase" is equal to (ω_d-ω_0) where ω_d and ω_0 are the angular frequencies of demodulation and that of the dominant component within the bandpass used in the demodulation process, respectively. Therefore, I can use this slope to get the instantaneous period at every data point except at the end points of the series because I need at least two points to calculate the slope. In this analysis I have used demodulation periods of 24 h and 12 h in order to be able to analyse the dominant component around these tidal periods. I have used a symmetric band-pass filter with a centre frequency of 0 cpd and a bandpass range of –0.2 to 0.2 cpd. We see in Figure 5.17 that the instantaneous amplitudes for Case 1 show variation that is sometimes oscillatory with periods of several days. There is no correlation between the diurnal and the semidiurnal amplitude variations as also mentioned in the previous section. If the amplitude variations are indeed due to transient source variations, the lack of correlation between the diurnal and the semidiurnal changes is due to the fact that the two tides respond differently to various forcing mechanisms.

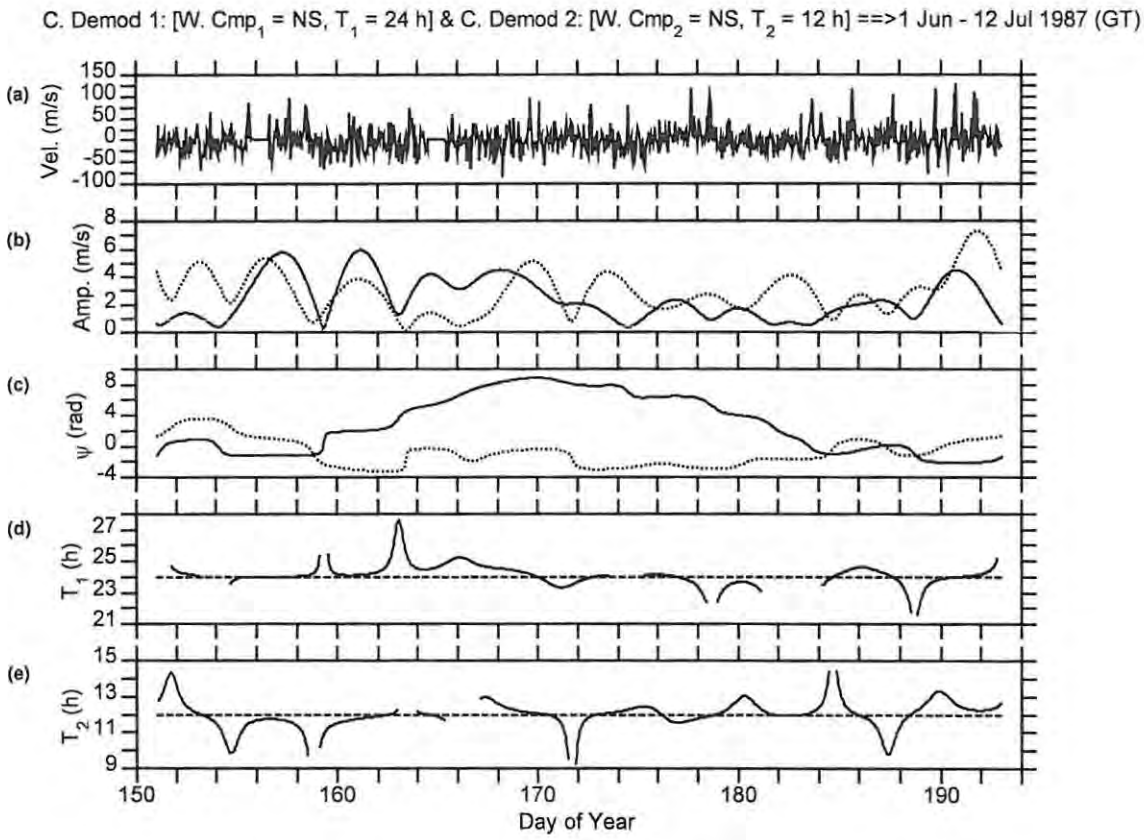

Figure 5.17 Complex demodulation analysis for 1 June to 12 July 1987 (Case 1). (a) The mean corrected meridional velocity. (b) The instantaneous amplitudes (A) of the diurnal demodulation (solid line) and the semidiurnal demodulation (dotted line). (c) The instantaneous phase (ψ) of the diurnal demodulation (solid line) and the semidiurnal demodulation (dotted line). (d) The instantaneous period (T_1) for the diurnal demodulation. (e) The instantaneous period (T_2) for the semidiurnal demodulation.

I deduced the instantaneous periods of the dominant components near tidal periods and these are shown in Figure 5.17(d) and (e). In this analysis, I have calculated periods for cases where the instantaneous amplitude is at least 1 ms^{-1} and hence the gaps in the period plots. Periods corresponding to amplitudes below 1 ms^{-1} tend give large period deviations. Even with this cut-off there are still periods that should be treated cautiously as they correspond to relatively small amplitudes. In general, we observe that there is also a variation in the period of the dominant components near tidal periods. The statistics of the periods are shown in Figure 5.18 and Figure 5.19 for the diurnal and the semidiurnal demodulations, respectively. Each histogram bin is 30

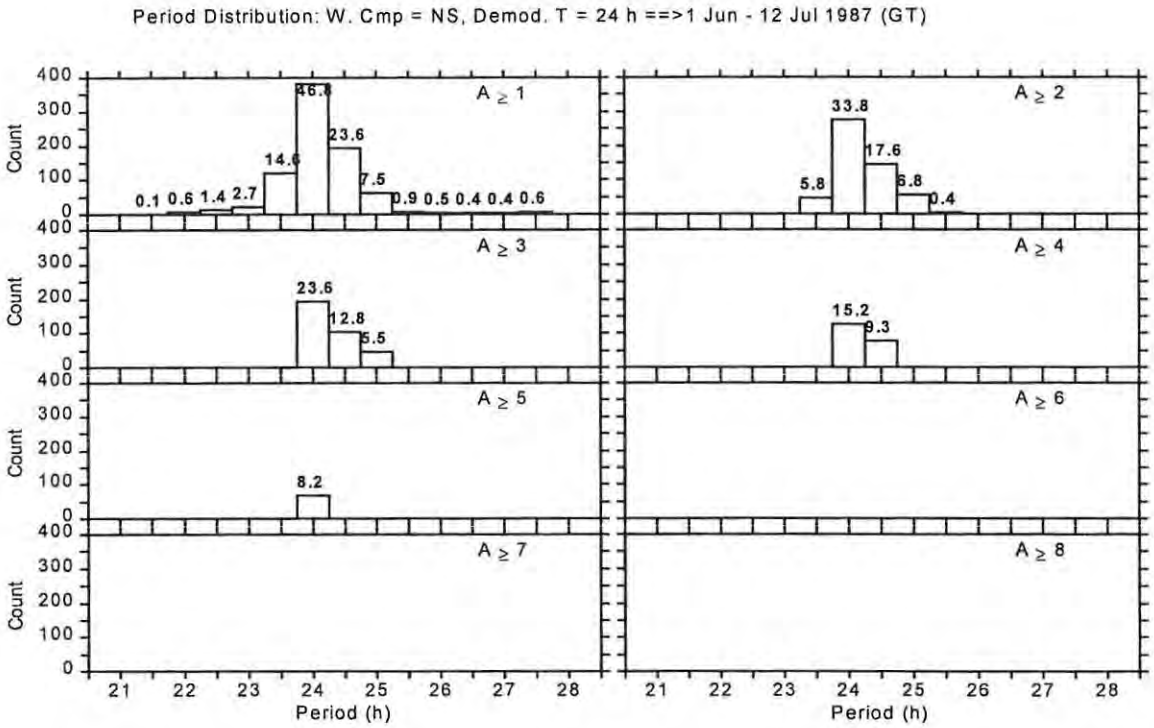

Figure 5.18 For Case 1. The distribution of instantaneous periods for the demodulation period T = 24 h for different amplitude (A) cut-off values in ms^{-1}. The percentage contribution to all periods in indicated next to each bin.

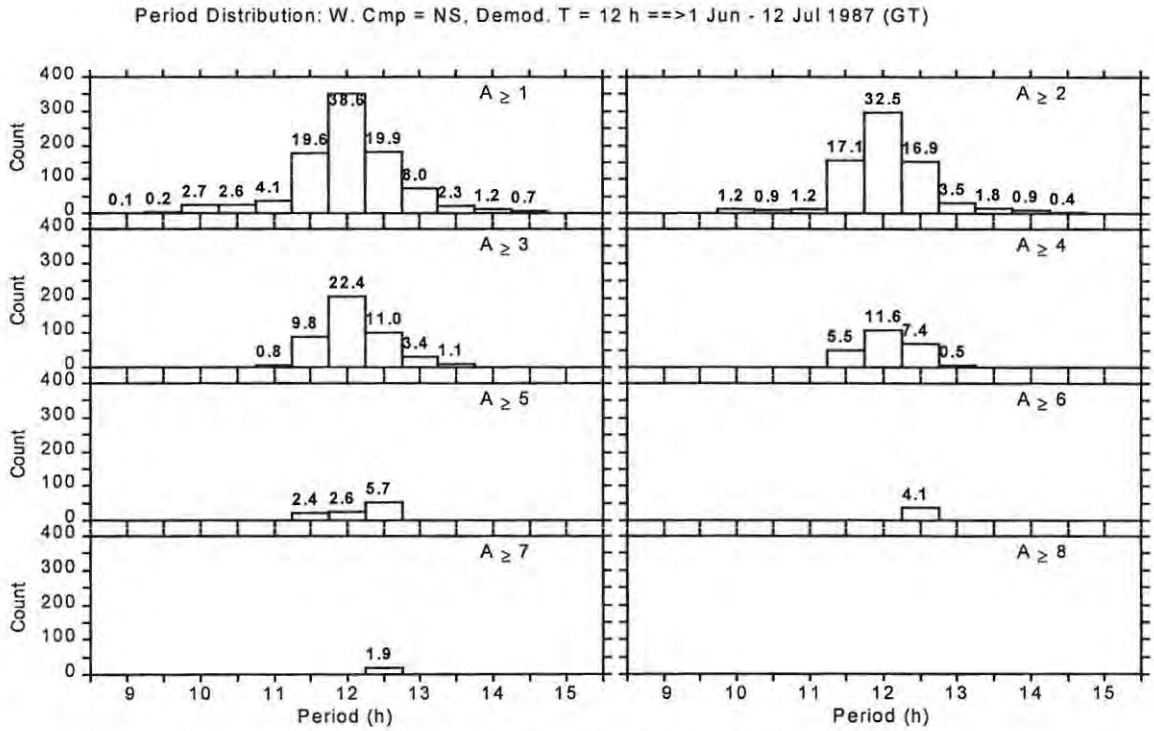

Figure 5.19 Same as Figure 5.18 but for a demodulation period of 12 h.

minutes wide and the percentage contribution of each bin to *all* the instantaneous periods considered (i.e. those meeting the above amplitude cut-off) is indicated near the relevant bin.

For the diurnal demodulation (Figure 5.18) we observe that the 24 h period is the most frequent for all amplitude cut-offs. But, at the same, this period accounts for less than 50 % of all periods. The period spread ranges from ~22 h to ~27 h. As the amplitude cut-off increases, the period converge to 24 h but even at the 4 ms^{-1} cut-off at least 9 % of the periods are different (~24.5 h) from the tidal period. The semidiurnal demodulation periods (Figure 5.19) show similar features to those of the diurnal demodulation but, in this instance, the periods interestingly converge to ~12.5 h with increasing amplitude cut-off. For Cases 2 and 3, we observe similar features to those in Case 1: there is variation of amplitudes and periods with time (Figure 5.20 and Figure 5.21); the tidal periods (24 and 12 h) are the most frequent and contribute ~35-40 % of all periods; there is a period spread that converges to tidal frequencies with increasing amplitude cut-off except for the diurnal tide in Case 3 (Figure 5.24).

Basically these results show amplitude modulation and frequency variations. One possible source of these variations is the transient modification of the source and the associated injection of energy near tidal frequencies. *Vial et al.* [1991] used a time-dependent numerical model to investigate the influence of the transient forcing on the tidal mode structure. This transience in tidal excitation could be due to factors like the variation in water vapour densities, cloud cover and ozone concentrations [*Vial et al.*, 1991] over time scales that are similar to those of the planetary oscillations observed in Section 5.3. For instance, some of these variations can be of the order of about 20 % at mid-latitudes (see *Vial et al.* [1991] for a relevant reference source). The variation in water vapour and cloud cover is expected to significantly affect the diurnal tide while the variation in ozone concentration is expected to have greater impact on the semidiurnal tide [*Vial et al.*, 1991].

More specifically, the model results presented by *Vial et al.* [1991] show that the transient modification of tidal excitation results in the oscillation of the wind amplitudes of tidal modes about some steady state values. These amplitude oscillations tend to decay (in some cases exponentially) to the steady state value. For the (1, 1) modes this steady state value is reached

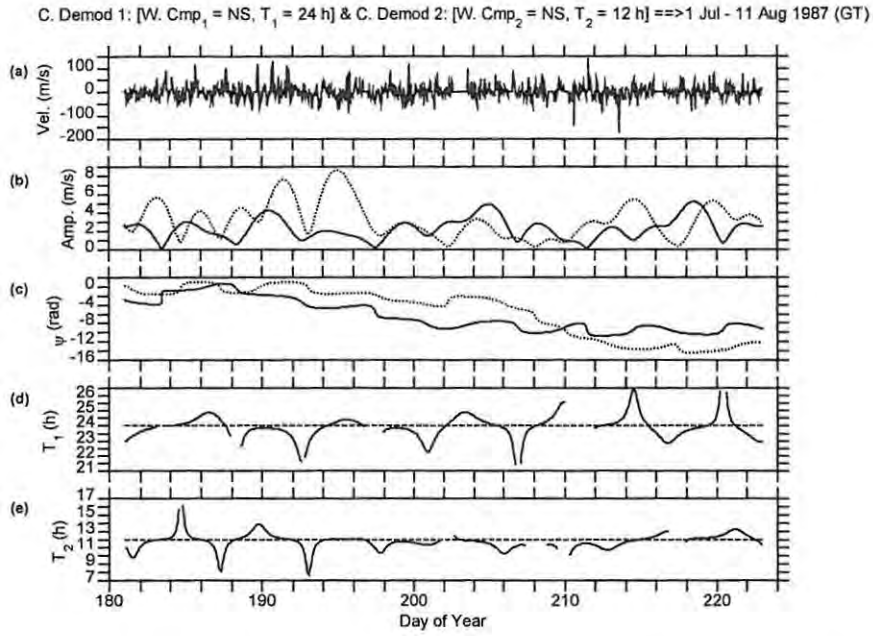

Figure 5.20 Complex demodulation analysis for 1 July to 11 August 1987 (Case 2). (a) The mean corrected meridional velocity. (b) The instantaneous amplitudes (A) of the diurnal demodulation (solid line) and the semidiurnal demodulation (dotted line). (c) The instantaneous phase (ψ) of the diurnal demodulation (solid line) and the semidiurnal demodulation (dotted line). (d) The instantaneous period (T_1) for the diurnal demodulation. (e) The instantaneous period (T_2) for the semidiurnal demodulation.

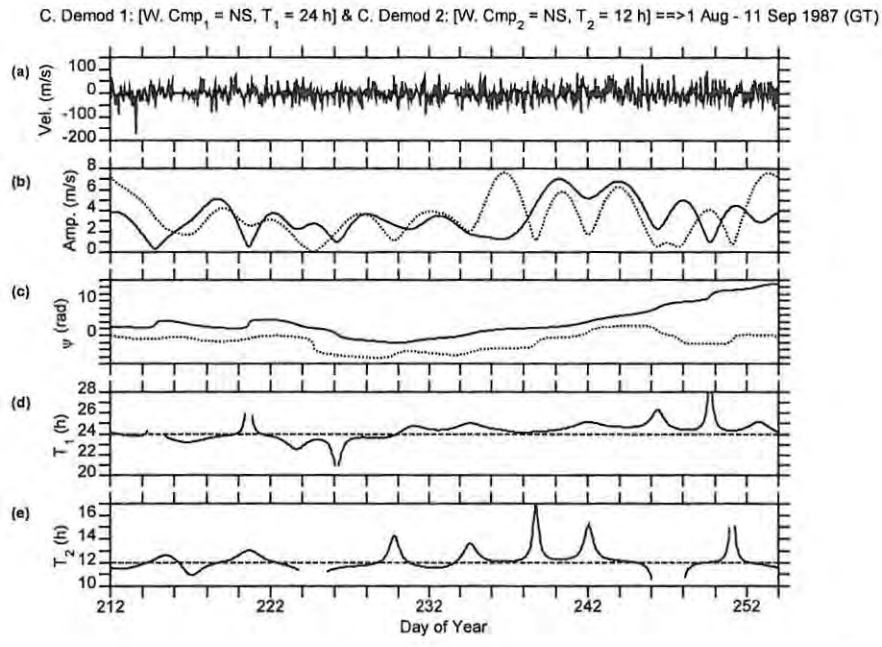

Figure 5.21 Same as **Figure 5.20** but for 1 August to 11 September 1987 (Case 3).

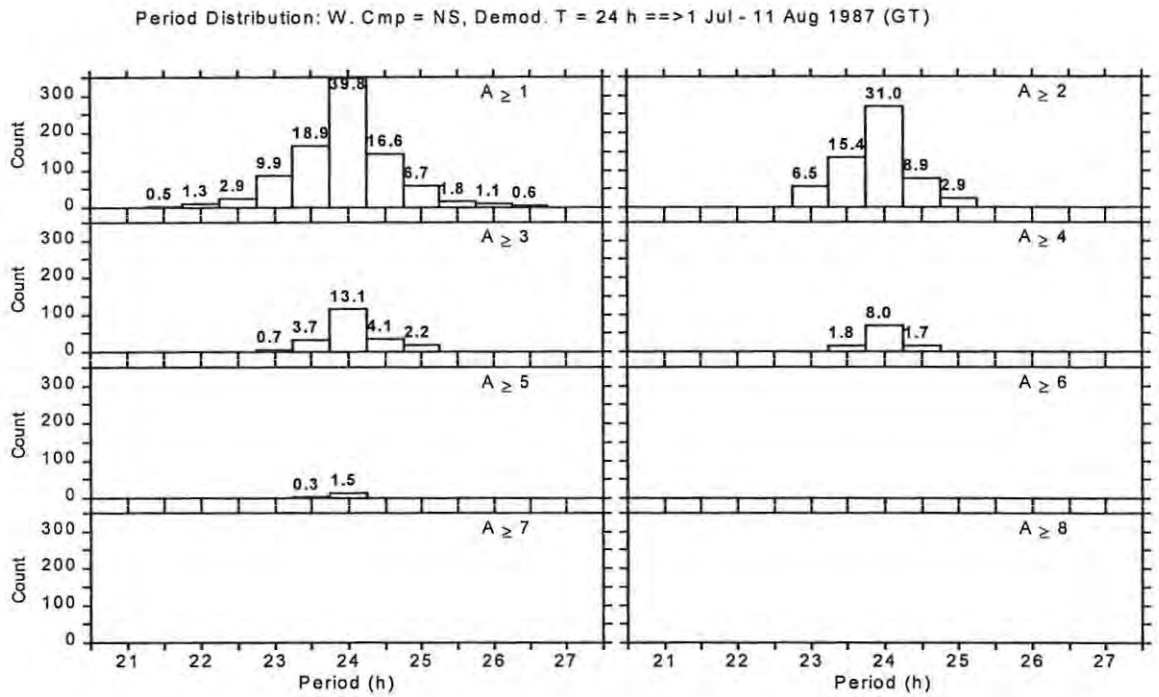

Figure 5.22 For Case 2. The distribution of instantaneous periods for the demodulation period $T = 24$ h for different amplitude (A) cut-off values in ms^{-1}. The percentage contribution to all periods in indicated next to each bin.

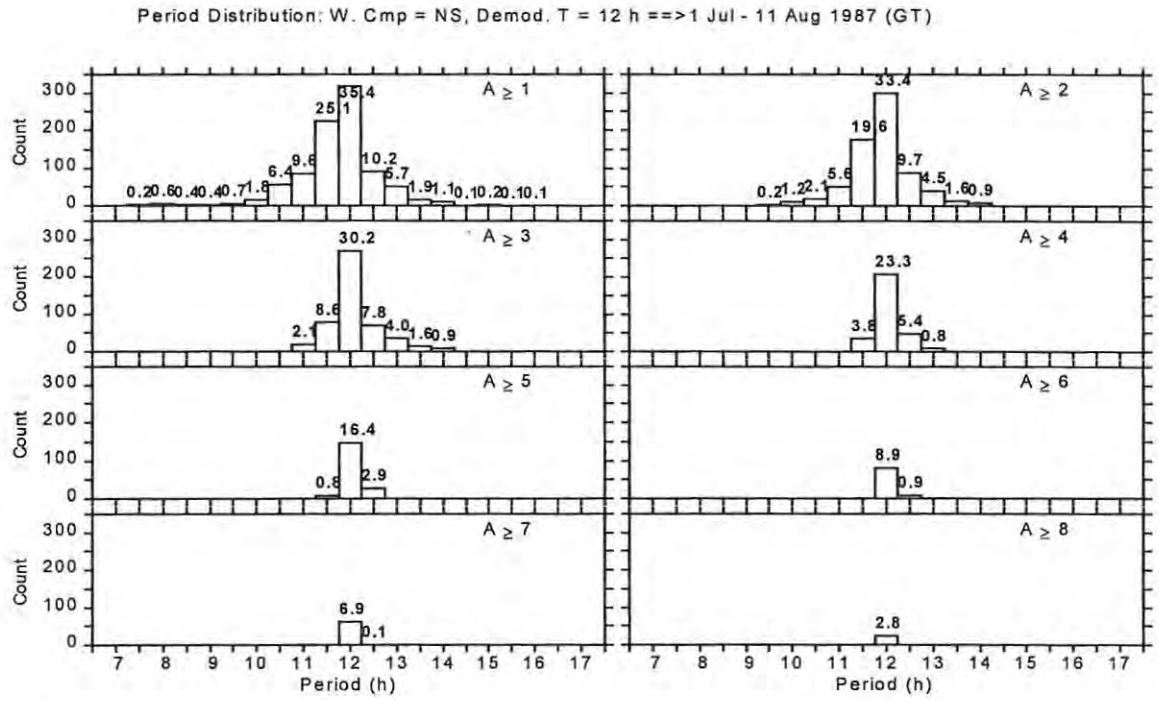

Figure 5.23 Same as **Figure 5.22** but for the demodulation period $T = 12$ h.

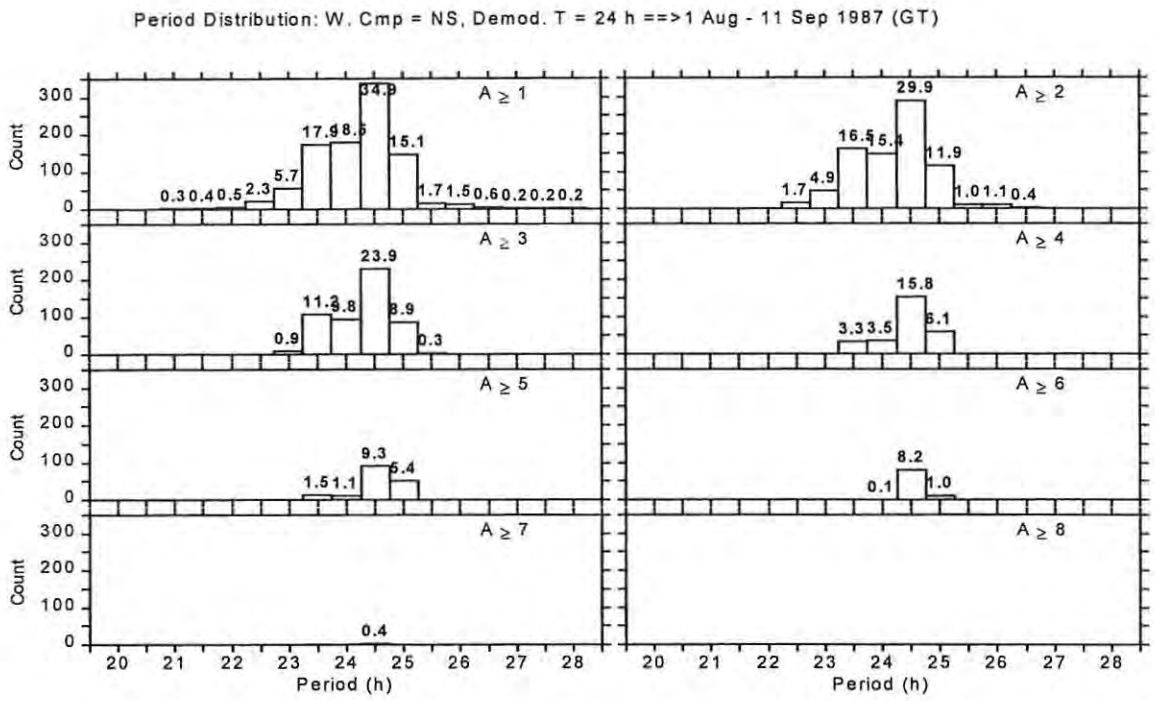

Figure 5.24 For Case 3. The distribution of instantaneous periods for the demodulation period $T = 24$ h for different amplitude (A) cut-off values in ms^{-1}. The percentage contribution to all periods in indicated next to each bin.

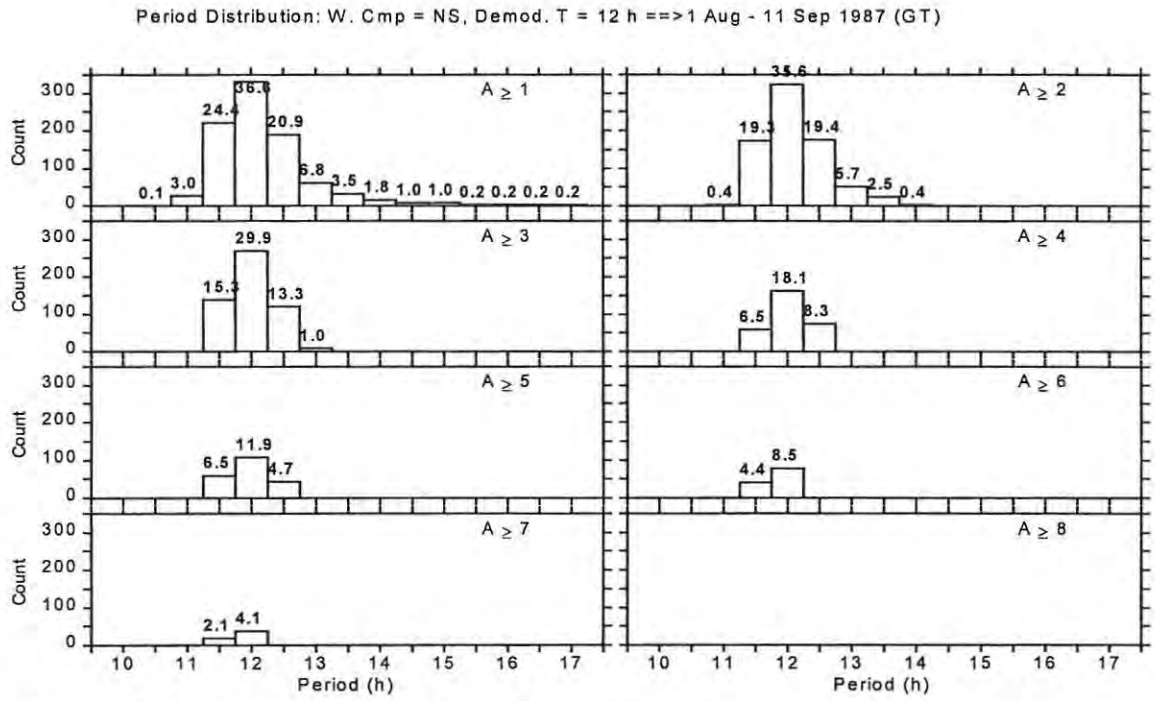

Figure 5.25 Same as **Figure 5.24** but for the demodulation period $T = 12$ h.

after several weeks while oscillations can still be evident even after 60 days for the (2, 2) mode [*Vial et al.*, 1991]. Vial explains that the observed oscillatory response in tidal amplitudes is a result of a superposition on the steady state tidal component of one or more waves generated by the transient modification of thermotidal excitation. He also observed that the period of the oscillation about the steady state decreases with increasing time and that after a few tidal periods have elapsed from the onset of excitation, the variation tends to have periods close to tidal periods. This led Vial to interpret the variations as beats between a tide and waves generated by the transient modification of tidal excitation. The frequency variation that is associated with the transient modification of the tidal excitation is most likely a contributing factor to the period variations observed above. In particular, those instances with non-tidal periods and large amplitudes may indicate times of large injection of energy at non-tidal frequencies.

Since in most of the work in this thesis we assume the period to be a constant harmonic of a solar day and assume that the amplitude and the phase are the variables, it is important to link the period variations to the phase variations. Following *Bloomfield* [1976] the observed tide can be expressed as

$$x_t = A_t \cos(\omega_t t - \phi)$$

Equation 5.1

where the amplitude (A_t) and the angular frequencies (ω_t) are slowly changing with time while the phase (ϕ) is constant, or if ω_t fluctuates about a typical value Ω, Equation 5.1 can also be written as

$$x_t = A_t \cos(\Omega t - \phi_t)$$

Equation 5.2

where the amplitude and the phase ϕ_t are now variable. Therefore, the period variations that I observe in my results can equally be considered as a phase variations in the tides. This link between the period and the phase of the tide implies that some of the period variations observed above could equally be due to the phase changes resulting from gravity wave-tidal interactions

(see Section 5.2). This goes to support the statement made in the Section 5.1 that the study of short-term tidal variations is partly complicated by the fact that the there could be several mechanisms involved which could act together or independently [*Teitelbaum & Vial*, 1991]. Some of the observed amplitude and period/phase fluctuations could also be due to non-linear wave-wave interactions and this will be investigated below.

5.5 NON-LINEAR WAVE-WAVE INTERACTIONS

The non-linear interaction of planetary waves and tides is another possible cause of the amplitude and period/phase variations discussed in the sections above. To investigate this, I will once again focus on the intervals corresponding to Cases 1 to 3 (Section 5.4). In Figure 5.26 (i.e. Case 1) to Figure 5.28 (i.e. Case 3) I have shown plots that will help us understand the non-linear interaction between tides and planetary waves. The (a) panels of these figures depict the band-pass filtered time series of the hourly wind velocities that are shown on Figure 5.17(a), Figure 5.20(a) and Figure 5.21(a). I chose the frequency ranges of the band-pass filters to be 0.8-1.2 cycles per day (cpd) and 1.8-2.2 cpd such that the centre frequencies of the two series of panel (a) correspond to the tidal frequencies of 1 and 2 cpd, respectively. It is assumed that these ranges are sufficiently wide to produce filtered series that are true representations of the variations of tidal components. These filtered series clearly show that the amplitudes of both the diurnal and the semidiurnal tide are modulated at planetary time scales.

Studies (e.g. *Teitelbaum & Vial* [1991]) have shown that as a result of the advection terms of the momentum equation, non-linear interactions of gravity waves, tides and planetary waves are important in the dynamics of the upper middle atmosphere. The suggestion made is that at least two waves, which are referred to as primary waves, interact through these non-linear advective terms resulting in a family of secondary waves which are not spontaneously generated and include, among others, two waves with frequencies corresponding to the sum and difference of the primary waves [*Jacobi et al.*, 1998]. Therefore, at the height at which the non-linear interaction between a planetary wave and a tide occurs, the spectrum of the wind field is expected to show peaks at the planetary frequency f_p, the tidal frequency f_t and at frequencies $f_p \pm f_t$ corresponding to the secondary waves. Since f_t is larger than f_p the secondary waves appear as frequency side-bands next to the tide.

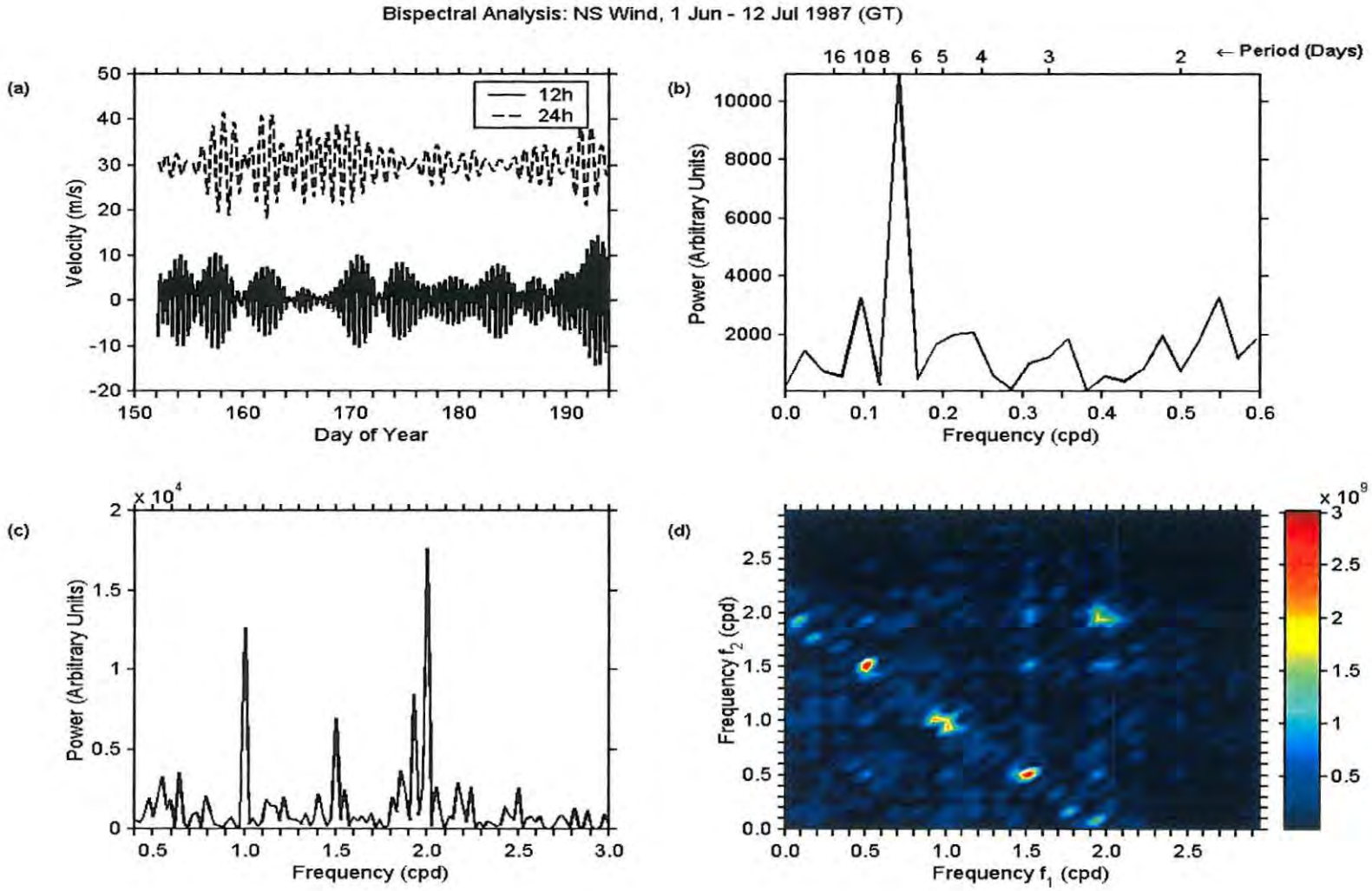

Figure 5.26 Bispectral analysis for Case 1. (a) Band-pass filtered wind velocity for the indicated centre frequencies. The two series have been relatively shifted vertically by some arbitrary amount. (b) and (c) The power spectrum for different frequency ranges. The power is in identical arbitrary units. (d) The bispectrum and the colour bar is in arbitrary units which are not simply related to those of panel (b) and (c).

Teitelbaum & Vial [1991] demonstrated that if the primary waves are linearly superimposed, the wind velocity is merely the sum of the planetary wave and the tide and the peak-to-peak velocity is constant. However, if there is some non-linear interaction between the primary waves the peak-to-peak velocity is modulated. This is due to the fact that, if the amplitudes of the secondary waves are not too small compared to that of the tide, the secondary waves beat with the tide and so modulate its amplitude with a period that is equal to that of the planetary wave [*Teitelbaum & Vial*, 1991; *Jacobi et al.*, 1998; *Beard et al.*, 1999].

For Case 1 (Figure 5.26) we see from panel (b) that there is a strong planetary oscillation at about 0.15 cpd and other possible minor peaks at ~0.1 and 0.55 cpd. Looking at panel (c) of the same figure we observe sidebands especially around the semidiurnal tide. The strongest ones are at ~1.9, ~1.85 and ~1.5 cpd which could be a result of the non-linear interaction of the semidiurnal tide and the planetary waves mentioned above. Such secondary waves have also been observed by a number of other authors (e.g. *Rüster* [1994], *Beard et al.* [1999]). As pointed out by *Teitelbaum & Vial* [1991], if one observes the two primary waves and the two corresponding secondary waves, it highly likely that one is observing a *local* non-linear interaction. The use of *local* here should be understood to mean that the primary waves and the secondary wave(s) are present in the observing volume. However, it should be noted that the actual interaction could have taken place at lower altitudes with the primary waves and secondary wave(s) subsequently propagating upwards to the observing volume [*Beard et al.*, 1999].

The results for the semidiurnal tide, seem to suggest that a significant proportion of the observed amplitude modulation (Figure 5.26(a)) could be due to *local* non-linear interactions based on Figure 5.26(b) and (c). Sometimes only one secondary wave is observed and this is similar to observations made by other workers (e.g. *Clark & Bergin* [1997]). *Beard et al.* [1999] mention that it is possible that both secondary waves are generated with one managing to propagate upwards while the other is attenuated. However, *Beard et al.* [1999] further highlight the fact that the above possibility does not explain the absence of one secondary wave when the volume in which the interaction actually occurs is being studied. Therefore, it is possible that both preferential propagation and production are a factor in this phenomenon.

The drawback in such analysis is that, as opposed to tides which tend to last longer, planetary

waves are short-lived and typically last for a few weeks or less [*Beard et al.*, 1999]. This creates a problem because we need a long time series to improve the frequency resolution of the power spectra and the bispectrum (to be discussed shortly) but, at the same time, intervals extending outside the duration of planetary activity would result in spurious spectral peaks that are unrelated to the non-linear event being studied [*Beard et al.*, 1999]. Therefore there is a trade off between frequency resolution and the focus on the event of interest. It should also be borne in mind that planetary waves tend to be quasi-periodic (i.e. period tends to drift) resulting in peak-broadening and poor frequency resolution [*Beard et al.*, 1999]. This fact also complicates matters in that the period variations that were interpreted as possibly resulting from gravity wave-tidal interactions (Section 5.2 and 5.4) or the transient modification of tidal forcing (Section 5.4) could also be due to this quasi-periodicity of the planetary waves and the associated secondary waves that beat with the tide. This goes to emphasise the difficulty of separating the effects of the different mechanisms that cause tidal variability.

In the discussion above, we have used the presence of secondary waves to infer a possible occurrence of non-linear interaction. *Beard et al.* [1999] cautioned that sometimes the secondary waves are too small to be detected with confidence. In such cases, additional confirmation can be obtained through the bispectrum, which is able to detect quadratic phase coupling that characterise non-linear interactions (see Chapter 2, Section 2.8). In Figure 5.26(d), I have plotted the bispectrum for Case 1. A bispectrum value at a bifrequency (f_1, f_2) should be considered as a response to the quadratic phase coupling of spectral components at frequencies f_1, f_2 and the sum or difference frequency where the initial mixing occurs between components at any two of the above three frequencies [*Clark & Bergin*, 1997]. An important point to note here is that the bispectrum does not give an indication as to which two of the three spectral components interact to give the third [*Clark & Bergin*, 1997]. It is also important to mention that for any real process the bispectra $B(f_1, f_2)$ are symmetric about the line $f_1 = f_2$ [*Rüster*, 1994].

With this understanding, the peaks at (2, 1.9), (1.5, 0.5), and (1.0, 0.9) [Figure5.26(d)] can be associated with the following frequency triplets (0.1, 2.0, 1.9), (0.5, 2.0, 1.5), and (0.1, 1.0, 0.9), respectively. The triplets represent $(f_p, f_t, f_p \pm f_t)$ except in the cases where we have a tide-tide interaction in which case f_p represents the low frequency component. It is interesting to note that even though the interaction involving the diurnal tide could not be picked up with

confidence from panels (b) and (d), one can conclude that they exist based on the bispectral analysis. In general these results indicate that some of the observed tidal variations in this case could be due to non-linear interactions. Unfortunately, the bispectrum does not tell us whether the non-linear coupling is in the driving function or in the atmospheric response [*Clark & Bergin*, 1997]. To understand other aspects of non-linear interaction I consider an analysis of the meridional wind for Case 2 (Figure 5.27). The filtered series (panel (a)) shows some planetary modulation of the tidal amplitudes. The planetary range spectra (panel (b)) shows spectral peaks at ~0.06, ~0.22, ~0.29, ~0.38, 0.45 and ~0.55 cpd. However, one has to caution that the spectral power of these components is small casting doubt on the observed peaks. The tidal spectra (panel (c)), on the other hand, show a very strong semidiurnal tide with some sidebands. The diurnal tide is very weak and is comparable to some of the sidebands around the semidiurnal tide. Looking at the spectra in conjunction with the bispectrum the following strong frequency triplet (0.3, 2.0, 1.7) is identified, and there is also evidence of weak triplets, (0.55, 2.00, 1.45) and (~0.5, 2, ~1.5).

The strong bispectral peak at (2, 2) could be an artefact of some constant phase relationships between tidal components. It is important to note that the presence of a strong diurnal tide and a strong semidiurnal tide *with constant phases* might result in a bispectral peak at some tidal frequencies (e.g. diurnal, semidiurnal, and terdiurnal tides). These components are harmonically related and, in general, tides tend to have some degree of phase consistency due to their common generation mechanism [*Beard et al.*, 1999].

Comparing the planetary range spectra of Figure 5.26 and Figure 5.27 we see that Case 1 had a stronger planetary scale activity noting that the scale of the arbitrary units used is the same in both figures as well as in Figure 5.28. Two possible reasons can be advanced to explain this. One, it could be that there is indeed a real low level of planetary activity for Cases 2 and 3. Two, it is possible that the non-linear interaction occurred at some lower height and the planetary components have subsequently been partially filtered during the upward propagation. In relation to number one, it is important to note that *Teitelbaum & Vial* [1991] explain that in instances that involve primary waves with different periods and wave numbers but moderate amplitudes, the non-linear effects can, under certain conditions, be significant. These authors point out that this is due to the fact that the significance of the non-linearity depends on the

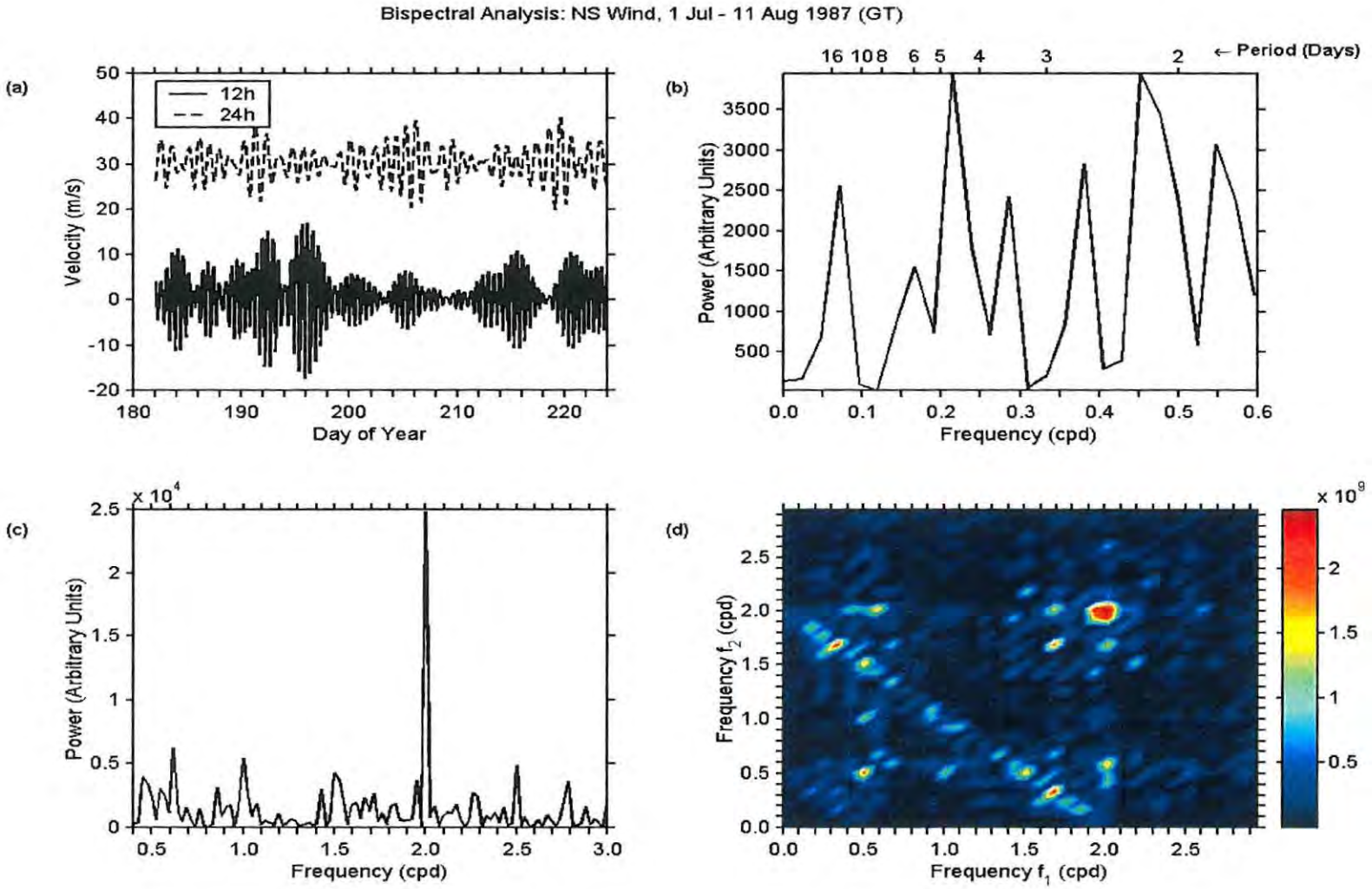

Figure 5.27 Bispectral analysis for Case 2. (a) Band-pass filtered wind velocity for the indicated centre frequencies. (b) and (c) The power spectrum for different frequency ranges. The power is in identical arbitrary units. (d) The bispectrum and the colour bar is in arbitrary units which are not simply related to those of panel (b) and (c).

amplitude of the fluid velocity in the wave propagation direction in comparison to the wave propagation velocity. For transverse waves, the fluid velocity and the propagation velocity are perpendicular to each other but in a case of two waves propagating simultaneously, the fluid velocity can have a large component in the propagation direction of one of the two waves [*Teitelbaum & Vial*, 1991]. These authors point out that this can enhance the advection terms, which, as mentioned earlier, are the forcing terms for the secondary waves.

In concluding the subject of non-linear interactions, I consider Case 3 (Figure 5.28). The band-pass filtered series of Case 3, clearly bear evidence of tidal amplitude modulation at planetary time scales. In Case 3 we see even weaker planetary wave activity and tidal activity than in the previous two cases. Strong peaks in the planetary range spectra are at 0.05, 0.1, 0.25 and 0.45 cpd. From the tidal range spectra a few sidebands can be distinctly identified at ~0.5, ~1.1, ~1.4, ~1.5, ~1.6, ~2.25, ~2.4 and ~2.6 cpd. It also seems as if there could be a sideband at 1.05 cpd that is masked by the broad peak of the diurnal tide. Although not much confidence can be attached to this, these results suggest the following non-linear interaction frequency triplets (0.05, 1.0, 1.05), (0.1, 1.0, 1.1), (0.45, 1.0, 1.45) and (0.25, 2.00, 2.25). The last triplet which corresponds to a planetary modulation of 4 days can be clearly be seen on the series filtered around the semidiurnal tide from around day number 226 to 252.

However, the bispectrum of this case does not show any sign of the above interactions. In fact the bispectrum is only strong at the bifrequency (1.0, 1.0) and has a week peak at (1.0, 2.0), which could merely be due to the presence of the diurnal and the semidiurnal tides with constant phases, as mentioned earlier. There are a number of possible reasons that could explain the absence of the (0.25, 2.00, 2.25) triplet in the bispectrum. The bispectrum can only detect a non-linear interaction if the primary waves, and at least one of the secondary waves are present in the measuring volume being studied [*Beard et al.*, 1999]. This does not necessarily mean that the non-linear interaction should happen *in situ*, but if it happens below the level of interest, the primary waves and at least one of the secondary ones should successfully propagate into volume of interest for a bispectral detection. The fact that the power in the planetary range activity is relatively small make it doubtful that the strong 4 day modulation observed in the semidiurnal tide could have been effected *in situ*.

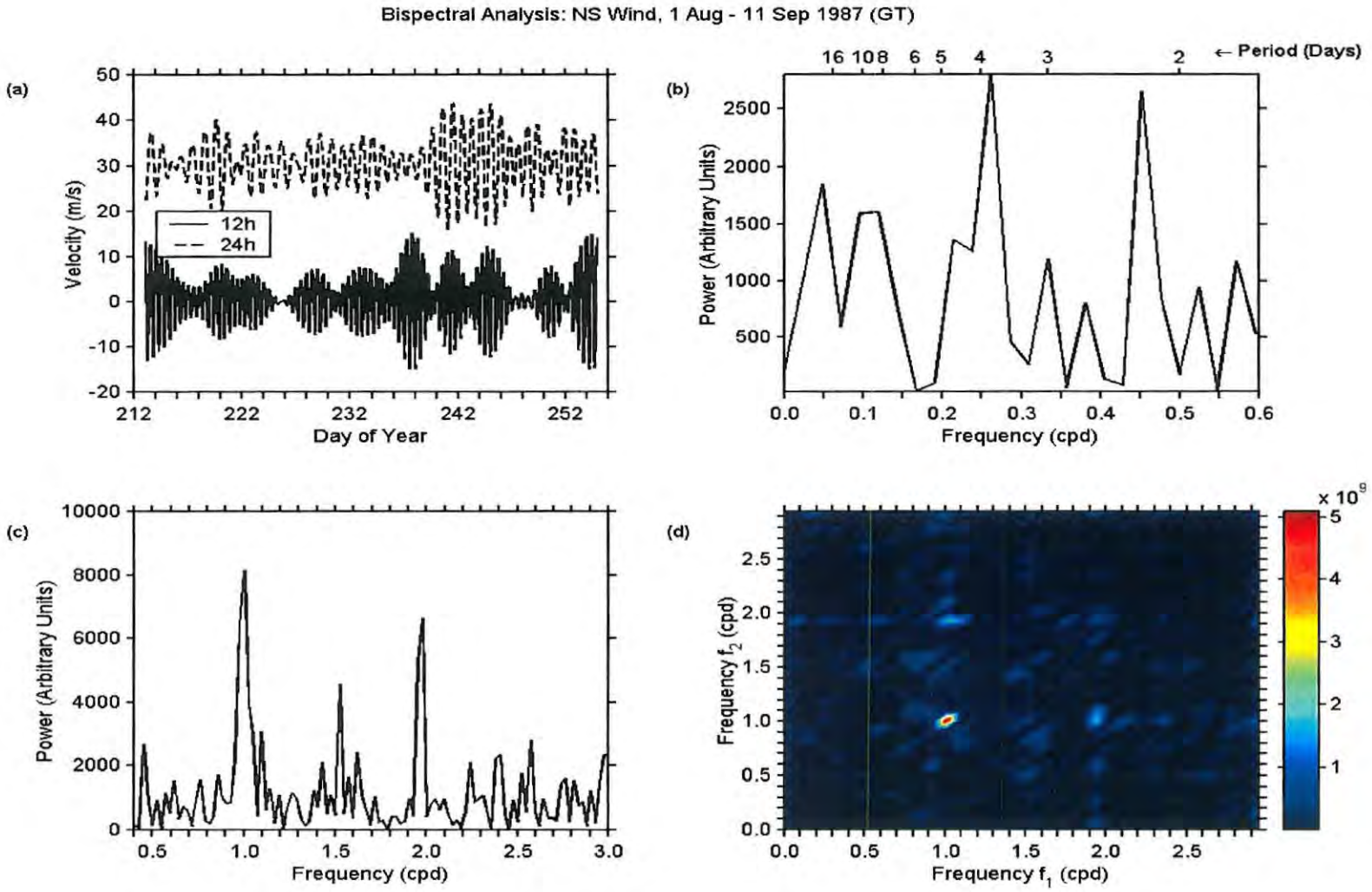

Figure 5.28 Bispectral analysis for Case 3. (a) Band-pass filtered wind velocity for the indicated centre frequencies. (b) and (c) The power spectrum for different frequency ranges. The power is in identical arbitrary units. (d) The bispectrum and the colour bar is in arbitrary units which are not simply related to those of panel (b) and (c).

My suggestion is that the non-linear interaction occurred lower down the atmosphere with the modulated semidiurnal tide and the secondary wave at ~2.25 cpd managing to propagate into the MLT region while the associated ~4-day (~ 0.25 cpd) planetary wave was significantly/completely attenuated below the MLT region. The only problem with this is how to explain the ~4 day wave observed on panel (b). It could be that this ~4-day was generated at a level higher than where the non-linear interaction occurred and there is no phase relationship between this particular ~4 day wave, the semidiurnal tide and the 2.25 cpd secondary wave. This is in line with the fact that the presence of planetary activity does not always result in planetary scale tidal modulation. *Beard et al.* [1999] reported on such examples leading these authors to note that the exact conditions for the occurrence of non-linear interaction are, as yet, not fully understood. A similar argument can be presented that the secondary wave observed at ~2.25 cpd is not directly related to the non-linear interaction and hence the absence of a bispectral peak.

Another, possible explanation is that the tidal variation of ~4-day periodicity is dominated by beating between a steady semidiurnal tide and a component with ~2.25 cpd due to the transient modification of the tidal source. Such an interaction will result in a modulation envelope of ~4-day periodicity but the wind spectra will only show the steady semidiurnal component and the ~2.25 cpd components and no ~4-day component will be detected. This is in line with the fact that if the observed tidal modulation is due to the planetary modulation of tidal heating, it is most likely that only the tide and the two sidebands would be spectrally detectable [*Teitelbaum & Vial*, 1991]. This argument might serve to explain the weak presence of the 4-day component in the planetary spectra.

To summarise, I have analysed data for Cases 1 to 3 and each of these cases reveals certain features about the short-term tidal variability. Case 1 shows that a significant portion of this variation is due to non-linear interactions which are taking place either within the observing volume or lower down with the associated waves successfully and efficiently propagating to the observing volume. Case 2 also shows non-linear interactions, which most probably occurs lower down in the atmosphere with the associated waves being attenuated during their upward propagation. In Case 3, we are looking at a situation that is

similar to Case 2 or one that is dominated by most probably the transient modulation of tidal excitation or some other mechanism.

CHAPTER 6 LONG-TERM DIURNAL TIDE VARIATIONS

6.1 INTRODUCTION

The diurnal tide is one of the dominant waves observed in the MLT region with HRDI results giving peaks of ~60 ms^{-1} (EW) [*Khattatov et al.*, 1997b] and ~90 ms^{-1} (NS) [*Khattatov et al.*, 1997a] at ~20-30°S. As mentioned in Chapter 1, Section 1.2.2.2 it is a global-scale atmospheric oscillation with a period of a solar day (i.e. 24 h). The diurnal tide consists of a migrating or Sun-synchronous component which propagates westward following the apparent motion of the sun and has a zonal wavenumber $s = 1$. The migrating modes of the tide are characterized by phases that are longitude independent [*Williams & Avery*, 1996]. The migrating modes are primarily excited by the absorption of solar radiation in the near infrared (IR) range by tropospheric H_2O [*Hagan*, 1996]. There are also secondary forcing mechanisms that include the absorption of solar radiation (i) in the ultraviolet (UV) range by O_3 in the stratosphere and lower mesosphere, and (ii) in the Schumann-Runge bands and continuum by O_2 in the lower thermosphere [*Hagan*, 1996].

However, strictly speaking the migrating tide results only if the absorbing medium has a global distribution that is zonally uniform [*Williams & Avery*, 1996]. Any deviation from this longitudinal uniformity results in nonmigrating or Sun-asynchronous tidal components. The nonmigrating tide, like the migrating tide, is global in scale and its period is a harmonic of a solar day [*Hagan et al.*, 1997]. However, unlike the migrating tidal component, the nonmigrating one may be stationary, propagate eastward or westward with the only restriction on permissible zonal wavenumbers being that they should be different from the tidal frequency (day^{-1}) [*Hagan et al*, 1997].

Theoretically, the migrating component is the most dominant in the MLT region with the maximum around the subtropics (latitudes of ±20°) and a minimum around the equator and the poles for all seasons [*Hagan*, 1996]. *Vincent et al.* [1998] report observed amplitudes of ~20-30 ms^{-1} at Kauai (22°N) compared to <~20 ms^{-1} at Christmas Island (2°N). The latitudinal structure of the phases is more complicated but it tends to follow the pattern of the dominant forcing due to tropospheric H_2O [*Hagan*, 1996]. The vertical wavelength of the tide is ~30 km.

The diurnal tide, as mentioned in Chapter 5, varies over different time scales. In this chapter, I focus on the seasonal and interannual variations of the amplitudes and phases at Grahamstown

and Adelaide. A number of factors have been advanced as possible causes of these variations and these include gravity wave stress, QBO effects and changes in thermotidal forcing. In order to study how the diurnal tidal activity changes with season and interannually, I have used a dynamic spectral approach (Section 6.2). Although in Section 6.2 I deal with both the diurnal and the semi-diurnal tide, in the remainder of the chapter I focus on the diurnal tide while the semi-diurnal tide is the subject of Chapter 7. In Sections 6.3 and 6.4 I deal with the amplitude and phase behaviour of the diurnal tide, respectively.

6.2 SPECTRAL ANALYSIS

In my study, I begin by spectrally analysing the wind field in order to determine which spectral components that dominate the MLT dynamics in the ~6–48-h period range. For this purpose I have used short time Fourier transform (STFT) techniques (see Chapter 2, Section 2.6). I used data windows that consisted of hourly wind values covering an interval of 21 days and the data window was advanced by 10 days each time. Each of these data windows had to have at least 50 % of the possible number of observations to be acceptable and data gaps in any acceptable data window were linear interpolated. A similar analysis was followed for the cross-spectrum and associated cross-amplitude and coherency spectra.

In Figure 6.1 I have plotted the auto-spectra for the different wind components at both Grahamstown and Adelaide. At these two sites it is clear that the dynamics of the MLT region is dominated by the diurnal and the semidiurnal tide throughout most of the years. At Grahamstown, the semidiurnal tide is as strong as the diurnal tide whereas at Adelaide, the semidiurnal tide tends to be weaker than its diurnal counterpart. Another feature that is observed at Grahamstown is the stronger tidal activity in the zonal flow than in the meridional flow something that is not clearly evident at Adelaide. The level of tidal activity tends to be seasonally dependent. Apart from the tidal components, there is also a significant signature of the two-day wave especially in the meridional flows of both sites. This wave tends to be consistently strong in summer and seem to be very correlated between Grahamstown and Adelaide but data gaps hamper a clear assessment in this regard. There is also evidence of weak

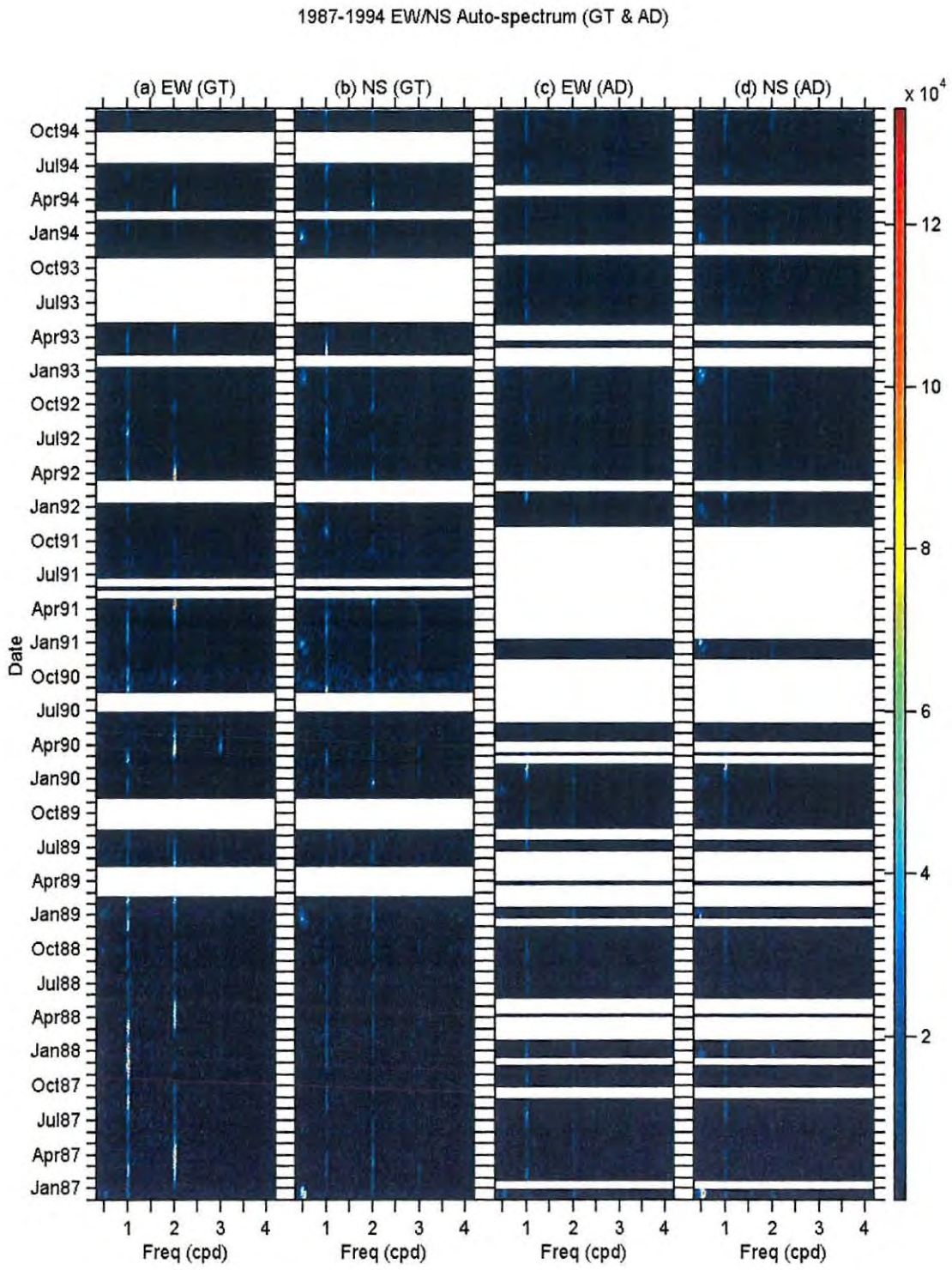

Figure 6.1 The auto-spectrum for the (a) EW wind (GT), (b) NS wind (GT), (c) EW wind (AD) and (d) NS wind (AD) for the years 1987-1994. Units of the colour bar are arbitrary.

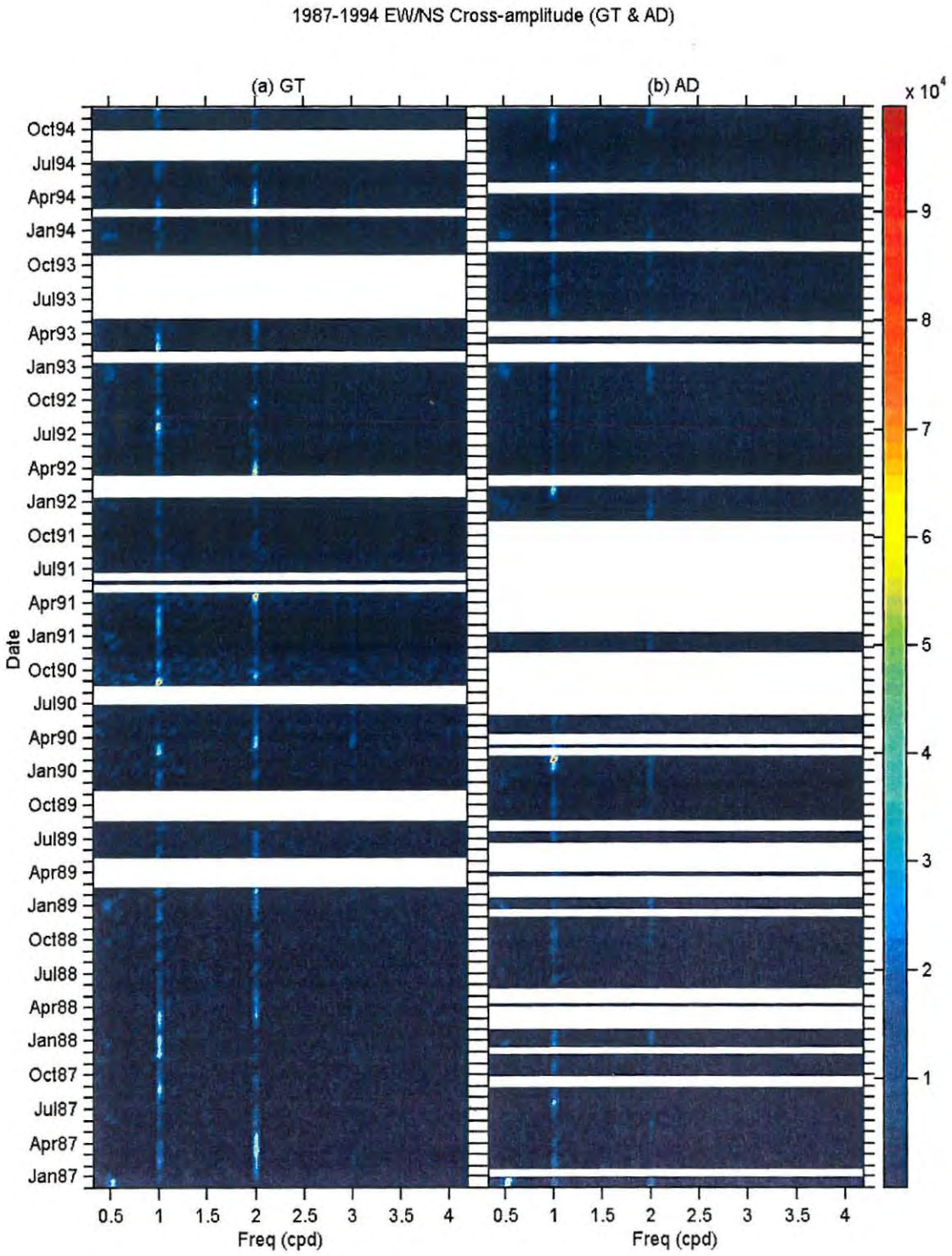

Figure 6.2 The EW/NS cross-amplitude for (a) Grahamstown and (b) Adelaide for the years 1987-1994. Units of the colour bar are arbitrary.

spectral energy at 3 cpd (= cycle per day) and there is no sign of spectral activity at 4 cpd.

Another way of presenting the above information is by using the cross-amplitude, which gives the average of the product of the amplitudes of spectral components in two series (e.g. $x(t)$ and $y(t)$) with a common frequency f (see Chapter 2, Section 2.6.2). The EW/NS cross-amplitudes (Figure 6.2) confirm an earlier observation that tides dominate zonal and meridional wave activity in the ~6-48 h period range of the MLT region. Once again we see the stronger activity at Grahamstown compared to Adelaide.

To investigate a possible linear correlation in the seasonal variation of the wave activity of the zonal and the meridional flows, I have used the coherency $C_{xy}(f)$, which is capable determining the degree of linear correlation between two processes at frequency f (see Chapter 2, Section 2.6). The closer $C_{xy}(f)$ is to zero (one) the less (higher) the linear correlation of the bivariate process. The only blemish with the coherency is that if unsmoothed periodograms are used in its computation it is identically equal to one at all frequencies [*Priestley*, 1981; *Bloomfield*, 1976]. *Priestley* [1981] explains this puzzling feature of the coherency in detail. There is, therefore, a need for some smoothing but, at the same time, too much smoothing introduces some bias [*Priestley*, 1981]. In my analysis, I used a 17-term (i.e. 8^{th} order) smoothing function (see *Diggle* [1990]). Even with such smoothing, the coherency can sometimes be high where it is not expected to be as can be seen from Figure 6.3. The picture improves when the coherency for a number of years is averaged, as we will see towards the end of this section (Figure 6.5 to Figure 6.8). Even with this shortcoming, the coherency shows that tidal frequency components tend to have a higher degree of linear correlation than the other components even though the frequency resolution is poor. Adelaide has a higher degree of linear correlation than Grahamstown.

Another aspect that needs consideration is the relationship between the tidal activity at Grahamstown and Adelaide. In Figure 6.4, I have plotted the GT/AD cross-amplitude for both the zonal and the meridional components. From this figure we see that the tides (diurnal and semidiurnal) and the 2-day wave are the only components that prevail when products of spectral amplitudes are considered. The weak components that were seen in Figure 6.1 fade off

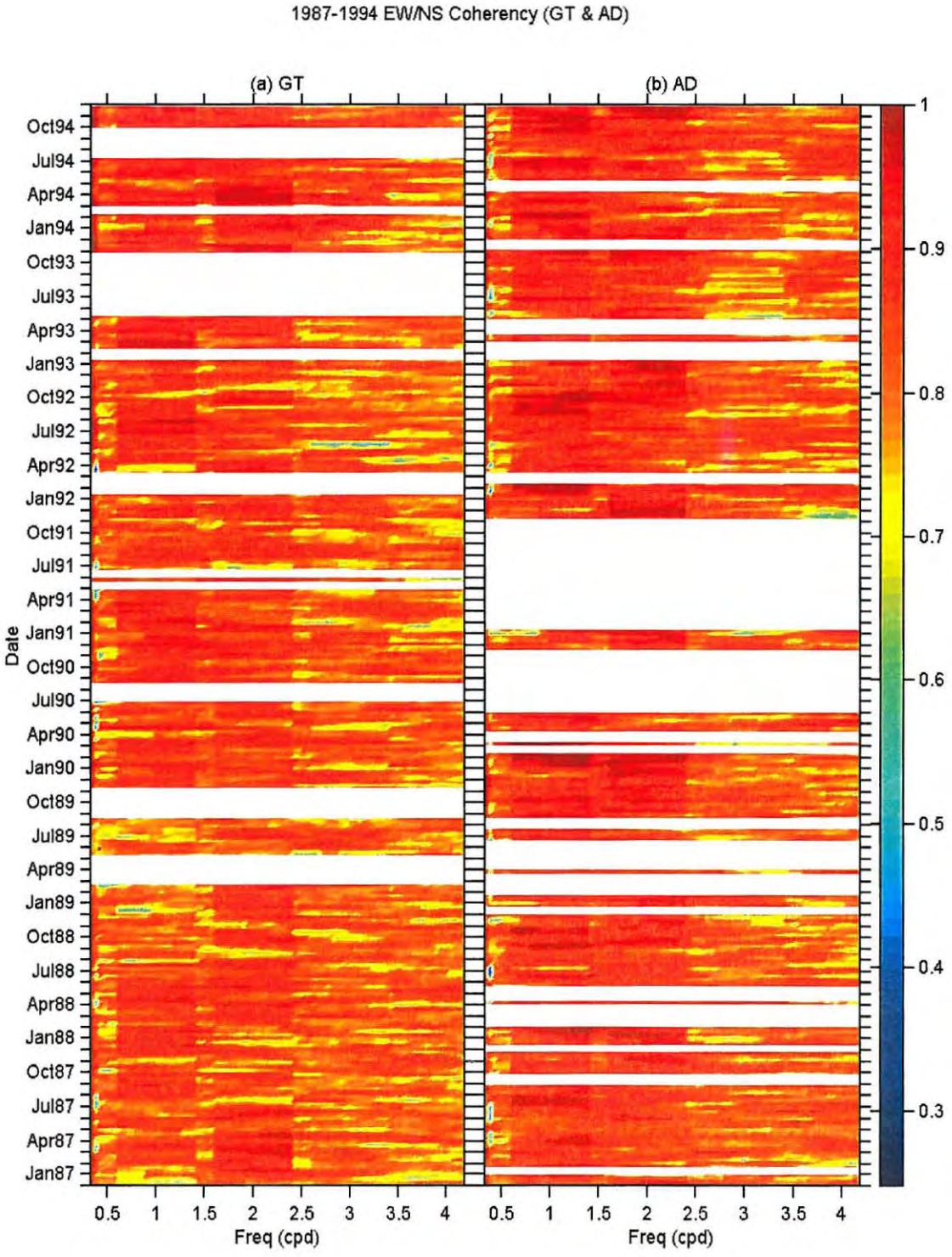

Figure 6.3 The EW/NS coherency for (a) Grahamstown and (b) Adelaide for the years 1987-1994.

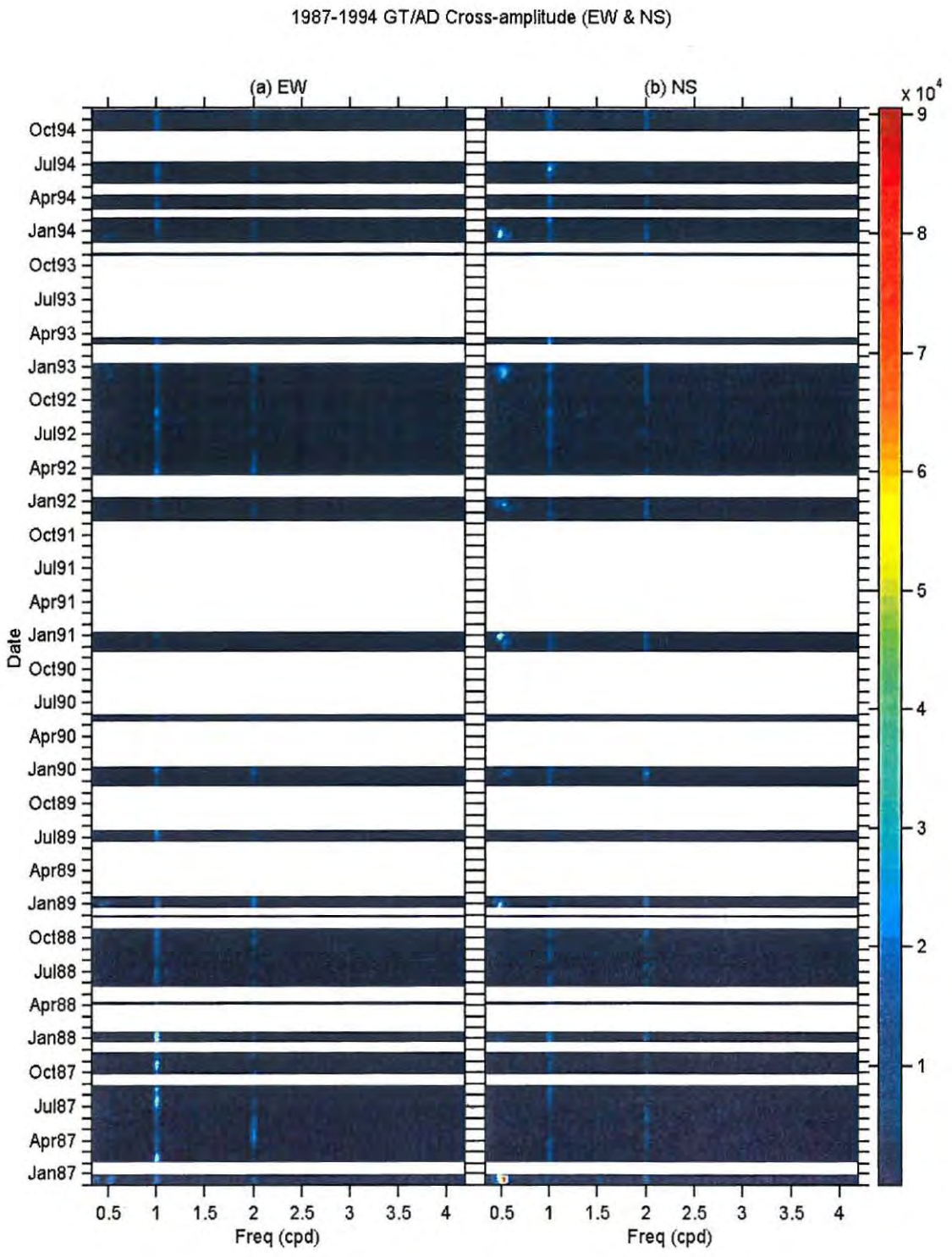

Figure 6.4 The GT/AD cross-amplitude for the (a) zonal flow and (b) the meridional flow for the years 1987-1994. Units of the colour bar are arbitrary.

completely indicating that they were either not real features or that they were more local in nature. A noteworthy feature is the strength of the GT/AD cross-amplitude of the 2-day wave in the meridional component. Apart from the seasonal and interannual consistency revealed by this, this observation also shows that the 2-day wave has a large horizontal extent.

An even clearer picture of the behaviour of the various atmospheric waves discussed above is deduced from a consideration of long-term spectral trends that are shown in Figure 6.5 to Figure 6.8. These figures show the 8-year (1987-1994) spectral averages. Starting with Grahamstown (Figure 6.5(a) to (c)), we observe that, in general, the seasonal dependency of tidal activity alluded to earlier show that there is more energy at tidal frequencies during the equinoxes for both wind components (EW and NS). The spectral peak of the diurnal tide tends to lag that of the semidiurnal tide by about a month. For the zonal component, the semidiurnal tide reaches stronger peaks than the diurnal tide whereas the opposite is true for the meridional component. The interannual consistency of the 2-day wave in the meridional flow is revealed here by the high 8-year average. The averaged coherency (Figure 6.5(d)) shows a clearer higher degree of linear correlation around tidal components especially during the equinoxes.

At Adelaide (Figure 6.6), similar general features are observed with some differences as outlined below. At Adelaide, the diurnal tide is stronger than the semidiurnal tide for both the zonal and the meridional wind flows. Also, the diurnal spectral peaks are in February and November in contrast to the May and September peaks observed at Grahamstown. At Adelaide there is a higher degree of linear correlation between the zonal and the meridional components near tidal frequencies compared to Grahamstown. A cross-spectral analysis between Grahamstown and Adelaide is shown in Figure 6.7 and Figure 6.8. Due to the weak semidiurnal tide at Adelaide, the cross-amplitudes of both the zonal (Figure 6.7(c)) and the meridional (Figure 6.8 (c)) components are stronger for the diurnal tide than its semidiurnal counterpart. The meridional 2-day wave has a very strong cross-amplitude indicating (i) the consistency of this wave in time (i.e. time of occurrence between Grahamstown and Adelaide) and (ii) the regularity of the wave from year to year. This further confirms the fact that this wave has a long horizontal extent. From the coherency Figure 6.7(d) and Figure 6.8(d), we observe that a higher degree of linear correlation occurs around tides and the 2-day wave.

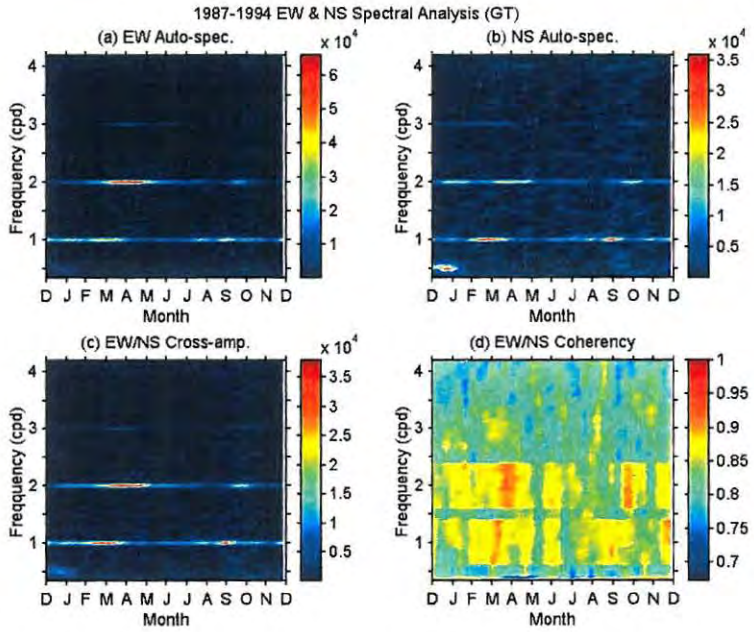

Figure 6.5 The 1987-1994 spectral average of the wind at Grahamstown. (a) The zonal power spectrum. (b) The meridional power spectrum. (c) The EW/NS cross-amplitude spectrum. (d) The EW/NS coherency. Colour bars for (a) to (c) have arbitrary units.

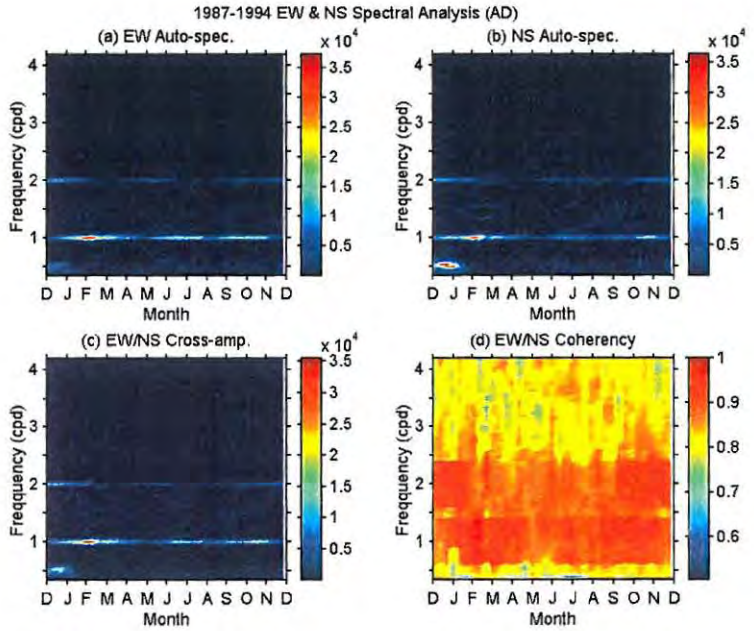

Figure 6.6 Same as **Figure 6.5** but for Adelaide.

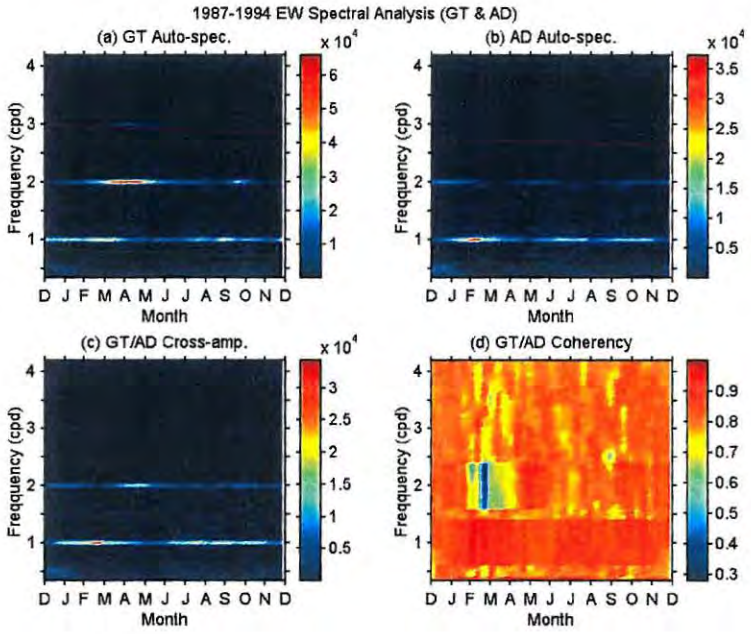

Figure 6.7 The zonal 1987-1994 spectral average of Grahamstown and Adelaide. (a) The zonal power spectrum for Grahamstown. (b) The zonal power spectrum for Adelaide. (c) The zonal GT/AD cross-amplitude spectrum. (d) The zonal GT/AD coherency. Colour bars for (a) to (c) have arbitrary units.

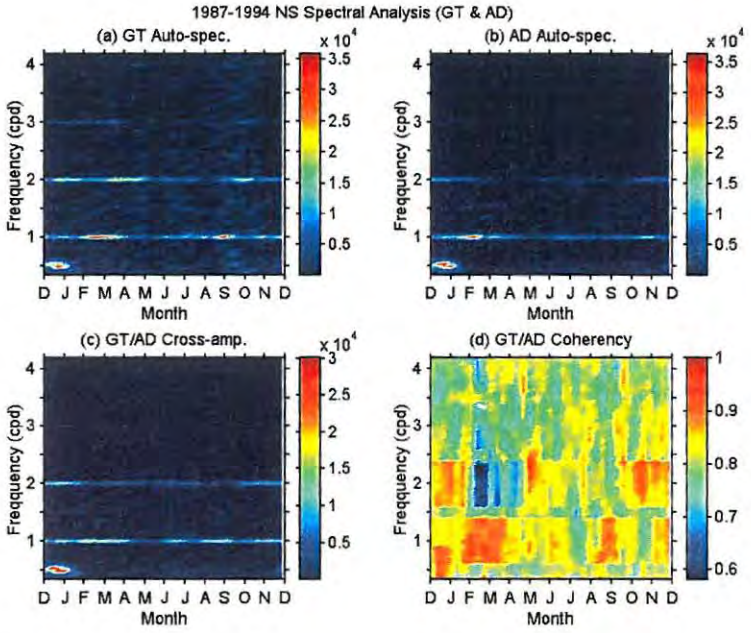

Figure 6.8 Same as **Figure 6.7** but for the meridional component.

This concludes the dynamic spectral analysis of the diurnal and the semidiurnal tides. For the rest of this chapter, I focus on the main subject of the chapter—the diurnal tide. The semidiurnal tide will be discussed in Chapter 7.

6.3 AMPLITUDES

6.3.1 Seasonal Trends

This section is broken into two sub-sections Section 6.3.1.1 and 6.3.1.2. Although the first sub-section is focussed on the seasonal behaviour of the diurnal tide at a given site, I will from time to time, make Grahamstown-Adelaide comparisons where appropriate. However, a one-to-one comparison of the two sites is the main thrust of Section 6.3.1.2.

6.3.1.1 Local Seasonal Trends

Figure 6.9 shows the seasonal behaviour of the zonal and the meridional vector amplitudes of the diurnal tide at Grahamstown. Each data point represents the monthly mean, which is a vector average of all (4-day) amplitudes deduced as described in Chapter 5, Section 5.2 and falling within a particular month. A month was considered to be acceptable if it had at least 15 out of all possible (4-day) amplitudes and hence phases within the month in question. The same procedure was followed for the semidiurnal tide monthly amplitudes (Chapter 7, Section 7.2) as well as the for the monthly average phases of the diurnal tide (Section 6.4) and the semidiurnal tide (Chapter 7, Section 7.3). A comparison between vector means and algebraic means is shown in Figure 1 to Figure 16 of Appendix A for Grahamstown and Adelaide. At both sites the differences between these two types of amplitudes have averages of ~2 ms^{-1} or less for both the diurnal and the semidiurnal tidal amplitudes (zonal and meridional). In general, the vector amplitudes are smaller than the algebraic ones, which is indicative of phase fluctuations in the tides. It must be noted that monthly mean values may give suppressed amplitudes due to destructive interference if the changes in the phases over the averaging interval are significant *Portnyagin et al.* [1993b]. Generally, the incoherent contribution to the vector average cancels out such that the monthly amplitudes average represents the salient features of the atmosphere that are persistent and characteristic of long term behaviour of the month being averaged.

The diurnal amplitudes at both Grahamstown (Figure 6.9) and Adelaide (Figure 6.10) show great semi-annual seasonal variations with the IAs indicating a higher tendency for amplitude peaks to occur during the equinoxes and some minima during the solstices. However, at Adelaide the meridional amplitudes also tend to remain high even in summer. At both sites the zonal amplitude peaks show an equinoctial asymmetry characterised by larger amplitudes in autumn than in spring while the meridional amplitude peaks are characterised by some degree of equinoctial symmetry.

The GSWM diurnal tide results for equinoctial times at 18°N show that the infrared (IR) tidal source dominates the ultraviolet (UV) source [*Hagan*, 1996]. Hagan found that these two forcing mechanisms are 12 h out of phase such that, for the most part, the diurnal tidal amplitude was a difference between the two forcings and the associated phase tracks that of the dominant IR source. She also found that whereas the H_2O source does not change much between autumn and spring at 18°N, the O_3 and O_2 forcing was 40 % weaker in autumn compared to spring such that the combined amplitude (which is mostly the difference between the two, as explained above) is larger in autumn than in spring. This might possibly explain the similar equinoctial asymmetry observed at Grahamstown and Adelaide in the zonal amplitudes. The solstice condition at Grahamstown show solstitial symmetry (Figure 6.9) which is in line with the results of GSWM-95 at ~33°S which show that although both the H_2O and the O_3/O_2 have solstitial asymmetries, the resulting combined tide is solstitially symmetric at our latitude [*Hagan*, 1996]. The amplitude behaviour at Adelaide (Figure 6.10) shows some solstitial asymmetry (larger summer amplitudes than winter amplitudes) in the meridional amplitudes while the zonal amplitudes show a degree of symmetry.

As shown by the IAs of Figure 6.9 and Figure 6.10 and confirmed by the frequency distributions on Figure 6.11 and Figure 6.12, the zonal amplitudes tend to be larger than the meridional ones especially at Grahamstown as can also be seen from the statistics in Figure 6.11 and Figure 6.12. The bulk (~60 %) of the differences are in the 0-10 ms^{-1} range at both Grahamstown and Adelaide. From the seasonal frequency distributions and the IAs, we see that at Grahamstown the zonal amplitudes tend to be larger than the meridional amplitudes for all seasons whereas at Adelaide, there is deviation from this in summer.

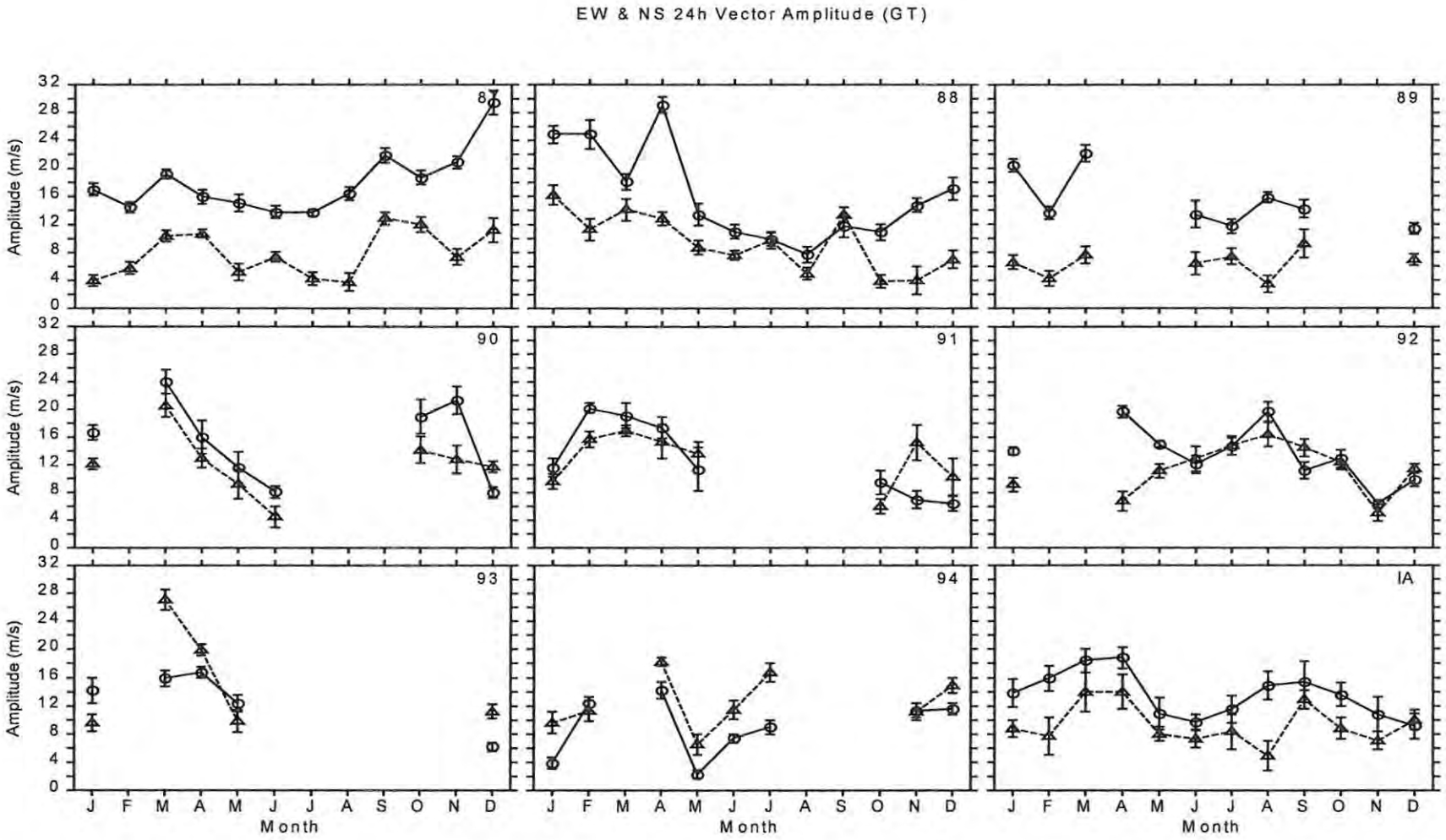

Figure 6.9 The zonal (circles) and the meridional (triangle) amplitudes of the diurnal tide at Grahamstown for the years 1987-1994 and the IA. The error bars represent one standard error of the mean (1 α).

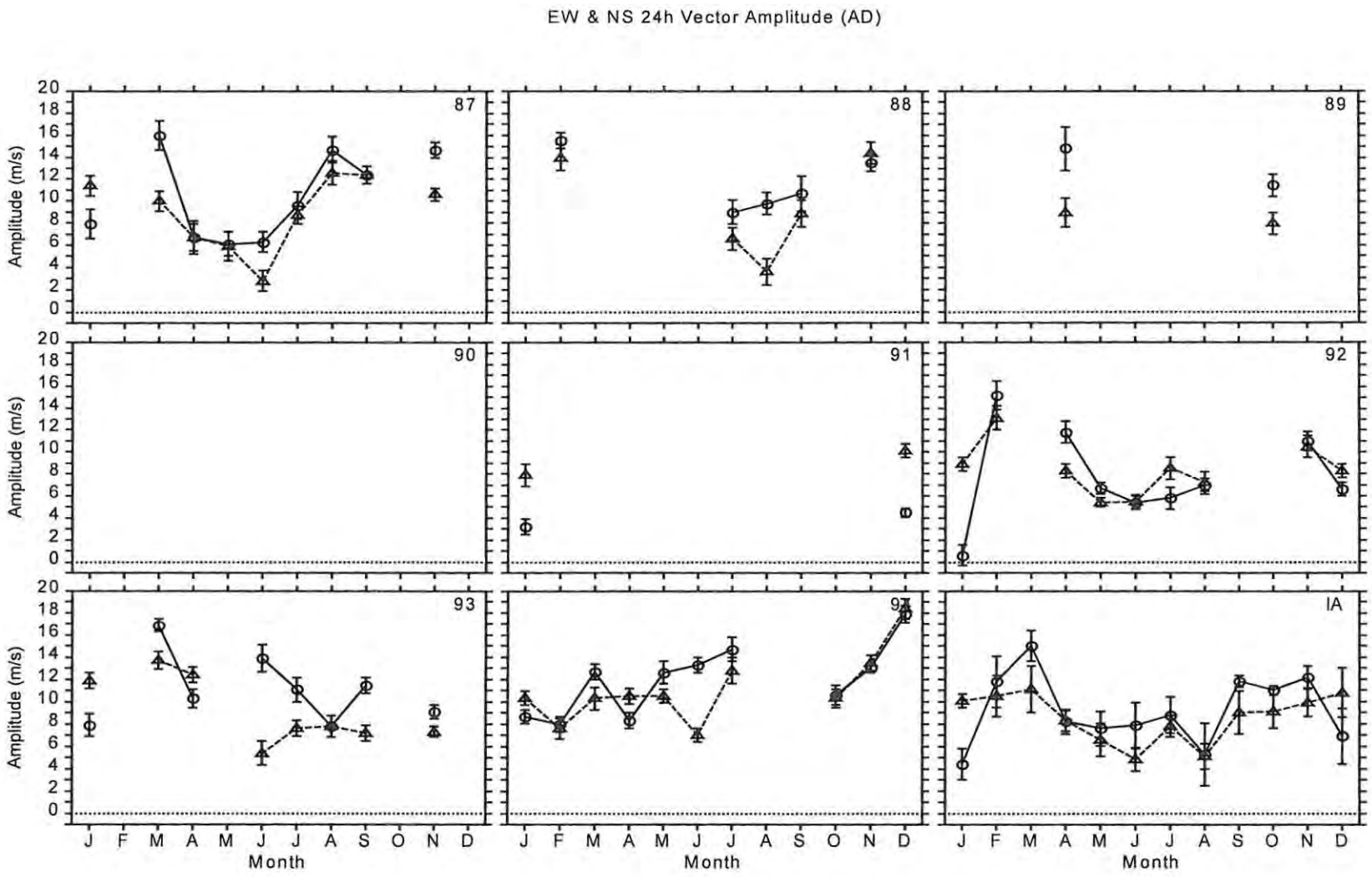

Figure 6.10 Same as **Figure 6.9** but for Adelaide.

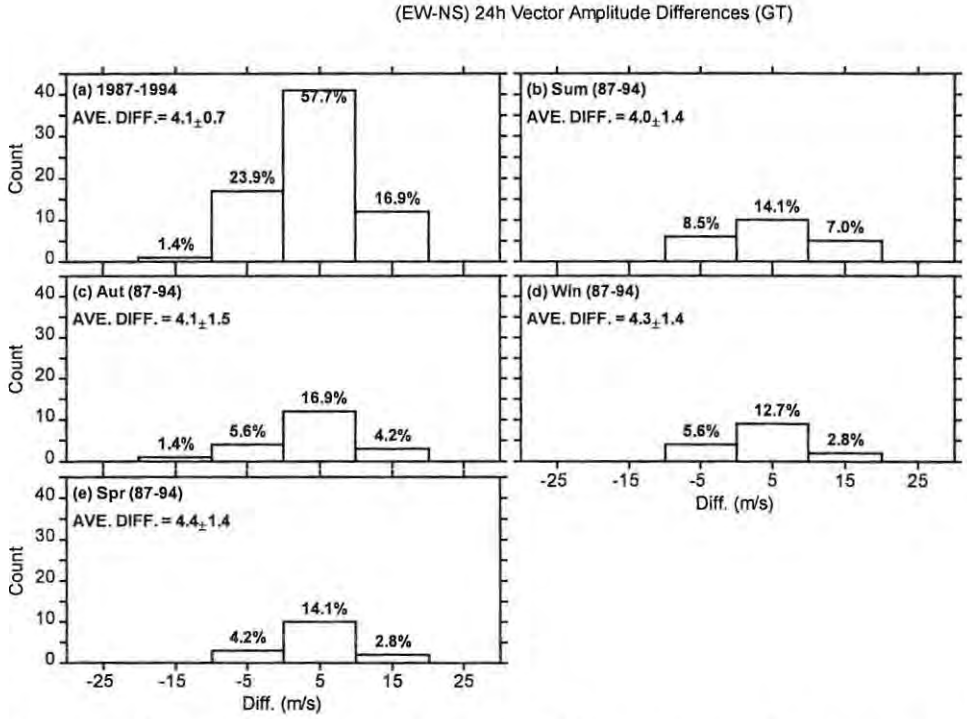

Figure 6.11 The distribution of the (EW-NS) amplitude differences for the diurnal tide at Grahamstown for the years 1987-1994. The weighted average differences are also given and the percentage count of each bar.

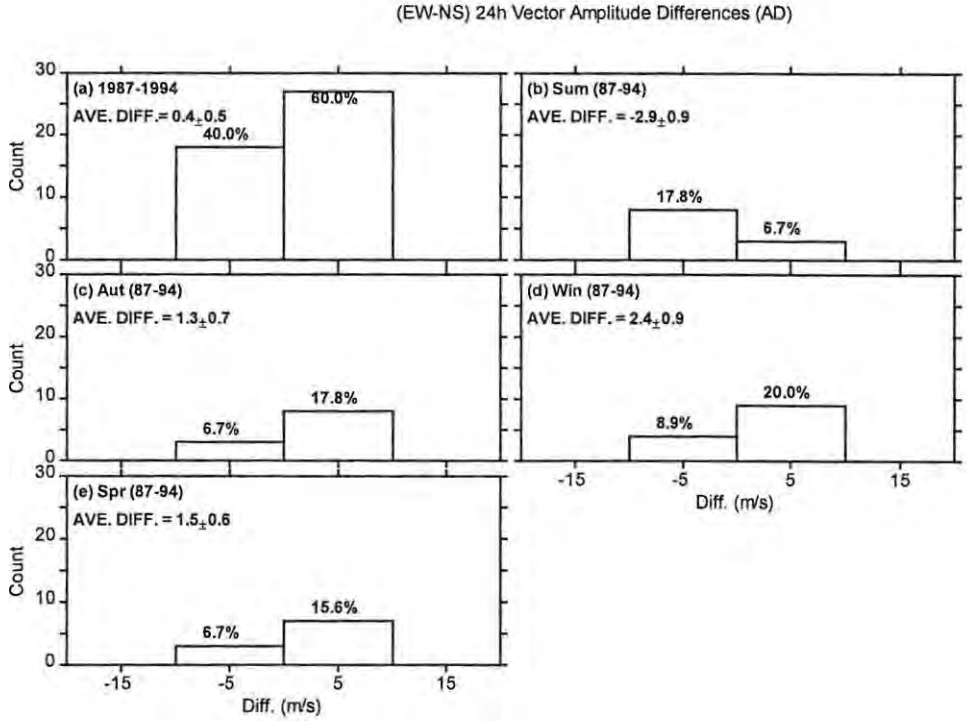

Figure 6.12 Same as **Figure 6.11** but for Adelaide.

To put the main features of the observations made at Grahamstown and Adelaide in a global context, I considered observations made by other authors from ground-based observations as well as by satellite instruments. Starting with ground-based observations, we find that there are reports of a semi-annual variation of tidal amplitudes. For instance, *Vincent et al.* [1988] reported this behaviour for the period 1983-1985 at Adelaide. This seasonal pattern was also observed at high latitudes by *Fraser et al.* [1995], who found peak tidal amplitudes during late winter/spring and in autumn in 2-year (1983-1984) means at Heiss Island (81°N). However, this behaviour seems to slightly fade in their long-term (1965-1985) means especially in the case of zonal amplitudes. These authors found that the long-term trend (1971-1986) of the meridional amplitude at Molodezhnaya (68°S) was more annual in nature with a peak in summer and a minimum in winter. For the zonal amplitude at this site, they found very small seasonal changes.

For a satellite perspective, I consider results from both HRDI and WINDII. The 1992 HRDI results show somewhat similar diurnal tidal behaviour for the ~90 km height range at 30°S latitude to those presented above [*Khattatov et al.*, 1997a]. The meridional monthly mean amplitudes show equinoctial peaks of about 50 ms^{-1} in March/April and a secondary peak of ~40 ms^{-1} in spring [*Khattatov et al*, 1997a]. The sense of this equinoctial asymmetry is similar to that at Grahamstown and Adelaide but the satellite peaks are more than twice as large. For the solstices these authors found values of ~10-30 ms^{-1}. From HRDI observations made during November 1991 to February 1995, *Burrage et al.* [1995a] found that the amplitudes of the (1, 1) diurnal tide (for 20° latitude and 95 km altitude) showed a semi-annual variation characterised by equinoctial maxima and solstitial minima.

The WINDII results [*McLandress et al.*, 1996] for 30°S at 90 km also show that the diurnal tidal amplitudes have a semi-annual pattern characterised by equinoctial maxima ($\geq$20 ms^{-1}) and solstitial minima. For the meridional component the autumn and spring maxima are comparable whereas for the zonal component the autumn maximum is larger than the spring one. This satellite meridional symmetry and zonal asymmetry in equinoctial amplitudes are similar to observations made at Grahamstown and Adelaide. The WINDII results also show some solstitial asymmetry with larger amplitudes in summer than in winter for the meridional component while the opposite seems to be true for the zonal component. In fact the summer

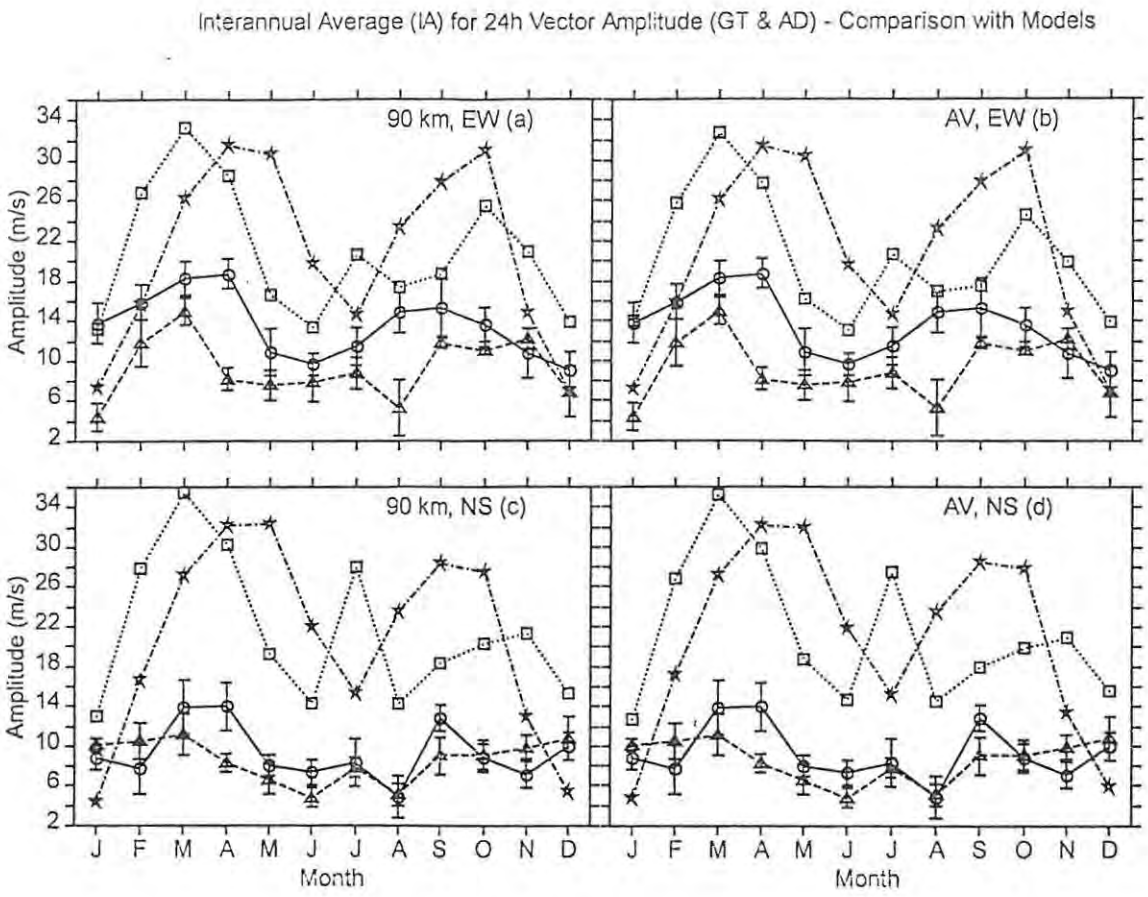

Figure 6.13 Comparison of the diurnal amplitude IAs at Grahamstown and Adelaide with the GSWM-00 and the diurnal tide model (DTM) of *Portnyagin et al.* (a) Zonal amplitudes with different symbols representing Grahamstown IA (circles), Adelaide IA (triangles), GSWM-00 (pentagons) and DTM (squares) for model heights of ~ 90 km. (b) Same as (a) but for Gaussian weighted model amplitudes. (c) and (d) are similar to (a) and (b) respectively but for meridional amplitudes.

meridional amplitudes are comparable to the equinoctial values, which is similar to the Adelaide observations.

Having compared my results to ground-based and satellite observations, I now compared them to model results. In particular, I have compared my results to the GSWM, which is widely used in the MLT community (e.g. *Akmaev et al.*, 1996; *Vincent et al.*, 1998) for comparison. The GSWM version used in this thesis (e.g. Figure 6.13) is the GSWM-00 [*Hagan et al.*, 1995; *Hagan et al.*, 1999; *Hagan et al.*, 2000, in press] that was obtained through Hagan from the CEDAR Database. The GSWM results used in this figure correspond to 90.57 km altitude and 33°S latitude. Also shown in Figure 6.13 is the diurnal tide model (DTM) of *Yu. Portnyagin*

[private communication] for a height of 90 km and 32.5°S latitude. As I did in Section 4.3.1.1, the model results have been appropriately height integrated for some of the plots.

The IAs at Grahamstown and Adelaide for both the zonal and the meridional diurnal amplitudes are qualitatively similar to both models. Another important point to note is that height averaging does not significantly affect the model amplitudes. In line with the observations at Grahamstown and Adelaide, the underlying structure of diurnal amplitudes is characterized by semi-annual variation with peaks during the equinoxes. However, the DTM also shows some winter peaks. With the exception of summer when the observed amplitudes are comparable or larger than the model results, the general trend for the other seasons show large model amplitudes. The largest discrepancies are recorded around the equinoxes with models tending to overestimate the amplitudes. This is a direct opposite of the GSWM-95 [*Hagan et al.*, 1999], which underestimated equinoctial amplitudes (see, for instance Figure 2 of *Hagan et al.* [1999]). However, looking at individual years (Figure 6.9 and Figure 6.10) we see that the equinoctial amplitude peaks of ~30-34 ms^{-1} given by the models are comparable to observed amplitude peaks of ~29 ms^{-1} especially at Grahamstown for some years (e.g. 1988, 1990 and 1993). The winter amplitudes of the models also compare well with those for some years. These similarities suggest that some of the discrepancies observed in Figure 6.13 can be explained by interannual variations, which are the subject of the next subsection (Section 6.3.2). Although height integration has an insignificant effect on model amplitudes, this averaging process cannot be discounted as a possible source of the discrepancy as well. It has to be borne in mind that turbulent effects and gravity wave drag can cause amplitude reduction [*Hagan et al.*, 1995], which may have serious implications on height integration.

In general, the results I have presented so far indicate that the diurnal tide varies with season. Some of these seasonal changes could be due to changes in the atmospheric basic state. From their comparative investigation using different atmospheric inputs, *Hagan et al.* [1999] found that changes in background mean wind and ozone densities do change the diurnal tidal structure especially at altitudes (90-110 km) and latitudes (20-30°) at which the tide maximizes. More specifically, they found that strato-mesospheric ozone reductions produce enhancements in the diurnal tidal amplitudes during both the solstices and the equinoxes, and an enhancement of the solstice semidiurnal tide but no clear pattern during the equinoxes. However, *Hagan et al.* [1999] point out that the effects of ozone were overshadowed by changes in the background

wind field, which can cause changes of up to 30 % in the GSWM MLT tides. *Hagan et al.* [1999] found that during the equinoxes the diurnal tide is more sensitive to stratospheric wind changes whereas the semidiurnal tide responds more to the MLT wind field. During the solstices the sensitivities are reversed i.e. the diurnal tide is more sensitive to MLT wind changes and the semidiurnal tide to stratospheric wind modifications.

A dominant feature of the seasonal trend of the tidal amplitudes is the semi-annual variation, which has been observed at Grahamstown, Adelaide, by other ground-based instruments, by satellite (HRDI and WINDII) and has also been shown to exist in tidal models. As mentioned by *McLandress* [1997], the cause of this semi-annual variation is not yet known. However, a number of suggestions have been made regarding its source and some of these will be discussed below.

Hagan et al. [1999] showed that the GSWM-98 equinoctial coefficients of effective Rayleigh friction are an order of magnitude smaller than the solstitial ones. This equinox-solstice asymmetry could possibly account for the above semi-annual variation. Further work on the seasonal variation of the diurnal tide has been done by *McLandress* [1997]. This author used the Canadian Middle Atmosphere Model (CMAM) to model the diurnal tide. He found that 2-year simulations of meridional amplitudes for 19°N and 19°S show that in the upper mesosphere there is a strong semi-annual variation with equinoctial maxima (60 ms^{-1}) with amplitude dropping to below 10 ms^{-1} at 70 km in summer. This author also simulated a similar semi-annual variation in the diurnal temperature tide at 90 km. *McLandress* [1997] used the CMAM to investigate two possible sources of the seasonal diurnal tide variability, which are tidal heating and planetary waves. With regard to tidal heating, he considered the different diurnal tidal heating mechanisms, namely, absorption of ultraviolet radiation by stratospheric ozone, mesospheric heating by ozone, absorption of infrared solar radiation by tropospheric water vapour and deep convective heating. To quantify the importance of solar and deep convection heating in tidal variability, *McLandress* [1997] used CMAM heating to force a simple mechanistic tidal model. From his results, he concluded that the semi-annual variation simulated by CMAM is not caused by the variations of the dominant thermotidal heating mechanisms.

Coming to the role of planetary waves in causing seasonal modulations of the diurnal tide,

McLandress [1997] used the Eliassen-Palm flux divergence (EPFD) which, as he mentions, is a diagnostic of the zonally averaged circulation and also indicates the existence of transient and dissipative waves. He found that there was correlation in time and space between the regions of strong EPFD and weak diurnal tide amplitudes suggesting a possible damping of the diurnal tide through non-linear effects. Support for this view came from *Norton & Thuburn* [1999] who, based on their General Circulation Model (GCM) results, concluded that non-linear interaction between the 2-day wave and the diurnal tide results in the leakage of energy from the diurnal tide. *Norton and Thuburn* [1999] further argue that since the 2-day wave is most active during both solstices, the associated damping of the diurnal tide results in the observed semi-annual tidal amplitude variation.

To investigate a possible damping of the diurnal tide through the non-linear processes suggested above, I have plotted the summer instantaneous amplitudes of the diurnal tide and the 2-day wave obtained through complex demodulation (Figure 6.14). There are instances that are in line with the leakage of diurnal tidal energy as a result of a possible non-linear interaction. For instance around 24 January in 1987 and 1992 small diurnal amplitudes are recorded during peak 2-day amplitudes. Conversely, large diurnal amplitudes are recorded during times of weak 2-day wave activity. Examples that stand out in this regard include the following approximate dates: 14 January 1989, 07 January 1990, and 31 January 1993. However, this apparent inverse correlation between the diurnal tide and the 2-day wave does not always hold as can be seen from around 29 January to 23 February of 1990. This seems to indicate that even if there is a damping of diurnal amplitudes through non-linear interactions there are other factors that complicate this process.

As discussed in Chapter 4, Section 4.3.1.1, gravity waves can cause significant wave drag at the level of their deposition and this process is strongly influenced by the mean flow environment through which these waves propagate. It is therefore expected that since the diurnal tide strongly modulates the mesospheric wind field, there could be a similar modulation of the wave drag, which will in turn damp or amplify the diurnal tide (see Section 5.2 for details regarding this mechanism). *Norton and Thuburn* [1999] conducted an experiment in which an interaction

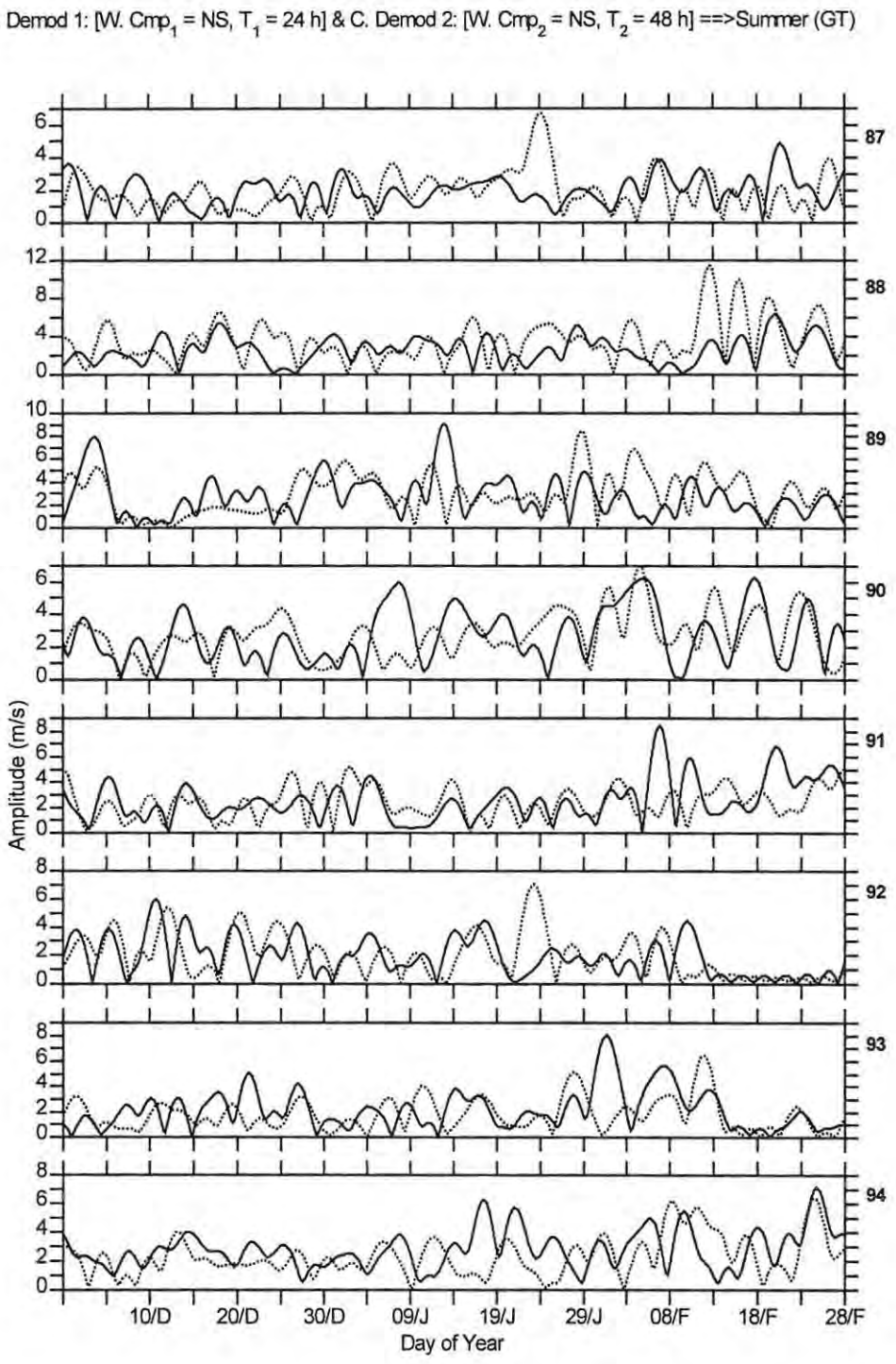

Figure 6.14 The instantaneous amplitude of the diurnal tide (solid line) and the 2-day wave (dotted line) for the summer seasons of the years 1987-1994 (indicated next to each panel) at Grahamstown. Day of year is given by day of month/month (D = December, J = January, F = February).

between the tide and gravity waves was suppressed. Similar to their other results (see a few paragraphs above), they still found results that showed a possible leakage of the energy of the diurnal tide as a result of its non-linear interaction with the 2-day wave. Based on this, these authors concluded that the direct interaction of gravity waves and tides is not necessary for the production of the semi-annual variation of tidal amplitudes.

On the contrary, work by various other authors seem to suggest that the semi-annual variation of the diurnal tide could be linked, in one way or another, to gravity wave effects. *Mayr et al.* [1998] used Hines' Doppler Spread Parameterization (DSP) [*Hines*, 1997a, b] and a Numerical Spectral Model (NSM) [*Chan et al.*, 1994] to study gravity wave effects. These authors found that while the effect of gravity wave momentum was small below ~60 km, it increases the amplitude at higher altitudes. From their model results, they found that near the equator, the zonal mean flow is dominated by a semi-annual oscillation (SAO) with the annual oscillation (AO) assuming dominance outside the tropics. For the AO the zonal mean flow is westward in summer and eastward in winter at 50 km and the opposite is true at 80 km. These authors suggest that the AO results in a preferential absorption of gravity waves during the solstices, a time at which the zonal winds are at their peak. Consequently, a significant proportion of gravity waves with large magnitudes are able to reach the upper mesosphere during the equinoxes resulting in amplitude amplification. These authors also found that gravity waves tend to reduce the vertical wavelength of the tide in the 80-120 km altitude range, the net effect of this being a shift of phases to earlier times during the equinoxes. The significance of this will be discussed when we come to phases in Section 6.4.

By using the GSWM and a 'hybrid Lindzen/Matsuno' gravity wave parameterisation, *Meyer* [1999] came to the following conclusions regarding the effect of gravity waves on the diurnal tide. The observed seasonal variation of the diurnal tide can be explained by the seasonal variations in the gravity-wave-based eddy diffusion and wave stress. This seasonal variation in the eddy diffusion and wave stress are due to the seasonal variation of the background atmosphere which, in turn, results in a seasonally dependent selective transmission of gravity waves according to linear saturation theory. An important point to note here is that, *Meyer* [1999] ran a test which showed that if one uses a varying background atmosphere and a seasonally invariant eddy diffusion, Rayleigh friction and tidal forcing, the tide departs from the usual semi-annual behaviour. Therefore, the background atmosphere indirectly influences

the diurnal tide. In fact, Meyer concluded that it is both the mean eddy diffusion $\overline{\nu}_{eddy}$ and the diurnal harmonic of the momentum flux divergence (i.e. diurnal wave stress) f_x' that have a damping effect on the tide with larger damping from both happening during the solstice. This might explain the semi-annual variation reported above.

6.3.1.2 Longitudinal Seasonal Trends

The amplitude behaviour at Grahamstown and Adelaide is shown in Figure 6.15 and Figure 6.16 for the zonal and meridional amplitudes, respectively. For both components there are clear differences in the amplitudes observed at the two sites. In general, the zonal amplitudes have a tendency to be larger at Grahamstown than at Adelaide except in November (see IA). The frequency distribution (Figure 6.17) shows that larger amplitudes at Grahamstown than at Adelaide account for 74 % of the zonal amplitude differences. The meridional amplitudes show a somewhat complicated comparison characterised by larger amplitudes at Grahamstown from March to June and in September. During the other months, the meridional amplitudes are either larger at Adelaide or they are equal at both sites. In the meridional case, as it was for the zonal amplitudes, larger amplitudes at Grahamstown than at Adelaide account for most (60 %) of the differences (see Figure 6.18(a)).

Since Grahamstown and Adelaide are almost on the same latitude (34°S) some of the above tidal amplitudes differences at the two sites are due to longitudinal differences in the tidal structure. Such longitudinal differences have been studied observationally (e.g. *Lysenko et al.* [1994]) and theoretically (e.g. *Miyahara et al.* [1993]; *Williams & Avery* [1996]; *Hagan et al.* [1997]; *Ekanayake et al.* [1997]). Satellite results have also shown longitudinal differences in the diurnal tide and these have been attributed to nonmigrating tidal components [*Khattatov et al.*, 1996]. A number of mechanisms have been suggested as possible sources of non-migrating modes. *Forbes & Groves* [1987] used an equivalent gravity wave *f*-plane model to show that longitudinal changes in the diurnal insolation absorption by tropospheric H_2O can result in longitudinal differences of at least ±12-15% about the zonal mean of diurnal tidal amplitudes in the 0-20° latitude belt and 80-100 km altitude. These authors also report phase variations of ±0.75 h.

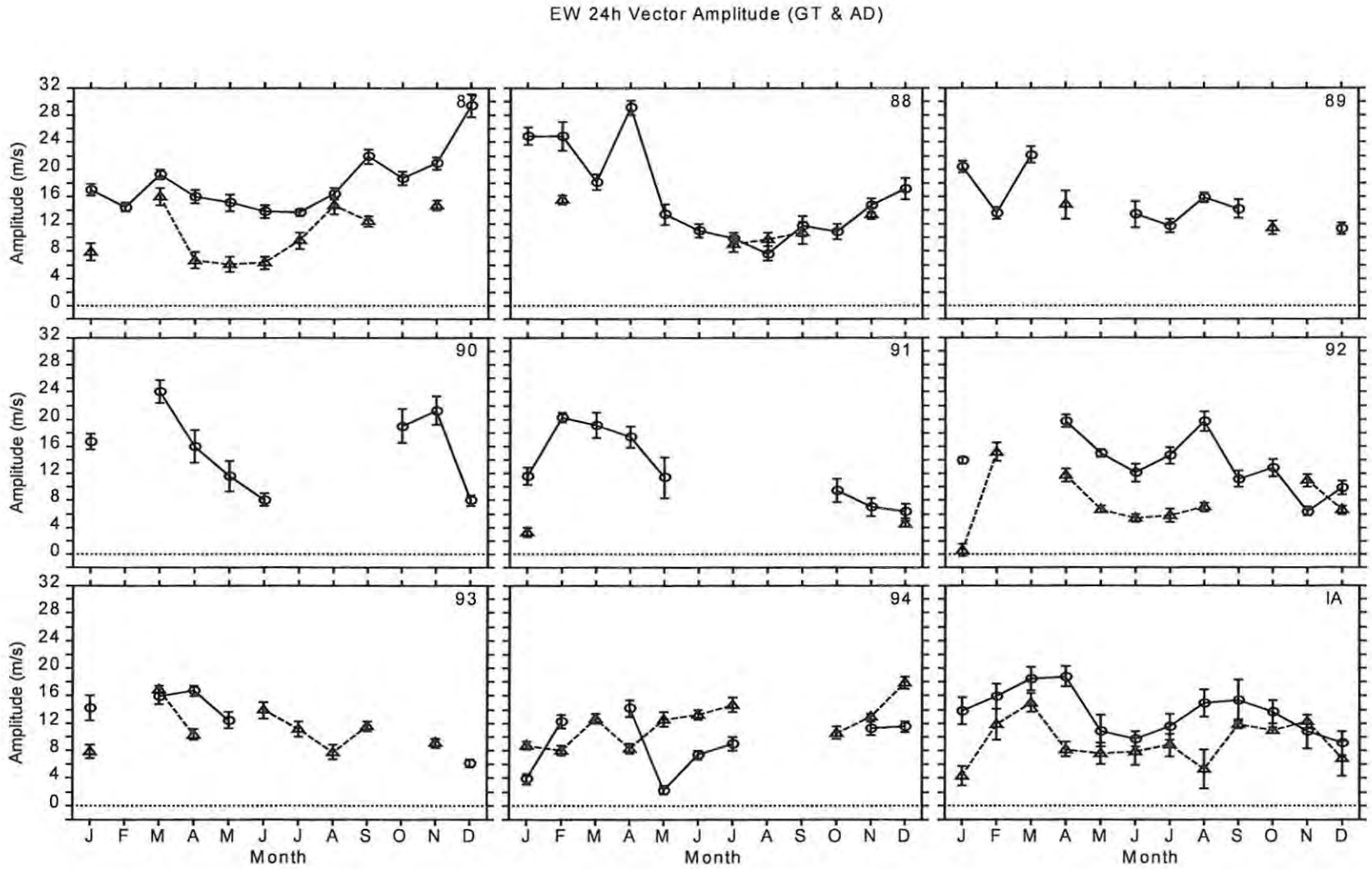

Figure 6.15 The zonal amplitudes of the diurnal tide at Grahamstown (circles) and Adelaide (triangles) for the years 1987-1994 and the IA. The error bars represent one standard error of the mean (1 α).

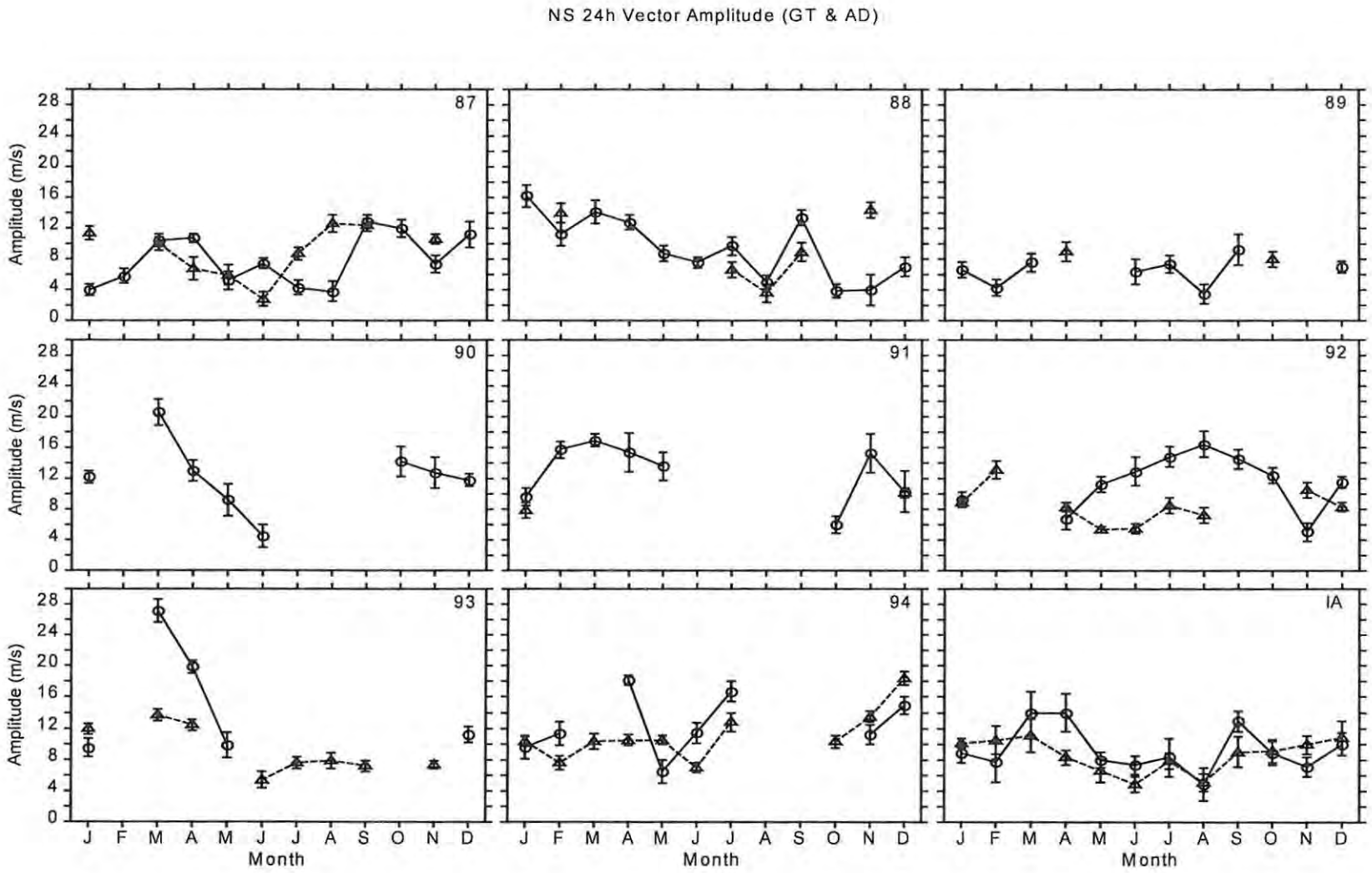

Figure 6.16 Same as **Figure 6.15** but for the meridional amplitudes.

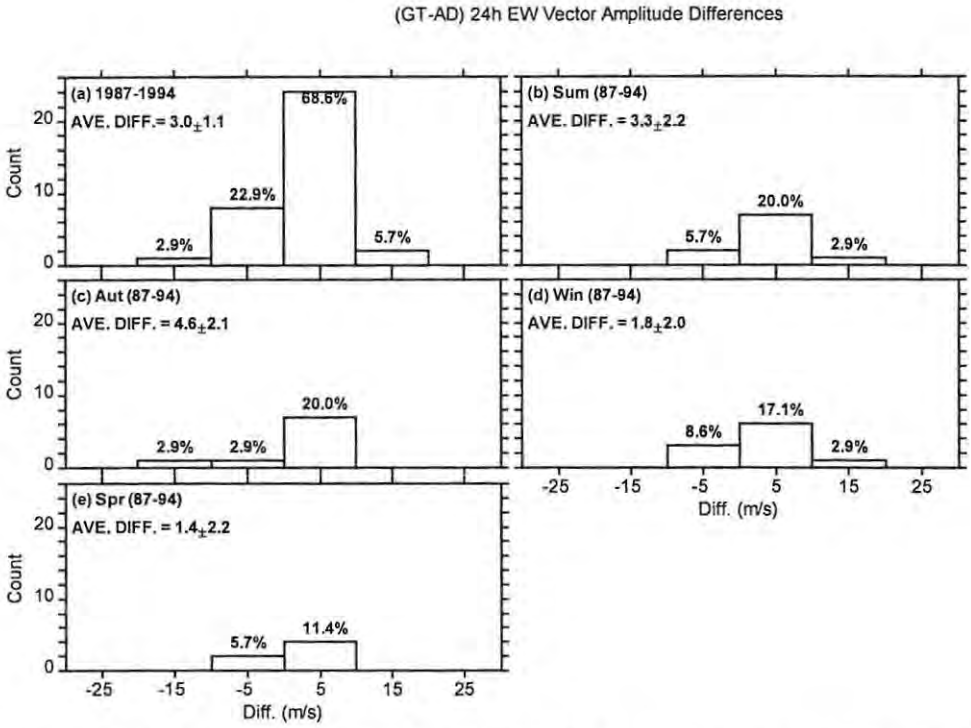

Figure 6.17 The distribution of the (GT-AD) amplitude differences for the zonal diurnal tide for the years 1987-1994. The weighted average differences are also given and the percentage count of each bar.

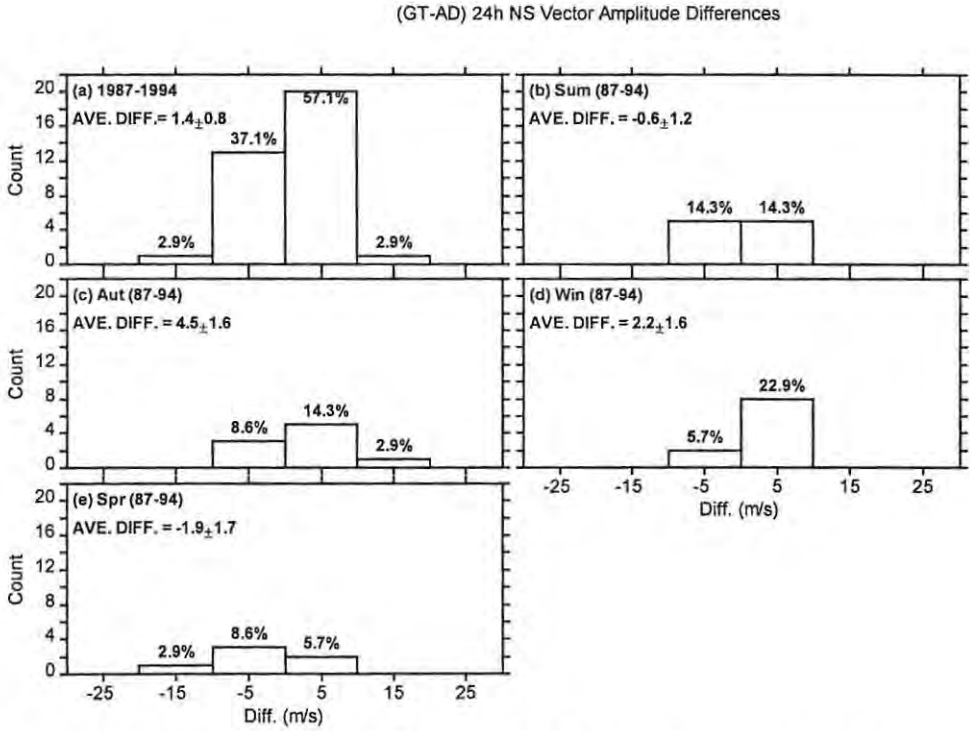

Figure 6.18 Same as **Figure 6.17** but for the meridional amplitudes.

Williams & Avery [1996] considered the generation of nonmigrating modes due to latent heat released by nonmigrating diurnal oscillations in deep convective precipitating clouds. This study showed important results with the only drawback being the fact that it is limited to latitudes within ±30°.*Williams & Avery* [1996] found that at the equator, the diurnal tide due to latent heat release was comparable to that due to solar insolation absorption by water vapour and reached values of 10 ms^{-1}. The phases were however found to be different due to the difference in the zonal numbers associated with each mechanism something that will be relevant to the phases to be discussed in Section 6.4. The water vapour tide was dominated by the migrating (1, 1, 1) mode while the cloud related tide was dominated by either the nonmigrating (1, 5, 5) mode up to about 75 km altitude or the (1, -3, 3) mode above 75 km altitude [*Williams & Avery*, 1996]. The mode notation adopted by *Williams & Avery* [1996] is (σ, s, n) where σ, s, and n represent the 'radian frequency' of the tide, the integer zonal wavenumber and the meridional index, respectively.

Further work on this subject was conducted by *Hagan et al.* [1997] who used the GSWM. These authors applied the latent heat release associated with deep convective activity (DCA) based on *Williams & Avery* [1996] and heating due to absorption of solar IR radiation by water vapour based on *Groves'* [1982] work. *Hagan et al.* [1997] found that the IR nonmigrating contribution was negligible ($\leq 2ms^{-1}$) compared to the migrating tide (max ~60 ms^{-1}). This is in contrast to the relatively higher contribution (reported above) found by *Forbes and Groves* [1987] who used identical IR heating rates. *Hagan et al.* [1997] suggest that the difference could be attributed to the fact that *Forbes and Groves* [1987] used a windless model.

Regarding DCA forcing, *Hagan et al.* [1997] found that the DCA nonmigrating diurnal signatures were comparable to the DCA migrating ones. They found the strongest (max ~6 ms^{-1}) components for the meridional amplitudes at latitudes within ±35° to be those associated with zonal wavenumbers s = 0, +1 and +2. For zonal amplitudes, the s =-3 component was the strongest (max > $8ms^{-1}$) for the same latitude range. More specifically, *Hagan et al.* [1997] found that while the IR nomigrating contribution in the MLT region is insignificant, that due to the combined effects of the s = -3, 0, +2 and +5 components of latent heat forcing modulate the diurnal tide by up to 10 ms^{-1} (30 %). These magnitudes are consistent with the amplitude differences between Grahamstown and Adelaide which are mainly (68.6 % (EW) and (57.1 %

(NS)) in the 0-10 ms^{-1} range (Figure 6.17 and Figure 6.18)

More work in this area has also been done by *Ekanayake et al.* [1997] using a 2-D steady state model. The thermotidal heating sources included latent heating, dry convective heating and eddy thermal conduction heating. *Ekanayake et al.* [1997] found that although the average zonal amplitudes of the diurnal tide in the 27.5-85°S latitude range at 90 km altitude was dominated by the migrating mode with a mean amplitude of about 8.5 ms^{-1}, there was also some contribution from non-migrating modes. Their zonal wavenumber amplitude spectrum also shows that (at 27.5-85°S latitude range at 90 km altitude) there is a stronger (amplitude total ~8 ms^{-1}) contribution from the eastward nonmigrating components than from their stationary and westward propagating counterparts, which have total amplitudes of <0.5 ms^{-1} and ~2 ms^{-1}, respectively. These authors also found that nonmigrating westward (eastward) propagating tides have larger mean amplitudes than those propagating eastward (westward) in the 30-85°N (30-85°S) at 60 km and 80 km where the zonal is eastward (westward). *Ekanayake et al.* [1997] point out that the Doppler effect makes it possible for the nonmigrating tides to propagate vertically poleward of ±30° latitudes in agreement with the findings of *Miyahara et al.* [1993].

6.3.2 Interannual Trends

Figure 6.19 and Figure 6.20 show the EW/NS comparison of the interannual variation at Grahamstown and Adelaide, respectively. These figures show that tidal amplitudes exhibit great interannual variability that is comparable to the seasonal variability discussed in Section 6.3.1. The interannual variations of similar magnitudes have been reported by *Fraser et al.* [1989] at a number of sites. In general my results do not show any clear pattern in the interannual changes. However, the zonal amplitudes at Grahamstown tend to be larger than the MIA for the years 1987-1990 in November to January. The interannual variation in the zonal amplitudes is not necessarily correlated to those of their meridional counterpart. However, correlation between the zonal and the meridional component can occur e.g. in January and February at Grahamstown.

More interesting is the fact that there is no obvious relationship between the interannual

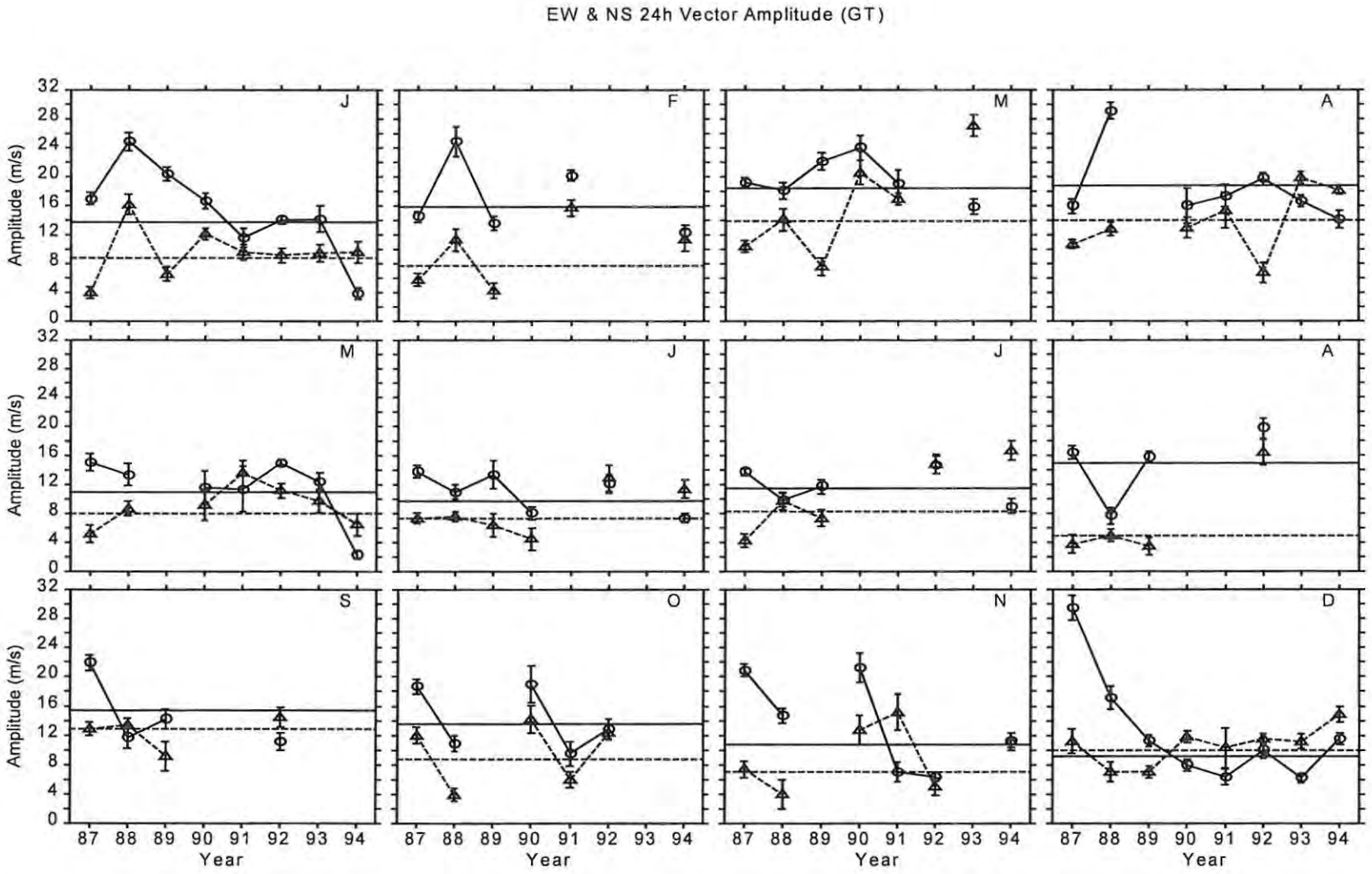

Figure 6.19 The interannual variation of the zonal (circles) and meridional (triangles) of the diurnal amplitudes at Grahamstown for different months. The horizontal solid and dashed lines represent the corresponding MIA for the zonal and the meridional amplitudes, respectively. The error bars represent one standard error of the mean (1 α).

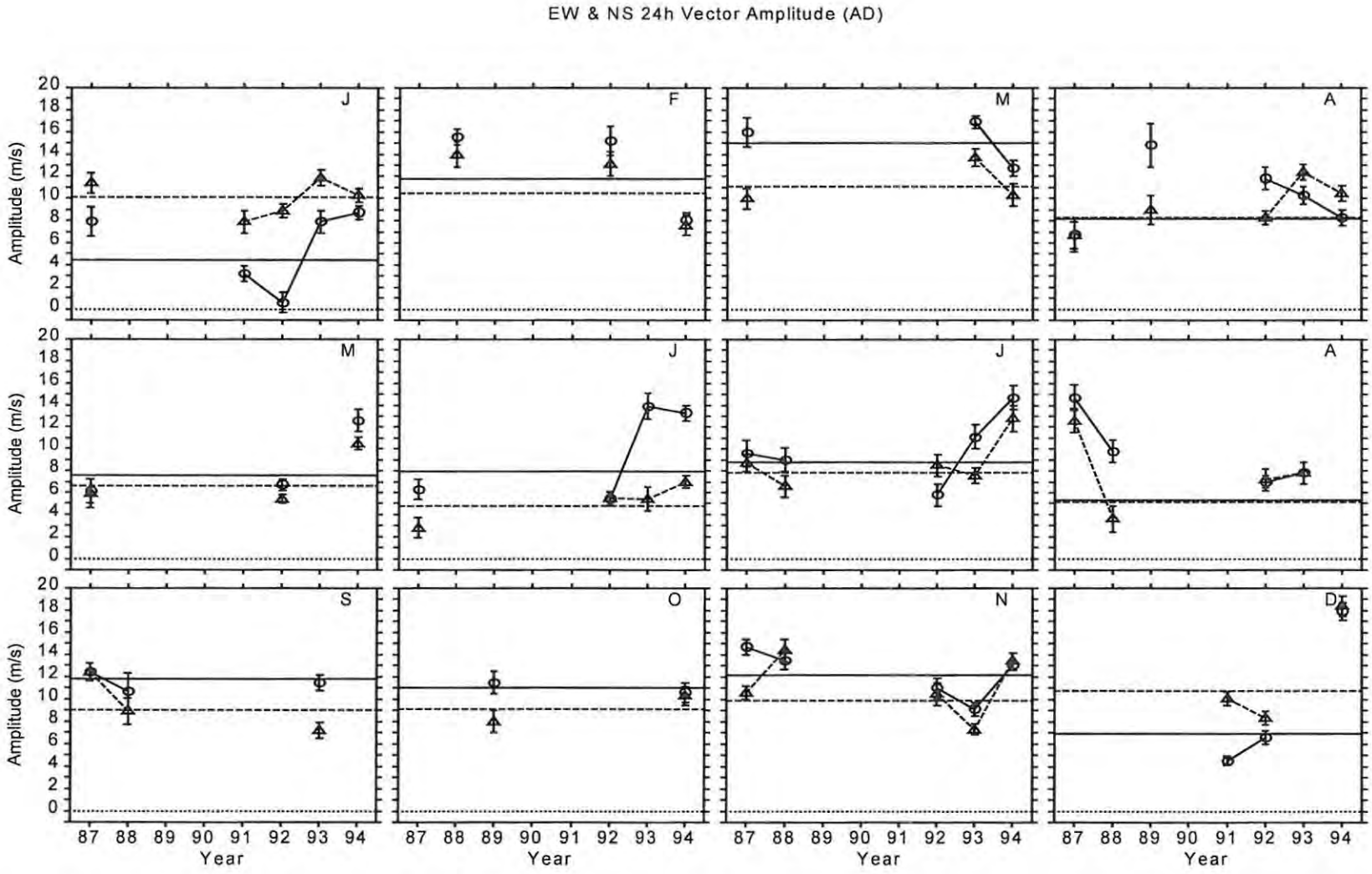

Figure 6.20 Same as **Figure 6.19** but for Adelaide.

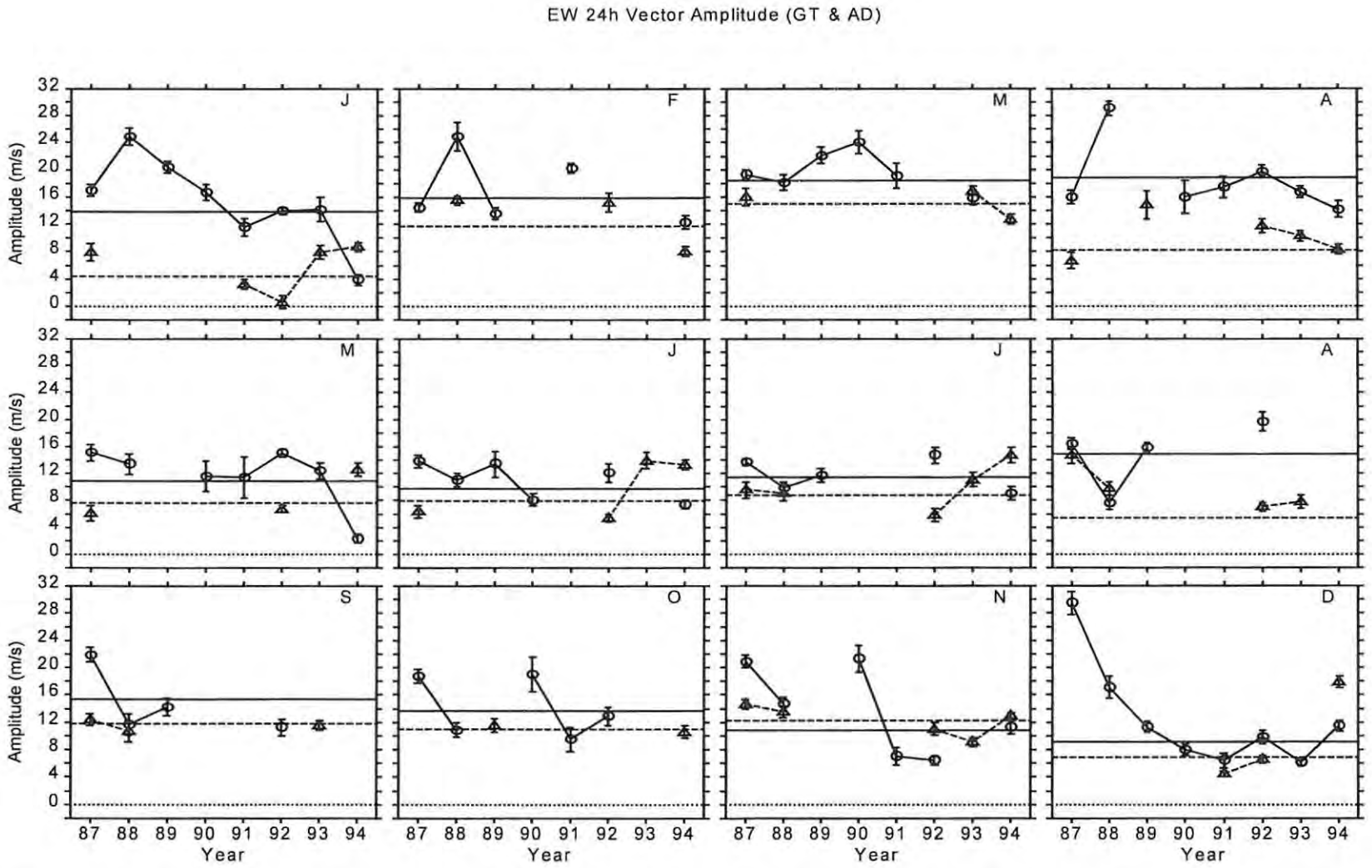

Figure 6.21 The interannual variation of the zonal amplitudes of the diurnal tide at Grahamstown (circles) and Adelaide (triangles) for different months. The horizontal solid and dashed lines represent the corresponding MIA for Grahamstown and Adelaide amplitudes, respectively. The error bars represent one standard error of the mean (1 α).

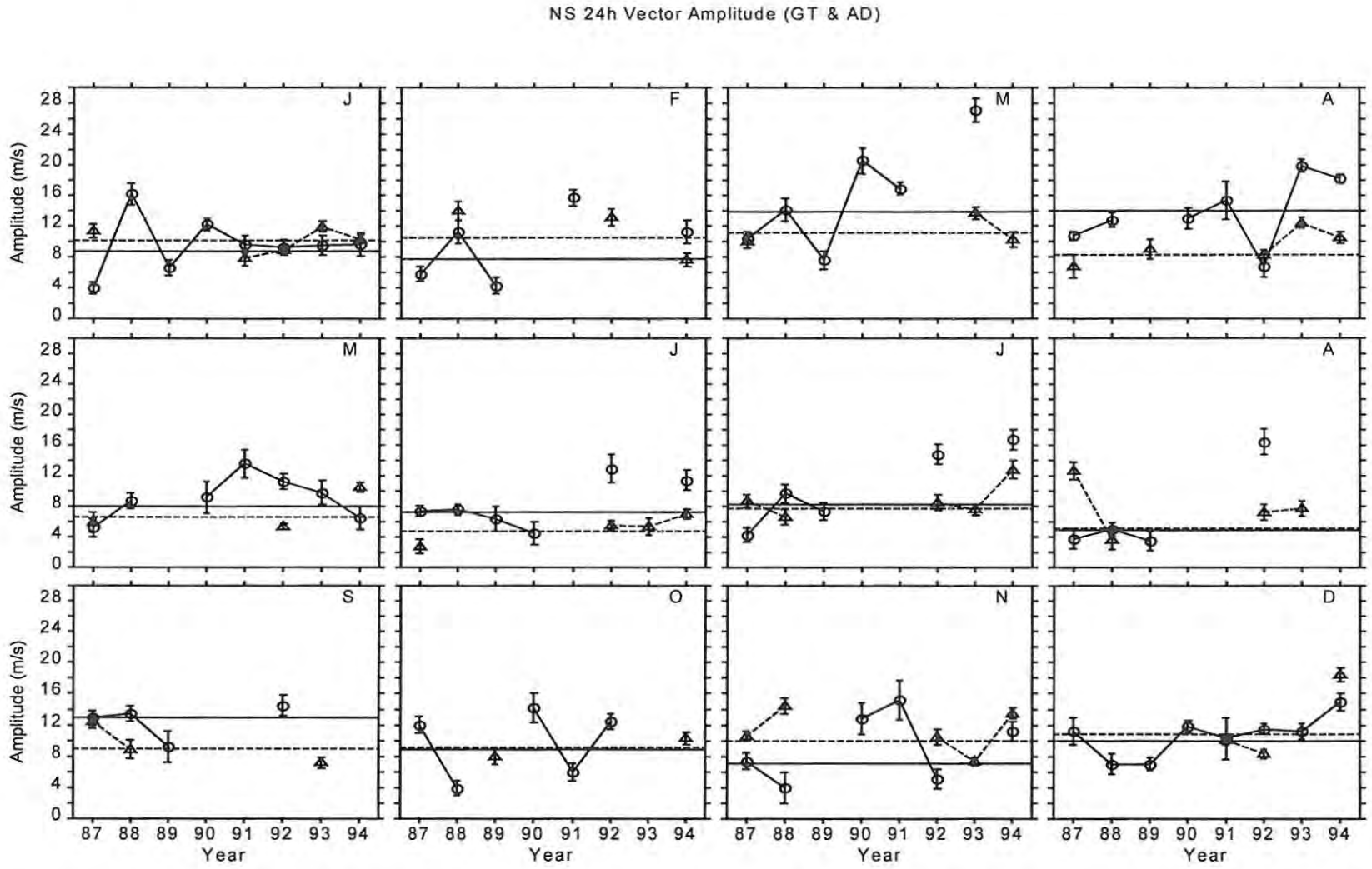

Figure 6.22 Same as **Figure 6.21** but for meridional amplitudes.

variations at Grahamstown and those at Adelaide for both the zonal (Figure 6.21) and meridional (Figure 6.22) amplitudes. This shows that there is a complex response in the nonmigrating tides to interannual variations. Whereas at Grahamstown the interannual changes are more intense in late spring/summer and to some extent also in autumn, at Adelaide they are more pronounced in autumn (March and April). *Vincent et al.* [1998] found that 12-year data from Adelaide show an approximately biennial change in diurnal amplitudes. From their investigation of the possible link between the equatorial zonal QBO and tidal variations, they found that during the years when the QBO flow is mainly eastward, the diurnal amplitudes are mostly larger than the 12-year average from January to June and were almost always smaller than this average during years of a predominantly westward QBO flow. For the rest of the year they did not find any clear pattern.

The link between the QBO and the tides is not fully understood and could be related to variations in forcing, in the background atmosphere and in dissipation [*Vincent et al.*, 1998]. These authors suggested a number of possible mechanisms in this regard. Noting *Hagan's* [1996] results that show, as mentioned earlier, that the total diurnal tide in the MLT region involves a dominant tropospheric IR forcing and a weaker out-of-phase stratospheric UV forcing by ozone, *Vincent et al.*, [1998] suggest that QBO related changes to ozone profiles would result in similar changes in the interferences between the IR and the UV forcing. This effect is more likely to affect the amplitudes than the phases because phases follow those of the dominant IR source even when the UV forcing changes.

The second suggestion made by *Vincent et al.* [1998] has to do with dissipative effects. Although experiments based on the GSWM show that the diurnal tide is comparatively insensitive to changes in MLT background winds [*Burrage et al*, 1995a], the mean wind can still indirectly affect this tide through dissipative effects. Any QBO modulated variation of mesospheric gravity wave fluxes and dissipation as a result of, say, selective filtering (see e.g. Chapter 4, Section 4.2.3), could result in similar modulations of tidal amplitudes [*Vincent et al*, 1998]. How these suggestions can possibly explain the longitudinal differences in the interannual variability (or conversely interannual variability in longitudinal differences) at Grahamstown and Adelaide is not clear, but as suggested by the semidiurnal tide observations of *Jacobi et al.* [1999], the longitudinal differences in tides could also change with time. We will look at this in detail in Chapter 7.

6.4 PHASES

6.4.1 Seasonal Trends

As mentioned in Section 5.2, the phase of a tide is the local solar time (LST) of the first maximum eastward (northward) for the zonal (meridional) component of the tide. The monthly phases were obtained through vector averaging as explained in Section 6.3.1.1. The seasonal changes of the zonal and meridional phases of the diurnal tide are shown in Figure 6.23 (Grahamstown) and Figure 6.24 (Adelaide). These figures show that the phases are characterized by great seasonal fluctuations as well as interannual changes. Looking at the IA at Grahamstown there is a tendency for the solstice months to have later phases (especially in summer) compared to the equinoxes for both the zonal and the meridional component. This is consistent with the view held by *Mayr et al.* [1998], and discussed earlier in Section 6.3.1, that gravity waves reduce the vertical wavelength of the tide in the 80-120 km altitude range resulting in a phase advance during the equinoxes. In line with this, the HRDI results for 20° latitude and 95 km altitude also suggest a solstitial phase delay [*Burrage et al.*, 1995a]. As opposed to the semi-annual phase structure at Grahamstown, the Adelaide pattern is more annual in nature with latest phases recorded in summer followed by a phase advance between autumn and spring. At both sites the zonal and meridional phases are better correlated than their amplitude counterparts. WINDII results for 35°S at 90 km [*McLandress et al.* 1996] show less seasonal variation in meridional phases with values of ~12 h in October/November. Their zonal phases show greater seasonal variation with earlier (~6-9 h) phases in summer and the equinoxes and later (~24 h) phases in winter.

In Figure 6.25 I have shown a comparison of the phase IAs at Grahamstown and Adelaide with the GSWM-00 and DTM as I did for the amplitudes in Section 6.3.1. Both models and observations of the zonal phases compare well in autumn and winter, while the GSWM-00 shows a phase advance in spring and summer. For the meridional component, the DTM phases compare well with the observations at Grahamstown and Adelaide whereas the GSWM-00 show phases are ~10-18 h earlier than the other results. As was the case with the corresponding amplitude comparison (Figure 6.13), the application of height averaging does not significantly change the model amplitudes. This implies that even though the diurnal tide is expected to have

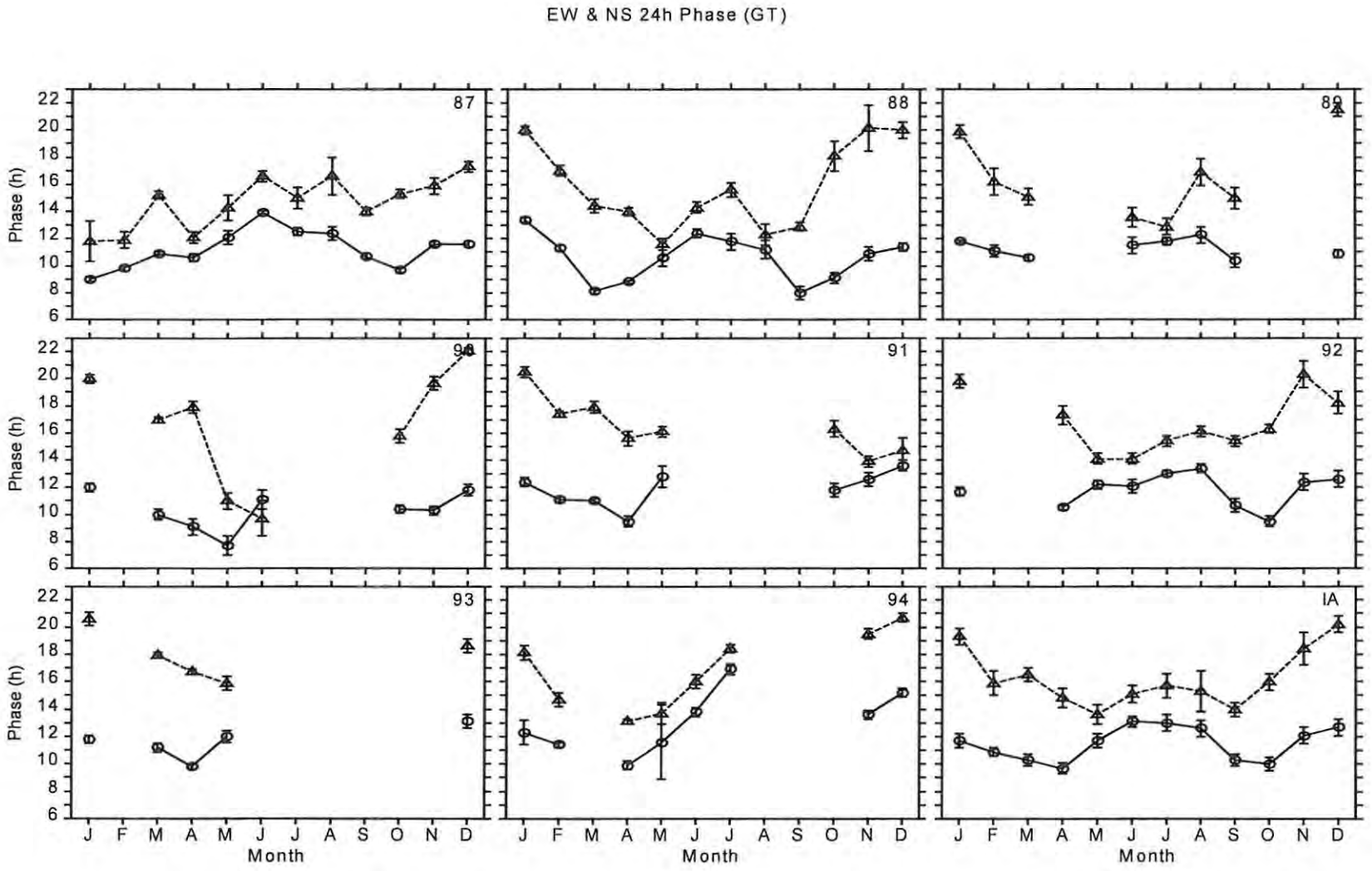

Figure 6.23 The zonal (circles) and the meridional (triangle) phases of the diurnal tide at Grahamstown for the years 1987-1994 and the IA. The error bars represent one standard error of the mean (1 α).

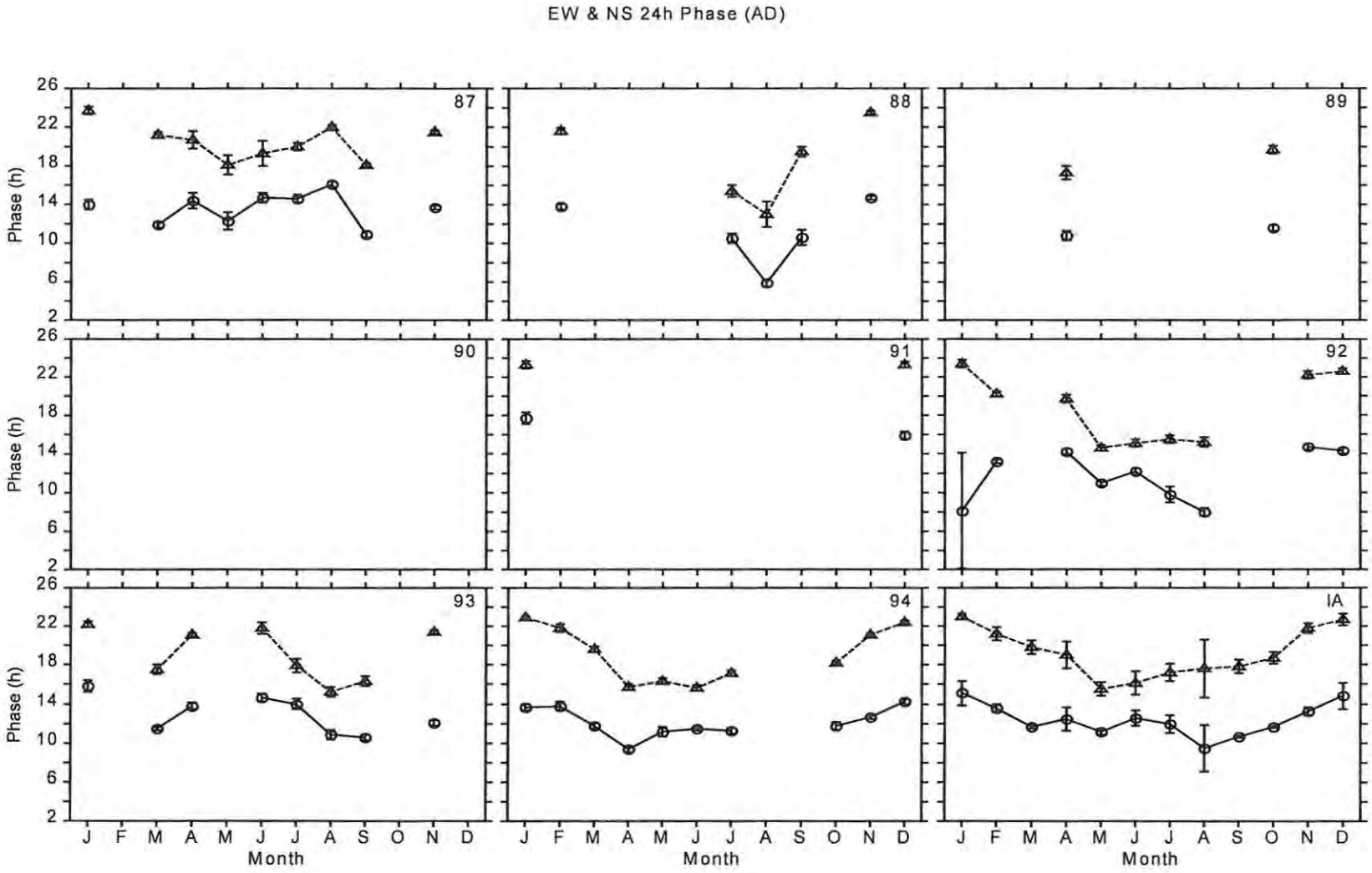

Figure 6.24 Same as **Figure 6.23** but for Adelaide.

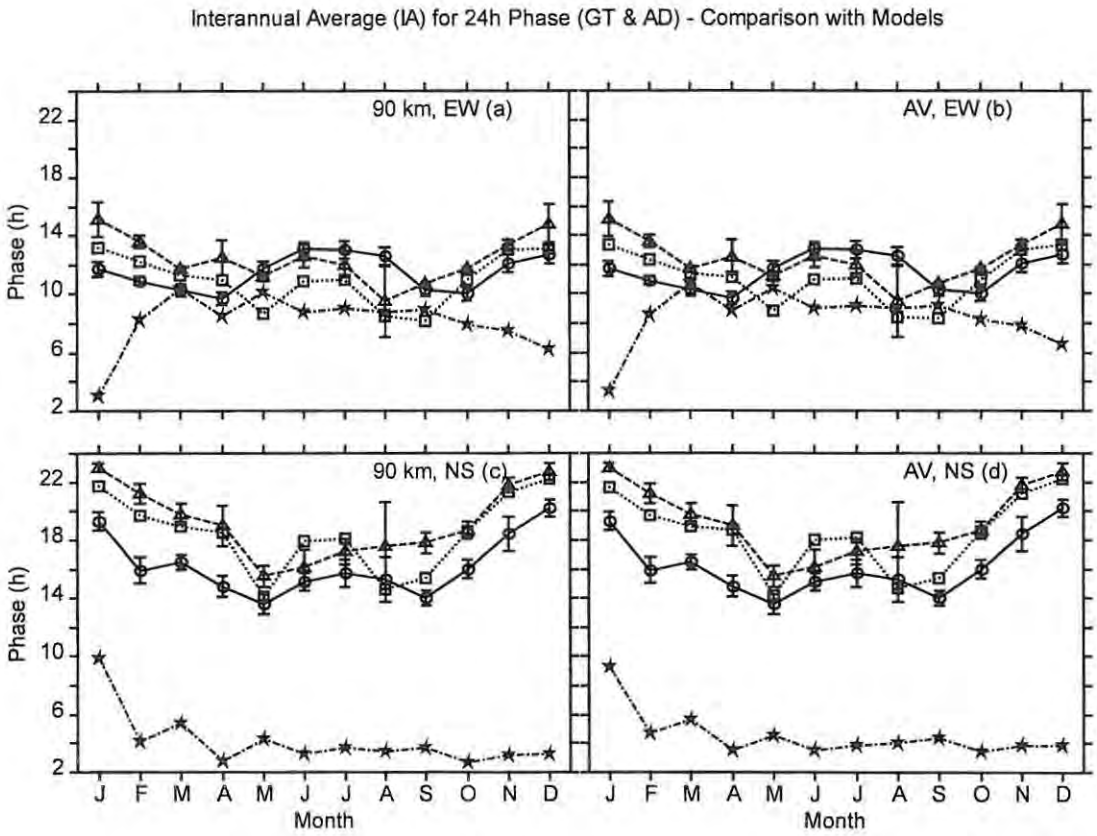

Figure 6.25 Comparison of the diurnal phase IAs at Grahamstown and Adelaide with the GSWM-00 and the DTM. (a) Zonal phases with different symbols representing Grahamstown IA (circles), Adelaide IA (triangles), GSWM-00 (pentagons) and DTM (squares) for model heights of ~90 km. (b) Same as (a) but for Gaussian weighted model phases. (c) and (d) are similar to (a) and (b) respectively but for meridional phases.

a short vertical wavelength (~30 km), the results from height-integrated observations (e.g. at Grahamstown) are not expected to be significantly affected by the lack of height resolution.

Figure 6.26 shows the seasonal variation of the (EW-NS) phase difference at both Grahamstown and Adelaide. These phase differences are obtained by differencing the phases obtained from harmonic analysis. The IAs of these differences indicate a pattern characterised by largest absolute differences in summer decreasing to the smallest absolute differences in winter. This pattern can also be seen in the frequency distributions of the phase differences (Figure 6.27 and Figure 6.28). These distributions also show a greater spread over the 1987-1994 period at Grahamstown than at Adelaide. At both sites the diurnal tide is close to

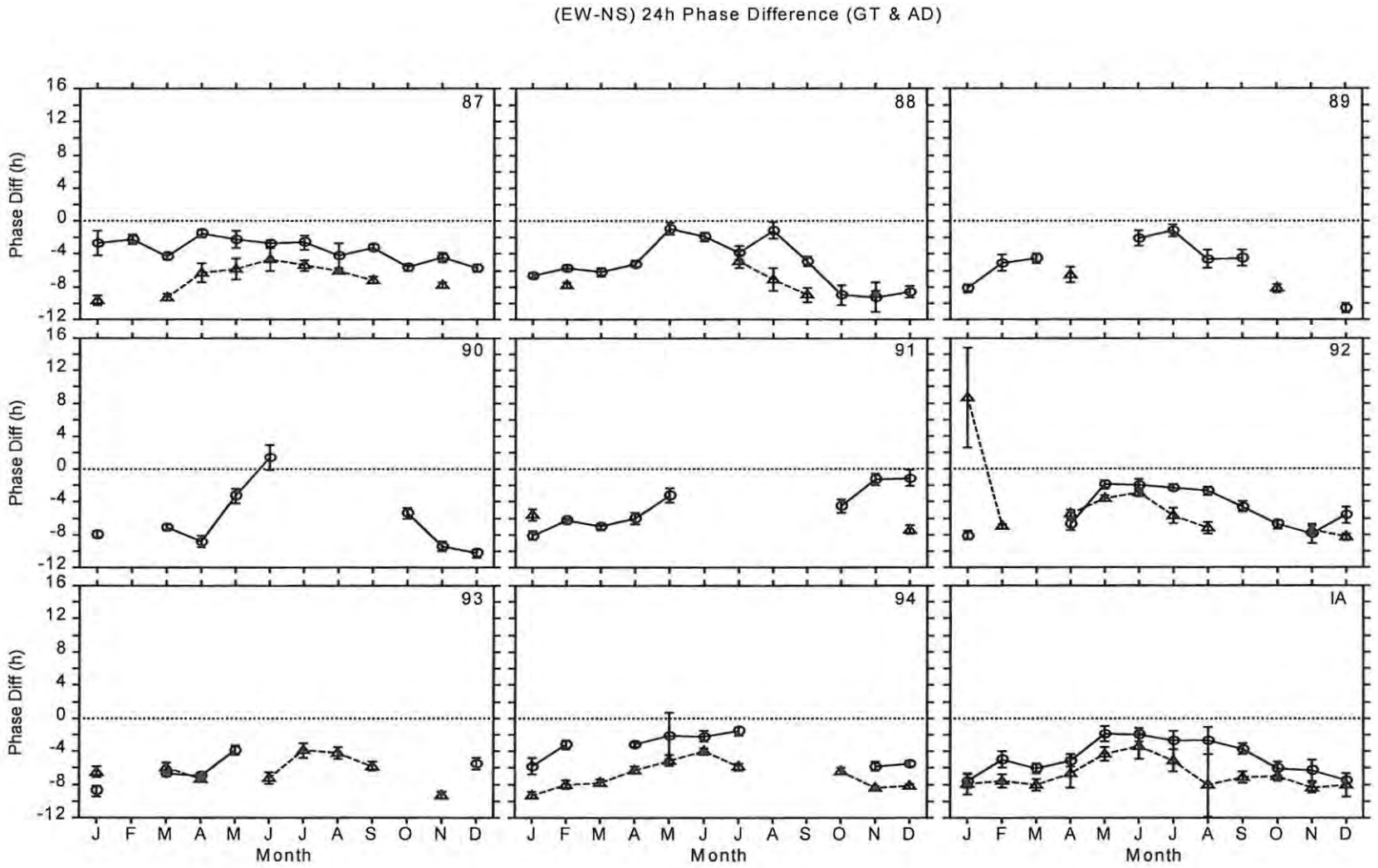

Figure 6.26 The (EW-NS) phase difference for the diurnal tide at Grahamstown (circles) and Adelaide (triangle) for the years 1987-1994 and the IA. The error bars represent one standard deviation of the mean (1 α).

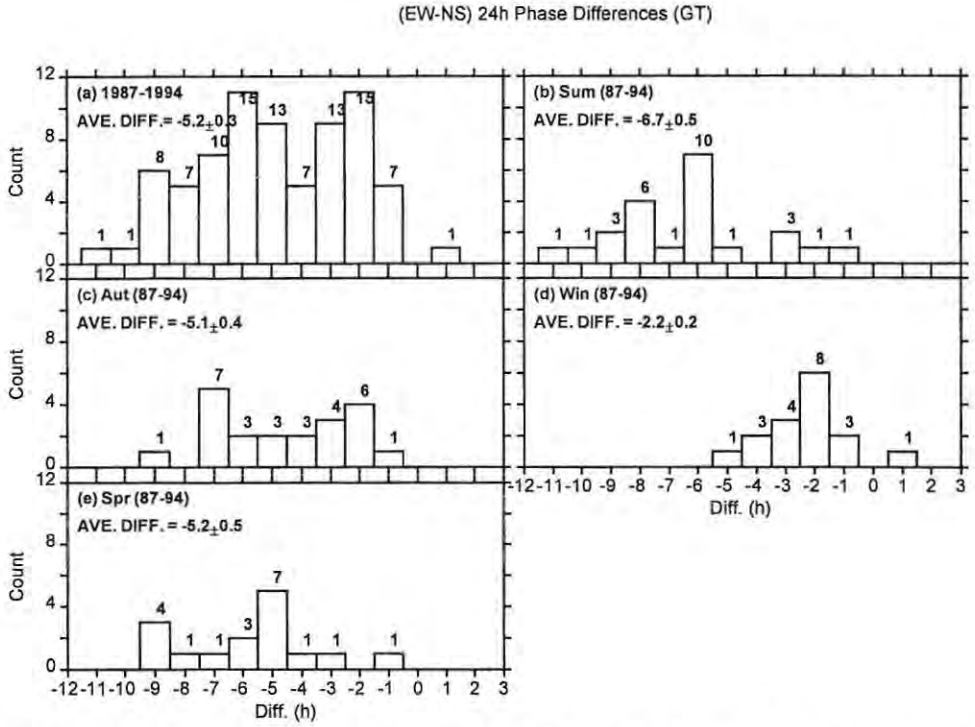

Figure 6.27 The distribution of the (EW-NS) phase differences for the diurnal tide at Grahamstown for the years 1987-1994. The weighted average differences and the percentage count (number at the top of bar) of each bar are also given.

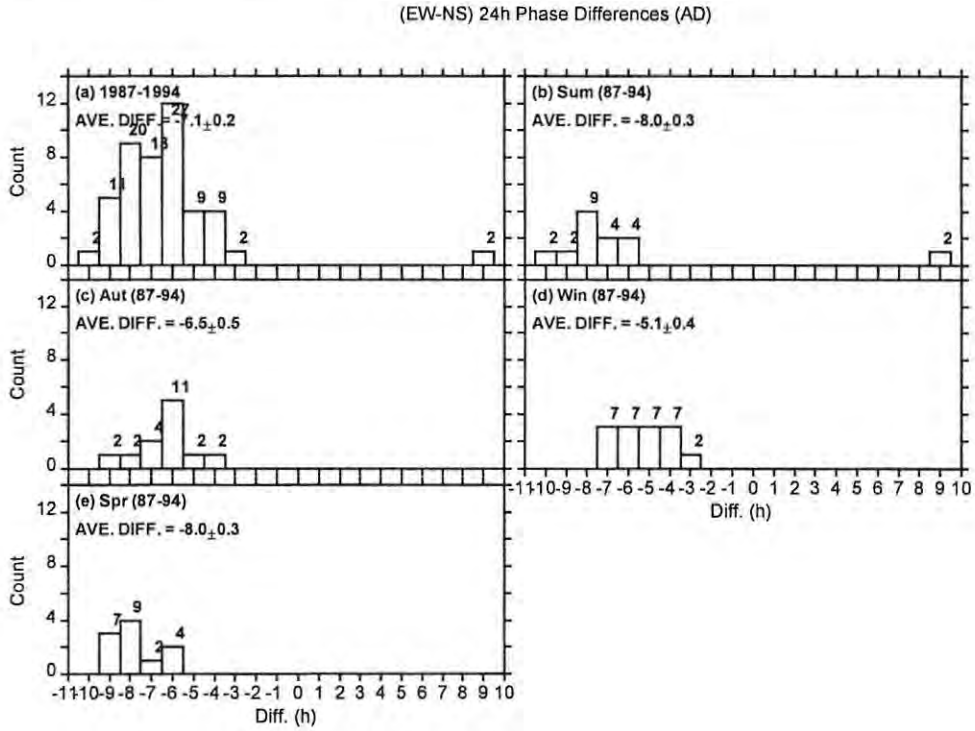

Figure 6.28 Same as **Figure 6.27** but for Adelaide.

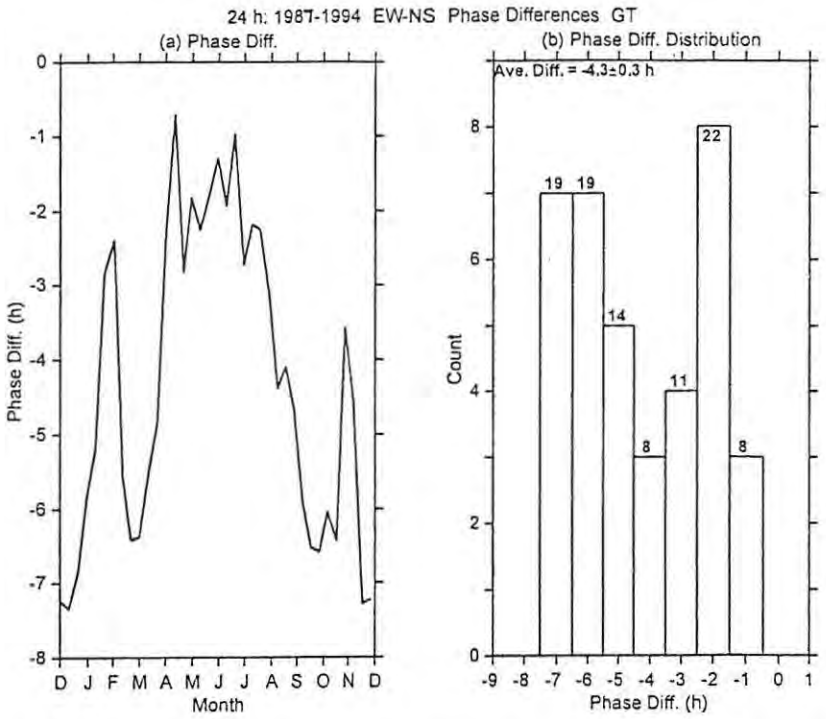

Figure 6.29 (EW-NS) Phase difference behaviour at Grahamstown for the 8-year (1987-1994) period: (a) monthly phase (EW-NS) differences. (b) Distribution of the phase differences.

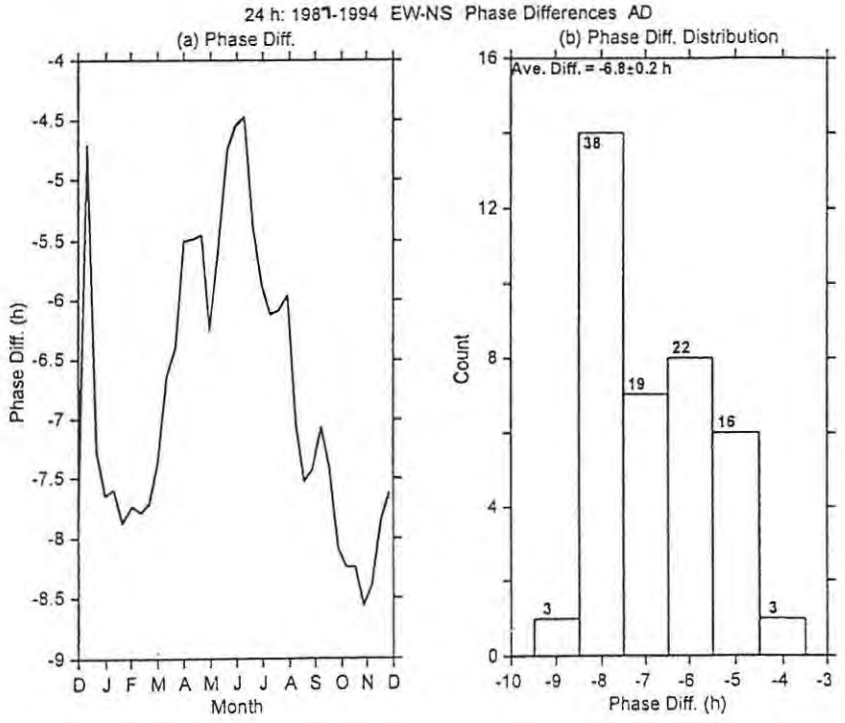

Figure 6.30 Same as **Figure 6.29** but for Adelaide.

quadrature (6 h) with the zonal component generally leading its meridional counterpart indicating the expected anticlockwise polarisation of the velocity vector in the Southern hemisphere. The phase differences have averages of -5.2 ± 0.3 h (GT) and -7.1 ± 0.2 h (AD) for the years 1987-1994. Seasonally this phase difference changes as indicated by the statistics on the frequency distributions.

Another way of studying phase differences is by using cross-spectral methods. For this purpose I used the same procedure as discussed in Section 6.2. The results of this analysis for the 1987-1994 period are shown in Figure 6.29 (Grahamstown) and Figure 6.30 (Adelaide). The seasonal variations of the phase differences as depicted by Figure 6.29(a) and Figure 6.30(a) bear some resemblance to the IAs of Figure 6.26. That is, small (large) absolute differences in winter (summer) and a tendency towards larger absolute differences during the equinoxes compared to winter. The differences in the details of Figure 6.26 to Figure 6.29 and Figure 6.30 can be explained by the use of 21-day data window and a 10-day step size in the cross-spectral method. Consequently this method has a better (10-day) resolution compared to the monthly resolution of the harmonic method. There are other factors that also come into play e.g. spectral leakage, bias etc that are associated with the cross-spectral method. The cross-spectral phase difference distributions (Figure 6.29(b) and Figure 6.30(b)) are also similar in form but different in detail to their harmonic analysis counterpart (Figure 6.27(a) and Figure 6.28(b)). The phase differences obtained by the cross-spectral technique have averages of -4.3 ± 0.3 h (GT) and -6.8 ± 0.2 h (AD) for the years 1987-1994 which compare favourably with the harmonic method values reported above.

A comparison of the phase behaviour at Grahamstown and Adelaide for the zonal (Figure 6.31) and meridional (Figure 6.32) component shows a close similarity in the phase structure at the two sites (see the IAs). The general trend shows that the zonal phases at the two sites are comparable to each other from May to September with Grahamstown having slightly later phases. For the rest of the year Adelaide phases lag the Grahamstown ones by ~1-3 h. Although some years (e.g. 1992) show a great degree of similarity in the meridional phases at Grahamstown and Adelaide, the long term picture as reflected by the IA of Figure 6.32 reveal that Adelaide tend to lag the Grahamstown phases by ~1-5 h throughout the year.

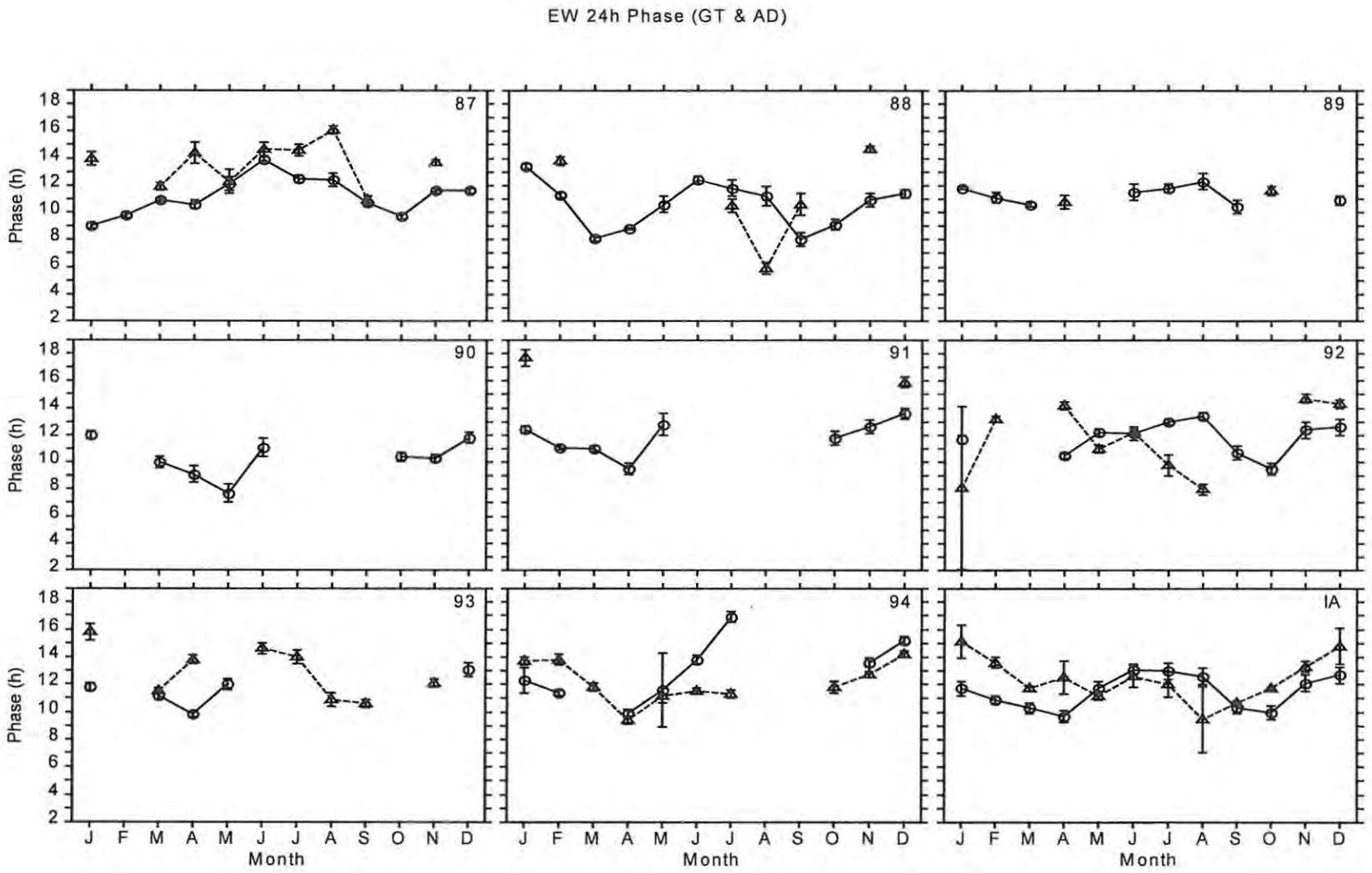

Figure 6.31 The zonal phases of the diurnal tide at Grahamstown (circles) and Adelaide (triangle) for the years 1987-1994 and the IA. The error bars represent one standard error of the mean (1 α).

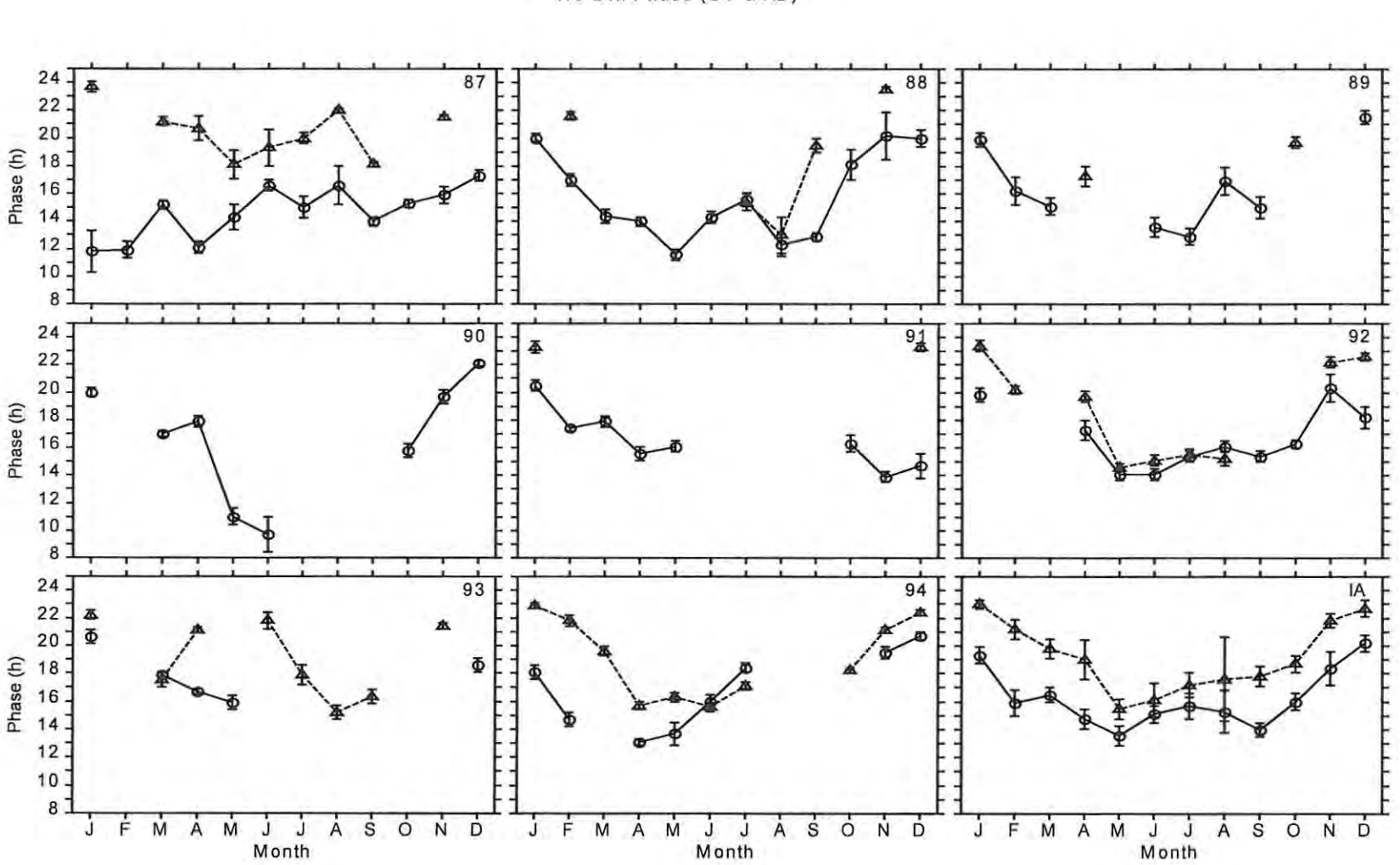

Figure 6.32 Same as **Figure 6.31** but for meridional phases.

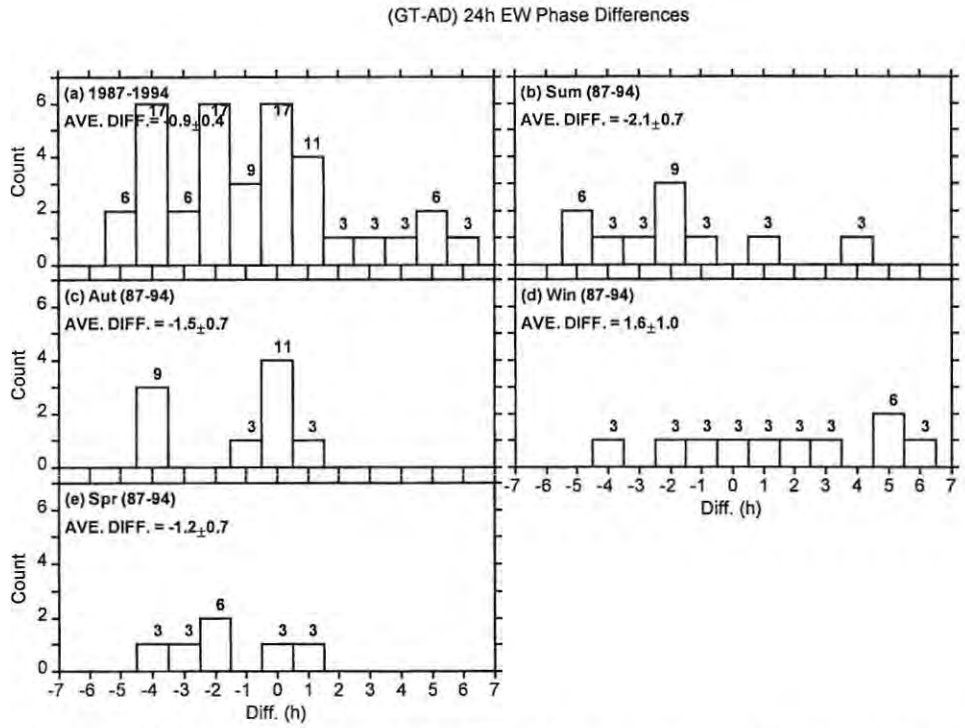

Figure 6.33 The distribution of the (GT-AD) zonal phase differences for the diurnal tide for the years 1987-1994. The weighted average differences and the percentage count (number at the top of bar) of each bar are also given.

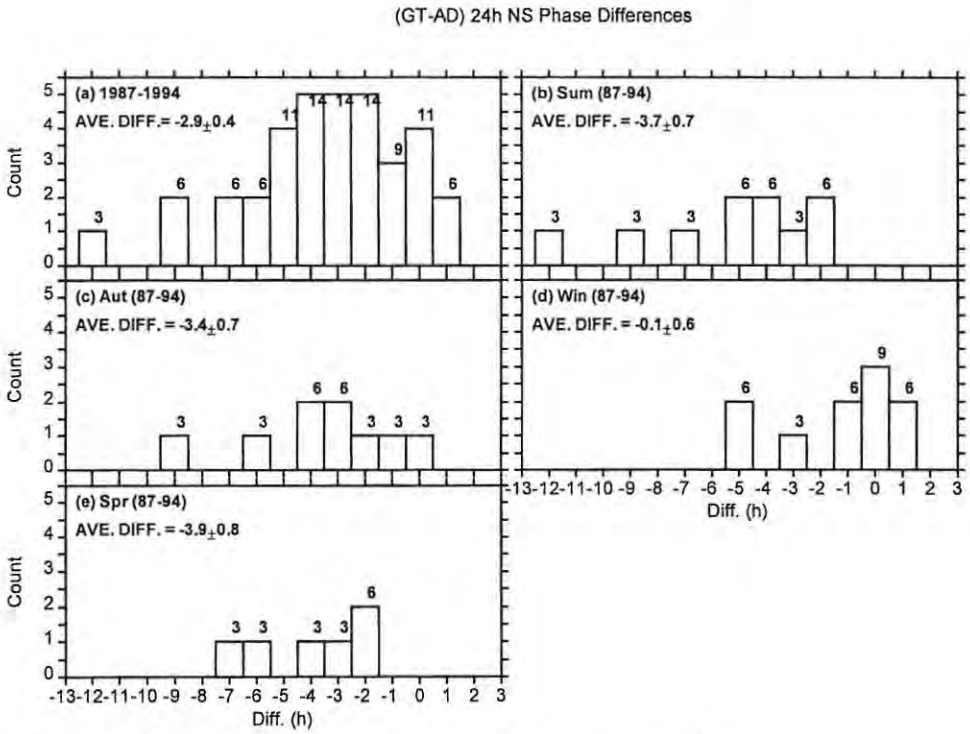

Figure 6.34 Same as **Figure 6.33** but for meridional phases

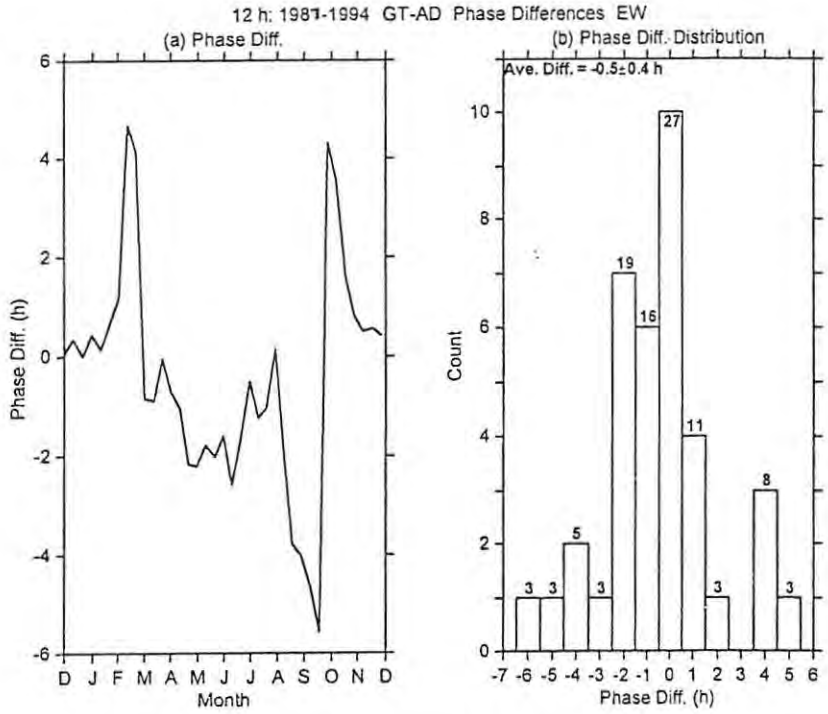

Figure 6.35 (GT-AD) phase difference for the zonal diurnal tide for the 8-year (1987-1994) period: (a) Monthly phase differences. (b) Distribution of the phase differences.

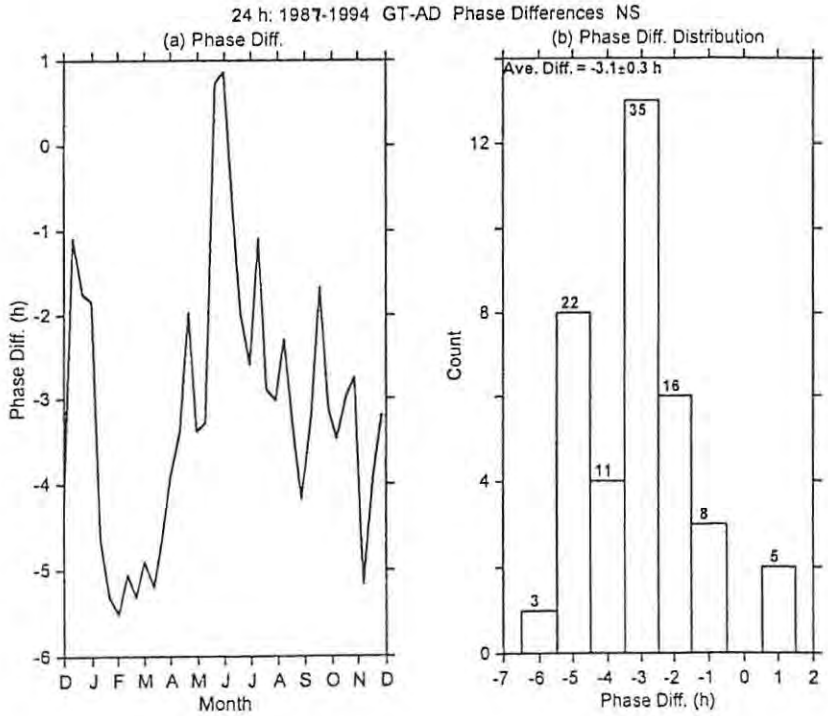

Figure 6.36 Same as Figure 6.35 but for the meridional diurnal tide.

Zonal Wavenumber, s	Phase Velocity (deg/h)	Phase Difference (h)
-7	-2.1	-59.7
-6	-2.5	-52.3
-5	-3.0	-44.8
-4	-3.8	-37.3
-3	-5.0	-29.9
-2	-7.5	-22.4
-1	-15.0	-14.9
0	Stationary	-7.5
1	15.0	0.0
2	7.5	7.5
3	5.0	14.9
4	3.8	22.4
5	3.0	29.9
6	2.5	37.3
7	2.1	44.8

Table 6.1 The theoretical phase difference (GT-AD) for monochromatic diurnal tide modes between Grahamstown and Adelaide and corresponding westward phase velocities. Positive phase differences represent later phases at Grahamstown compared to Adelaide.

Further insight about the phase differences between Grahamstown and Adelaide can be gained by looking at the distributions of these differences (Figure 6.33 and Figure 6.34) and the associated statistics. While the zonal differences are characterised by a spread of negative and positive differences with some bias towards the former, meridional differences are almost exclusively negative except in winter. Zonal differences have an 8-year average of -0.9 ± 0.4 h compared to -2.9 ± 0.4 h for the meridional component. The cross-spectral method (Figure 6.35 and Figure 6.36) shows similar results with 8-year averages of -0.5 ± 0.4 h (EW) and -3.1 ± 0.3 h (NS).

Table 6.1 shows computed theoretical phase differences between Grahamstown and Adelaide and the corresponding phase velocities assuming a wind field consisting of monochromatic modes. Looking at the possible theoretical phase differences in conjunction with the observed average phase differences, which have averages of <-4 h, it is clear that the diurnal tidal structure is dominated by the migrating tide. This is in agreement with model results presented in Section 6.3.1.2, which indicate that the diurnal tide is dominated by migrating modes. The deviation from a phase difference of 0 h could possibly be linked to nonmigrating tides. In particular the strong showing of negative phase differences suggest that, in agreement with *Ekanayake et al.* [1997], the

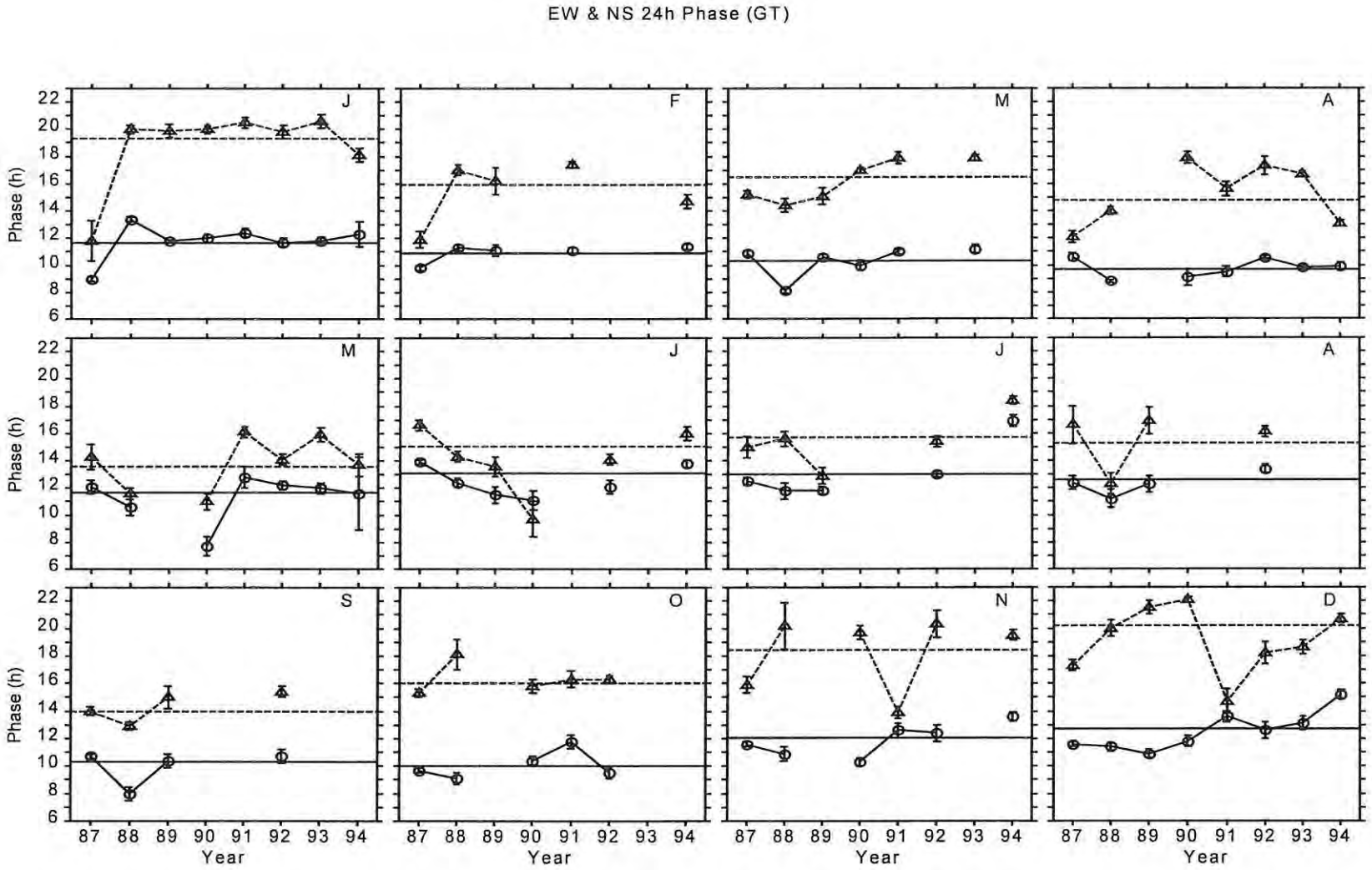

Figure 6.37 The interannual variation of the zonal (circles) and meridional (triangles) of the diurnal phases at Grahamstown for different months. The horizontal solid and dashed lines represent the corresponding MIA for the zonal and the meridional amplitudes, respectively. The error bars represent one standard error of the mean (1 α).

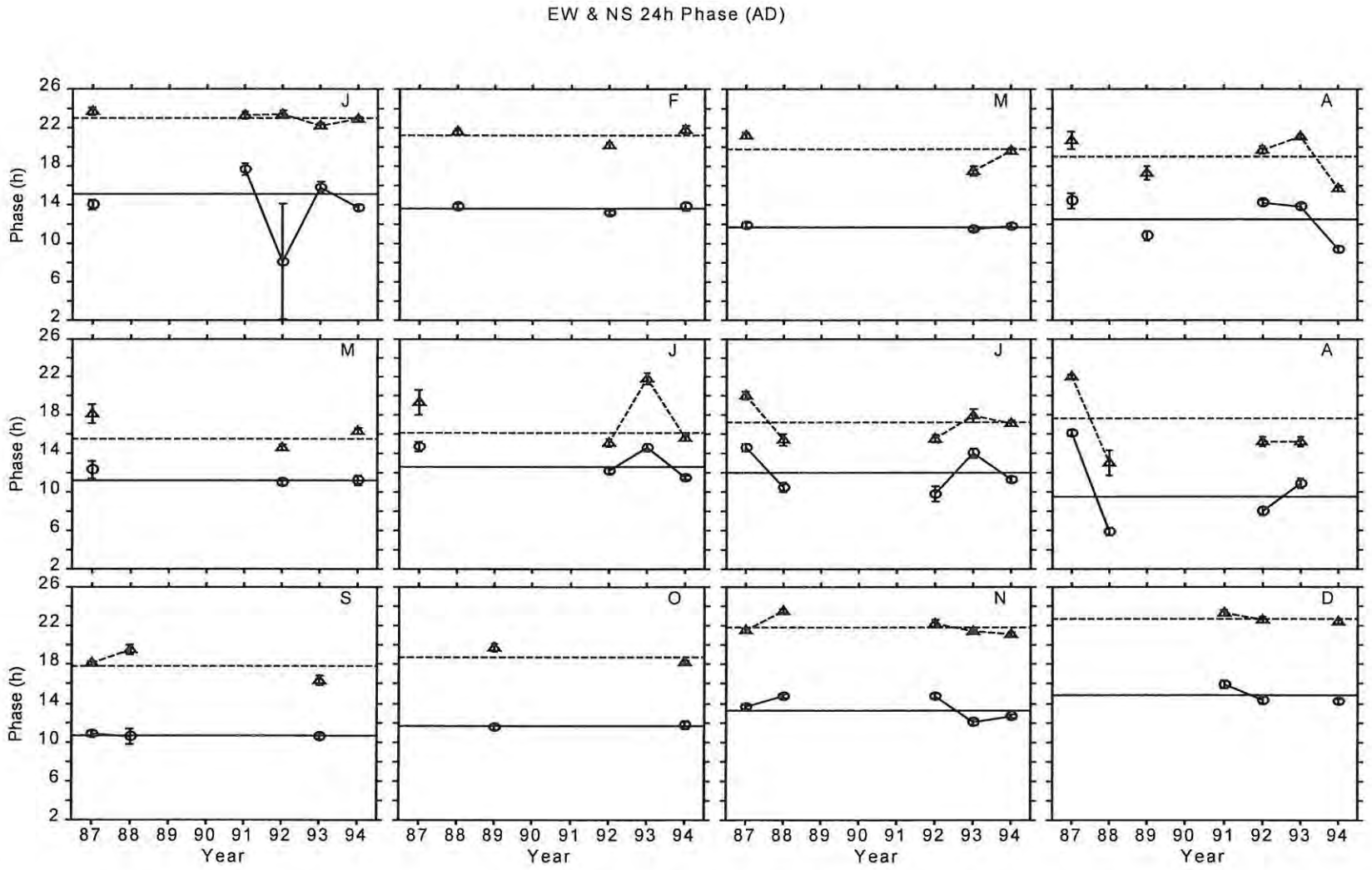

Figure 6.38 Same as **Figure 6.37** but for Adelaide.

nonmigrating tidal spectrum, is dominated by eastward propagating nonmigrating modes. Negative phase differences could also result from a strong contribution of stationary components but *Ekanayake et al.* [1997] found a weak (<0.5 ms^{-1}) stationary component.

6.4.2 Interannual Trends

The interannual variation of the diurnal tidal phases at Grahamstown and Adelaide are shown in Figure 6.37 and Figure 6.38, respectively. For most of the months the interannual variation in the zonal phases is correlated to that of meridional phases at both Grahamstown and Adelaide. However, there are a few interesting exceptions e.g. in December at Grahamstown. The phases are less variable from year-to-year compared to amplitudes (Section 6.3.2). I mentioned earlier that any interannual variation due to the QBO modulation of the UV-ozone forcing is not expected to have a major impact on phases since they are primarily determined by the H_2O-IR forcing of the diurnal tide [*Hagan*, 1996]. In fact the results of *Vincent et al.* [1998] show that although there are interannual variations in phases there is no perceptible preferred behaviour when comparing years of westward or eastward QBO flows. However, the QBO modulation of gravity wave fluxes and dissipation can affect the phases. We saw in Chapter 5, Section 5.2 that the diurnal modulation of the mean wind field through which gravity waves have to propagate results in a diurnally varying acceleration of the mean flow. The resulting nontidal (i.e. not thermotidally excited) 'tide' is ~6 h ahead of the thermal tide leading to phase advance of the apparent tide [*Fritts & Vincent*, 1987].

6.5 SUMMARY OF AMPLITUDES AND PHASES

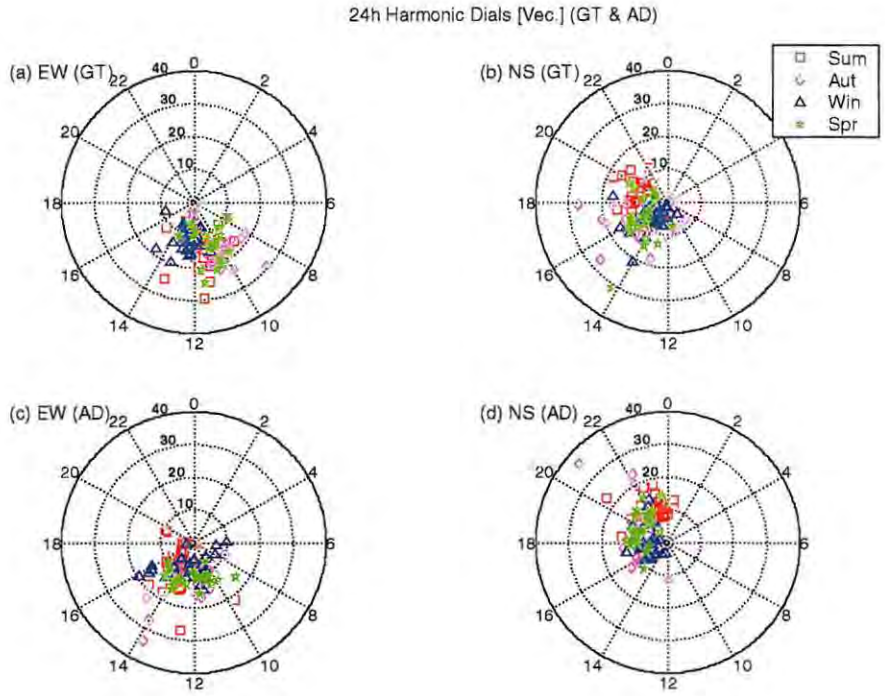

Figure 6.39 The harmonic dial of the zonal and meridional diurnal tide at Grahamstown and Adelaide for the years 1987-1994. The units of the radius of the dotted circles are in ms^{-1} and the peripheral numbers represent the phases in hours. Different symbols and colours represent different seasons.

To summarize the main features discussed in the previous sections we consider the tidal harmonic dials (Figure 6.39) where the radial distance from the origin to a data point gives the amplitude of the tide and the angle in hours with respect to 0 h gives the phase of the tide. We see the large amplitudes in autumn (diamond symbol); most amplitudes are less that 20 ms^{-1}; comparison of the phases of (a) versus (b) and (c) versus (d) shows the tendency towards phase quadrature with the zonal component leading; comparison of (a) versus (c) and (b) versus (d) clearly shows phase differences between Grahamstown and Adelaide.

Figure 6.40 to Figure 6.43 shows contour and shaded plots of the amplitudes and phases at Grahamstown and Adelaide. From these figures we see the features described in the previous

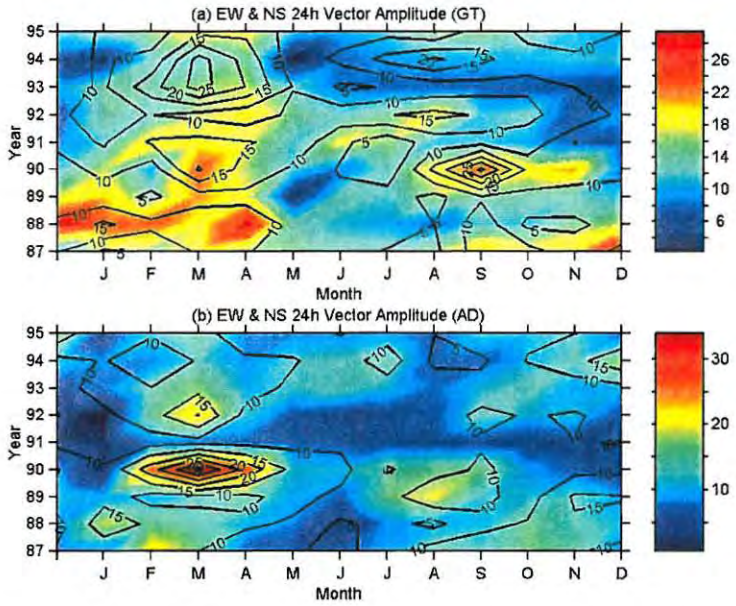

Figure 6.40 (a) The zonal diurnal amplitude (shading) and meridional diurnal amplitude (contours) at Grahamstown. Units of colour bar and contours are ms^{-1}. (b) Same as (a) but for Adelaide.

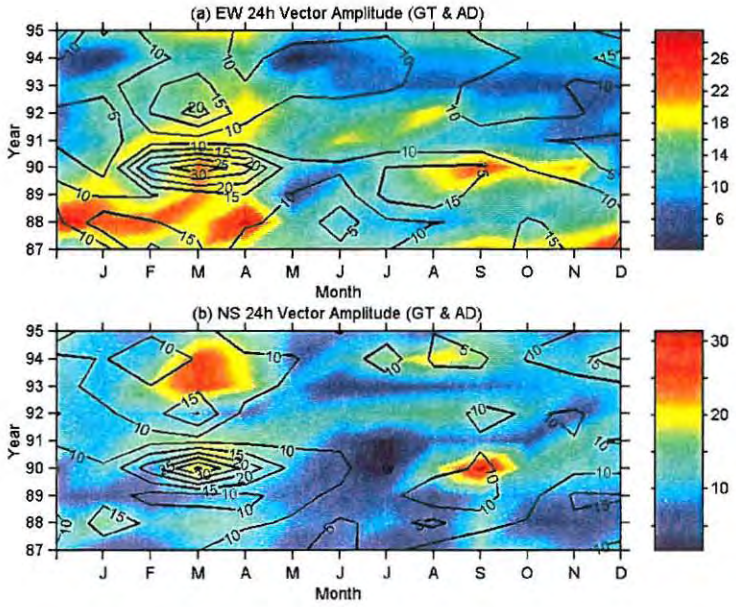

Figure 6.41 (a) The zonal diurnal amplitude at Grahamstown (shading) and Adelaide (contours). Units of colour bar and contours are ms^{-1}. (b) Same as (a) but for meridional diurnal amplitude.

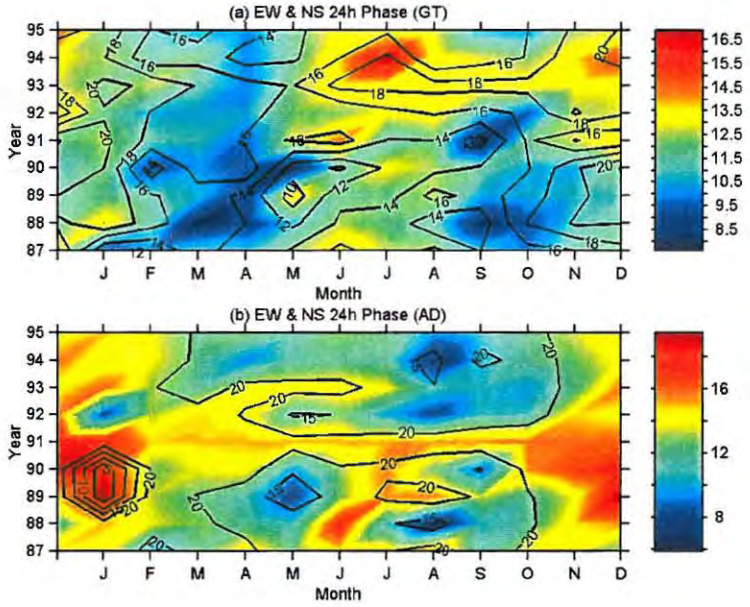

Figure 6.42 (a) The zonal diurnal phase (shading) and meridional diurnal phase (contours) at Grahamstown. Units of colour bar and contours are h. (b) Same as (a) but for Adelaide.

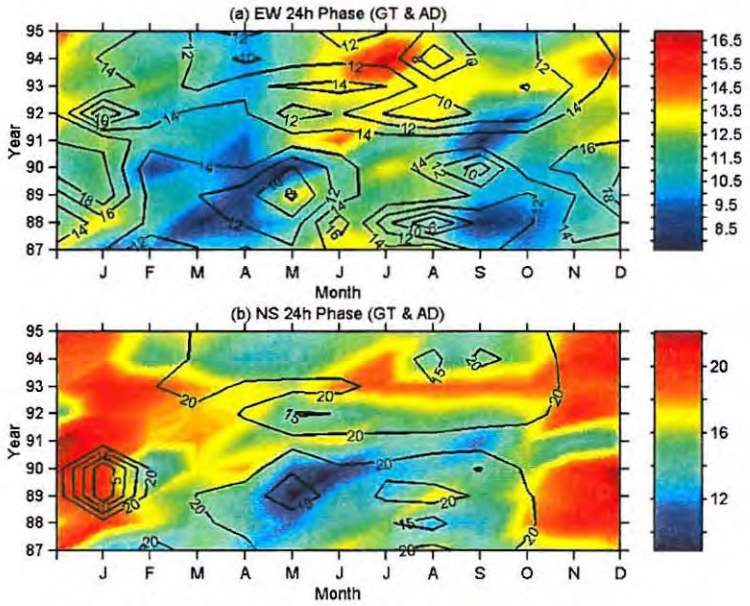

Figure 6.43 (a) The zonal diurnal phase at Grahamstown (shading) and Adelaide (contours). Units of colour bar and contours are h. (b) Same as (a) but for meridional diurnal phase.

paragraph and in the previous sections. Most importantly these figures highlight the seasonal and interannual variations discussed in the main body of the chapter.

CHAPTER 7 LONG-TERM SEMIDIURNAL TIDE VARIATIONS

7.1 INTRODUCTION

The semidiurnal tide, like the diurnal tide, is a global-scale atmospheric oscillation but has a period of 12 h. This tide is also excited as a result of the absorption of solar radiation by water vapour and ozone. The dominant heating rate is that of the (2, 2) mode [*Forbes*, 1982]. Like its diurnal counterpart, the semidiurnal tide has a migrating and a non-migrating component with the latter resulting from sources like latent heat release. *Hagan* [1996] found that the inclusion of latent heat forcing results in a semidiurnal tide that is 50 % larger than that excited via UV and IR forcing only.

The semidiurnal tide can have a mixture of modes. *Forbes* [1982] found that for the semidiurnal temperature tide the 70-90 km altitude range has an equal contribution from the (2, 2), (2, 3) and (2, 4) modes for solstice conditions with the (2,4) mode assuming dominance in the 90-120 km altitude region [*Forbes*, 1982]. This has serious implications for the MLT region because the total tide is expected to change with height and latitude as a result of this mode mixing. For instance, *Manson et al.* [1999] found that for most of the sites they studied, if not all, the phases change with height especially in winter compared to summer. They also observed vertical amplitude changes at some sites e.g. Saskatoon (winter especially) whereas other sites showed minimal height dependence e.g. Christmas Island and Hawaii (during both solstices). Observations show that at ~22° latitude the diurnal tide tends to dominate the semidiurnal tide [*Vincent et al.*, 1998]. However, due to the decay of the diurnal tide poleward from its peak at ~20-30° [*Hagan*, 1996], the semidiurnal tide gain the ascendancy at middle to high latitudes. At latitudes 40-55° and ~90 km *Manson et al.* [1989] reported semidiurnal amplitudes of 10-25 ms^{-1} compared to 5-15 ms^{-1} for the diurnal tide. This domination extends to high latitudes (> 60°) as shown by values of 10-25 ms^{-1} (semidiurnal) and 5-10ms^{-1} (diurnal) at ~ 90 km [*Avery et al.*, 1989].

The semidiurnal tide has a relatively long vertical wavelength compared to the diurnal tide making the former tide less susceptible to dissipative and height integration effects. For the 0-100 km region, *Forbes* [1982] quotes average vertical wavelengths of 90-150 km for the (2, 3) and (2, 2) modes and 35-45 km for the (2, 5) and (2, 4) modes. Depending on the exact mode composition these wavelengths can vary. *Hagan* [1996] reports that for UV and IR heating the vertical wavelengths are ~50 km for the winter mid-latitudes and are ~20 km for the tropical

MLT.

7.2 AMPLITUDES

7.2.1 Seasonal Trends

7.2.1.1 Local Seasonal Trends

The zonal amplitudes at Grahamstown (Figure 7.1) follow a well-defined annual cycle characterized by a peak that can be as large as ~33 ms^{-1} in autumn. This behaviour is different from semi-annual cycle observed in the mean climatology of the 52-56°N latitude range at 92.5 km, which is characterized by a peak (~22 ms^{-1}) vector amplitude in autumn and a secondary peak (~16 ms^{-1}) vector amplitude in winter [*Jacobi et al.*, 1999]. At Mawson (67°S) and Molodezhnaya (68°S) the semidiurnal amplitudes at ~95 km show a spring peak (~20 ms^{-1}) in 1985 whereas the peak is in autumn in 1986 [*Portnyagin et al.*, 1993b]. This shows that there can be great interannual variations, as we will see again in Section 7.2.2. The meridional amplitudes at Grahamstown (Figure 7.1) do not exhibit a clearly defined seasonal pattern. However, looking at the IA there is a tendency for large amplitudes in autumn as well. This autumnal peaking is not very clear in 1987-1988 but tends to manifest itself in subsequent years. While the difference between the seasonal behaviour in the zonal and the meridional tidal amplitudes cannot be explained, it is worth noting that similar differences have been observed elsewhere. *Vincent et al.* [1998] found that at Kauai (22°N°, 160°W) the zonal amplitudes exhibit an essentially annual behaviour with a peak (~10 ms^{-1}) in summer whereas the meridional amplitudes are characterized by a semi-annual cycle with peaks (~10 ms^{-1}) in late spring/summer and winter at ~90 km.

Coming to Adelaide (Figure 7.2), we observe a closer similarity in the seasonal pattern of the zonal and the meridional amplitudes (see IAs in particular). The general trend shows a primary peak (~12 ms^{-1}) in summer and two secondary peaks in late autumn/early winter and in late winter/early spring. Consistent with the results of *Vincent et al.* [1998] based on 12 years of data, the semidiurnal amplitudes at Adelaide show an essentially annual cycle. By contrast, these authors found that at the low latitude site of Christmas Island (2°N, 157°W) the semidiurnal amplitudes were generally weak and did not show a clear systematic seasonal behaviour. This shows the variability of this tide with latitude. *Hagan* [1996] found that, unlike

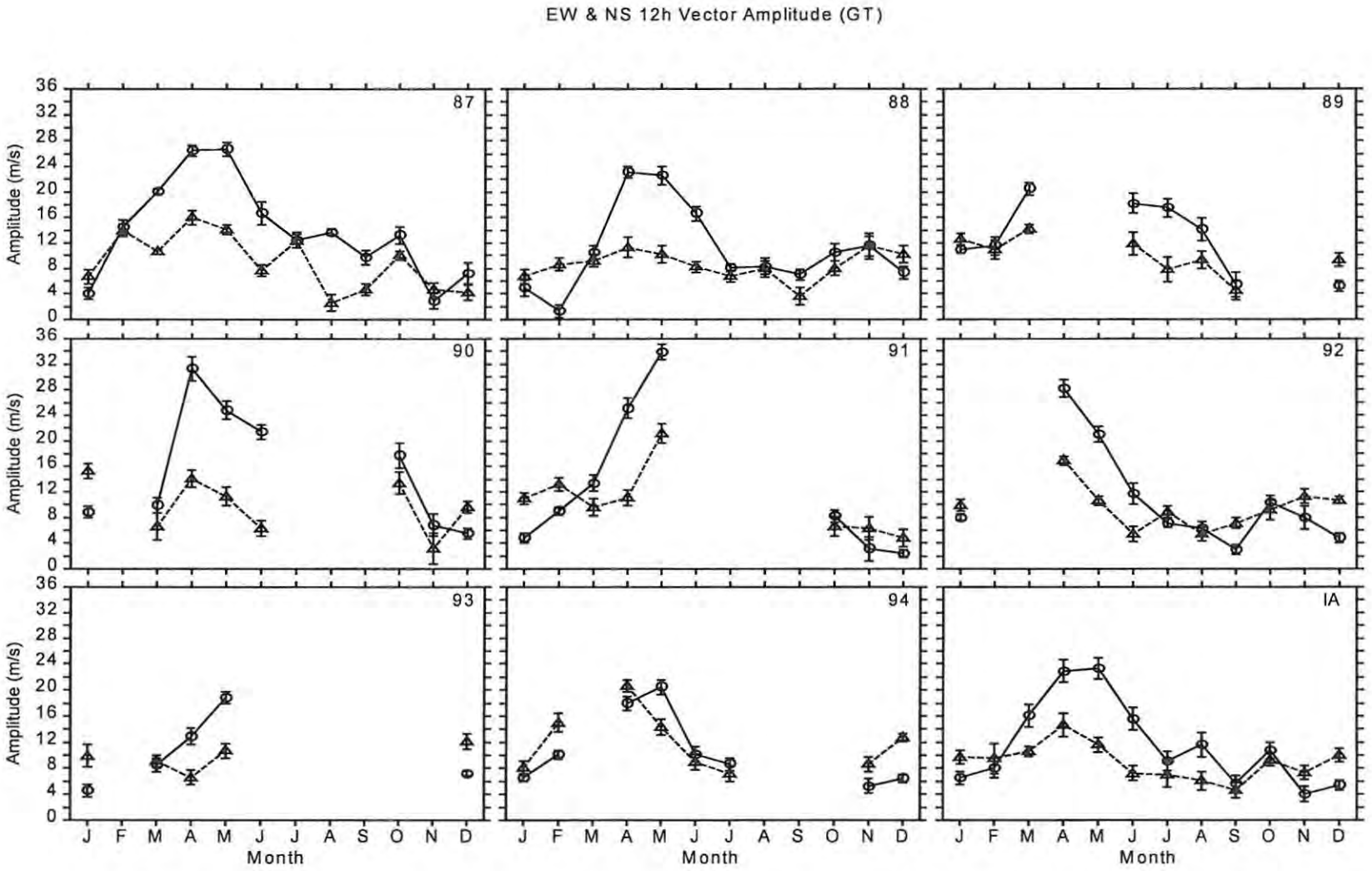

Figure 7.1 The zonal (circles) and the meridional (triangle) amplitudes of the semidiurnal tide at Grahamstown for the years 1987-1994 and the IA. The error bars represent one standard error of the mean (1 α).

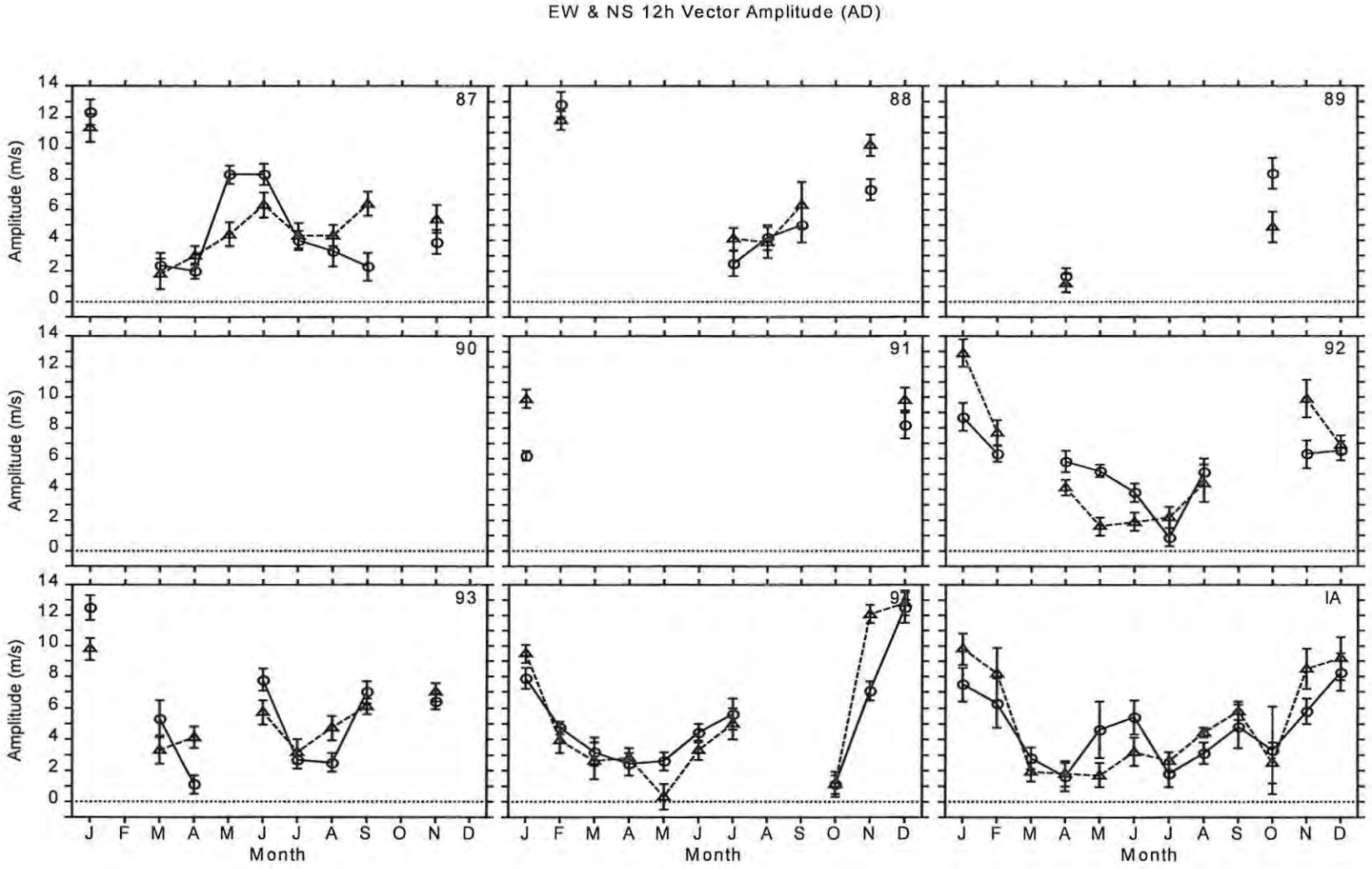

Figure 7.2 Same as **Figure 7.1** but for Adelaide.

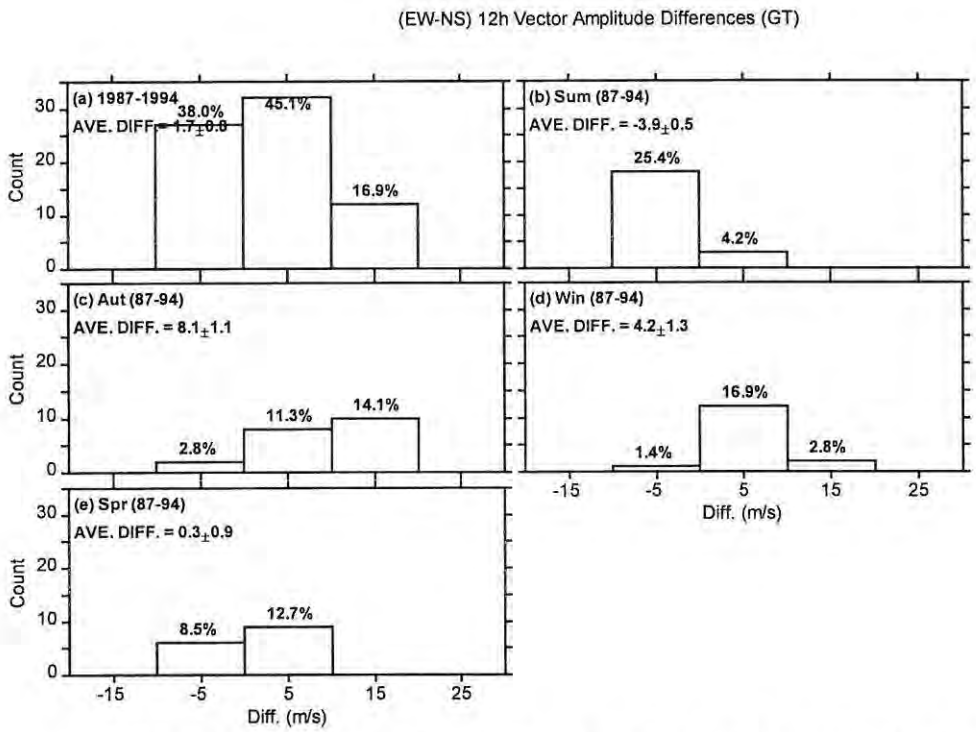

Figure 7.3 The distribution of the (EW-NS) amplitude differences for the semidiurnal tide at Grahamstown for the years 1987-1994. The weighted average differences are also given and the percentage count of each bar.

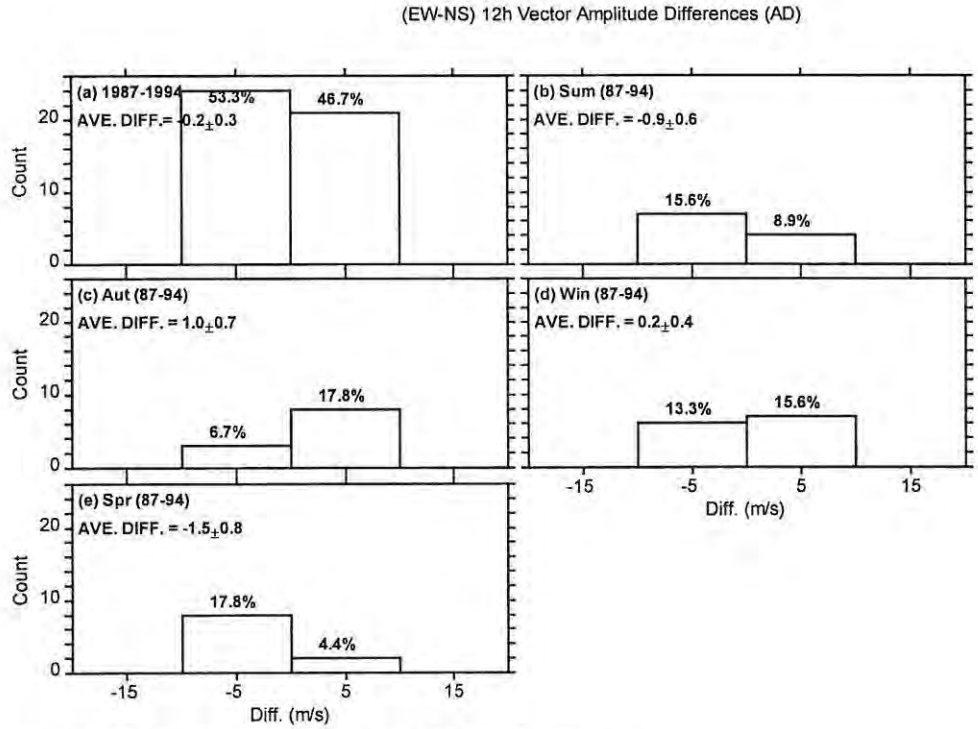

Figure 7.4 Same as **Figure 7.3** but for Adelaide.

the diurnal tide which shows a clear seasonal and latitudinal pattern, the behaviour of the semidiurnal tide in the temperature field is very complex and shows significant variation with season.

The distribution of the differences between the zonal and the meridional amplitudes are shown in Figure 7.3 and Figure 7.4 for Grahamstown and Adelaide, respectively. From these distributions as well as Figure 7.1 we see that at Grahamstown the bulk (60 %) of the differences are due to larger zonal amplitudes. In general, the zonal amplitudes at Grahamstown tend to be larger than meridional amplitudes for all seasons except in summer when meridional amplitudes are larger (see Figure 7.3). As expected from Figure 7.2 and contrary to the wide spread in differences at Grahamstown, the EW/NS amplitude differences at Adelaide are confined to the two bins centred at -5ms^{-1} and 5 ms^{-1}. Unlike at Grahamstown, the meridional amplitudes at Adelaide are marginally larger (53.3 %) than their zonal counterparts.

In Figure 7.5 I have compared the semidiurnal amplitudes observed at Grahamstown and Adelaide to those of the GSWM-00 [*Hagan et al.*, 1995; *Hagan et al.*, 1999; *Hagan et al.*, 2000, in press] and the empirical semidiurnal migrating tide model [*Portnyagin & Solovjova*, 1998], which I will call the "Semidiurnal Tide Model" (STM). As I did for the diurnal tide, I have plotted the ~90 km results and the height averaged results for the model. Once again we see that height integration does not significantly affect the results. For the zonal amplitudes Figure 7.5(a) & (b), we observe that a feature that stands out is the autumn peak (~24 ms^{-1}) at Grahamstown. Although the GSWM-00 also shows a peak in autumn, this peak is less than half that at Grahamstown. The STM and Adelaide, by contrast, show a minimum in autumn. From winter through to end of summer, the model results and the observations are comparable and are in the 2-14 ms^{-1} range.

Now focusing on the meridional amplitudes (Figure 7.5(c) & (d)), we observe that the amplitudes at Grahamstown are larger than the observations at Adelaide and the GSWM-00 results in autumn, but are comparable to the STM results during this time. From winter through to the end of summer the observations at Grahamstown and Adelaide compare well with the GSWM-00 results while the STM tends to be larger from May to November. The large

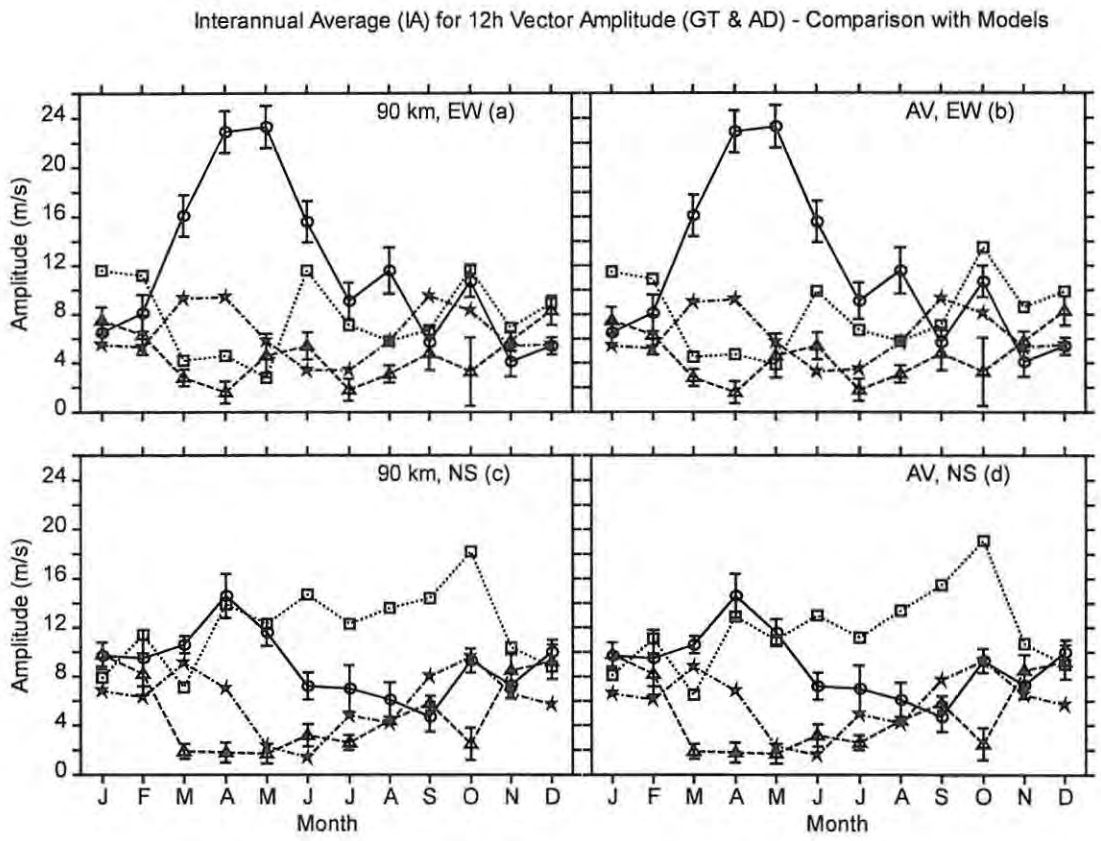

Figure 7.5 Comparison of the semidiurnal amplitude IAs at Grahamstown and Adelaide with the GSWM-00 and STM. (a) Zonal amplitudes with different symbols representing Grahamstown IA (circles), Adelaide IA (triangles), GSWM-00 (pentagons) and STM (squares) for model heights of ~ 90 km. (b) Same as (a) but for Gaussian weighted model amplitudes. (c) and (d) are similar to (a) and (b) respectively but for meridional amplitudes.

amplitudes at Grahamstown during autumn are difficult to explain, but their consistency from year to year as shown in Figure 7.1 (especially for the zonal component) shows that they are a real feature of the MLT dynamics near Grahamstown. Consistent with the above results, the WINDII results for 35°S and ~90 km show an annual cycle with both the zonal and meridional amplitudes of the semidiurnal tide reaching their peaks (>25 ms-1) around autumn [*McLandress et al.*, 1996]. The observations from HRDI also show a predominantly annual variation characterized by a late summer/autumn peak (~25 ms^{-1}) for the zonal component and an autumn peak ~15-20 ms^{-1} for the meridional amplitudes at ~30°S and 95 km [*Burrage et al.*, 1995b].

The seasonal variation of the semidiurnal tide, and in particular the autumnal amplitude peak

observed at Grahamstown and by WINDII and HRDI, is most likely due to the seasonal changes of higher order modes. *Forbes* [1982] point out that for H_2O and O_3 heating, the dominant (2, 2) mode is less (20 %) variable with season while the (2, 4) and (2, 6) modes are more (25-100 %) seasonally variable. The heating rates of the (2, 4) mode reach higher peaks during the equinoxes compared to the December solstice for both H_2O and O_3 heating [*Forbes*, 1982]. It is this enhancement that might possibly explain the large autumnal amplitudes observed at Grahamstown and by HRDI and WINDII especially because the (2, 4) can make a significant and sometimes dominant contribution to the semidiurnal tide [*Forbes*, 1982]. However, this does not explain why a similar autumnal peak is not observed at Adelaide not unless there are different modal compositions between Grahamstown and Adelaide. Based on the different vertical wavelengths observed at Saskatoon (52°N, 107°W) and Kazan (56°N, 49°E), *Lysenko et al.* [1994] presumed that the modal mix between the two sites could be different during the months studied.

Another cause of this autumnal discrepancy could be the differences in the mean flow between Grahamstown and Adelaide. According to *Hagan* [1996] the seasonal changes of the semidiurnal tide, with its relatively long vertical wavelength, are due to its sensitivity to variations in the zonal mean flow. *Hagan et al.* [1999] conducted experiments that showed that during the equinoxes the semidiurnal tide is more sensitive to MLT wind changes and less sensitive to stratospheric changes in the wind field. These authors report that during the solstices the semidiurnal tide is more sensitive to stratospheric wind changes. The sensitivity of the semidiurnal tide to the MLT wind field could have serious implications for semidiurnal amplitudes observed at Grahamstown and Adelaide. Figure 4.20 shows that there are major differences in the structure of the zonal mean flow between Grahamstown and Adelaide. The results presented by *Hagan et al.* [1999] show that the effect of the modification of the background wind on the semidiurnal tide changes with height and latitude in a very complicated manner. This makes it difficult to assess the possible effects of the observed differences in the mean flow between Grahamstown and Adelaide (Figure 4.20) on the semidiurnal tide. However, we will look it this in more detail in the next section.

The solstice condition at Grahamstown shows larger amplitudes in winter than in summer for the zonal component and the reverse is true for the meridional amplitudes (see IAs in Figure 7.5 or even more clearly in Figure 7.1). At Adelaide (Figure 7.2 and Figure 7.5) both the zonal

and the meridional amplitudes are larger in summer than in winter. The GSWM-95 results of semidiurnal tide temperatures show a very complicated response to the competing influences of IR and UV forcings [*Hagan*, 1996]. According to *Hagan* [1996], IR heating at 42°N dominates below 105 km and the phase difference between the IR and UV excitations is within 2 h during January and approach 6 h during July. Therefore there is constructive interference in January (northern hemisphere winter) and destructive interference July (northern hemisphere summer), which is in line with the larger winter zonal amplitudes at Grahamstown compared to summer. However, this differs from the reversed solstitial asymmetry in the meridional amplitudes at Grahamstown and in amplitudes of both components at Adelaide.

7.2.1.2 Longitudinal Seasonal Trends

From the previous section we saw at least one obvious difference in the tidal amplitudes at Grahamstown and Adelaide—the large autumnal amplitudes at Grahamstown compared to Adelaide. In this section I am going to consider, in detail, the longitudinal similarities and differences between the two sites. Figure 7.6 and Figure 7.7 show a Grahamstown-Adelaide comparison of tidal amplitudes for the zonal and the meridional component, respectively. Starting with the zonal comparison (Figure 7.6), a feature that stands out are the larger amplitudes at Grahamstown compared to Adelaide. Looking at the IA, we see that these differences are more pronounced from around February/March to November with largest discrepancies observed in autumn, as already mentioned. A point worth noting is the fact that a significant proportion of the February-November duration coincides with the duration (April-September) of closer similarity in the zonal mean flow at Grahamstown and Adelaide (see Figure 4.20, IA especially). This suggests that as much as the semidiurnal tide is sensitive to the mean flow, some of the observed longitudinal variations are not caused by longitudinal differences in the mean circulation. Coming to the meridional comparison (Figure 7.7), we observe a somewhat similar trend, i.e. larger amplitudes at Grahamstown than at Adelaide. Even more interesting is the fact that the largest discrepancies tend to coincide with those of the zonal amplitudes. It is very puzzling that both the zonal and the meridional amplitudes at Adelaide tend toward a minimum in autumn when the Grahamstown amplitudes are peaking.

The statistics in the (GT-AD) difference distributions (Figure 7.8 and Figure 7.9) emphasize

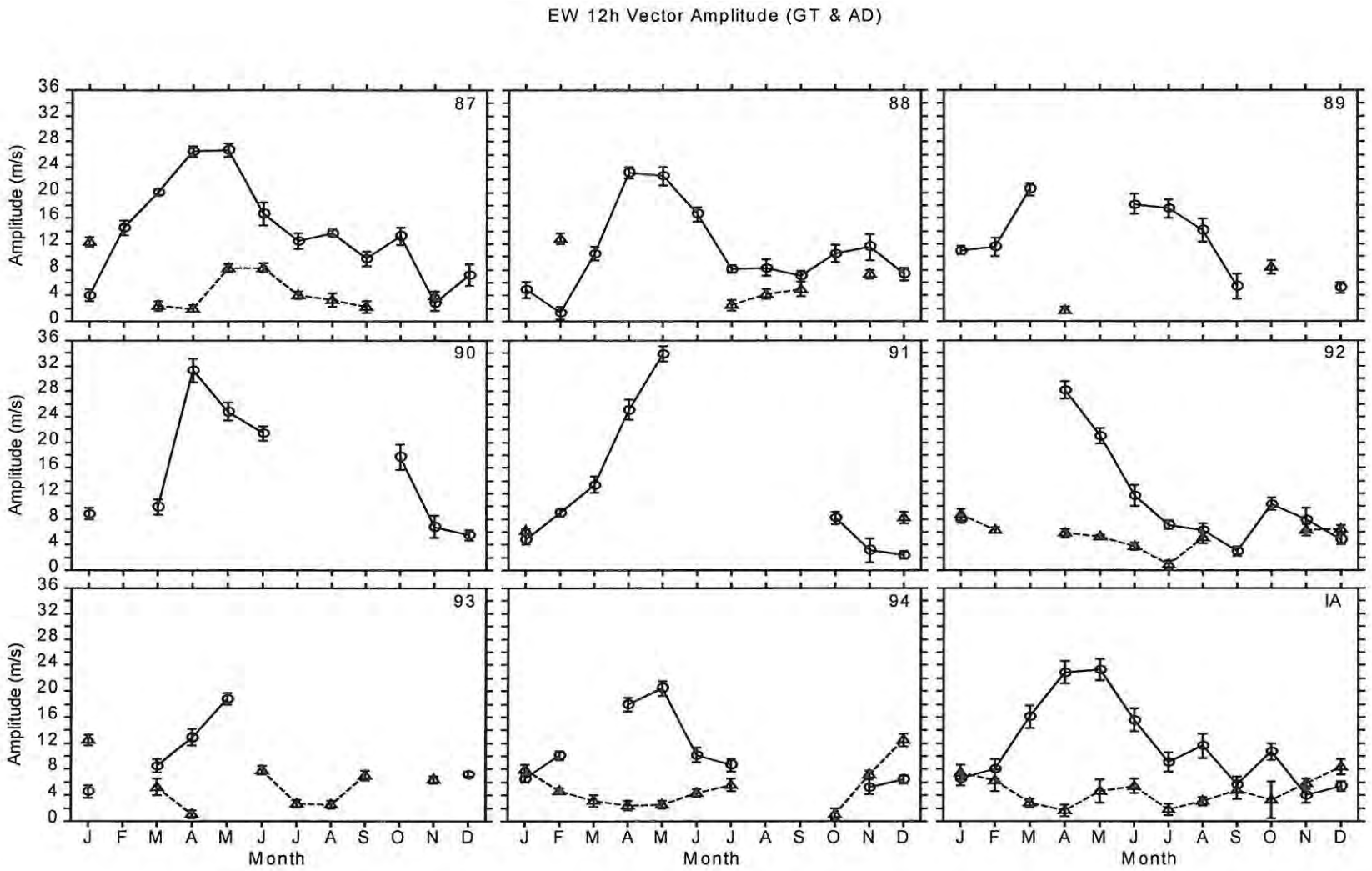

Figure 7.6 The zonal amplitudes of the semidiurnal tide at Grahamstown (circles) and Adelaide (triangles) for the years 1987-1994 and the IA. The error bars represent one standard error of the mean (1 α).

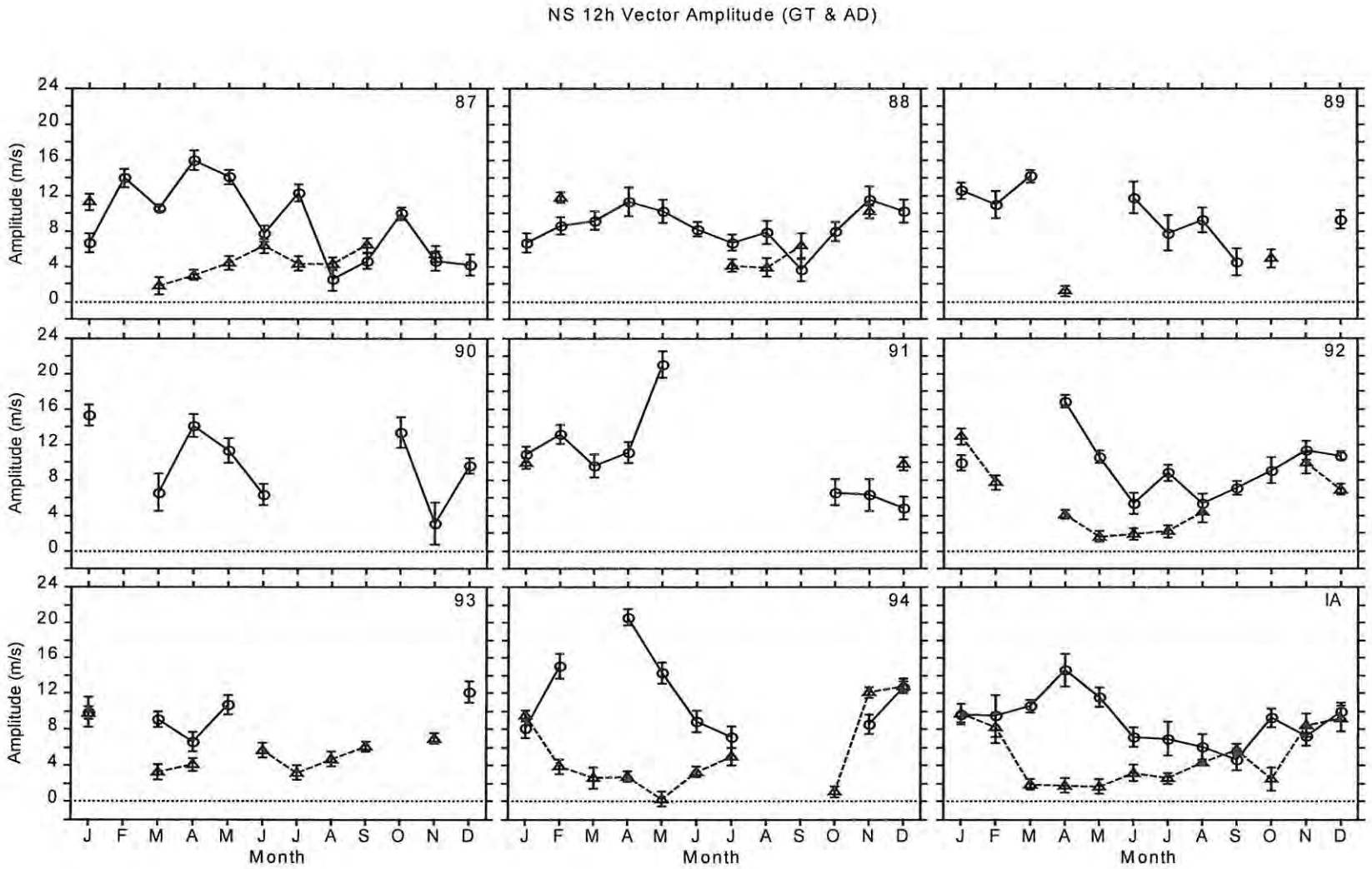

Figure 7.7 Same as **Figure 7.6** but for the meridional amplitudes.

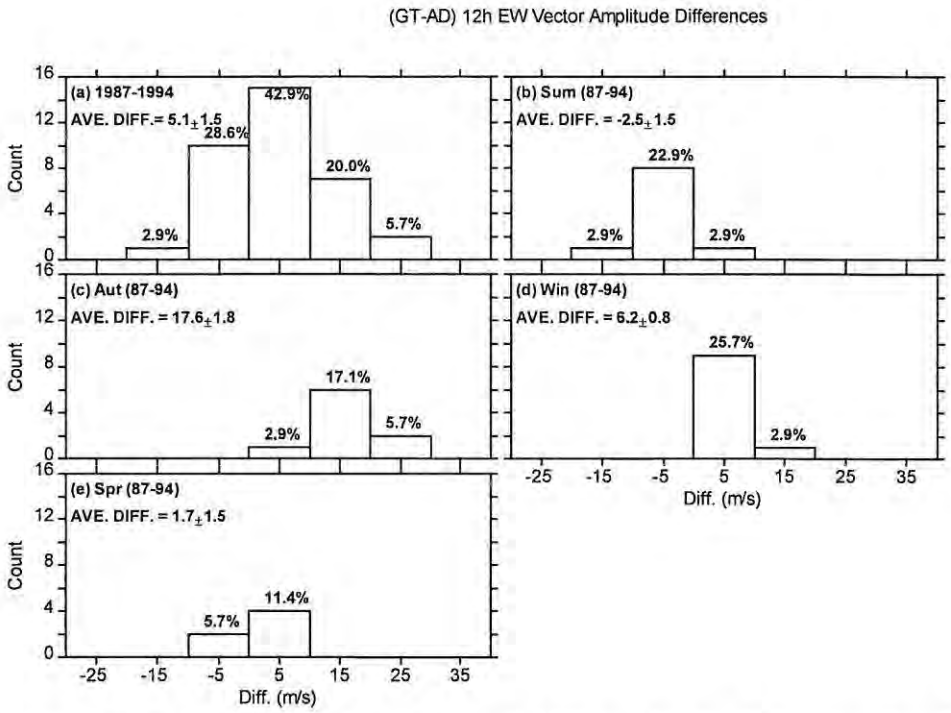

Figure 7.8 The distribution of the (GT-AD) amplitude differences for the zonal semidiurnal tide for the years 1987-1994. The weighted average differences are also given and the percentage count of each bar.

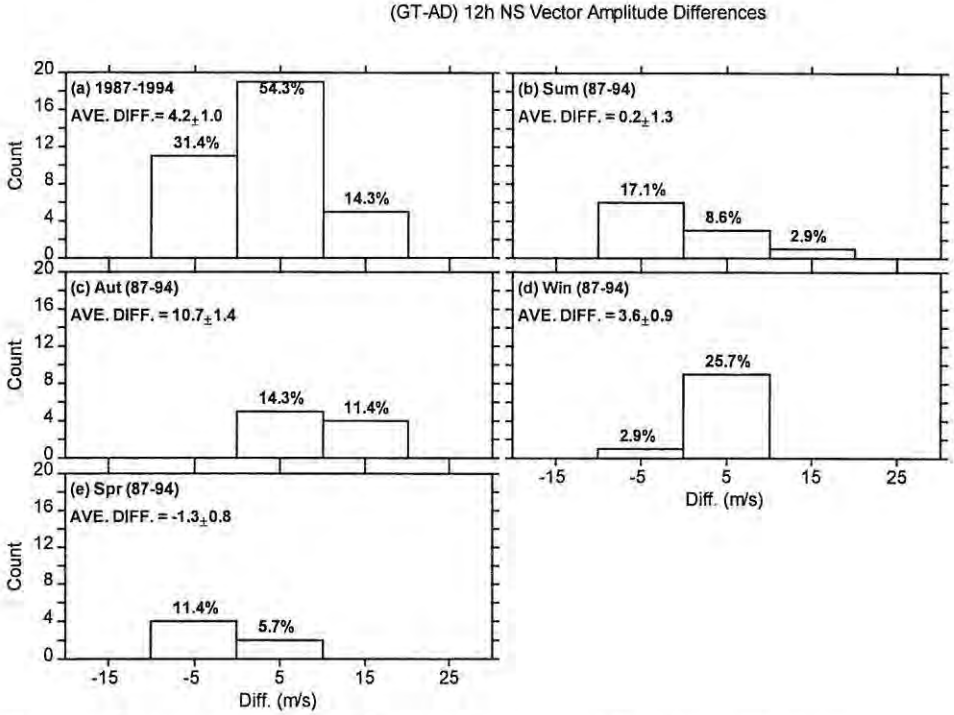

Figure 7.9 Same as **Figure 7.8** but for the meridional amplitudes.

that the bulk (~69 % for both the zonal and the meridional component) of the discrepancies between amplitudes at Grahamstown and Adelaide are due to larger amplitudes at Grahamstown. In agreement with the observations made at various sites in the 52-56°N latitude range [*Jabobi et al.*, 1999], the largest longitudinal differences between Grahamstown and Adelaide are recorded in autumn [average differences 17.6±1.8 ms^{-1} (EW) and 10.7±1.4 ms^{-1} (NS)] and winter [average differences 6.2±0.8 ms-1 (EW) and 3.6±0.9 ms^{-1} (NS)] (Figure 7.6 to Figure 7.9). *Jabobi et al.* [1999] suggest that some of the autumnal longitudinal differences could be due to the general variability of the background atmosphere and tides during this time while the winter longitudinal differences could be partly due to the interaction between tides and quasi-stationary waves in the lower atmosphere.

The contribution of non-migrating modes to the above longitudinal differences can also not be overlooked. For ~30°S latitude and at 95 km altitude, *Sivkov & Shved* [1993] calculated maximum longitudinal variations of 1-4 ms^{-1} due to zonal non-uniformity in the distribution of ozone and water vapour. These authors found that ozone excitation dominates water vapour excitation in the generation of migrating modes, but when it comes to the generation of non-migrating ones their respective contributions are comparable to each other.

7.2.2 Interannual Trends

A comparison of the interannual variation of the zonal and meridional amplitudes of the semidiurnal tide is shown in Figure 7.10 and Figure 7.11 for Grahamstown and Adelaide, respectively. At Grahamstown there is evidence of correlation in the interannual changes of the zonal and the meridional components for most months but less so in winter. Adelaide results also show some correlation but the numerous data gaps make it difficult to discern the pattern, if any. Figure 7.10 shows that at Grahamstown, there is greater (up to ~20 ms^{-1}) variability during autumn and winter whereas at Adelaide (Figure 7.11) greater variability is observed in summer.

There are a few possible sources of the interannual variation in the semidiurnal amplitudes. Solar dependence is one possible source that has been investigated by various authors but as yet there is no conclusive view on the true influence of solar activity on the semidiurnal tide.

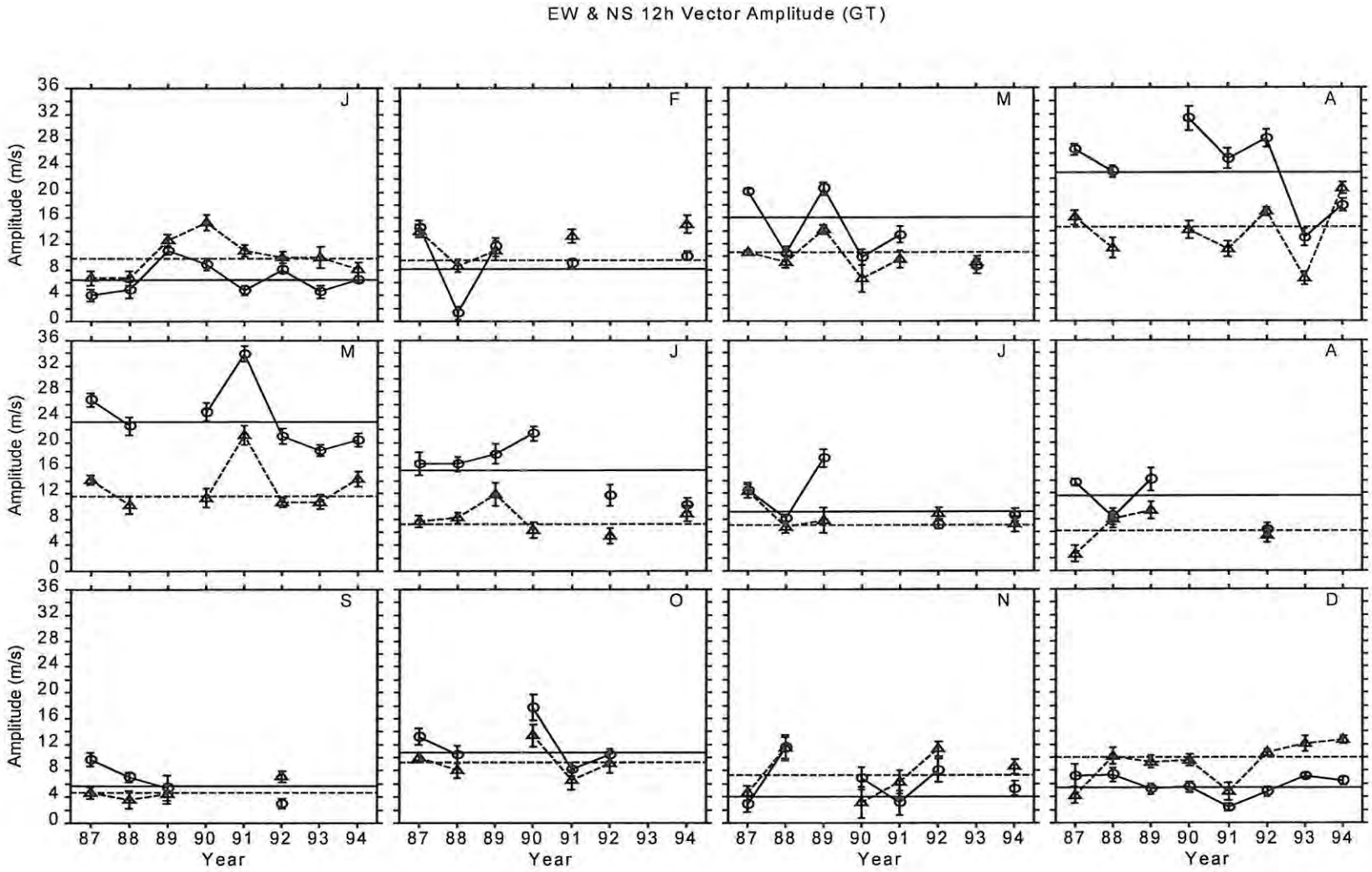

Figure 7.10 The interannual variation of the zonal (circles) and meridional (triangles) of the semidiurnal amplitudes at Grahamstown for different months. The horizontal solid and dashed lines represent the corresponding MIA for the zonal and the meridional amplitudes, respectively. The error bars represent one standard error of the mean (1 α).

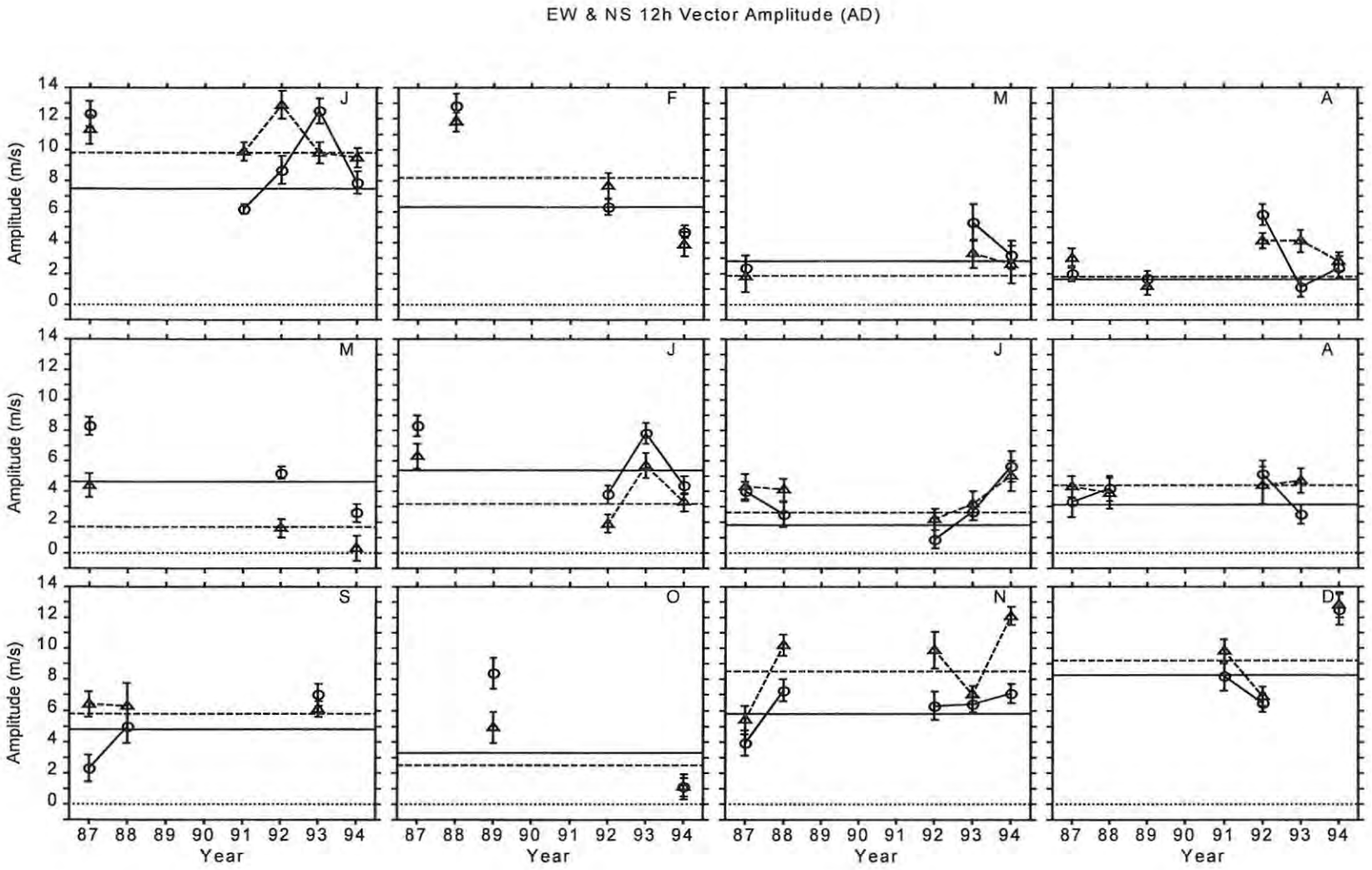

Figure 7.11 Same as **Figure 7.10** but for Adelaide.

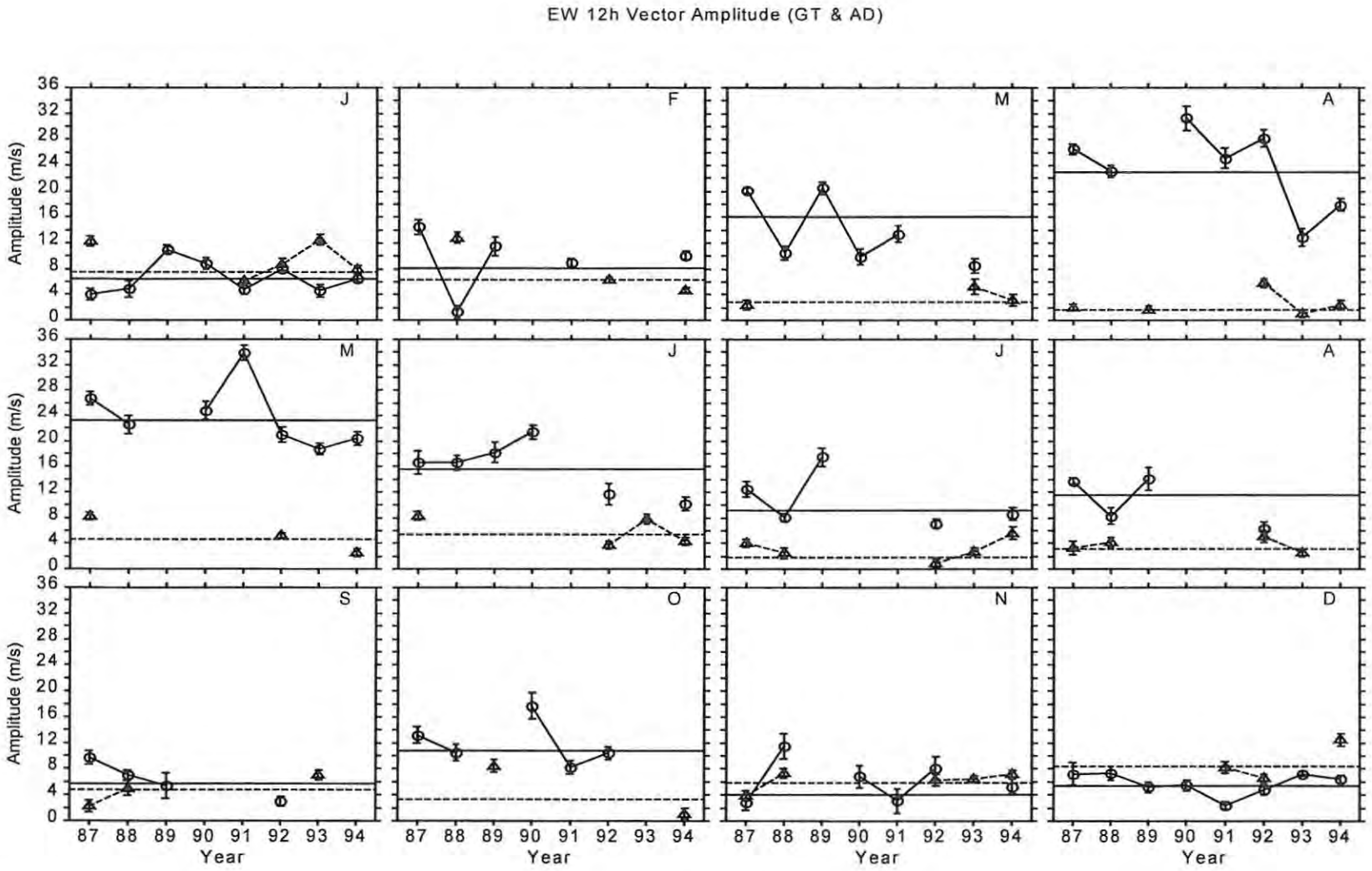

Figure 7.12 The interannual variation of the zonal amplitudes of the semidiurnal tide at Grahamstown (circles) and Adelaide (triangles) for different months. The horizontal solid and dashed lines represent the corresponding MIA for Grahamstown and Adelaide amplitudes, respectively. The error bars represent one standard error of the mean (1 α).

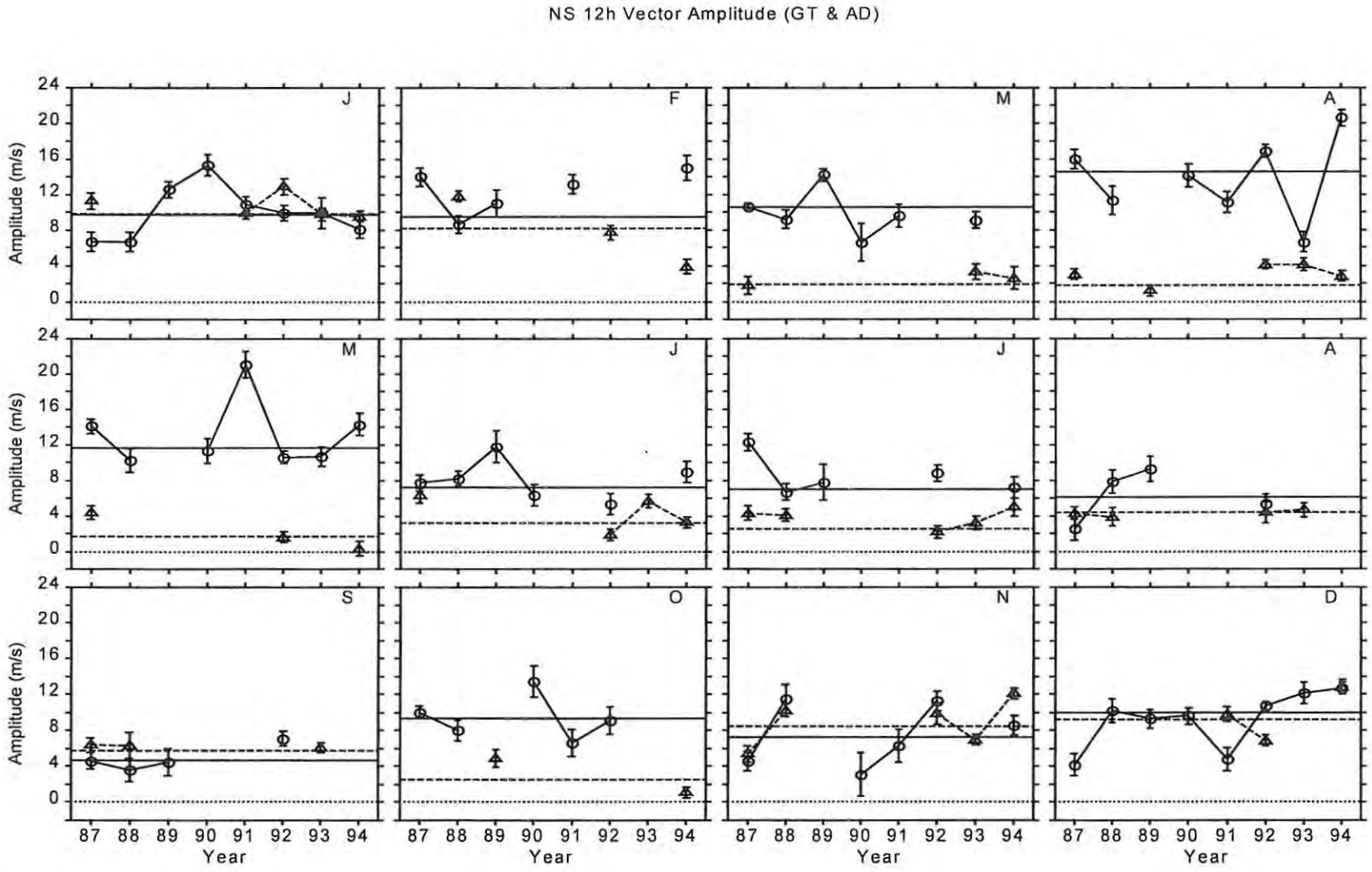

Figure 7.13 Same as **Figure 7.12** but for the meridional amplitudes.

Namboothiri et al. [1993,1994] report an apparent negative correlation characterized by smaller zonal and meridional semidiurnal tidal amplitudes during high solar activity and vice versa. In particular *Namboothiri et al.* [1993] found that this pattern existed in summer amplitudes, the winter amplitudes and the annual mean amplitudes of the semidiurnal tide. On the other hand, these authors found that the seasonal diurnal tidal amplitudes are not dependent on solar activity while the annual mean amplitudes of this tide show some apparent negative correlation with solar activity. However, *Namboothiri et al.* [1993] caution that the confidence levels associated with the correlations are low. *Bremer et al.* [1997] found that the zonal prevailing wind and the zonal semidiurnal amplitudes had a weak negative correlation with solar activity for most months while the meridional component and the diurnal tidal amplitudes show negligible correlation. Likewise, *Fraser et al.* [1989] did not find any strong evidence of solar dependence in the semidiurnal tide. However, *Jacobi et al.* [1999] report that the Collm data of *Jacobi et al.* [1997] indicate a positive solar-cycle dependence.

Another possible source of long-term changes in tidal amplitudes is the secular change in ozone forcing which may in turn be linked to changes in UV solar fluxes or ozone concentrations as suggested by *Portnyagin et al.* [1993b]. However, *Hagan et al.* [1992] found that the ozone QBO has no effect on the upward propagating semidiurnal tide. These authors attribute this to the fact that the peak heating of the tide (between 40-50 km altitude) occurs in the height range of small QBO effect (i.e. above the height level of peak ozone density). On the other hand, *Hagan et al.* [1992] found significant (5-20 ms^{-1}) variability of the mesospheric semidiurnal tide as a result of the QBO in stratospheric mean winds and temperature. Whereas the lower atmospheric zonally averaged wind and temperature QBO is largely confined to the low latitudes, the mesospheric semidiurnal tide QBO variations are largely manifested in the neutral wind at high latitudes [*Hagan et al.*, 1992].

A one-to-one comparison of Grahamstown and Adelaide is shown in Figure 7.12 and Figure 7.13 for the zonal and the meridional component, respectively. These figures show that there is no evidence of correlation of the semidiurnal tidal changes at the two sites. What stands out however is the interannual consistency of the longitudinal differences between the two sites. This pattern, as mentioned in Section 7.2.1.2, shows larger longitudinal differences in autumn and winter compared to summer and spring from year-to-year. However, superimposed on this year-to-year consistency in the longitudinal differences there is also a interannual variability.

That is, the longitudinal differences show some time dependence. For instance, for the zonal amplitudes (Figure 7.12) there is a tendency for the longitudinal differences to be smaller in autumn and winter for the years 1992-1994 compared to 1987-1991.

From their results, *Jabobi et al.* [1999] suggested that there could be a 11-year solar-cycle dependence in the longitudinal variations between Saskatoon (52°N, 107°W) and a number of European sites. These authors point out that such behaviour would be similar to the interannual changes that characterise the stratospheric polar vortex, which depend on the QBO in a different fashion during solar maximum as compared to during solar minimum. *Jabobi et al.* [1999] conducted an investigation for Saskatoon and Collm and found results that suggest that there could be a link between the change of the stratospheric polar vortex and the longitudinal differences of the semidiurnal tide. Their results indicated that on an interannual timescale, the semidiurnal amplitudes at Saskatoon are larger than those at Collm when the stratospheric 30 hPa heights in the North American region are below their long-term mean. According to *Jabobi et al.* [1999] the work of *Pawson et al.* [1993] indicates that the long-term averages of the mean polar stratospheric vortex are elongated resulting in higher stratospheric pressure levels over the North American region compared to the European region. From this fact, *Jabobi et al.* [1999] concluded that large amplitude differences are linked to smaller stratospheric height differences between the North American and the European regions. The correlation of the small stratospheric pressure level differences and larger amplitude differences on interannual timescales introduces a time dependent variation in the observed longitudinal tidal differences. A similar mechanism to this one could possibly explain the interannual change in the difference in the amplitudes at Grahamstown and Adelaide.

7.3 PHASE

7.3.1 Seasonal Trends

Phases of the semidiurnal tide and in particular at Grahamstown are around 12 noon. Consequently, some monthly phases are just before 12 h while the others are very close to 0 h. To avoid this deceptive phase jump, the phases of the semidiurnal tide were computed in such a way that the shortest time (positive or negative) from zero was considered. That is, the phases (ϕ) are defined such that $-6\text{ h} \leq \phi \leq 6\text{ h}$. The phases of the semidiurnal tide at Grahamstown and

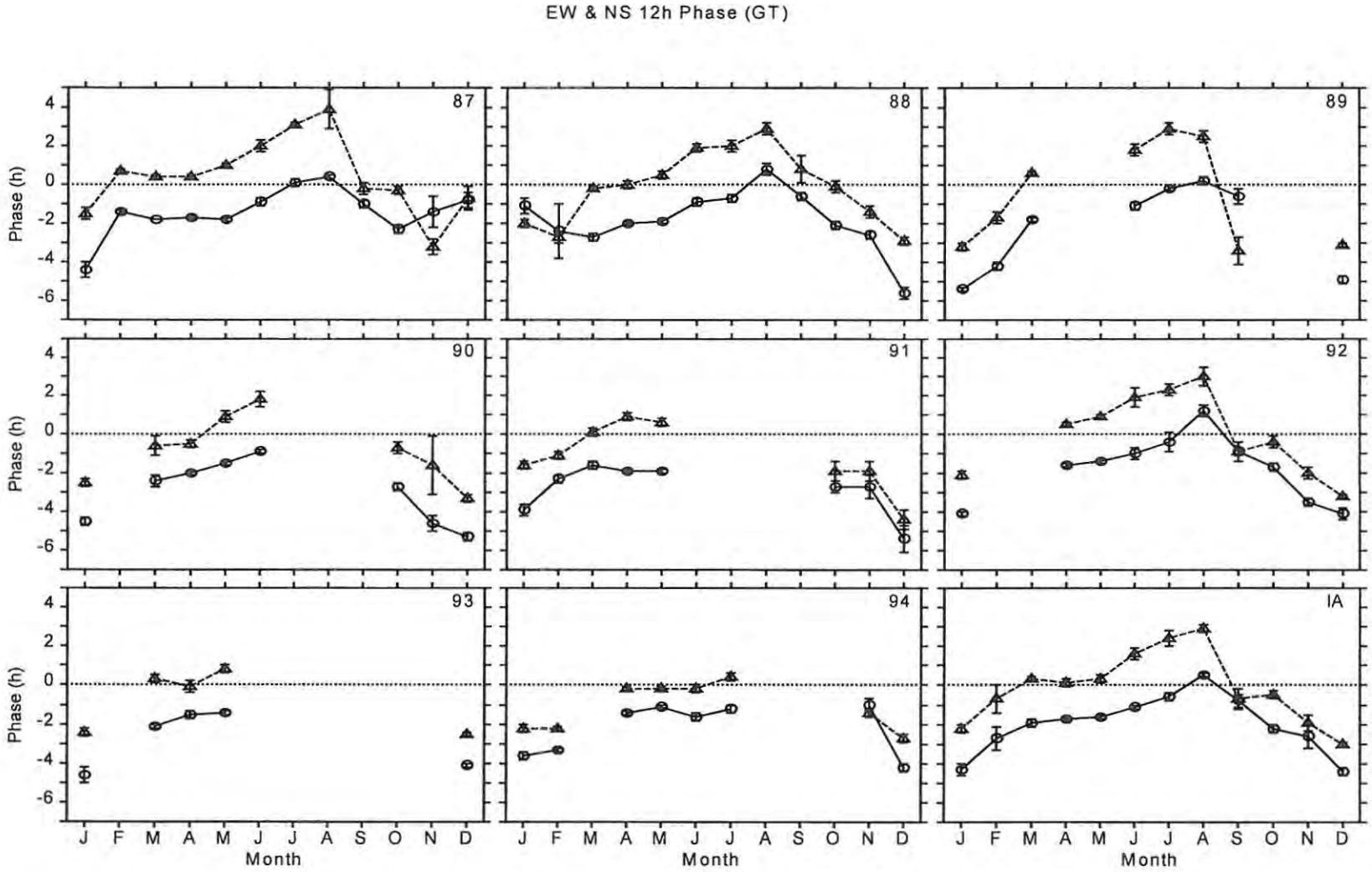

Figure 7.14 The zonal (circles) and the meridional (triangle) phases of the semidiurnal tide at Grahamstown for the years 1987-1994 and the IA. The error bars represent one standard error of the mean (1 α).

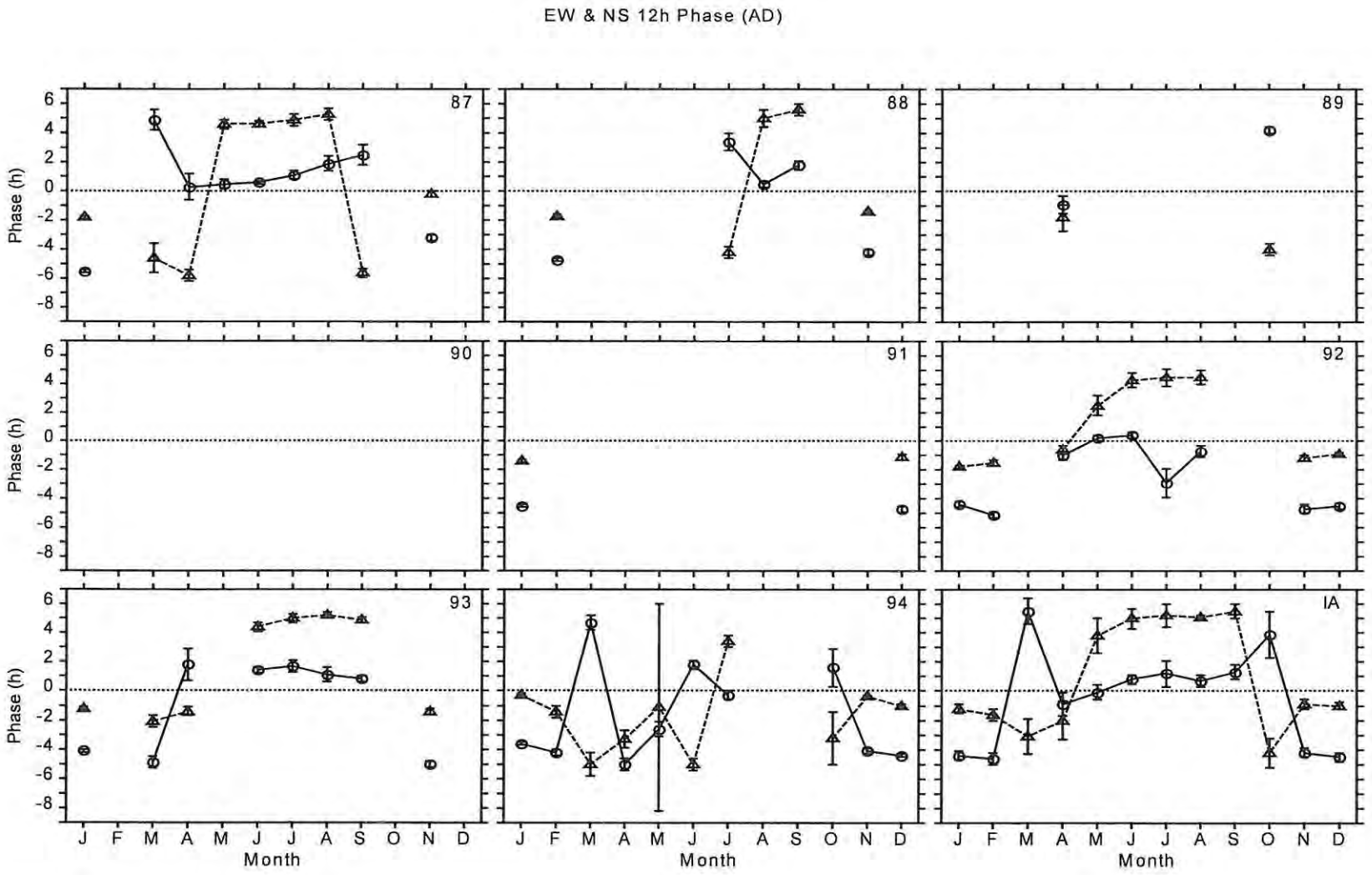

Figure 7.15 Same as **Figure 7.14** but for Adelaide.

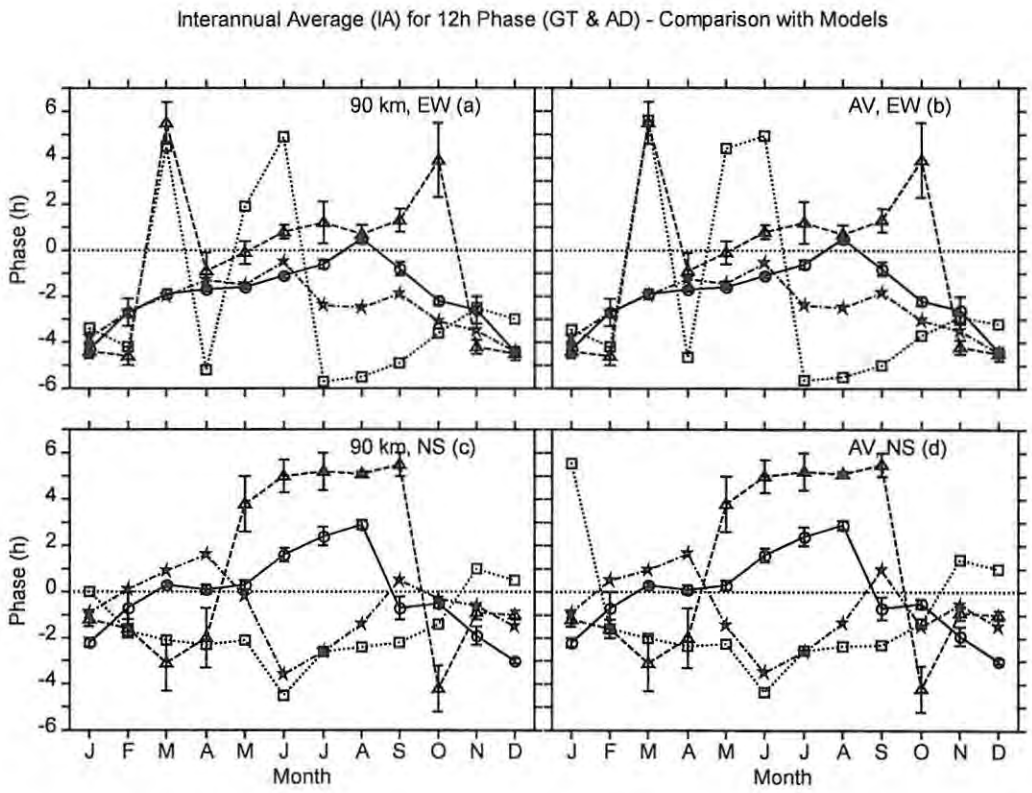

Figure 7.16 Comparison of the semidiurnal phase IAs at Grahamstown and Adelaide with the GSWM-00 and the STM. (a) Zonal phases with different symbols representing Grahamstown IA (circles), Adelaide IA (triangles), GSWM-00 (pentagons) and STM (squares) for model heights of ~ 90 km. (b) Same as (a) but for Gaussian weighted model phases. (c) and (d) are similar to (a) and (b) respectively but for meridional phases.

Adelaide are illustrated in Figure 7.14 and Figure 7.15, respectively. The zonal and the meridional phases at Grahamstown follow similar patterns. The general trend at Grahamstown shows a solstitial phase bi-modality characterized by earlier phases [~-4 h (EW) and ~3 h (NS)] in summer and late phases in winter [~0 h (EW) and ~3 h (NS)]. I have used the term "earlier" with respect to zero hours where negative phases are considered to be earliest. The equinoxes also show some asymmetry with a tendency towards later phases in autumn than in spring. Unlike at Grahamstown, the zonal and the meridional phases at Adelaide (Figure 7.15) follow complicated patterns, which are not similar to each other. The IAs at Adelaide, however, are more systematic and are similar to the Grahamstown pattern with both the zonal and the meridional components showing a phase bi-modality with earlier phases [~-4 h (EW) and ~-1 h (NS)] in summer and later phases [~0-1 h (EW) and ~5 h (NS)] in winter. However, at Adelaide the equinoctial transitions are sharper and also exhibit some overshoots in the IAs.

WINDII results [*McLandress et al.*, 1996] also show earlier [~5 h (EW) ~1 h (NS)] phases in summer and later [~ 0 h (EW) and 1 h (NS)] in winter. The zonal phases from WINDII show a sharp equinoctial transition that is somewhat similar to Adelaide while the meridional phases change more gently [*McLandress et al.*, 1996, their Figure 19]. Results from HRDI for latitudes 40°S, 50°S, and 60°S show a seasonal pattern that is quantitatively and qualitatively similar to the Grahamstown IAs for both the zonal and the meridional components [*Burrage et al.*, 1995b]. Generally, these HRDI results show a seasonal structure characterized by earlier [~-3 to -5 h (EW) and ~-2 h (NS)] in summer and later [~-1 to -3 h (EW) and ~0-2 h (NS)] in winter/spring. The two HRDI solstitial phase states, like the Grahamstown ones, are joined by gentle equinoctial transitions. Note that for easy comparison with satellite data, I have adjusted *McLandress et al.'s* [1996] and *Burrage et al.'s* [1995b] phases to be in line with my negative and positive definition of phases.

A comparison of the observed phases to the model phases is shown in Figure 7.16. Apart from the phase overshoot at Adelaide the observed (GT and AD) zonal phases have a very similar form to the GSWM-00 phases. In summer this comparison is even good quantitatively but in winter the good qualitative comparison is accompanied by GSWM-00 phases that are ~2-4 h earlier than observed phases. The zonal phases of the STM, on the other hand, shown a picture that might seem different but on closer examination is qualitatively similar to observations and the GSWM-00. Noting that all the phases that are ~5 h and ~6 h can equally be considered to be between ~7 h and ~6 h, respectively, then we see that the STM zonal phases are indeed qualitatively similar to the other results. The only difference is that the solstitial phase shift is larger (~ 8-10 h) for the STM than for the other results. For the meridional component there is good qualitative agreement between the models and the observations during summer and the equinoxes. However, during winter the observations at the Grahamstown and Adelaide show a phase delay as opposed to the phases advance indicated by models. From the GSWM, *Hagan* [1996] found that, as it was the case with the diurnal tide, the competing effects of the IR and UV forcing determine the phases and they follow the phase behaviour of the stronger of the two heating mechanisms.

The (EW-NS) phase differences for Grahamstown and Adelaide are shown in Figure 7.17 and

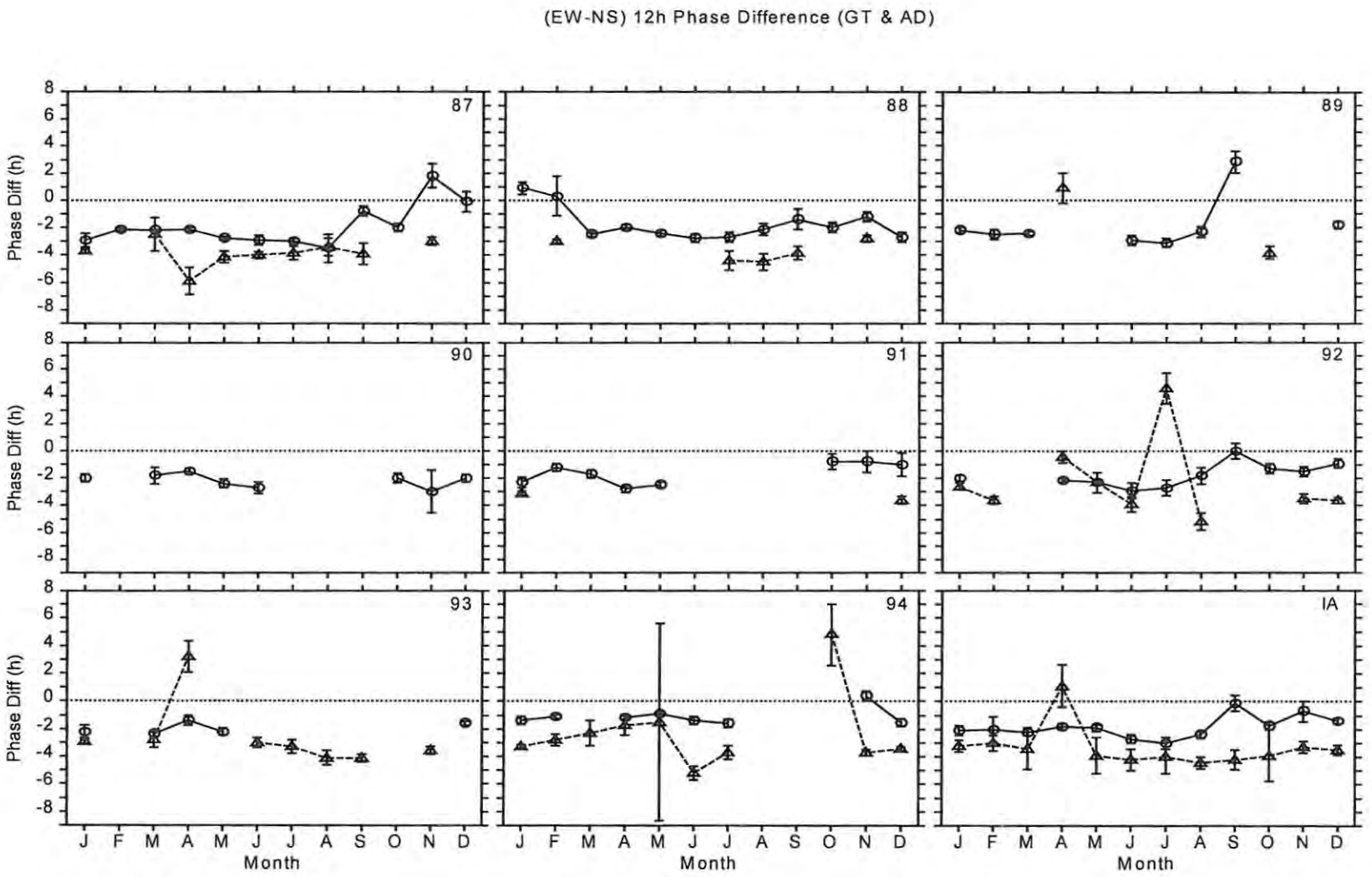

Figure 7.17 The (EW-NS) phase difference for the semidiurnal tide at Grahamstown (circles) and Adelaide (triangle) for the years 1987-1994 and the IA. The error bars represent one standard error of the mean (1 α).

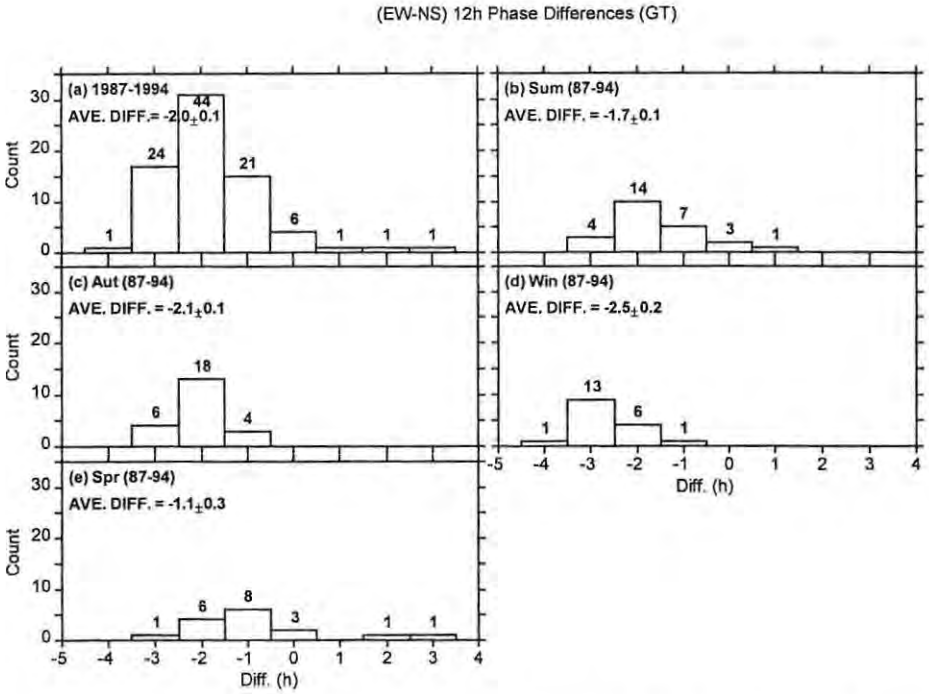

Figure 7.18 The distribution of the (EW-NS) phase differences for the semidiurnal tide at Grahamstown for the years 1987-1994. The weighted average differences and the percentage count (number at the top of bar) of each bar are also given.

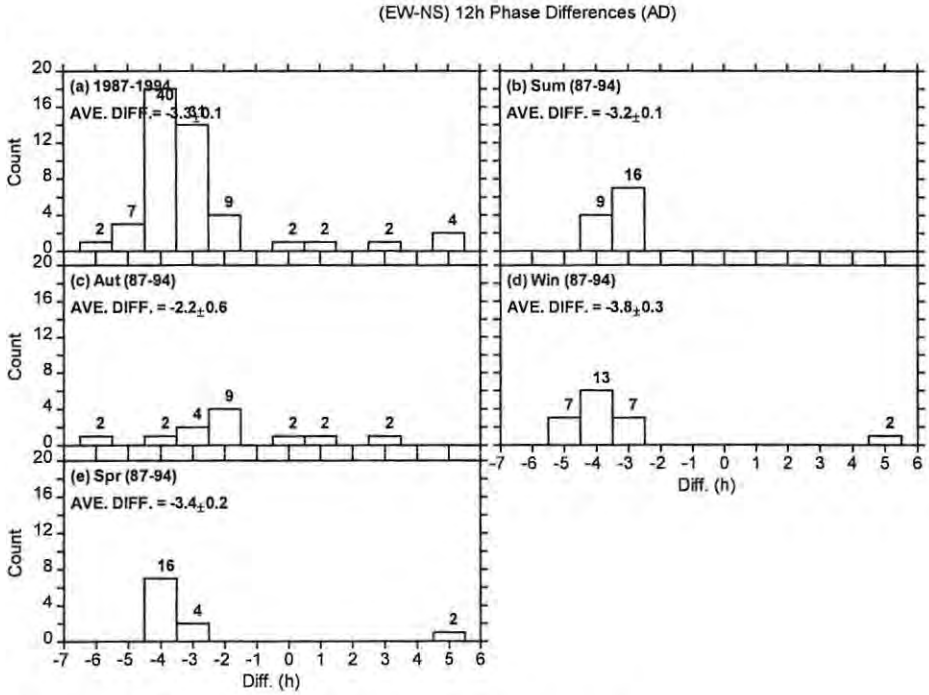

Figure 7.19 Same as **Figure 7.18** but for Adelaide.

Zonal Wavenumber, s	Phase Velocity (deg/h)	Phase Difference (h)
-7	-4.3	-33.6
-6	-5.0	-29.9
-5	-6.0	-26.1
-4	-7.5	-22.4
-3	-10.0	-18.7
-2	-15.0	-14.9
-1	-30.0	-11.2
0	Stationary	-7.5
1	30.0	-3.7
2	15.0	0.0
3	10.0	3.7
4	7.5	7.5
5	6.0	11.2
6	5.0	14.9
7	4.3	18.7

Table 7.1 The theoretical phase difference for monochromatic semidiurnal tide modes between Grahamstown and Adelaide and corresponding phase velocities. Positive phase differences represent later phases at Grahamstown compared to Adelaide.

the corresponding distributions are illustrated in Figure 7.18 (Grahamstown) and Figure 7.19 (Adelaide). The long-term trends of the phase differences at both sites do not change much with season and remain around ~-1 to ~-2 h at Grahamstown and ~3 to ~-4 h at Adelaide (except in April). From Figure 7.18 and Figure 7.19 we see that the long-term (1987-1994) average phase differences are -2.0±0.1 h (Grahamstown) and -3.3±0.1 h (Adelaide) with the majority [44% (Grahamstown) and 40 % (Adelaide)] of the differences in the bins centred at -2 h (Grahamstown) and -4 h (Adelaide). At both sites the largest average differences are recorded in winter even though the margins between these averages and those of the other seasons are not large. In line with anticlockwise polarisation of the velocity vector in the southern hemisphere, the zonal component tends to lead the meridional component. A cross-spectral analysis (not shown), similar to that in Chapter 6, Section 6.4.1, give results that are in agreement with those presented above yielding long-term average differences of -1.7±0.1 h (Grahamstown) and –3.2±0.2 h (Adelaide). The above results show that at both sites and especially at Adelaide the semidiurnal tide, like the diurnal tide, is close to quadrature (3 h).

The comparison of the zonal phases between Grahamstown and Adelaide is depicted in Figure 7.20 and a similar comparison for the meridional component is presented in Figure 7.21.

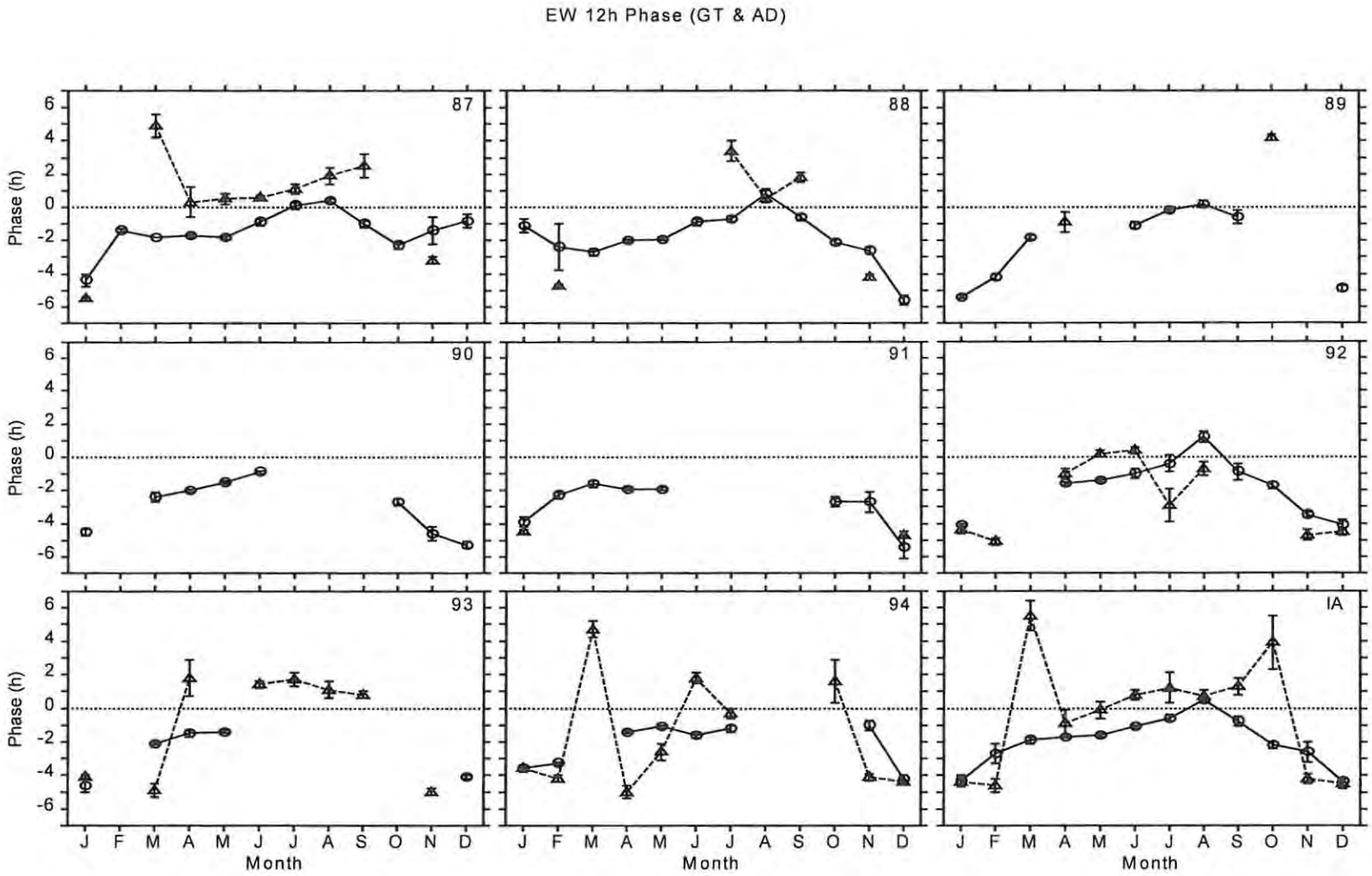

Figure 7.20 The zonal phases of the semidiurnal tide at Grahamstown (circles) and Adelaide (triangle) for the years 1987-1994 and the IA. The error bars represent one standard error of the mean (1 α).

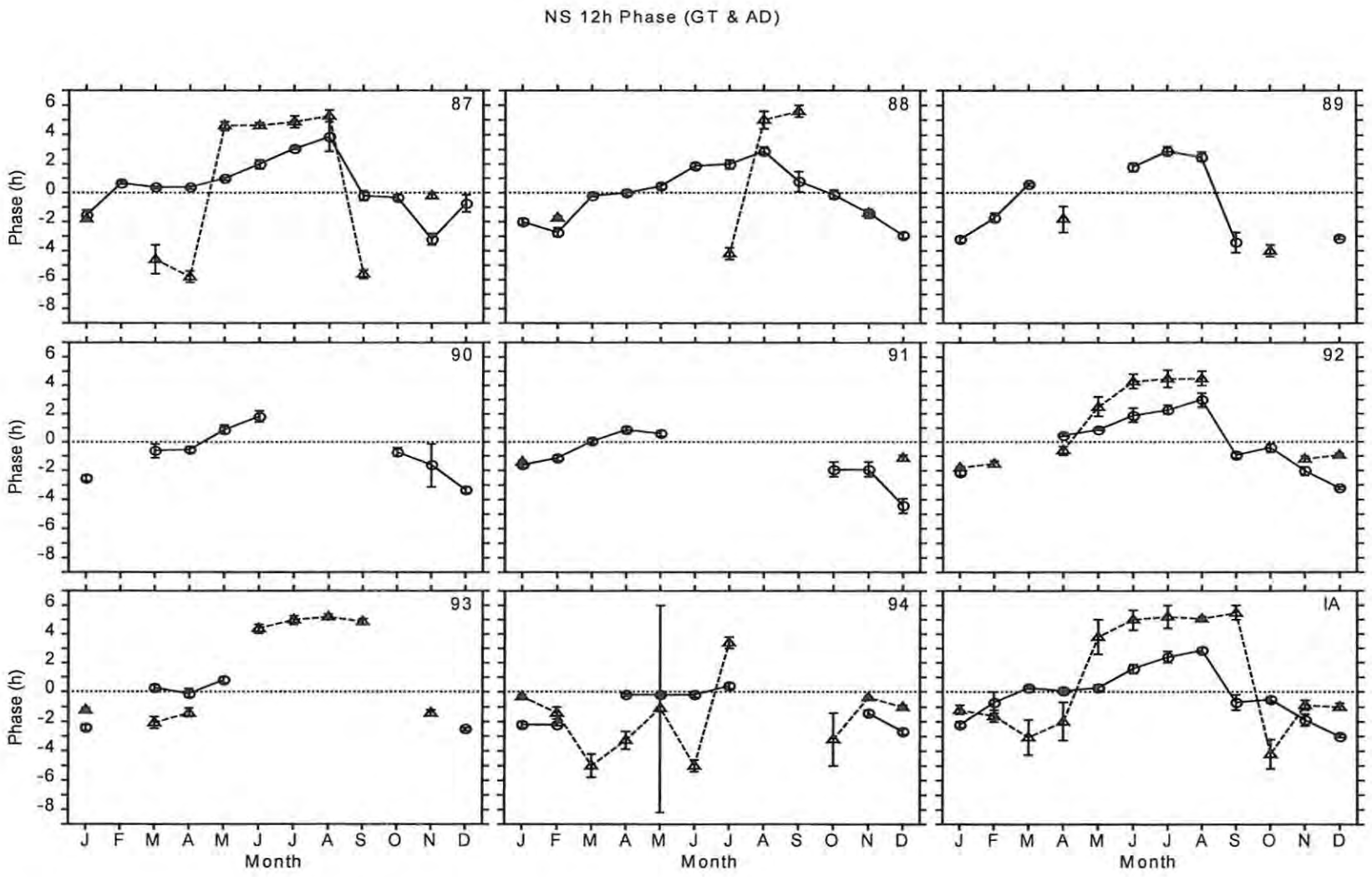

Figure 7.21 Same as **Figure 7.20** but for meridional phases.

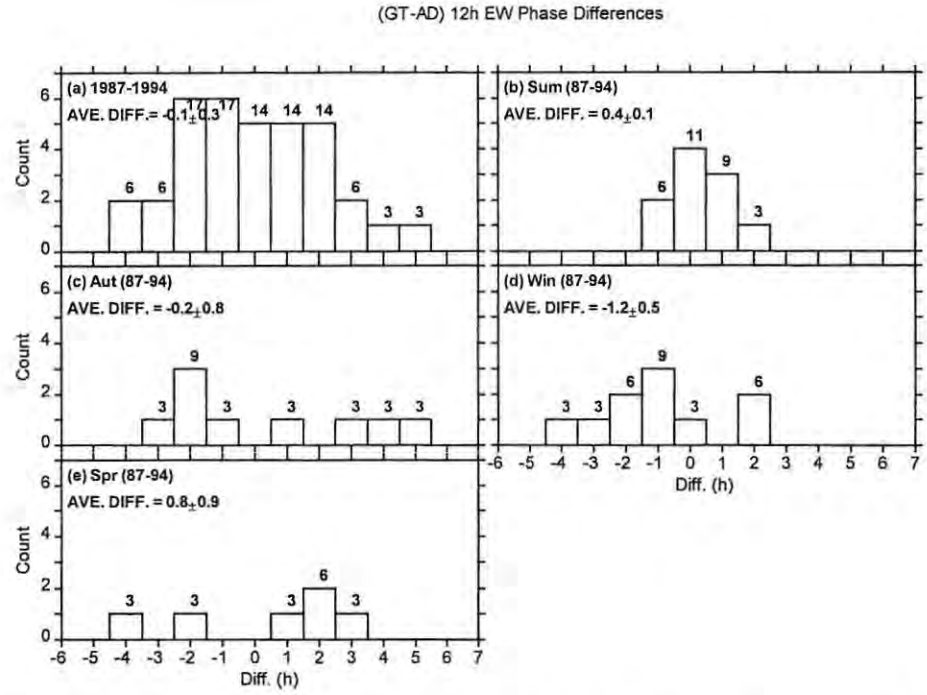

Figure 7.22 The distribution of the (GT-AD) zonal phase differences for the semidiurnal tide for the years 1987-1994. The weighted average differences and the percentage count (number at the top of bar) of each bar are also given.

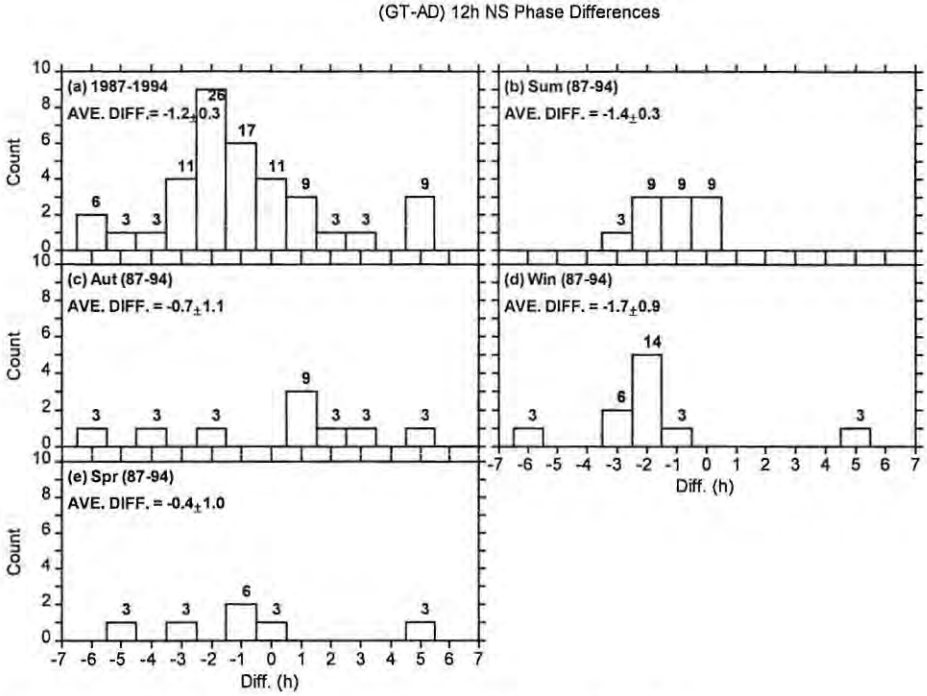

Figure 7.23 Same as **Figure 7.22** but for meridional phases

Generally the zonal phases (see IAs) at Adelaide are later by ~1-7 h than the Grahamstown ones except in summer when the Grahamstown phases are either comparable or later than the Adelaide ones. The long-term trend of the comparison of meridional phases (Figure 7.21, IA) show larger differences in phases between Grahamstown and Adelaide compared to zonal phases. The meridional phases at Adelaide tend to be later than the Grahamstown ones by ~1-8 h except around the equinoxes when Grahamstown tend to lead Adelaide by ~3 h.

The distribution of the (GT-AD) phase differences (Figure 7.22 and Figure 7.23) show a large spread with differences ranging from –6 h to 5 h. The majority of the differences are in the -2 or -1 h bins for both components and the long-term (1987-1994) averages of the differences are -0.1±0.3 h (EW) and -1.2±0.3 h (NS). From the cross-spectral analysis (not shown), these averages are -1.2±0.3 h (EW) and -3.1±0.3 h (NS). These phase differences suggest the existence of non-migrating semidiurnal modes between Grahamstown and Adelaide. These results are in line with the calculations of *Sivkov & Shved* [1993] which give maximum longitudinal phase variations that are generally < 2 h at ~30°S and 95 km.

Table 7.1 gives the calculated theoretical phase differences between Grahamstown and Adelaide and the corresponding phase velocities assuming the semidiurnal tide consists of monochromatic modes. Looking at the possible theoretical phase differences in conjunction with the observed average phase differences, which are in the range -2 to 1 h, it is clear that the semidiurnal tidal structure is dominated by the migrating tide in agreement with *Sivkov & Shved* [1993].

7.3.2 Interannual Trends

Unlike the diurnal tide (Figure 6.41 and Figure 6.42), the semidiurnal phases (Figure 7.24 and Figure 7.25) show less interannual variation especially at Grahamstown. Figure 7.24 shows that while the Grahamstown phases show significant seasonal changes, interannual changes, while measurable, are less pronounced. In June, for instance, there is essentially no interannual variation in the phases at Grahamstown. Since the phases of the semidiurnal tide, like those of the diurnal tide, follow the phase of the dominant heating mechanism, the interannual consistency of the phases seem to suggest that these heating mechanisms behave in a consistent

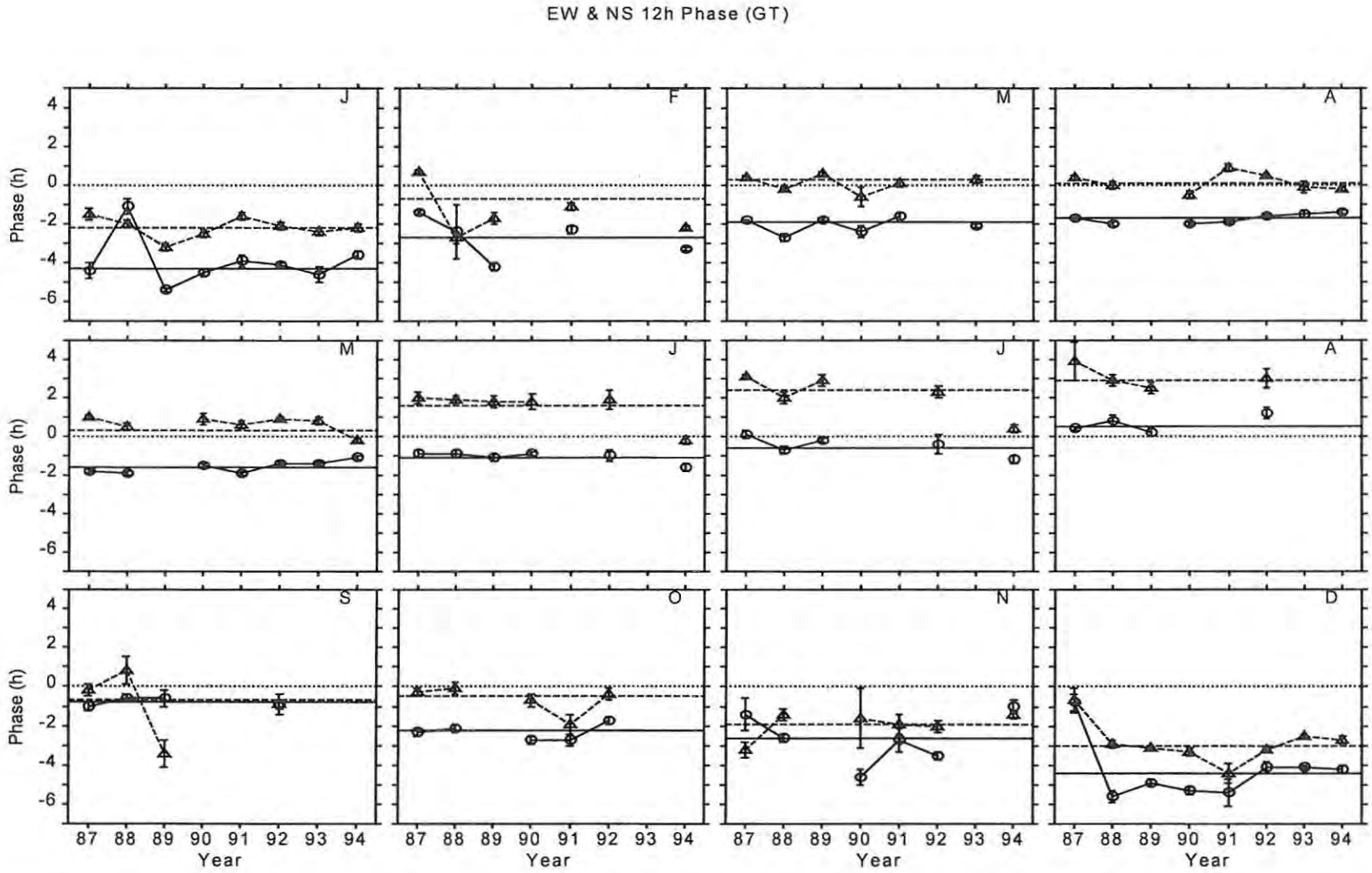

Figure 7.24 The interannual variation of the zonal (circles) and meridional (triangles) of the semidiurnal phases at Grahamstown for different months. The horizontal solid and dashed lines represent the corresponding MIA for the zonal and the meridional amplitudes, respectively. The error bars represent one standard error of the mean (1 α).

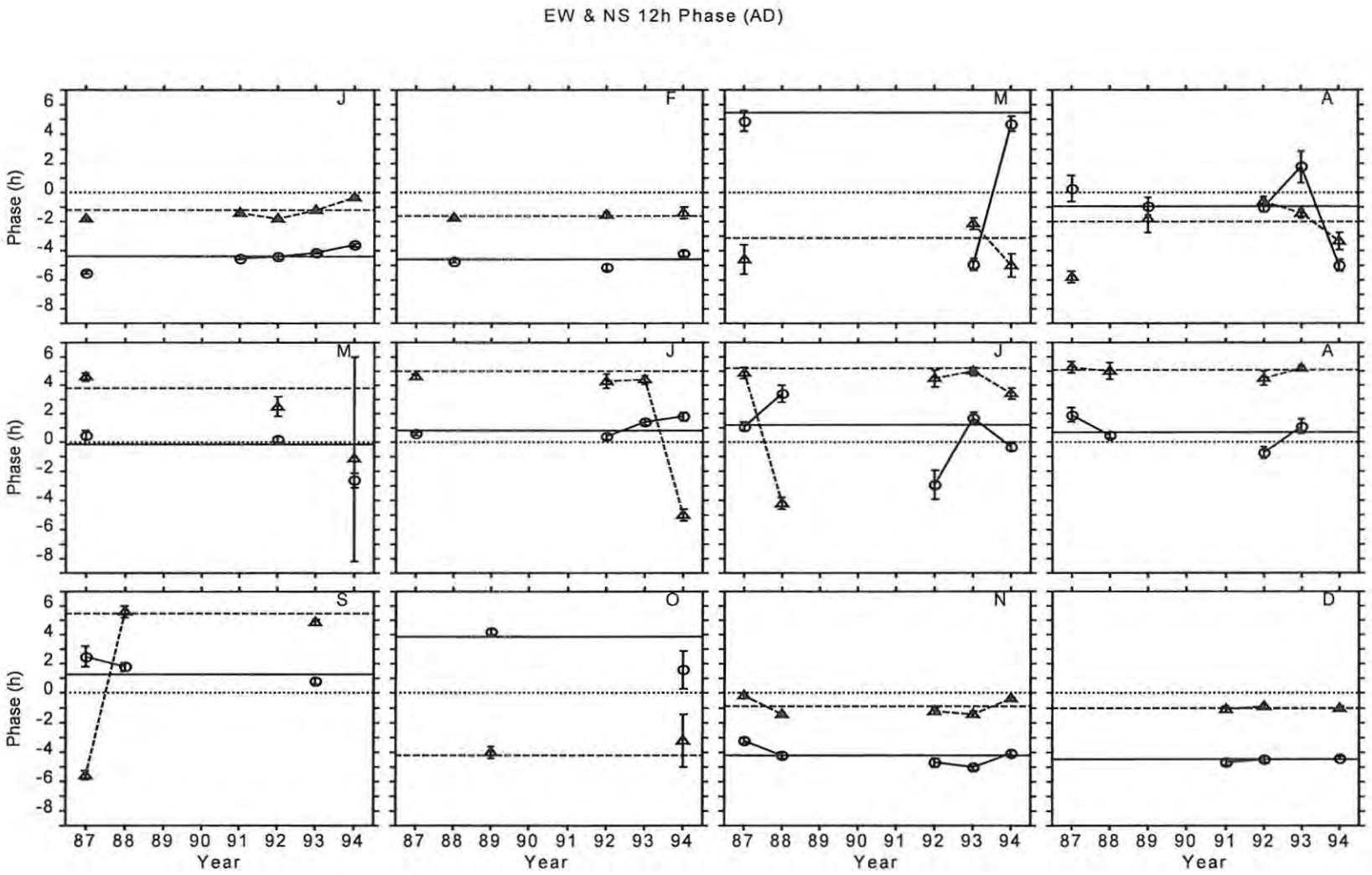

Figure 7.25 Same as **Figure 7.24** but for Adelaide.

manner from year to year. Of interest is the fact that the amplitudes of the semidiurnal tide (Figure 7.10 and Figure 7.11) show a relatively higher level of interannual variation compared to phases. This suggests that whereas the magnitudes of the competing forcing mechanisms may change from year to year, the relatively dominant component remain the same even if it is with a changed level of dominance. For instance, consider a situation in which the magnitudes of the IR and UV forcing significantly changes interannually but with, say, UV forcing remaining the dominant component over the years. In this case the amplitude might change interannually while the phase, being determined largely by the dominant component, generally remains unchanged.

Interestingly, some of the observable interannual changes show correlation between the zonal and the meridional component. Good examples of these are March, July and January (with one exception) at Grahamstown and January and November at Adelaide. The implication of this is that during such months the phase difference between the zonal and the meridional component is interannually invariant suggesting a similar invariance in the mode composition of the tide during these months. At Adelaide there is less interannual variation from late spring to end of summer with winter and the equinoxes, and the latter in particular, being more variable. At Grahamstown, on the contrary, there is more variability during the summer months.

7.4 SUMMARY OF AMPLITUDES AND PHASES

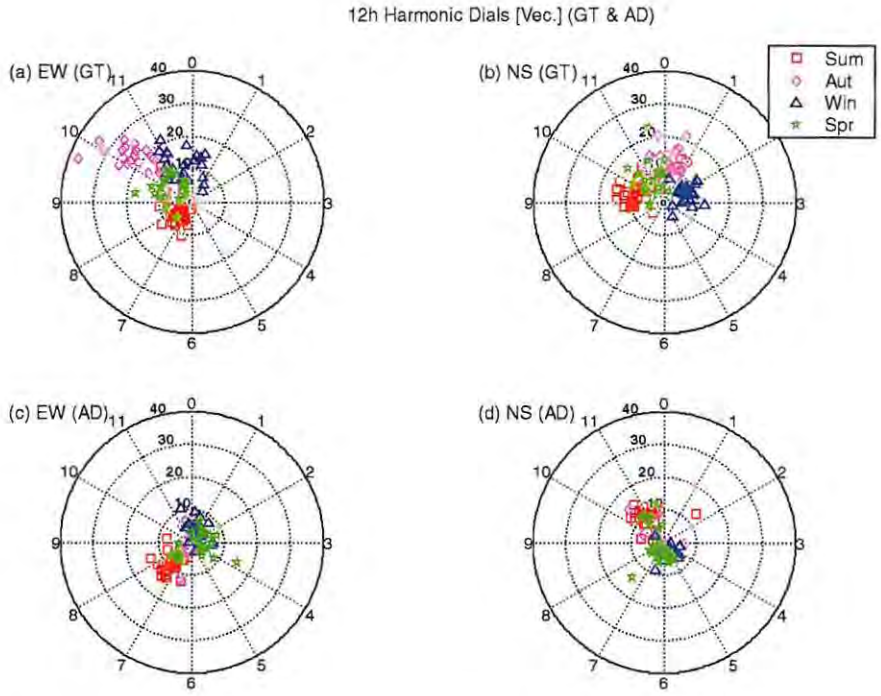

Figure 7.26 The harmonic dial of the zonal and meridional semidiurnal tide at Grahamstown and Adelaide for the years 1987-1994. The units of the radius of the circles are ms^{-1} and the peripheral numbers represent the phase in hours. Different symbols and colours represent different seasons.

Figure 7.26 to Figure 7.30 summarise all of the features that were discussed about the observations made at Grahamstown and Adelaide. The amplitudes at both sites follow a predominantly annual cycle. At Grahamstown, in agreement with results from WINDII, HRDI and GSWM-00, the peak amplitudes (zonal in particular) are in autumn (see Figure 7.26(a) especially). The stronger semidiurnal activity at Grahamstown can clearly be seen from Figure 7.26, which shows that the amplitudes at Adelaide are mainly confined to within the 10 ms^{-1} circle whereas at Grahamstown they spread even beyond the 30 ms^{-1} circle. The seasonal and interannual features discussed in the previous sections can be seen in the contour plots (Figure 7.27 to Figure 7.30).

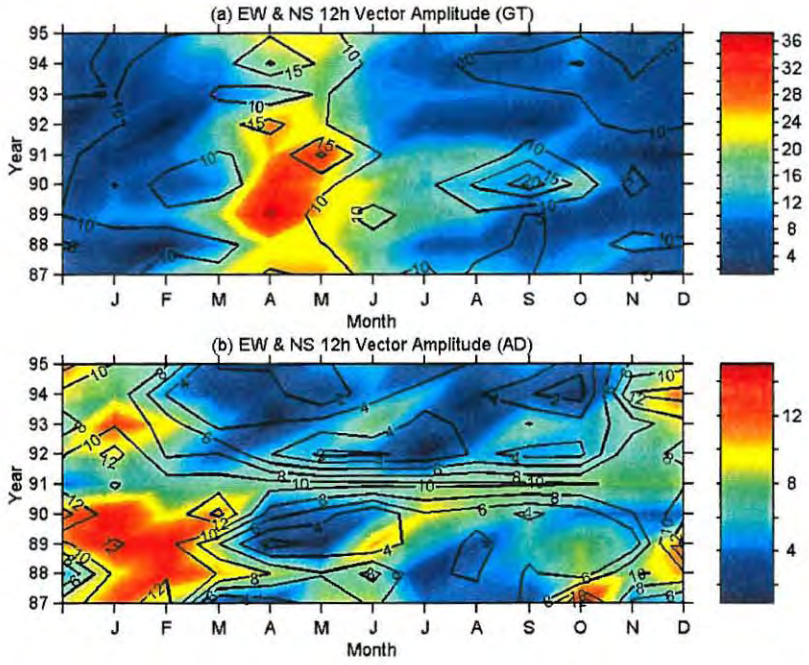

Figure 7.27 (a) The zonal semidiurnal amplitude (coloured shading) and meridional semidiurnal amplitude (contours) at Grahamstown. Units of the colour bars are in ms^{-1}. (b) Same as (a) but for Adelaide.

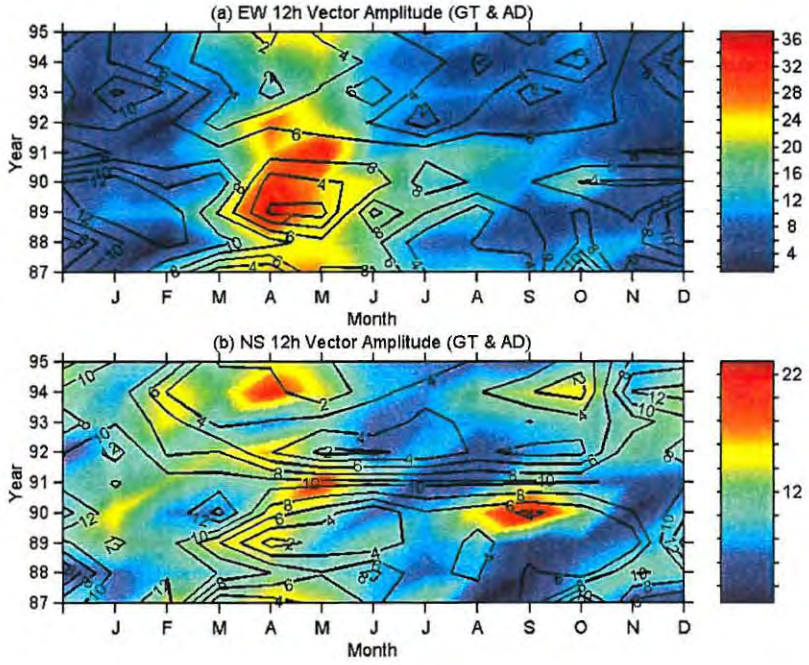

Figure 7.28 (a) The zonal semidiurnal amplitude at Grahamstown (coloured shading) and Adelaide (contours). Units of colour bars are in ms^{-1}. (b) Same as (a) but for meridional semidiurnal amplitudes.

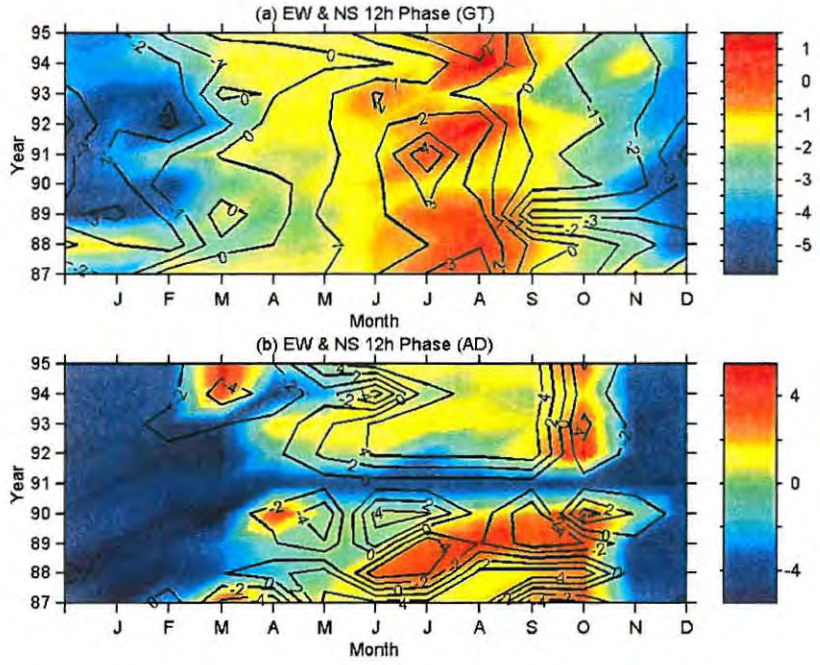

Figure 7.29 (a) The zonal semidiurnal phase (coloured shading) and meridional semidiurnal phase (contours) at Grahamstown. Units of the colour bars are in h. (b) Same as (a) but for Adelaide.

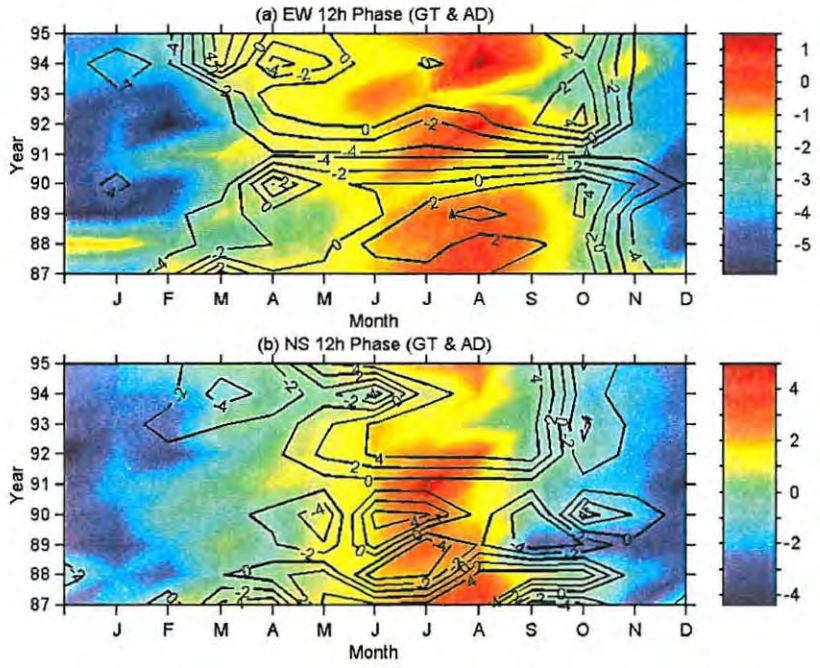

Figure 7.30 (a) The zonal semidiurnal phase at Grahamstown (coloured shading) and Adelaide (contours). Units of colour bars are in ms^{-1}. (b) Same as (a) but for meridional semidiurnal phases.

CHAPTER 8 SUMMARY & CONCLUSION

Broadly this thesis was concerned with the dynamics of the atmosphere near 90 km at ~34°S. More specifically my goal was to (a) deduce the dynamical structure of the mean flow, the diurnal and semidiurnal tides at Grahamstown (33.3°S, 26.5°E) and Adelaide (34.5°S, 138.5°E), (b) compare the respective dynamical structures in order to ascertain longitudinal effects since the two sites are in latitudinal proximity but are widely separated in longitude, and (c) compare my results with observations made by other authors, models and theory. To achieve this, I used various numerical techniques, which were reviewed in Chapter 2. This was followed by Chapter 3, in which I focused on observational techniques with special emphasis on the Grahamstown and Adelaide systems. The two sites use different observational techniques (meteor versus spaced antenna) and, also, the Grahamstown radar does not have height resolution while the Adelaide one does. I addressed these two problems and concluded that (i) both the meteor and the spaced antenna methods give a true representation of the motion of the neutral atmosphere in the MLT region, and (ii) with the averaging process applied on the Adelaide data, the results presented here can, with a reasonable level of confidence, be considered to be a valid comparison of atmospheric motion at ~90 km altitude at Grahamstown and Adelaide. Chapters 4 to 7 focus on achieving goals (a) to (c) above based on data obtained at the two sites from 1987 to 1994. The main points of the findings of these chapters are summarised in the next sections.

8.1 THE MEAN FLOW

Both the zonal and the meridional components of the mean flow at Grahamstown and Adelaide are characteristically variable and, as found by other authors, exhibit a strong planetary scale activity. In general, the spectra at Grahamstown and Adelaide show a number of planetary scale oscillations with the quasi-16-day (periods of ~12-20 days) oscillation being the most frequent and dominant for both the zonal and the meridional components. Such oscillations have also been observed in mesospheric temperatures [*Espy & Witt*, 1996; *Espy et al.*, 1997]. So far there is no conclusive theory about the source of these waves but it is widely assumed that they are due to Rossby-gravity normal modes that originate in the lower atmosphere [*Vincent*, 1990; *Williams and Avery*, 1992; *Forbes et al.*, 1995].

Since the 16-day wave is more dominant in the 2-20-day period range, I conducted a more detailed analysis of this oscillation. In general, at both Grahamstown and Adelaide this wave

does not always show correlation between the zonal component and the meridional component. This could be due to the fact that (i) the zonal and meridional velocities of Rossby waves have different horizontal characteristics [*Salby & Roper*, 1980], (ii) the difference in zonal and meridional responses of the interhemispheric ducting of this wave [*Forbes et al.*, 1995], and (iii) the differences in the gravity wave spectrum. The third mechanism can also explain the lack of correlation in the behaviour of the wave at Grahamstown compared to Adelaide especially because the distribution of gravity waves, especially the orographically generated ones, is geographically dependent.

Apart from the short-term variations of the mean flow, I also considered the long-term trends of the mean flow. We observe that at both Grahamstown and Adelaide, the zonal mean flow is generally stronger than the meridional component. While at Grahamstown, the zonal flow is always eastward at Adelaide it sometimes turns westward. The zonal mean circulation at Grahamstown tends to have a primary maximum in November or summer and a secondary maximum in winter. Adelaide also has solstitial peaks but, contrary to Grahamstown, the primary peak is in winter with the secondary one occurring in summer. The meridional flow at both sites is mostly northward/equatorward (positive) but also shows some southward/poleward (negative) and more so at Adelaide. The seasonal pattern of the meridional flow at Grahamstown and Adelaide is characterised by strong northward flow from November to January/February and a weak northward or southward flow from about March to October. This behaviour is in line with the pattern of equatorward flow in summer and poleward flow in winter as a result of wave drag [*Thomas*, 1996]. The zonal mean flow of the MWM is similar to Grahamstown for the first four months of the year and tends to follow the pattern at Adelaide for the rest of the year. Qualitatively the observed meridional mean flow is similar to the MWM flow but the model southward flow reach stronger peaks ($\sim$8 ms^{-1}) and tends to start earlier in the year.

A fundamental difference between Grahamstown and Adelaide is that the zonal and the meridional speeds at Grahamstown are about twice those at Adelaide. The source of this discrepancy is not known but there are a number of possibilities. These include (i) stationary planetary waves (see e.g. *Forbes et al.* [1995]; *Kazimirovsky et al.* [1988]), (ii) a possible difference between the two sites in the interface level between the oppositely directed stratospheric and mesospheric jets. Judging by the higher occurrence rates of the westward

flows and the southward flows at Adelaide compared to Grahamstown, the second point seems to be a strong possibility.

8.2 SHORT-TERM TIDAL VARIATIONS

At both Grahamstown and Adelaide the diurnal and the semidiurnal tidal amplitudes, like the mean flow, show short-term variations. A number of mechanisms have been suggested as possible causes of these variations but the extent of the contribution of each of these is not known. A more detailed analysis of these short-term variations at Grahamstown and Adelaide shows that in the 2-20 day period range the dominant spectral components are the ~10 day and (once again) ~16 day oscillations. As was the case with the mean flow, the occurrence of the planetary activity is not necessarily correlated between the zonal and the meridional component at both sites. Although the 16-day wave dominates both the mean flow and the tidal amplitudes, there is no obvious correlation between the mean flow and the tidal 16-day waves nor is there any apparent correlation in the 16-day wave of the diurnal tide to that of the semidiurnal tide. However, such a link cannot be discounted especially because any 16-day modulation of the mean flow in the lower atmosphere can results in a similar modulation of the gravity wave drag. Since this drag affects both the mean flow and tides (or at least the diurnal tide), it becomes clear that the possibility of a correlation in the 16-day oscillation of the mean flow and that of tides is distinctly possible. A more detailed study of this subject is necessary and could help us understand this oscillation in more detail.

The instantaneous (hourly) amplitudes of the tides show variation that is sometimes oscillatory with periods of several days. There is no correlation between the diurnal and the semidiurnal amplitude variations. Instantaneous (hourly) periods show deviation from tidal (24- and 12-h) periods with these exact periods accounting for less that 50% of the observed periods. These period/phase variations could possibly be associated with the transient modification of the tidal excitation. More specifically, those instances with non-tidal periods and large amplitudes may indicate times of large injection of energy at non-tidal frequencies. Another possible source of period/phase fluctuations are gravity wave-tidal interactions as found by *Fritts & Vincent* [1987] that the gravity wave effects can result in tidal phase advance. Further investigation of tidal variability involved the use of auto-spectral and bispectral techniques. This analysis indicates that the meridional flow at Grahamstown is influenced by non-linear interactions

between planetary waves and tides. I considered different cases and each of these gave us a different perspective on possible non-linear interactions.

8.3 LONG-TERM TRENDS FOR TIDES

8.3.1 General

The dynamic auto-spectral and cross-spectral analysis shows that at both Grahamstown and Adelaide the dynamics of the MLT region is dominated by the diurnal and the semidiurnal tides in the ~6-48 h period range throughout most of the years considered. This is consistent with well-established expectations. For Grahamstown, the semidiurnal tide is as strong as the diurnal tide whereas at Adelaide, the semidiurnal tide tends to be weaker than its diurnal counterpart. Another difference between the two sites is that at Grahamstown there is stronger tidal activity in the zonal flow than in the meridional flow and this is not clearly evident at Adelaide. In general, the level of tidal activity tends to be seasonally dependent.

Apart from the tidal components, there is also a significant manifestation of the two-day wave and more so in the meridional flows of both sites. This wave tends to be consistently strong in summer and seem to be very correlated between Grahamstown and Adelaide but a conclusive judgement in this regard is hampered by data gaps at the latter site. Coherency plots show that tidal frequency components tend to have a higher degree of linear correlation than the other components with Adelaide having a higher degree of linear correlation than Grahamstown.

The GT/AD cross-spectral analysis show that tides and the two-day wave are the only components that prevail while the other weak spectral components fade off completely in this analysis indicating that they were either not real features or that they were more local in nature. The GT/AD cross-spectral analysis shows that the 2-day wave is (i) a regular summer phenomenon, (ii) consistent from year to year, and (iii) has a large horizontal extent.

8.3.2 The Diurnal Tide

8.3.2.1 Amplitude

The diurnal amplitudes at both Grahamstown and Adelaide are characterised by a great semi-annual seasonal variations with the IAs indicating a higher tendency for amplitude peaks to

occur during the equinoxes and some minima during the solstices. At both Grahamstown and Adelaide the zonal amplitude peaks show an equinoctial asymmetry characterised by larger amplitudes in autumn than in spring while the meridional amplitude peaks are characterised by some degree of equinoctial symmetry. The zonal equinoctial asymmetry could possibly be due to a similar asymmetry in the interference between the H_2O and the O_3/O_2 forcings [*Hagan*, 1996]. The zonal amplitudes tend to be larger than the meridional ones especially at Grahamstown.

The results of Grahamstown and Adelaide and, in particular the semi-annual variations observed at the two sites, are in broad agreement with models (GSWM-00, DTM), other ground based results (e.g. *Vincent et al.* [1988]; *Fraser et al.* [1995]) and satellite results from HRDI [*Khattatov et al.*, 1997a; *Burrage et al.*, 1995a] and from WINDII [*McLandress et al.*, 1996]. This semi-annual variation has also been simulated by *McLandress* [1997] who also concluded that this variation is not caused by the variations of the dominant thermotidal heating mechanisms. A number of possible sources of this semi-annual variation have been advanced and they include the non-linear interaction of the 2-day wave and the diurnal tide, which results in the leakage of energy from the diurnal tide during the solstices [*Norton and Thuburn*, 1999]. In line with the above view, some complex demodulation results at Grahamstown show an inverse relationship between the 2-day wave and the diurnal tide. However, a more detailed study in this regard is necessary before any firm conclusion can be made based on the Grahamstown results. Gravity waves can also play a role in causing the semi-annual variation. While other authors e.g. *Norton and Thuburn* [1997] discount a direct link between gravity waves and the semi-annual variation of the diurnal tide, there are those whose results seem to be in line with such a possibility (e.g. *Mayr et al.* [1998]; *Meyer* [1999]).

Apart from the seasonal trends discussed above, the tidal amplitudes at Grahamstown and Adelaide also show interannual variations. Interestingly, the interannual variation in the zonal amplitudes is not necessarily correlated to those of their meridional counterpart and there is no obvious relationship between the interannual variation at Grahamstown and that at Adelaide for both the zonal and meridional amplitudes either. It has been suggested [*Vincent et al.*, 1998] that the interannual variation of the diurnal tides could be due to QBO effects on tidal forcing and wave drag. Due to time constraints, I did not do a detailed investigation to find out if there are any QBO signatures in the tidal amplitudes presented in this thesis. This is an area that

could be investigated in the future.

A direct comparison of Grahamstown and Adelaide shows that the structure of the diurnal tide in the MLT region of about 34°S is characterized by longitudinal differences. In general, as was the case with the mean flow, both the zonal and meridional amplitudes tend to be larger at Grahamstown than at Adelaide. For both components larger amplitudes at Grahamstown account for at least 60% of the observed differences. Similar longitudinal differences have been observed by other ground-based instruments and via satellite. These differences have also been simulated and are thought to be largely caused by non-migrating tidal components, which are in turn caused by various zonally non-uniform excitation mechanisms.

8.3.2.2 Phase

The zonal and meridional phases of the diurnal tide are characterized by great seasonal fluctuations as well as interannual changes. At Grahamstown there is a tendency for the solstice months to have later phases (especially in summer) compared to the equinoxes for both the zonal and the meridional component. This is consistent with the view held by *Mayr et al.* [1998] that gravity waves reduce the vertical wavelength of the tide in the 80-120 km altitude range resulting in a phase advance during the equinoxes. Contrary to the semi-annual phase structure at Grahamstown, the Adelaide pattern is more annual in nature with latest phases recorded in summer followed by a phase advance between autumn and spring. At both sites, the zonal and meridional phases are better correlated than their amplitude counterparts. Also, at both sites the diurnal tide is close to quadrature with the zonal component generally leading its meridional counterpart as expected for an anticlockwise rotation of the velocity vector in the southern hemisphere. The phases at Grahamstown and Adelaide compare favourably with the GSWM-00 and DTM except for an advance of ~10-18 h in the GSWM-00 phases.

For most of the months, the interannual variation in the zonal phases is correlated with that of meridional phases at both Grahamstown and Adelaide. The phases are less variable from year-to-year compared to amplitudes. While the QBO related modulation of the UV-ozone forcing is not expected to have a major impact on phases, the QBO modulation of gravity wave fluxes and dissipation can affect the phases.

A comparison of the phase behaviour at Grahamstown and Adelaide show a close similarity in the phase structure at the two sites. The general trend shows that the zonal phases at the two sites are comparable to each other from May to September with Grahamstown having slightly later phases. For the rest of the year Adelaide phases lag the Grahamstown ones by ~1-3 h. For the meridional component, Adelaide phases tend to lag the Grahamstown ones by ~1-5 h throughout the year. Zonal (GT-AD) differences have an 8-year average of about –1 h compared to about –3 h for the meridional component. Being small, these differences suggest that the diurnal tidal structure is dominated by the migrating tide. This is in agreement with *Ekanayake et al. 's* [1997] results for the 27.5-85°S latitude range at 90 km. The deviation from a phase difference of 0 h could be attributed to nonmigrating tides. The strong showing of negative phase differences suggest that, in agreement with *Ekanayake et al.* [1997], the nonmigrating tidal spectrum, is dominated by eastward propagating nonmigrating modes.

8.3.3 The Semidiurnal Tide

8.3.3.1 Amplitude

The zonal amplitudes at Grahamstown follow a well-defined annual cycle characterized by a peak in autumn. On the other hand, the meridional amplitudes at this site do not exhibit a clearly defined seasonal pattern but show a slight tendency to also have larger amplitudes in autumn. While the differences in the seasonal pattern of the two horizontal components cannot be explained, similar differences have been observed by other authors (e.g. *Vincent et al.* [1998]). Contrary to Grahamstown, Adelaide has a closer similarity in the seasonal pattern of the zonal and the meridional amplitudes. The general trend shows a primary peak in summer and two secondary peaks in late autumn/early winter and in late winter/early spring. The distribution of the differences between the zonal and the meridional amplitudes at Grahamstown show that the bulk (60 %) of the differences are due to larger zonal amplitudes. Unlike at Grahamstown, the meridional amplitudes at Adelaide are marginally larger (53.3 %) than their zonal counterpart.

Except for the large autumnal amplitudes at Grahamstown, the observations at Grahamstown and Adelaide compare reasonably well with the GSWM-00 and the STM but there are differences in detail. The seasonal variation of the semidiurnal tide, and in particular the autumnal amplitude peak observed at Grahamstown and by WINDII and HRDI, are thought to

be due to the seasonal changes of higher order modes [*Forbes*, 1982]. The absence of a similar peak at Adelaide suggests that this site might be having a different modal composition to Grahamstown. Such a situation is possible as presumed by *Lysenko et al.* [1994] based on the different vertical wavelengths observed at Saskatoon (52°N, 107°W) and Kazan (56°N, 49°E). The autumnal discrepancy between Grahamstown and Adelaide could also be due to the differences in the mean flow between the two sites. For instance, conclusions made by *Hagan* [1996] seem to suggest that the semidiurnal tide is sensitive to changes in the zonal mean flow. The contribution of non-migrating modes can also introduce differences between Grahamstown and Adelaide.

As with earlier findings regarding the mean flow and the diurnal tide, the semidiurnal tide is stronger at Grahamstown than at Adelaide. The statistics of the (GT-AD) difference distributions show that the bulk (~69 % for both the zonal and the meridional component) of the discrepancies between amplitudes at two sites are due to larger amplitudes at Grahamstown. At Grahamstown (where there is adequate data to delineate interannual patterns), we observe that there is evidence of correlation in the interannual changes of the zonal and the meridional components for most months but less so in winter. While it has been suggested that solar effects could contribute to the interannual variations of the semidiurnal tide, there is currently no conclusive view on the actual influence, if any.

8.3.3.2 Phase

The zonal and the meridional phases at Grahamstown, unlike at Adelaide, follow similar patterns. The general trend at Grahamstown shows a solstitial phase bi-modality characterized by earlier phases [~-4 h (EW) and ~-3 h (NS)] in summer and later phases in winter [~0 h (EW) and ~3 h (NS)]. The IAs at Adelaide, are similar to the Grahamstown pattern with both the zonal and the meridional showing a phase bi-modality with earlier phases [~-4 h (EW) and ~-1 h (NS)] in summer and later phases [~0-1 h (EW) and ~5 h (NS)] in winter but in this case (contrary to Grahamstown) the equinoctial transitions are sharper and also exhibit some overshoots.

In general, the phase bi-modality observed at Grahamstown and Adelaide is consistent with

results from WINDII [*McLandress et al.*, 1996] and HRDI for latitudes 40°S, 50°S, and 60°S [*Burrage et al.*, 1995b]. The zonal phases at Grahamstown and Adelaide compare favourably with the GSWM-00 and the STM. For the meridional component there is good qualitative agreement between the models and the observations during the summer and the equinoxes. However, during winter the observations at the Grahamstown and Adelaide show a phase delay while the models have a phase advance.

At both Grahamstown and Adelaide the semidiurnal tide, like the diurnal tide, are close to quadrature (3 h) and the zonal component is generally leading its meridional counterpart. Unlike the diurnal tide, the semidiurnal phases show less interannual variation especially at Grahamstown. Some of the observable interannual changes show correlation between the zonal and the meridional component. Since during such months the phase difference between the zonal and the meridional component is interannually invariant, there is a possibility of a similar invariance in the mode composition of the tide during these months.

A comparison of the Grahamstown and Adelaide phases show that the zonal phases at the latter are generally later by ~1-7 h compared those at the former except in summer when they tend to be earlier or comparable to the Grahamstown ones. The meridional phases at Adelaide tend to be later than the Grahamstown ones by ~1-8 h except around the equinoxes when Grahamstown tend to lead Adelaide by ~3 h. The meridional (GT-AD) phases differences tend to be larger than their zonal counterparts. The distribution of the (GT-AD) phase differences show a large spread with differences ranging from –6 h to 5 h. The majority of the differences are -2 or -1 h for both components. These phase differences could be due to the existence of non-migrating semidiurnal modes between Grahamstown and Adelaide and are in line with the calculations of *Sivkov & Shved* [1993] which give maximum longitudinal phase variations of < 2 h at ~30°S and 95 km.

8.4 CONCLUSION

In this thesis, I have presented a comparison on the dynamic structure at ~ 90 km altitude and about 34°S with a special focus on the observations made at Grahamstown and Adelaide. In particular, I have considered the structure of the mean flow and tides at the two sites. In general there are broad similarities in the dynamics of the atmosphere at the two sites. Generally, my

results are consistent with theory as well as results from other workers based on simulations, ground-based observations and satellite observations. However, there are also differences in the dynamic structure between Grahamstown and Adelaide and these are most likely due to non-migrating components and similar effects. A feature that stands out regarding differences is that Grahamstown tends to have stronger mean and tidal components than Adelaide. The cause for this is not clear but it could be related to (i) systematic differences between observational techniques, (ii) difference in actual height being studied at the two sites, (iii) height integration, and (iv) genuine longitudinal differences in the dynamic structure between the two sites. Although in Chapter 3 I tried to address points (i) to (iii), the influence associated with these factors cannot be totally discounted.

APPENDIX A ADDITIONAL FIGURES

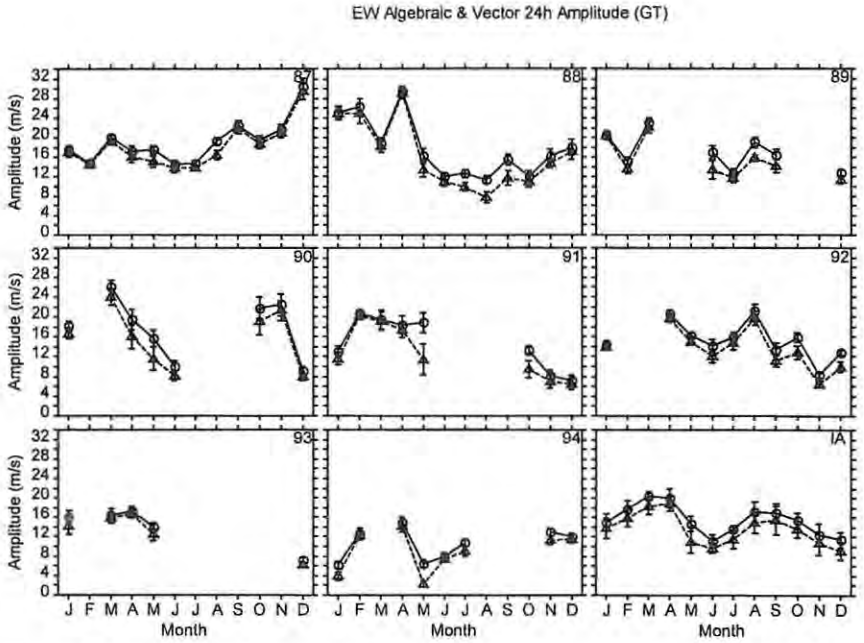

Figure 1 The algebraic (circles) and the vector (triangle) zonal amplitudes of the diurnal tide at Grahamstown for the years 1987-1994 and the IA. The error bars represent one standard error of the mean (1 α).

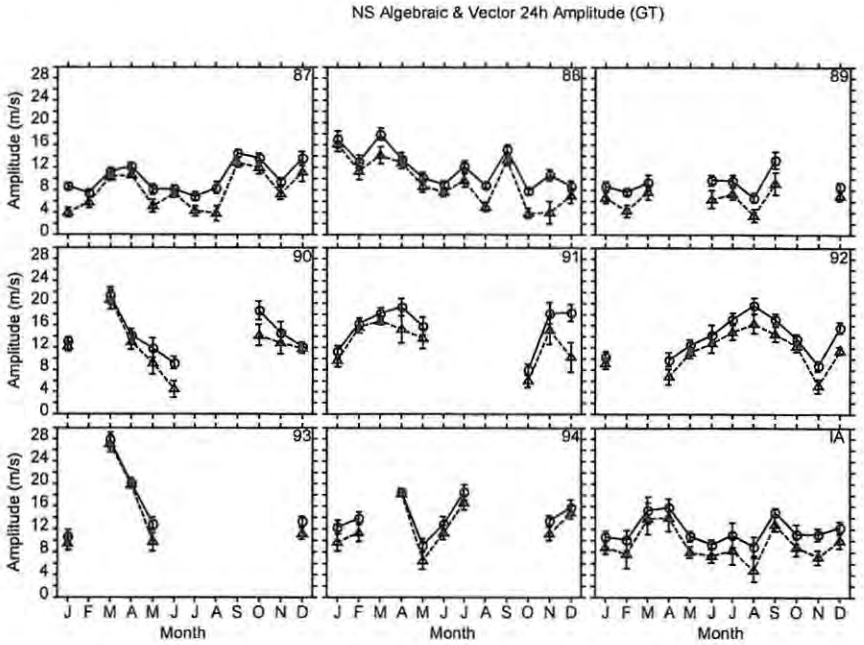

Figure 2 Same as **Figure 1** but for meridional amplitudes.

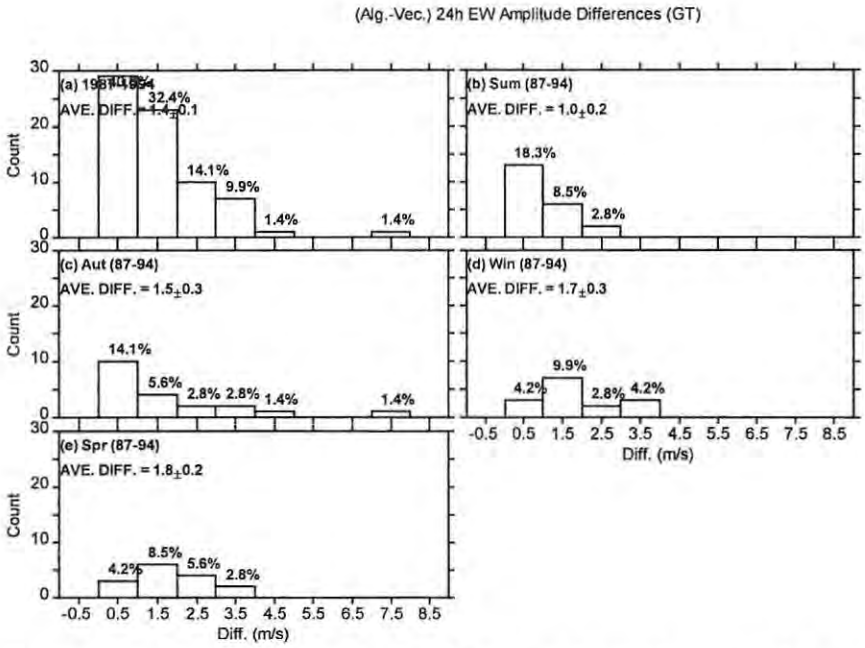

Figure 3 The distribution of the (Alg.-Vec.) zonal amplitude differences for the diurnal tide at Grahamstown for the years 1987-1994. The weighted average differences are also given and the percentage count of each bar.

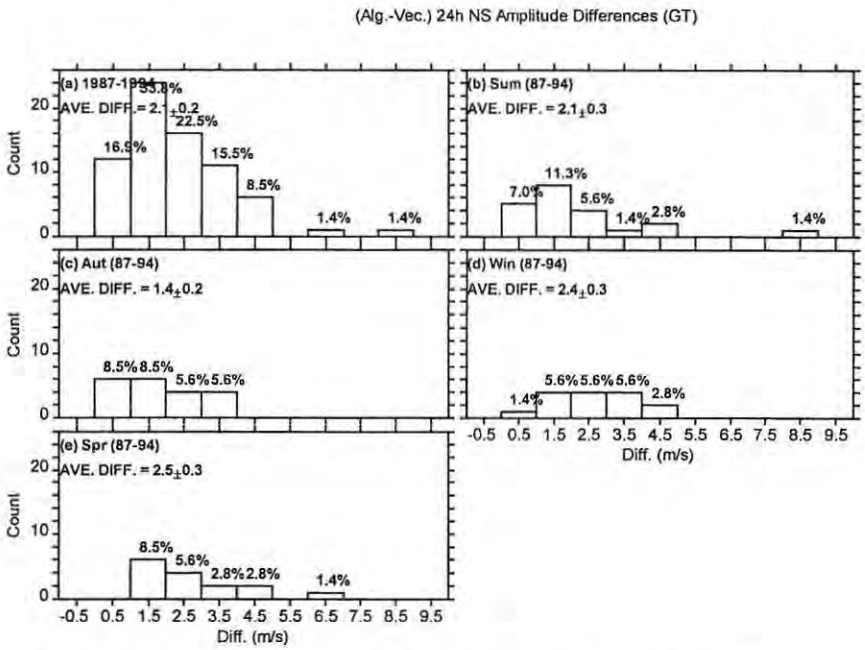

Figure 4 Same as **Figure 3** but for meridional amplitudes.

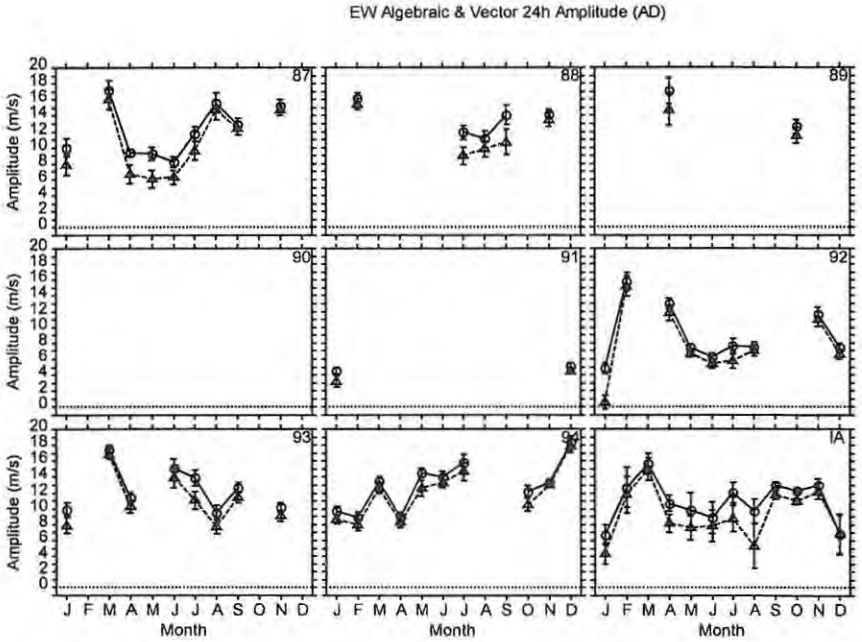

Figure 5 The algebraic (circles) and the vector (triangle) zonal amplitudes of the diurnal tide at Adelaide for the years 1987-1994 and the IA. The error bars represent one standard error of the mean (1 α).

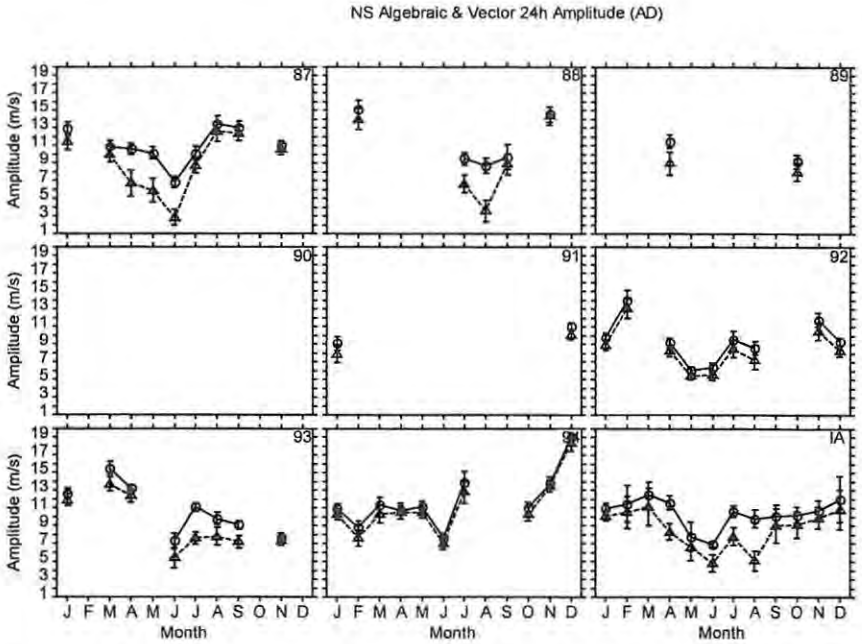

Figure 6 Same as **Figure 5** but for meridional amplitudes.

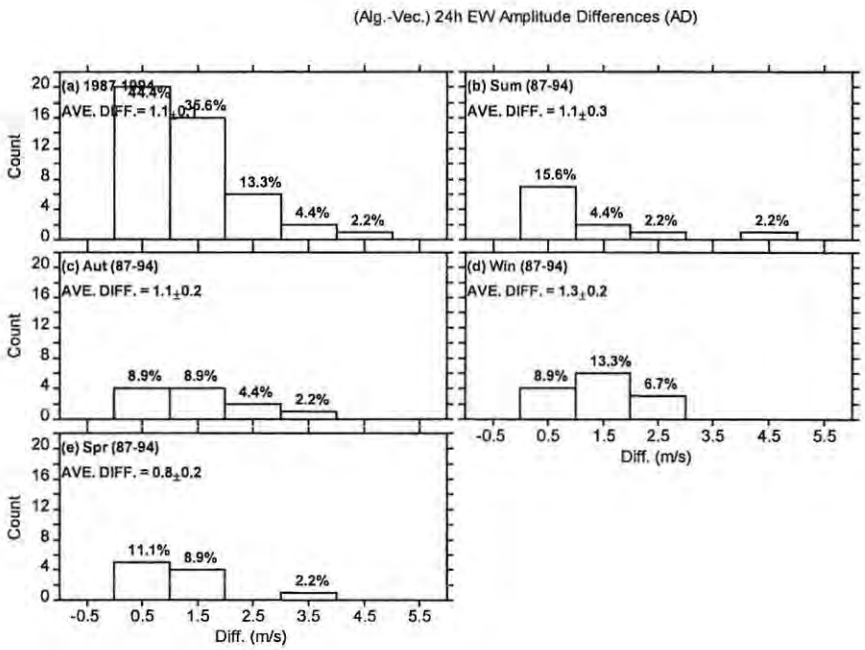

Figure 7 The distribution of the (Alg.-Vec.) zonal amplitude differences for the diurnal tide at Adelaide for the years 1987-1994. The weighted average differences are also given and the percentage count of each bar.

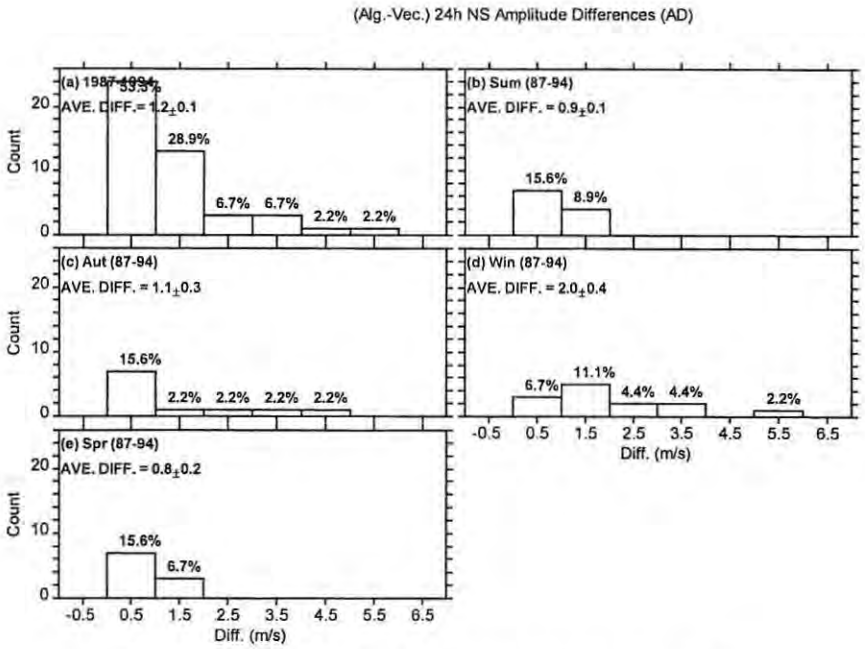

Figure 8 Same as **Figure 7** but for meridional amplitudes.

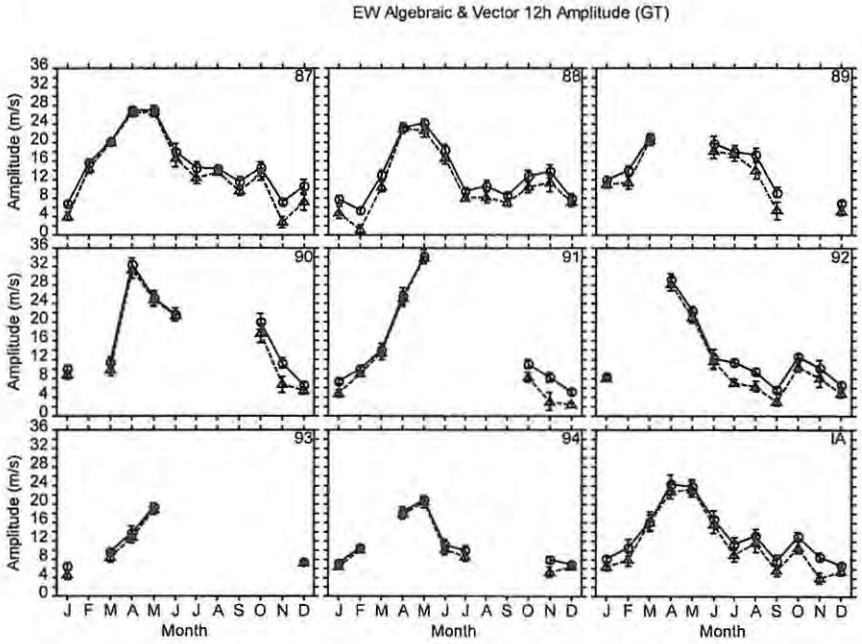

Figure 9 The algebraic (circles) and the vector (triangle) zonal amplitudes of the semidiurnal tide at Grahamstown for the years 1987-1994 and the IA. The error bars represent one standard error of the mean (1 α).

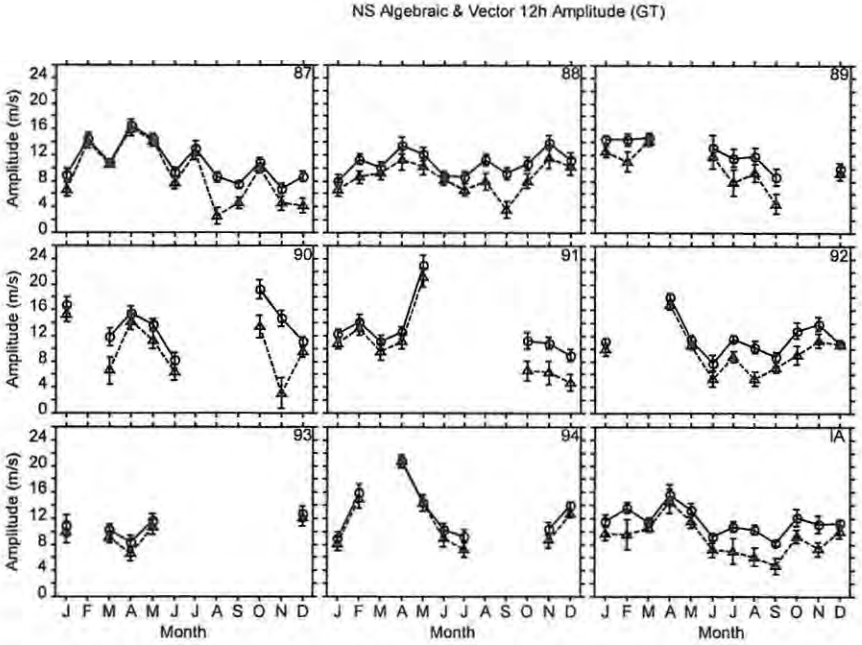

Figure 10 Same as **Figure 9** but for meridional amplitudes.

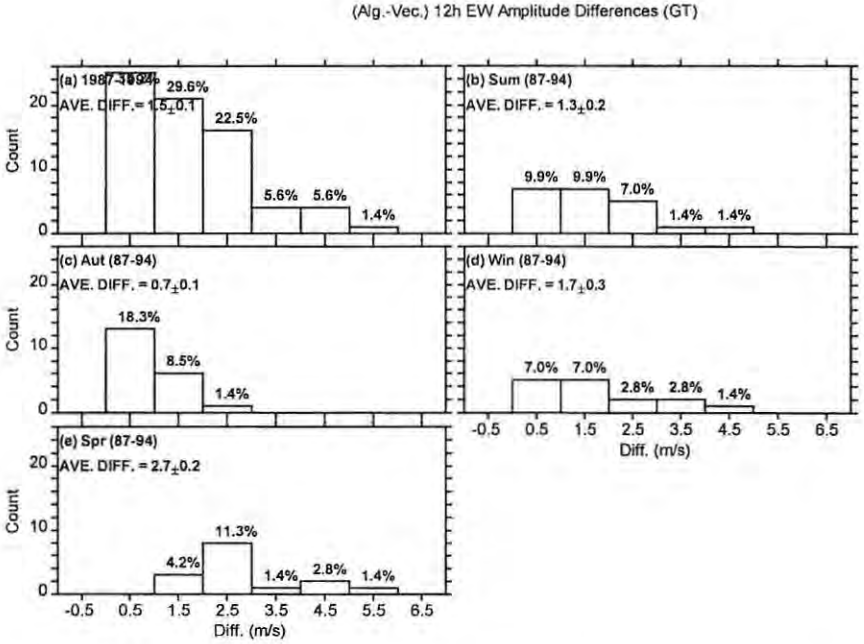

Figure 11 The distribution of the (Alg.-Vec.) zonal amplitude differences for the semidiurnal tide at Grahamstown for the years 1987-1994. The weighted average differences are also given and the percentage count of each bar.

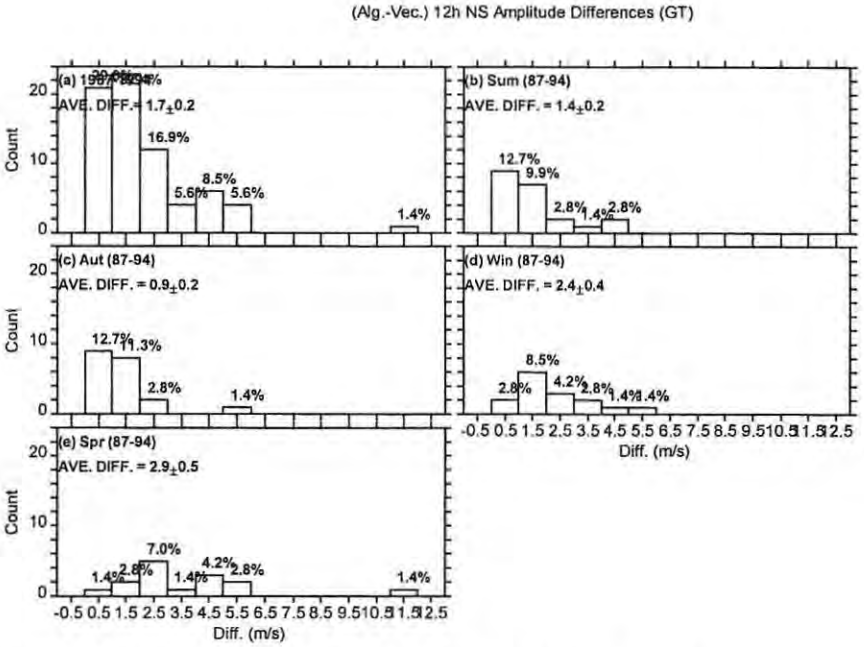

Figure 12 Same as **Figure 11** but for meridional amplitudes.

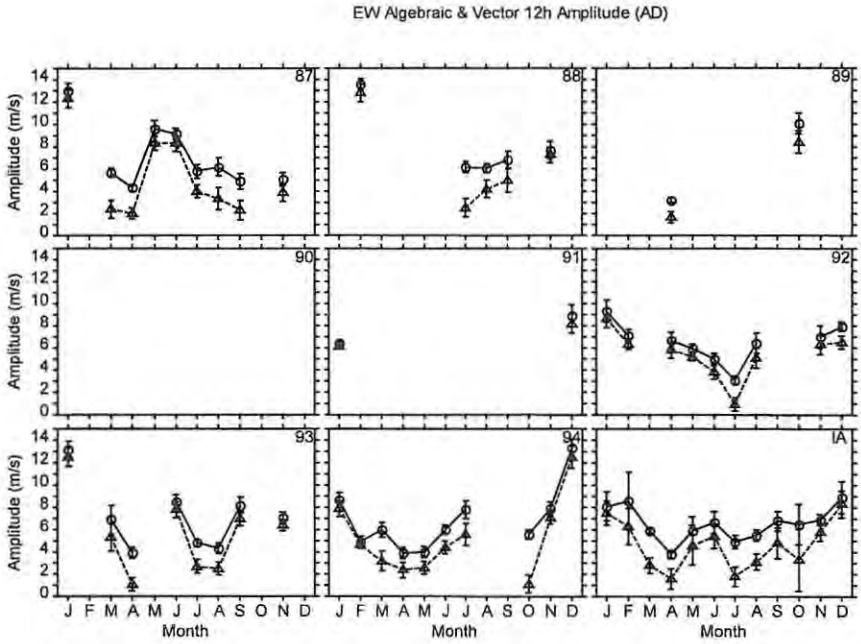

Figure 13 The algebraic (circles) and the vector (triangle) zonal amplitudes of the semidiurnal tide at Adelaide for the years 1987-1994 and the IA. The error bars represent one standard error of the mean (1 α).

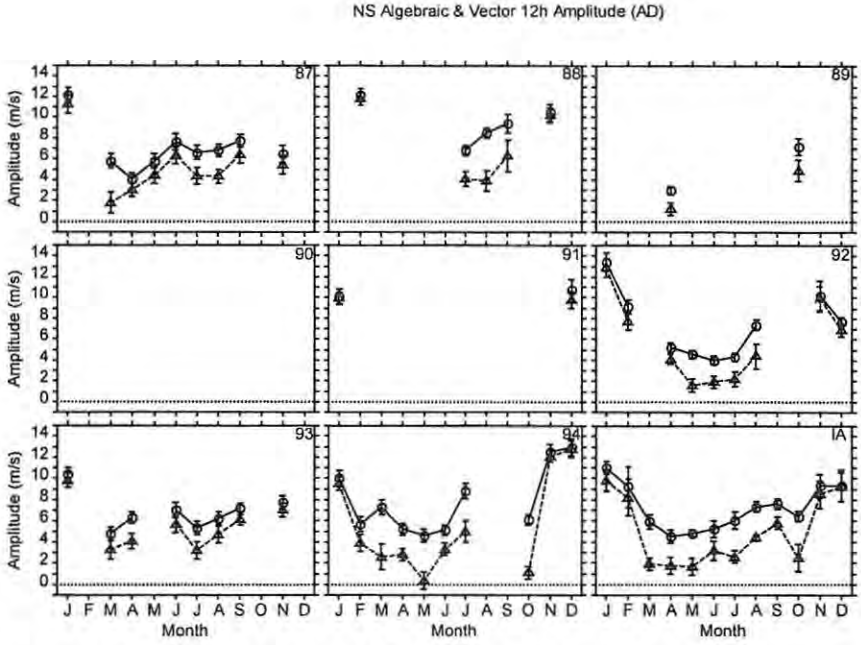

Figure 14 Same as **Figure 13** but for meridional amplitudes.

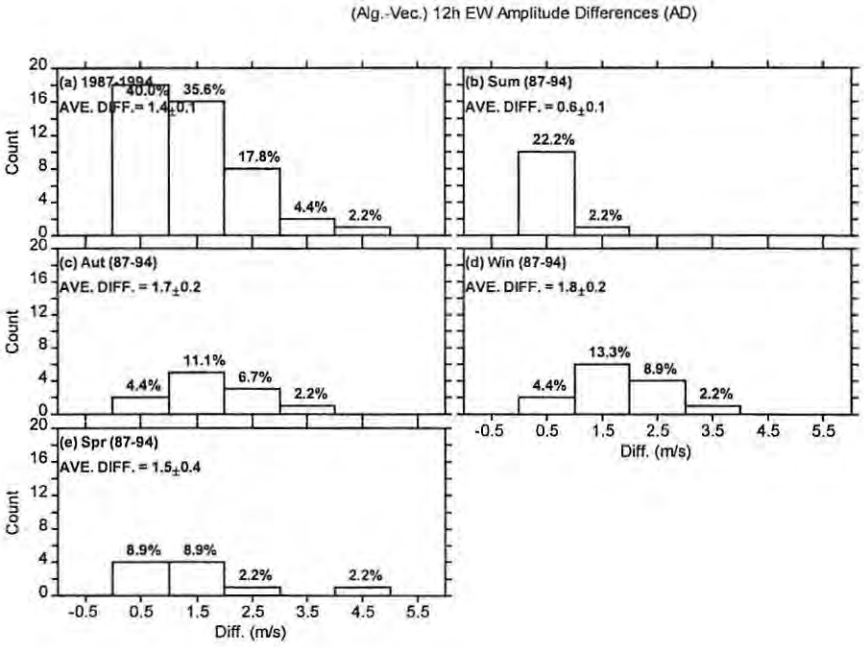

Figure 15 The distribution of the (Alg.-Vec.) zonal amplitude differences for the semidiurnal tide at Adelaide for the years 1987-1994. The weighted average differences are also given and the percentage count of each bar.

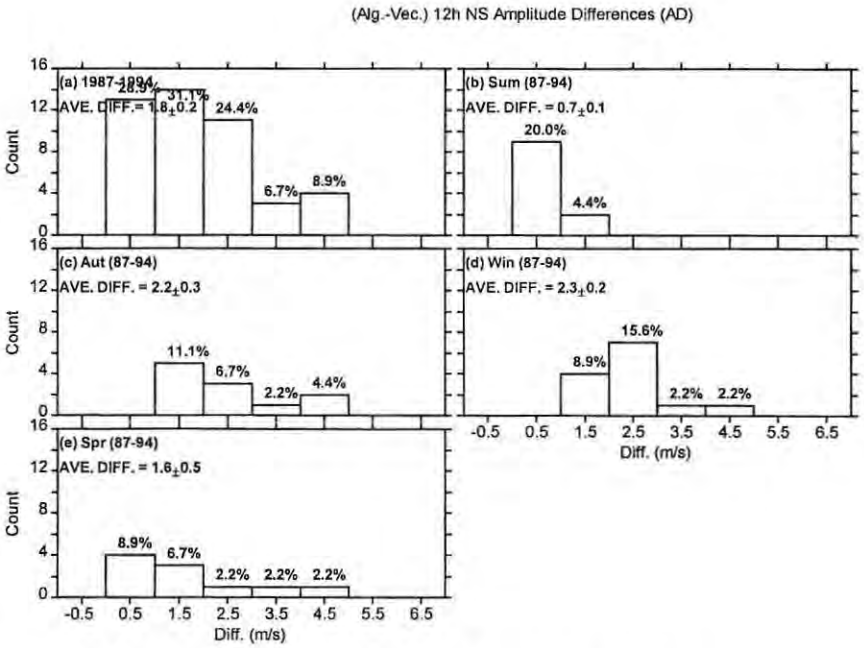

Figure 16 Same as **Figure 15** but for meridional amplitudes.

REFERENCES

Ahlquist, J. E., Normal-mode global Rossby waves: Theory and observations, *J. Atmos. Sci. 39*, 193-202, 1982.

Akmaev, R. A, J. M. Forbes, & M. E. Hagan, Simulations of tides with a spectral mesosphere/lower thermosphere model, *Geophys. Res. Lett., 23*, 2173-2176, 1996.

Alexander, M. J., A simulated spectrum of convectively generated gravity waves: Propagation from the tropopause to the mesopause and effects on the middle atmosphere, *J. Geophys. Res 101*, 1571-1588, 1996.

Alpert, J. C., M. A. Geller, & S. K. Avery, The response of stationary planetary waves to tropospheric forcing, *J. Atmos. Sci.*, 40, 2467-2483, 1983.

Avery, S. K., R. A. Vincent, A. Phillips, A. H. Manson, & G. J. Fraser, High-latitude tidal behavior in the mesosphere and lower thermosphere, *J. Atmos. Terr. Phys., 51*, 595-608, 1989.

Beard, A. G., N. J. Mitchell, P. J. S. Williams, & M. Kunitake, Non-linear interactions between tides and planetary waves resulting in periodic tidal variability, *J. Atmos. Solar Terr. Phys., 61*, 363-376, 1999.

Bernard, R., Variability of the semi-diurnal tide in the upper mesosphere, *J. Atmos. Terr. Phys., 43*, 663-674, 1981.

Bloomfield, P., *Fourier Analysis of time series: an introduction*, John Wiley & Sons, New York, 1976.

Braddick, H. J. J., *Vibrations, waves and diffraction*, McGraw-Hill, London, 1965.

Bremer, J., R. Schminder, K. M. Greisiger, P. Hoffmann, D. Kürschner, & W. Singer, Solar cycle dependence and long-term trends in the wind field of the mesosphere/lower thermosphere, *J. Atmos. Solar-Terr. Phys., 59*, 497-509, 1997.

Burrage, M. D., M. E. Hagan, W. R. Skinner, D. L. Wu, & P. B. Hays, Long-term variability in the solar diurnal tide observed by HRDI and simulated by the GSWM, *Geophys. Res. Lett., 22*,

2641-2644, 1995a.

Burrage, M. D., D. L. Wu, W. R. Skinner, D. A. Ortland, & P. B. Hays, Latitude and seasonal dependence of the semidiurnal tide observed by the high-resolution Doppler imager, *J. Geophys. Res., 100*, 11,313-11,321, 1995b.

Cervera, M. A. and I. M. Reid, Comparison of simultaneous wind measurements using colocated VHF meteor radar and MF spaced antenna radar systems', *Radio Science, 30*, 1245-1261, 1995.

Chan, K. L., H. G. Mayr, J. G. Mengel, & I. Harris, A spectral approach for studying middle and upper atmospheric phenomena, *J. Atmos. Terr. Phys., 56*, 1399-1419, 1994.

Charles, K., and G. O. L. Jones, Mesospheric mean winds and tides observed by the imaging doppler interferometer (IDI) at Halley, Antarctica, *J. Atmos. Solar-Terr. Phys. 61*, 351-362, 1999.

Chatfield, C., *The analysis of time series. An Introduction*, Chapman & Hall, London, 1989.

Clark, I., *Practical geostatistics*, Elsevier Applied Science Publishers Ltd, London, 1979.

Clark, R. R., & J. S. Bergin, Bispectral analysis of mesosphere winds, *J. Atmos. Solar. Terr. Phys., 59*, 629-639, 1997.

Daubechies, I., *Ten lectures on wavelets*, Society for Industrial and Applied Mathematics, Philadelphia, 1992.

Diggle, P. J., *Time series. A biostatical introduction*, Clarendon Press, Oxford, 1990.

Dunkerton, T. J., Theory of the mesopause semiannual oscillation, *J. Atmos. Sci., 39*, 2681-2690, 1982.

Eckermann, S. D., D. K. Rajopadhyaya, and R. A. Vincent, Intraseasonal wind variability in the equatorial mesosphere and lower theremosphere: long-term observations from the central

Pacific, *J. Atmos. Solar-terr. Phys. 59*, 603-627, 1997.

Ekanayake, E. M. P., T. Aso, & S. Miyahara, Background wind effect on propagation of nonmigrating diurnal tides in the middle atmosphere, *J. Atmos. Solar-Terr. Phys., 59*, 401-429, 1997.

Espy, P. J., & G. Witt, Observation of a quasi 16-day oscillation in the polar summer mesospheric temperature, *Geophys. Res. Lett.*, 23, 1071-1074, 1996.

Espy, P. J., J. Stegman, and G. Witt, Interannual variations of the quasi-16-day oscillation in the polar summer mesospheric temperature, *J. Geophys. Res., 102*, 1983-1990, 1997.

Fleming, E. L., S. Chandra, M. D. Burrage, W. R. Skinner, P. B. Hays, B. H. Solheim, & G. G. Shepherd, Climatological mean wind observations from the UARS high-resolution Doppler imager and wind imaging interferometer: Comparison with current reference models, *J. Geophy. Res., 101*, 10,455-10,473, 1996.

Forbes, J. M., Atmospheric tides 2. The solar and lunar semidiurnal components, *J. Geophys. Res., 87*, 5241-5252, 1982.

Forbes, J. M., & G. V. Groves, Diurnal propagating tides in the low-latitude middle atmosphere, *J. Atmos. Terr. Phys., 49*, 153-164, 1987.

Forbes, J. M., Atmospheric tides between 80 km and 120 km, *Adv. Space Res., 10*, (12)127-(12)140, 1990.

Forbes, J. M., J. Gu, & S. Miyahara, On the interactions between gravity waves and the diurnal propagating tide, *Planet. Space Sci.*, 39, 1249-1257, 1991.

Forbes, J. M., M. E. Hagan, S. Miyahara, F. Vial, A. H. Manson, C. E. Meek, and Y. I. Portnyagin, Quasi 16-day oscillation in the mesosphere and lower thermosphere, *J. Geophys. Res., 100*, 9149-9163, 1995.

Fovell, R. D. Durran, & J. R. Holton, Numerical simulations of convectively generated stratospheric gravity waves, *J. Atmos. Sci. 49*, 1427-1442, 1992.

Fraser, G. J., Partial reflection spaced antenna wind measurements, *Handbook for Middle Atmosphere Program, 13*, 233-247, 1984.

Fraser, G. J., R. A. Vincent, A. H. Manson, C. E. Meek, & R. R. Clark, Inter-annual variability of tides in the mesosphere and lower thermosphere, *J. Atmos. Terr. Phys., 51*, 555-567, 1989.

Fraser, G. J., Yu. I. Portnyagin, J. M. Forbes, R. A. Vincent, I. A. Lysenko and N. A. Makarov, Diurnal tide in the Antarctic and Arctic mesosphere/lower thermosphere regions, *J. Atmos. Terr. Phys., 57*, 383-393, 1995.

Fritts, D. C., & R. A. Vincent, Mesospheric momentum flux studies at Adelaide, Australia: Observations and a gravity wave-tidal interaction model, *J. Atmos. Sci.*, 44, 605-619, 1987.

Fritts, D. C., J. R. Isler, R. S. Lieberman, M. D. Burrage, D. R. Marsh, T Nakamura, T. Tsuda, R. A. Vincent, I. M. Reid, Two-day wave structure and mean flow interactions observed by radar and High Resolution Doppler Imager, *J. Geophys. Res. 104*, 3953-3969, 1999.

Groves, G. V., Annual and semi-annual zonal wind components and corresponding temperature and density variations, 60-130 km, *Planet. Space Sci., 20*, 2099-2112, 1972.

Groves, G. V., Hough components of water vapor heating, *J. Atmos. Terr. Phys., 44*, 281-290, 1982.

Hagan, M. E., F. Vial, & J. M. Forbes, Variability in the upward propagating semidiurnal tide due to effects of QBO in the lower atmosphere, *J. Atmos. Terr. Phys., 54*, 1465-1474, 1992.

Hagan, M. E., J. M. Forbes, & F. Vial, On modeling migrating solar tides, *Geophys. Res. Lett., 22*, 893-896, 1995.

Hagan, M. E. Comparative effects of migrating solar sources on tidal signatures in the middle

and upper atmosphere, *J. Geophys. Res., 101*, 21,213-21,222, 1996.

Hagan, M. E., J. L. Chang, & S. K. Avery, Global-scale wave model estimates of nonmigrating tidal effects, *J. Geophys. Res., 102*, 16,439-16,452, 1997.

Hagan, M. E., M. D. Burrage, J. M. Forbes, J. Hackney, W. J. Randel, & X. Zhang, GSWM-98: Results of migrating solar tides, *J. Geophys. Res., 104*, 6813-6827, 1999.

Hamilton, K., Comprehensive meterological modeling of the middle atmosphere: a tutorial review, *J. Atmos. Terr. Phys. 58*, 1591-1627, 1996.

Harris, T., *Large-scale dynamics of the upper mesosphere and lower thermosphere*, Ph.D. Thesis submitted to the University of Adelaide, Adelaide,1993.

Hays, B. P., V. J. Abreu, M. E. Dobbs, D. A. Gell, H. J. Grassl, & W. R. Skinner, The high-resolution Doppler imager on the upper atmosphere research satellite, *J. Geophys. Res., 98*, 10,713-10,723, 1993.

Hines, C. O., Gravity waves in the atmosphere, *Nature, 239*, 73-78, 1972.

Hines, C. O., Doppler-spread parameterization of gravity-wave momentum deposition in the middle atmosphere. Part 1: Basic formulation, *J. Atmos. Solar Terr. Phys., 59*, 371-386, 1997a.

Hines, C. O., G. W. Adams, J. W. Brosnahan, F. T. Djuth, M. P. Sulzer, C. A. Tepley and J. S. Van Baelen, Multi-instrument observations of mesospheric motions over Arecibo: comparisons and interpretations, *J. Atmos. Terr. Phys., 55*, 241-287, 1993.

Hines, C. O., Doppler-spread parameterization of gravity-wave momentum deposition in the middle atmosphere. Part 2: Broad and quasi monochromatic spectra, and implementation, *J. Atmos. Solar Terr. Phys., 59*, 387-400, 1997b.

Hinich, M. J. and C. S. Clay, The application of the discrete Fourier transform in the estimation of power spectra, coherence, and bispectra of geophysical data, *Reviews of*

Geophysics, 6, 347-363, 1968.

Hocking, W. K., Dynamic coupling processes between the middle atmosphere and lower ionosphere, *J. Atmos. Terr. Phys., 58*, 735-752, 1996.

Hocking, W. K. and T. Thayaparan, Simultaneous and colocated observation of winds and tides by MF and meteor radars over London, Canada (43°N, 81°W), during 1994-1996, *Radio Sci., 32*, 833-865, 1997.

Holton, J. R., The role of gravity wave induced drag and diffusion in the momentum budget of the mesosphere, *J. Atmos. Sci., 39*, 791-799, 1982.

Jacobi, Ch., R. Schminder, D. Kürschner, J. Bremer, K. M. Greisiger, P. Hoffmann, W. Singer, Long-term trends in the mesopause wind field obtained from D1 LF wind measurements at Collm, Germany, *Advances in Space Research, 20*, 2085-2088, 1997.

Jacobi, Ch., R. Schminder, & D. Kürschner, Non-linear interaction of the quasi 2-day wave and long-term oscillations in the summer midlatitude mesopause region as seen from LF D1 wind measurements over Central Europe (Collm, 52°N, 15°E), *J. Atmos. Solar Terr. Phys., 60*, 1175-1191, 1998.

Jacobi, Ch., Yu. I. Portnyagin, T. V. Solovjova, P. Hoffmann, W. Singer, A. N. Fahrutdinova, R. A. Ishmuratov, A.G. Beard, N. J. Mitchell, H. G. Muller, R. Schminder, D. Kürschner, A. H. Manson, C. E. Meek, Climatology of the semidiurnal tide at 52-56°N from ground-based radar wind measurements 1985-1995, *J. Atmos. Solar. Terr. Phys., 61*, 975-991, 1999.

Journel, A. G., & Ch. J. Huijbregts, *Mining geostatistics*, Academic Press, London, 1978.

Kaiser, G., *A friendly guide to wavelets*, Birkhäuser, Boston, 1994.

Kamalabadi, F., J. M. Forbes, N. M. Makarov, & Yu. I. Portnyagin, Evidence of nonlinear coupling of planetary waves and tides in the Antarctic mesopause, *J. Geophys. Res., 102*, 4437-4446, 1997.

Kazimirovsky, E., A. H. Manson, & C. E. Meek, Winds and waves in the middle atmosphere at Saskatoon (52°N, 107°W), Collm (52°N, 15°E) and Badary (52°N, 105°E), *J. Atmos. Terr. Phys.* 50, 243-250, 1988.

Khattatov, B. V. *et al.*, Dynamics of the mesosphere and lower thermosphere as seen by MF radars and by the high-resolution Doppler imager/UARS, *J. Geophys. Res., 101*, 10,393-10,404, 1996.

Khattatov, B. V., V. A. Yubin, M. A. Geller, B. P. Hays, & R. A. Vincent, Diurnal migrating tide as seen by the high-resolution Doppler imager/UARS. 1. Monthly mean global meridional winds, *J. Geophys. Res., 102*, 4405-4422, 1997a.

Khattatov, B. V., M. A. Geller, V. A. Yubin, & B. P. Hays, Diurnal migrating tide as seen by the high-resolution Doppler imager/UARS. 2. Monthly mean global zonal and vertical velocities, pressure, temperature, and inferred dissipation, *J. Geophys. Res., 102*, 4423-4435, 1997b.

Lu, W., & D. C. Fritts, Spectral estimates of gravity wave energy and momentum fluxes. Part III: Gravity wave-tidal interactions, *J. Atmos. Sci., 50*, 3714-3727, 1993.

Lysenko, I. A., Yu. I. Portnyagin, A. N. Fakhrutdinova, R. A. Ishmuratov, A. H. Manson, & C. E. Meek, Wind regime at 80-110 km at mid-latitudes of the northern hemisphere, *J. Atmos. Terr. Phys., 56*, 31-42, 1994.

Malinga S. B. and L. M. G. Poole, Atmospheric tides observed at Grahastown (33.3°S, 26.5° E), *J. Atmos. Solar-Terr. Phys., 59*, 2037-2050, 1997.

Malinga, S. B., L. M. G. Poole, R. A. Vincent, Simultaneous observations of atmospheric summer tides at Grahamstown (South Africa) and Adelaide (Australia), *J. Atmos. Solar Terr. Phys., 60*, 1459-1469, 1998.

Mallat, S. G., Multifrequency channel decompositions of images and wavelet models, *IEEE*

Transactions on Acoustics, Speech, and Signal Processing, 37, 2091-2110, 1989.

Manson, A. H., J. B. Gregory, & C. E. Meek, Atmospheric waves (≈10 min-30 days) in the mesosphere and thermosphere at Saskatoon (52°N, 107°W), October 1978 – September 1979, *Planet. Space Sci. 29*, 615-625, 1981.

Manson, A. H., C. E. Meek, J. L. Fellous & M. Massebeuf, Winds oscillations (~ 6 h-6 days) in the upper middle atmosphere at Mompazier (France, 45°N, 1°E) and Saskatoon (Canada, 52°N, 107°W) in 1979-1980, *J Atmos. Terr. Phys., 49*, 1059-1069, 1987.

Manson, A. H., C. E. Meek, H. Teitelbaum, F. Vial, R. Schminder, D.Kürschner, M. J. Smith, G. J. Fraser, R. R. Clark, Climatologies of semi-diurnal and diurnal tides in the middle atmosphere (70-110 km) at middle latitudes (40-55°), *J. Atmos. Terr. Phys., 51*, 579-593, 1989.

Manson, A, C. Meek, M. Hagan, C. Hall, W. Hocking, J. MacDougall, S. Franke, D. Riggin, D. Fritts, R. Vincent, M. Burrage, Seasonal variations of the semi-diurnal and diurnal tides in the MLT: multi-year MF radar observations from 2 to 70°N, and the GSWM tidal model,*J. Atmos. Solar Terr. Phys., 61*, 809-828, 1999.

Mayr, H. G., J. G. Mengel, K. L. Chan,& H. S. Porter, Seasonal variations of the diurnal tide induced by gravity wave filtering, *Geophys. Res. Lett., 25*, 943-946, 1998.

McFarlane, N. A., The effect of orographically excited gravity wave drag on the general circulation of the lower stratosphere and troposphere, *J. Atmos. Sci. 44*, 1775-1800, 1987.

McLandress, C., G. G. Shepherd, & B. H. Solheim, Satellite observations of thermospheric tides: Results from the Wind Imaging Interferometer on UARS, *J. Geophys. Res., 101*, 4093-4114, 1996.

McLandress, C., Seasonal variability of the diurnal tide: Results from the Canadian middle atmosphere general circulation model, *J. Geophys. Res., 102*, 29,747-29,764, 1997.

Meyer, C. K., Gravity wave interactions with the diurnal propagating tide, *J. Geophys. Res.,*

104, 4223-4239, 1999.

Misiti, M., Y. Misiti, G. Oppenheim, and J. Poggi, *Wavelet Toolbox*, The MathWorks, Inc. Natick, 1996.

Miyahara, S. Y. Yoshida, & Y. Miyoshi, Dynamic coupling between the lower and upper atmosphere by tides and gravity waves, *J. Atmos. Terr. Phys., 55*, 1039-1053, 1993.

Murphy, D. J., & R. A. Vincent, Mesospheric momentum fluxes over Adelaide during the 2-day wave: Results and interpretation, *J. Geophys. Res. 103*, 28,627-28,636, 1998.

Nakamura, T., T. Tsuda, and S. Fukao, Mean winds at 60-90 km observed with the MU radar (35°N), *J. Atmos. Terr. Phys. 58*, 655-660, 1996.

Namboothiri, S. P., A. H. Manson, & C. E. Meek, Variations of mean winds and tides in the upper middle atmosphere over a solar cycle, Saskatoon, Canada, 52°N, 107°W, *J. Atmos. Terr. Phys., 55*, 1325-1334, 1993.

Namboothiri, S. P., C. E. Meek, & A. H. Manson, Variations of mean winds and solar tides in the mesosphere and lower thermosphere over time scales ranging from 6 months to 11 yr: Saskatoon, 52°N, 107°W, *J. Atmos. Terr. Phys., 56*, 1313-1325, 1994.

Namboothiri, S. P., T. Tsuda, and T. Nakamura, Interannual variability of mesospheric mean winds observed with the MU radar, *J. Atmos. Solar-Terr. Phys. 61*, 1111-1122, 1999.

Nikias, C. L. and M. R. Raghuveer, Bispectrum estimation: a digital signal processing framework, *Proceedings of the IEEE, 75*, 869-891, 1987.

Norton, W. A., & J. Thuburn, Sensitivity of mesospheric mean flow, planetary waves, and tides to strength of gravity wave drag, *J. Geophys. Res., 104*, 30,897-30,911, 1999.

Otnes, R. K., & L. Enochson, *Applied time series analysis. Volume 1. Basic techniques*, John Wiley & Sons, New York, 1978.

Pancheva, D., Evidence for nonlinear coupling of planetary waves and tides in the lower thermosphere over Bulgaria, *J. Atmos. Solar Terr. Phys.*, 62, 115-132, 2000.

Pawson, S., K., Labitzke, R., Lenschow, B., Naujokat, B., Rajewski, M. Wiesner, R-C., Wohlfart, Climatology of the northen hemisphere stratosphere derived from Berlin analyses. Part 1: monthly means. *Meteorologische Abhandlungen des Instituts für Meteorologie der Freien Universität Berlin*, N. F. A 7 (3), 1993.

Plumb, A. R., Baroclinic instability of the summer mesosphere: a mechanism for the quasi-two-day wave?, *J. Atmos. Sci., 40*, 262-270, 1983.

Polikar, R., The wavelet tutorial, at URL
http://www.public.iastate.edu/~rpolikar/WAVELETS/WTpart1.html, 1996.

Poole, L. M. G., The Grahamstown all-sky meteor radar, J. *Atmos. Terr. Phys., 50*, 585-590, 1988.

Poole, L. M. G., The characteristics of the mesospheric two-day wave as observed at Grahamstown (33.3°S, 26.5°E), *J. Atmos. Terr. Phys., 52*, 259-268, 1990.

Poole, L. M. G. & T. J. Harris, The propagation of the mesospheric two-day wave in the southern hemisphere, *J. Atmos. Terr. Phys.,57*, 1661-1666, 1995.

Portnyagin, Yu. I., J. M. Forbes, G. J. Fraser, R. A. Vincent, S. K. Avery, I. A. Lysenko, and N. A. Makarov, Dynamics of the Antarctic and Arctic mesosphere and lower thermosphere regions—I. The prevailing wind, *J. Atmos. Terr. Phys. 55*, 827-841, 1993a.

Portnyagin, Yu. I., J. M. Forbes, G. J. Fraser, R. A. Vincent, S. K. Avery, I. A. Lysenko, and N. A. Makarov, Dynamics of the Antarctic and Arctic mesosphere and lower thermosphere regions—II. The semidiurnal tide, J. *Atomos. Terr. Phys.*, 55, 843-855, 1993b.

Portnyagin, Yu. I., T. V. Solovjova, Empirical semidiurnal migrating tide model for the upper mesosphere/lower thermosphere, *Adv. Space Res., 21*, 811-815, 1998.

Portnyagin, Yu.I., & T.V. Solovjova, Global empirical model for the upper mesosphere/lower thermosphere.I. Prevailing wind., *Ann. Geophysicae, 18*, 300-315, 2000.

Poulter, E. M., Winter motions in the southern hemisphere meteor region, *J. Atmos. Terr. Phys., 42*, 661-672, 1980.

Priestley, M. B., *Spectral analysis and time series. Volume 2: Multivariate series, prediction and control*, Academic Press, London, 1981.

Raghava, C. and G. Ramkumar, The annual and semi-annual wind fields in low latitudes, *J. Atmos. Solar-Terr. Phys., 59*, 487-495, 1997.

Reber, C. A., C. E. Trevathan, R. J. McNeal, & M. R. Luther, The upper atmosphere research satellite (UARS) mission, *J. Geophys. Res., 98*, 10, 643-10,647, 1993.

Roper, R. G., MWR – Meteo wind radars, *Handbook for Middle Atmosphere Program, 13*, 124-134, 1984.

Roux, D. G., *An investigation of the structure of the Southern Hemisphere radio-meteor streams*, MSc Thesis submitted to Rhodes University, Grahamstown, 1988.

Rüster, R., VHF radar observations of nonlinear interactions in the summer polar mesosphere, *J. Atmos. Terr. Phys., 56*, 1289-1299, 1994.

Salby, M. L., & R. G. Roper, Long-period oscillations in the meteor region,*J. Atmos. Sci., 37*, 237-244, 1980.

Salby, M. L., Rossby normal modes in nonuniform background configurations. Part I: Simple fields, *J. Atmos. Sci., 38*, 1803-1826, 1981a.

Salby, M. L., Rossby normal modes in nonuniform background configurations. Part II: Equinox and solstice conditions, *J. Atmos. Sci., 38*, 1827-1840, 1981b.

Salby, M. L., The 2-day wave in the middle atmosphere: observations and theory, *J. Geophys. Res., 86*, 9654-9660, 1981c.

Shepherd, G. G., G. Thuillier, W. A. Gault, B. H. Solheim, C. Hersom, J. M. Alunni, J.-F. Brun, S. Brune, P. Charlot, L. L. Cogger, D.-L. Desaulniers, W. F. J. Evans, R. L. Gattinger, F. Girod, D. Harvie, R. H. Hum, D. J. W. Kendall, E. J. Llewllyn, R. P. Lowe, J. Ohrt, F. Pasternak, O. Peillet, I. Powell, Y. Rochon, W. E. Ward, R. H. Wiens, J. Wimperis, WINDII, the wind imaging interferometer on the upper atmosphere research satellite, *J. Geophys. Res., 98*, 10,725-10,750, 1993.

Shepherd, T. G., The middle atmosphere, *J. Atmos. Solar-Terr. Phys., 62*, 1587-1601, 2000.

Sivkov, A. M., & G. M. Shved, Influence of latitudinal and longitudinal variations of ozone and water vapour on the solar semidiurnal tide, *J. Atmos. Terr. Phys.*, 55, 815-826, 1993.

Smith, A. K., Wave transience and wave-mean flow interaction caused by the interference of stationary and traveling waves, *J. Atmos. Sci., 42*, 529-535, 1985.

Sprenger, K., & R. Schminder, Solar cycle dependence of winds in the lower ionosphere, *J. Atmos. Terr. Phys., 31*, 217-221, 1969.

Starck, J.-L., F. Murtagh and A. Bijaoui, *Image Processing and Data Analysis– The Multiscale Approach*, Cambridge University Press, Cambridge, 1998.

Teitelbaum, H., & F. Vial, On tidal variability induced by nonlinear interaction with planetary waves, *J. Geophys. Res., 96*, 14,169-14,178, 1991.

Thomas, G. E. Global change in the mesosphere-lower thermosphere region: has it already arrived? *J. Atmos.Solar Terr. Phys., 58*, 1629-1656, 1996.

Topping, J., *Errors of observation and their treatment*, 4th ed., Chapman and Hall, London, 1972.

Torrence, C., G. P. Compo, Wavelet software text, 1995.

Torrence, C., & G. P. Compo, A practical guide to wavelet analysis,*Bull. Amer. Meteor. Soc., 79*, 61-78, 1998.

Torrence, C., & G. P. Compo, A practical guide to wavelet analysis, at URL http://paos.colorado.edu/research/wavelets/, 1998.

Tsuda, T., S. Kato, & R. A. Vincent, Long period wind oscillations observed by the Kyoto meteor radar and comparison of the quasi-2-day wave with Adelaide HF radar observations,*J. Atmos. Terr. Phys., 50*, 225-230, 1988.

Valens, C., Valens Home Page at URL http://perso.wanadoo.fr/polyvalens/clemens/clemens.html, 1999.

Valentic, T. A., J. P. Avery, S. K. Avery, M. A. Cervera, W. G. Elford, R. A. Vincent, & I. M. Reid, A comparison of meteor radar systems at Buckland Park, *Radio Sci., 31*, 1313-1329, 1996.

Valentic, T. A., J. P. Avery, S. K. Avery, & R. A. Vincent,A comparison of winds measured by meteor radar systems and an MF radar at Buckland Park, *Radio Science, 32*, 867-874, 1997.

Vial, F. & H. Teitelbaum, Some consequences of turbulent dissipation on diurnal thermal tide, *Planet. Space Sci., 32*, 1559-1565, 1984.

Vial, F., Tides in the middle atmosphere,*J. Atmos. Terr. Phys., 51*, 3-17, 1989.

Vial, F., J. M. Forbes, S. Miyahara, Some transient aspects of tidal propagation,*J. Geophys. Res., 96*, 1215-1224, 1991.

Vincent, R. A., MF/HF radar measurements of the dynamics of the mesopause region—A review', *J. Atmos. Terr. Phys., 46*, 961-974, 1984.

Vincent, R. A., T. Tsuda and S. Kato, A comparative study of mesospheric solar tides observed at Adelaide and Kyoto, *J. Geophys. Res.*, 93, 699-708, 1988.

Vincent, R. A., Planetary and gravity waves in the mesosphere and lower thermosphere, *Adv. Space Res., 10*, (12)93-(12)101, 1990.

Vincent, R. A., S. Kovalam, D. C. Fritts, J. R. Isler, Long-term MF radar observations of solar tides in the low-latitude mesosphere: Interannaul variability and comparisons with the GSWM, *J. Geophys. Res., 103*, 8667-8683, 1998.

Walterscheid, R. L., Inertio-gravity wave induced accelerations of mean flow having an imposed periodic component: implications for tidal observations in the meteor region, *J. Geophys. Res., 86*, 9698-9706, 1981.

Wang, D-Y, & D. C. Fritts, Evidence of gravity wave-tidal interaction observed near the summer mesopause at Poker Flat, Alaska, *J. Atmos. Sci., 48*, 572-583, 1991.

Weiss, A. A., The temporal variation of the heights of reflection points of meteor trails, *Astralian Journal of Physics, 12*, 116-126, 1959.

Widdel, H.-U., M. Bittner, & U.-P. Hoppe, Vertical velocities measured at Biscarrosse (44°N) and by EISCAT at Tromsø (69.6°N) during the DYANA campaign, *J. Atmos. Terr. Phys., 56*, 1779-1796, 1994.

Williams, C. R., and S. K. Avery, Analysis of long-period waves using the mesosphere-stratosphere-troposphere radar at Poker Flat, Alaska, *J. Geophys. Res., 97*, 20,855-20,861, 1992.

Williams, C. R., & S. K. Avery, Diurnal nonmigrating tidal oscillations forced by deep convective clouds, *J. Geophys. Res., 101*, 4079-4091, 1996.